UNIVERSITÄT
SIEGEN

Michael Groß

Higher-order accurate and energy-momentum consistent discretisation of dynamic finite deformation thermo-viscoelasticity

Herausgeber: Peter Betsch

Schriftenreihe des Lehrstuhls für Numerische Mechanik

Band II

Impressum

Prof. Dr.-Ing. habil. Peter Betsch
Lehrstuhl für Numerische Mechanik
Universität Siegen
57068 Siegen
ISSN 1866-1203
urn:nbn:de:hbz:467-3890
Zugl.: Siegen, Univ., Habil., 2009

Higher-order accurate and energy-momentum consistent discretisation of dynamic finite deformation thermo-viscoelasticity

dem Fachbereich Maschinenbau
der Universität Siegen
zur Erlangung der venia legendi für das Fach

MECHANIK

vorgelegte Habilitationsschrift

von

Dr.-Ing. Michael Groß
aus Münchweiler

begutachtet von

Prof. Dr.-Ing. habil. P. Betsch
Prof. Dr.-Ing. habil. C. Miehe

eingereicht am

8. Oktober 2008

Habilitationsverfahren vollzogen am

26. Juni 2009

VORWORT

Es ist immer eine sehr angenehme Tätigkeit, am Ende einer längeren wissenschaftlichen Arbeitsperiode, die zur Erreichung eines größeren Zieles diente, wie das seiner Promotion oder seiner Habilitation, Dank auszusprechen. Es beginnt schon damit dass man dafür dankbar ist, überhaupt die Gelegenheit bekommen zu haben die wissenschaftliche Arbeit aufnehmen zu können. Das setzt zum einen Vorgesetzte voraus, die an das Forschungsvorhaben glauben und einem eine gewissenhafte Bearbeitung zutrauen, und zum anderen eine Familie voraus, die einem die notwendige Zeit einräumt, die zur wissenschaftlichen Arbeit notwendig ist. Weiterhin ist man für die vielen Diskussionen mit Kollegen, mit Studenten in Vorlesungen und auch mit Freunden dankbar, die zur Aufmunterung, zur Entwicklung neuer Ideen und auch zu einer noch besseren Form der aktuellen Arbeit führen. Hinzu kommt, dass die Arbeit an einem Lehrstuhl einer Universität ohne Rechnerunterstützung heute nicht mehr denkbar wäre. Sei es um, wie in dieser Arbeit, numerische Simulationen durchzuführen oder um Zeichnungen zur Illustration anzufertigen und die Arbeit in ansprechender Form zu Papier zu bringen.

An erster Stelle möchte ich meinem Betreuer Herr Professor Peter Betsch danken, der auch als erster Gutachter in meinem Habilitationsverfahren gewirkt hat. Er gab mir die Gelegenheit und den Anstoß zur Bearbeitung der Thematik dieser Arbeit, und gewährte mir auch die notwendigen Freiräume die Arbeit in der hier gebotenen Form zu Papier zu bringen, die mir persönlich sehr am Herzen lag. Ohne sein ungebrochenes Interesse am Fortgang der Arbeit, hätte sie nicht beendet werden können.

An zweiter Stelle möchte ich mich bei Herrn Professor Christian Miehe bedanken, der den Zeitaufwand nicht scheute das Habilitationsverfahren als zweiter Gutachter zu begleiten. Wie viele Stunden er dem Lesen und kritischen Beurteilen widmen musste wage ich nicht zu schätzen. Ich hoffe aber, dass es für ihn nicht nur Mühe bedeutet hat, sondern dass auch ein gewisses Maß an Freunde dabei war. Denn seine wissenschaftlichen Arbeiten, und die von Professor Juan Carlos Simo, waren ständige Inspirationen für die wissenschaftliche Ausarbeitung der behandelten Thematik.

Weiterhin möchte ich es nicht versäumen, mich bei Herrn Professor Claus-Peter Fritzen zu bedanken, der sich bereiterklärt hat den Vorsitz meines Habilitationsausschusses zu übernehmen, und somit auch den gesamten Verwaltungsaufwand zu bewältigen hatte. Den Mitgliedern des Habilitationsausschusses, und insbesondere Herrn Professor Klaus Schiffner, möchte ich dafür danken, dass sie den zügigen Fortgang des Verfahrens unterstützt haben, und meine Habilitation an der Universität Siegen ermöglichten.

Eine wissenschaftliche Arbeit kann nur dann effektiv durchgeführt werden, wenn die tägliche Verwaltungsarbeit nicht überhand nimmt. Es ist mir daher eine besondere Freude, mich bei Frau Gisela Thomas und bei Frau Ursula Schmidt für die vielfältige Unterstützung in den letzten Jahren zu bedanken. Zudem möchte ich mich bei Herrn Gerhard Knappstein nicht nur für die sehr angenehme Atmosphäre im Büro bedanken, sondern auch für die umfassende Unterstützung im Lehrbetrieb. Bei Herrn Jürgen Beumelburg möchte ich mich für die Beantwortung so mancher Fragen zu experimentellen Arbeiten bedanken, die mich während meiner Habilitation beschäftigten.

Was die numerischen Arbeiten angeht möchte ich Melanie Krüger und Stefan Uhlar besonders danken, da die stets fruchtbaren fachlichen Diskussionen mit ihnen für die vorliegende Arbeit einen nennenswerten Mehrwert bedeuteten. Herrn Dr. Hesch möchte ich für die uneingeschränkte Hilfe bei der Nutzung der elektronischen Infrastruktur des Lehrstuhls danken. In diesem Zusammenhang spreche ich auch Herrn Sänger meinen Dank aus, der mir stets meine zahlreichen Fragen zur Thematik der elektronischen Textverarbeitung beantworten konnte. Herrn Ralf Siebert und Herrn Marlon Franke danke ich besonders für die großartige Unterstützung bei der Lehre der Höheren Technischen Mechanik.

Zuletzt möchte ich mich bei meinen Eltern herzlichst bedanken, die mir mein Universitätsstudium ermöglichten, das den Grundstein meines wissenschaftlichen Werdeganges darstellt. Meinen Schwiegereltern danke ich für ihren starken Rückhalt und ihre großartige Unterstützung. Und mein ganz besonderer Dank gilt meiner Ehefrau Marion und meinem kleinen Sohn Jannis, die beide auf vieles verzichten mussten, besonders auf gemeinsamen Urlaub und gemeinsame Freizeit mit mir, damit ich meiner wissenschaftlichen Tätigkeit mit einer Konzentration nachgehen konnte, die für mich zur Fertigstellung dieser Arbeit notwendig war.

Siegen, Juli 2009 Michael Groß

ZUSAMMENFASSUNG

Diese Arbeit behandelt die energiekonsistente Simulation von Bewegungen eines viskoelastischen kontinuierlichen Körpers, unter Einbezug der Kopplung von thermischen und mechanischen Feldern. Der verwendete Algorithmus basiert auf einer Vier-Feld-Formulierung in Lagrangescher Darstellung, in der die Deformationsabbildung, das Geschwindigkeitsfeld, das Temperaturfeld und eine deformationswertige viskose innere Variable unabhängige Variablen darstellen. Die Bewegungsgleichungen sind deshalb Differentialgleichungen erster Ordnung. Das Lagrangesche Temperaturfeld wird bestimmt durch die lokale Entropiebilanz als dritte Differentialgleichung erster Ordnung, verbunden mit dem Fourierschen Gesetz für Wärmeleitung. Die letzte Differentialgleichung erster Ordnung stellt die viskose Evolutionsgleichung dar. Sie basiert auf einer inneren Dissipation, welche quadratisch in einem nichtlinearen viskosen Verzerrungsratentensor formuliert ist.

Dieses System von gekoppelten nichtlinearen Differentialgleichungen wird diskretisiert mittels einer neuen Raum-Zeit-Finite-Elemente-Methode, die sowohl zu kontinuierlichen als auch zu diskontinuierlichen Approximationen in der Zeit führt. Aufgrund spezieller Zeitapproximationen in den konstitutiven Gesetzen des Problems wird, neben der Gesamtimpuls- und Gesamtdrehimpulsbilanz, auch eine Stabilitätsabschätzung bezüglich einer relativen Energiefunktion noch nach der Raum-Zeit-Diskretisierung exakt erfüllt. Daher ist der resultierende Zeitintegrationsalgorithmus langzeitstabil, auch wenn Zeitschrittweitenänderungen vorgenommen werden.

Das erhaltene System von gekoppelten nichtlinearen algebraischen Gleichungen wird mittels einer monolithischen Strategie gelöst. Die damit verbundenen Newton-Raphson-Verfahren auf globaler Ebene und auf Elementebene basieren auf einer konsistenten Linearisierung. Die verwendeten neuen Konvergenzkriterien für die iterative Lösungsprozedur beziehen die Energiekonsistenz des Algorithmus' in Betracht, und sind frei von Skalierungseinflüssen in den vier unabhängigen Variablen. Repräsentative numerische Simulationen mit verschiedenen Randbedingungen zeigen die unbegrenzte Genauigkeit und die hervorragende Stabilität des neuen Zeitintegrationsalgorithmus'.

Schlagwörter: Multi-physikalische Problemstellungen, Starke thermomechanische Kopplung, Raum-Zeit-Finite-Elemente-Methode, Zeitschrittverfahren, Energie-Impuls-Konsistenz, Höhere Genauigkeitsordnung, Monolithische Lösungsstrategie, Konsistente Linearisierung, Skalierungsfreie Konvergenzkriterien.

ABSTRACT

This paper is concerned with the energy consistent simulation of motions of a viscoelastic continuum body, under inclusion of the coupling of thermal and mechanical fields. The corresponding algorithm is based on a four-field formulation in the Lagrangian description, in which the deformation mapping, the velocity field, the temperature field and a strain-like viscous internal variable field are independent unknowns. Hence, the equations of motion are formulated in first-order form. The Lagrangian temperature field is determined by the first-order entropy evolution equation, associated with Fourier's law of heat conduction. The first-order viscous evolution equation is derived from an internal dissipation being quadratic in a nonlinear viscous strain-rate tensor.

This coupled system of nonlinear differential equations is discretised by a new space-time finite element method, consisting of continuous as well as discontinuous finite element approximations in time. Owing to particular time approximations in the constitutive laws, beside the total linear momentum as well as the total angular momentum balance, a nonlinear stability estimate with respect to a relative energy function is exactly fulfilled in the fully discrete case as well. Hence, the resulting time integration algorithm is long-time nonlinear stable also when changing the time step size.

The obtained coupled system of nonlinear algebraic equations is solved by a monolithic solution strategy. The corresponding Newton-Raphson methods on the global and the element level are based on a consistent linearisation. The new convergence criteria used for these iterative solution procedures take the energy consistency into account, and is free of the scaling in the independent variables. Representative numerical simulations with various boundary conditions show the higher-order accuracy and the superior stability of the new time integration algorithm.

KEYWORDS: Multi-Physics Problems, Strong Thermo-Mechanical Coupling, Space-Time Finite Element Methods, Time-Stepping Algorithms, Energy-Momentum Consistency, Higher-Order Accuracy, Monolithic Solution Strategy, Consistent Linearisation, Scaling-Free Convergence Criteria.

CONTENTS

1. INTRODUCTION

In the dynamic finite deformation elasticity, it turned out that well-known stability estimates for linear problems are not valid for nonlinear problems. First statements about this topic can be found in Belytschko & Schoeberle [1] and Hughes [2]. On the other hand, representative numerical simulations reveal that time integration algorithms can possess instable behaviour (see Simo & Tarnow [3] and Crisfield & Shi [4], for instance). This numerical instability is identifiable through the divergence of the used iterative solution procedure, induced by unphysical time evolutions. In Crisfield & Shi [4], this behaviour is designated as locking in time, in the light of the well-known locking in space occurring in calculations with shells and quasi-incompressible material. In order to avoid the temporal locking with elastic material, two common approaches are the development of conserving, in particular energy conserving, time integration algorithms, or the introduction of numerical dissipation by the time integrator for damping out high-frequent modes.

The approach of energy conserving time integration algorithms is based on the fact that energy conservation means unconditional numerical stability (see Richtmyer & Morton [5] and Wood [6]). This knowledge is confirmed several times during the numerical time integration of conservative systems, especially of hyperelastic systems. For instance, the authors of LaBudde & Greenspan [7, 8] investigated energy conserving time integration algorithms for N-body problems. By considering Hamiltonian systems in Simo et al. [9], the meaning of total linear as well as total angular momentum conservation for the numerical time integration is realised. In Simo & Tarnow [3], this approach is applied to dynamic finite deformation elasticity, and leads to energy-momentum conserving time integration algorithms. Here, the stability of an exact energy conserving time integration is confirmed again. This algorithm is based on a midpoint approximation together with modified internal forces. In Gonzalez [10], the time integration algorithm is also composed of these two elements. However, the latter algorithm arise from the well-known approach of substituting a discrete derivative for an analytical derivative in the discretisation. The discrete derivative approach is already applied to the N-body problem in Greenspan [11,12]. The origin of this approach is the view of a conserving time integration algorithm as discrete conservative mechanical system, or discrete Hamiltonian system, respectively (see Greenspan [13]). From this perspective, the positive influence of exact algorithmic conservation properties on numerical stability and physical quality of the numerical solution is analytically proved for a model problem in Gonzalez & Simo [14]. Unlike a discrete stress tensor, a temporal continuous energy conserving stress approximation is presented in Sansour et al. [15]. In this reference, the energy-momentum conserving time integration algorithm for shells is based on a covariant continuum formulation. In Groß et al. [16], a temporal continuous and energy-momentum conserving stress approximation is given as well. However, this approach includes the effective discrete gradient in Gonzalez [10] in the case of a midpoint approximation. An alternative to modifying internal forces is to enforce the exact energy conservation iteratively as constraint by means of a Lagrange multiplier. The authors of Hughes et al. [17] apply this concept on the basis of the trapezoidal rule. In Laursen & Meng [18], exact energy conservation is also achieved iteratively, using the energy conservation condition as additional equation for determining a scalar-valued parameter field. Energy-momentum conserving time integration algorithms for nonlinear structural dynamic problems are constructed in Simo & Tarnow [19] and Simo et al. [20]. A similar proceeding in Crisfield & Shi [4, 21] leads to an energy-momentum conserving time integrator for trusses, in Galvanetto & Crisfield [22] for two-dimensional beams, and in Zhong & Crisfield [23] for shells. The authors of Stander & Stein [24] also present a conserving time integrator for two-dimensional beams, and Brank [25] deals with the extension of the conserving time integrator for dynamic shell motions in the foregoing Reference Brank et al. [26] to flexible laminates. In connection with an iterative enforcement of the energy conservation in structural dynamics, we mention Kuhl & Ramm [27], wherein, in addition to the total energy conservation, also the total linear and total angular momentum conservation is enforced by Lagrange multipliers. Unusually, the time approximation is based on a numerically dissipative time integration algorithm. Hence, high-frequent modes of the solution are damped out, however, the decrease of total energy owing to the numerical dissipation is balanced by the energy conservation constraint.

The approach of introducing numerical dissipation by means of a time integrator arise from the knowledge about linear stability of time integration algorithms. Since the maximum time step size of linear stable time integration algorithms is inversely proportional to the highest frequency of the discrete system, the approach of damping out high-frequent modes of the solution in order to increase the time step size stand to reason (see Hilber et al. [28]). Assumption is that these modes are not of primary interest for the considered motion. The locking effect in time of nonlinear problems, mentioned in Crisfield & Shi [4], is also traced back to high-frequent modes. In the dynamic finite deformation elasticity, this approach is applied, because a finite element approximation in space does not approximate high-frequent modes very well (see Strang & Fix [29]). Therefore, numerically dissipative time integration algorithms are developed for nonlinear elastic materials (compare Armero & Romero [30, 31] for elastic continuum elements and Ibrahimbegovic & Mamouri [32] for elastic beam elements). However, in the knowledge of the present authors, it is not sufficiently clear in the scope of nonlinear problems, if numerically dissipative time integration algorithms do not also damp out physically relevant modes of the solution. Therefore, this approach is not considered in the present work.

The aforementioned references show that the exact fulfilment of energy and momentum balances is an important quality feature of time integration algorithms for nonlinear elastodynamics. However, the therein presented time integrators are at most second order accurate. A more accurate solution can only be achieved by a smaller time step size. This, however, can be numerically more costly. For this reason, the approaches behind the energy-momentum conserving time integration algorithms in Gonzalez [10, 33] and Simo & Gonzalez [34] are carried forward into higher-order accurate time integration schemes in Groß et al. [16] and Groß [35]. These time integrators show the stability properties for arbitrary accuracy orders. The improved numerical stability allows to use larger time steps, and leads to more efficient calculations. The approach is based on the Galerkin method, which allows a systematical construction of implicit time integration algorithms of arbitrary accuracy order by means of finite elements in time. Temporal Galerkin methods are mainly subdivided into discontinuous Galerkin (dG) methods and continuous Galerkin (cG) methods (see Eriksson et al. [36]).

In dG methods, the approximation of the test function and the trial function is assumed to be discontinuous over the element boundaries. The dG method is traced back at least to Lasaint & Raviart [37], and is described in detail in Cockburn [38] and Thomee [39], for instance. A first application on linear elastodynamics is given in Hughes & Hulbert [40], wherein simultaneously a Galerkin method in space is applied. In Hulbert [41, 42], it is focused on the numerical treatment of the semi-discrete equations. Thereby, the authors decide between a single-field formulation and a two-field formulation. In the former formulation, one uses only trial functions in the displacements, where in the latter formulation, one also applies independent trial functions for the velocities. For example, in Li & Wiberg [43, 44], the dG method is implemented with linear finite elements in time for the displacements as well as for the velocities. This work is extended to a nonlinear model problem in Wiberg & Li [45]. Likewise, nonlinear model problems are considered in Bonelli & Bursi [46] and Bottasso [47]. The former reference elaborates on the connection between dG and Runge-Kutta methods. In the latter reference, the dG method is applied to stiff differential equation systems, and the numerical cost is compared. The application of the dG method to nonlinear beams is subject of Bauchau & Theron [48]. This formulation is extended to elastic multibody systems in Bauchau & Bottasso [49]. However, when applied to hyperbolic problems as the nonlinear elastodynamics, the dG methods lead to time integration algorithms with numerical dissipation. Using constant finite elements in time, for instance, we obtain the well-known implicit Euler method. Therefore, the dG method is a way of introducing numerical dissipation, and belongs to the second approach for obtaining stable time integration algorithms. For this reason, the time integration algorithms for the nonlinear problems in Bauchau & Bottasso [49] and Bauchau & Theron [48] is based on the dG method. In Groß et al. [50] and Groß [51], however, is shown that the ordinary dG method is not appropriate to construct momentum conserving time integration algorithms, owing to the jump in the time evolution. Only a reduced time integration in the resulting finite element method leads to total angular momentum conservation. This integration, with less Gauss points as in fact for the used polynomial degree of the shape functions is necessary, is already known from the volume integration in specific continuum elements. For example, it is used to avoid locking of continuum elements for quasi-incompressible material (see Wriggers [52] for an overview). On the other hand, the reduced time integration in the dG method leads to a time integration algorithm being identical to that, which follows by a consistent time integration from an ordinary cG method. For this reason, the authors of Groß et al. [50] and Groß [51] apply only the cG method for designing conserving time integrators of arbitrary order. Note that independent of the results in Groß [51], the authors of Larson & Niklasson [53] have shown that the cG method can be viewed as a limit of the dG method if a parameter tends to infinity.

In cG methods, the approximation of the trial functions is assumed to be continuous over the element boundaries, whereas the approximation of the test functions is further discontinuous. Therefore, we obtain implicit time integration algorithms. The cG method seems to go back to Douglas & Dupont [54] and Swartz & Wendroff [55] for parabolic problems, and to Hulme [56, 57] for ordinary differential equations. More details about the continuous Galerkin method can be found in Eriksson et al. [36] and Fairweather [58], for instance. In Aziz & Monk [59] and Winther [60], the cG method is also applied to solve partial differential equations. In French & Schaeffer [61], the time integration of ordinary and different nonlinear partial differential equations is investigated. In this reference, the aspect of exact energy conservation is also treated, and leads to an energy conserving time integration algorithm. In a follow up paper, the exact energy conservation is also considered as important for nonlinear wave propagation (see French & Peterson [62]). That the cG method is particulary appropriate to construct energy conserving time integration algorithms for conservative problems is also found by other authors. For example, in Betsch & Steinmann [63] is shown that just the cG method is inherently energy conserving, which means the energy conservation is achieved for exact calculation of time integrals. This property leads to a better and better conserved energy with increasing accuracy order of the numerical quadrature. Also in Larson & Niklasson [64], the conservation properties of the cG method is investigated and compared with that of the dG method. In Betsch & Steinmann [65], an energy-momentum conserving time integration is designed for the N-body problem. This formulation is extended to semidiscrete nonlinear elastodynamics in a follow up paper (see Betsch & Steinmann [66]). Since the exact energy-momentum conserving time integration algorithms in these works are at most second order accurate, the part Groß et al. [16] of this publication series shows the extension to higher-order accurate energy-momentum conserving time integration of both problem classes. The third part also describes the conserving time integration of coupled elastic and rigid bodies with second-order accurate integrators (see Betsch & Steinmann [67]).

In the present work, we also apply the Galerkin method in time combined with a Galerkin method in space. In this way, we obtain a space-time approximation, which is not restricted in the accuracy order. Whether we use a cG or dG method in time is based upon the consistency with energy balances of our now dissipative problem.

1.1. Literature review

In all of the mentioned references about energy conserving time integrators for nonlinear elastodynamics is found that an indicator for an unstable numerical integration is the so-called blow-up behaviour. This phenomenon means a steadily increased total energy with increasing calculation duration. An energy blow-up is noticed particularly with high material stiffness. If no blow-up behaviour is observed, the energy oscillates around a constant energy level. Consequently, energy inconsistent non-dissipative algorithms produce algorithmic energy during the integration of elastic systems. In dynamic problems of dissipative materials is expected that this algorithmically produced energy is compensated if the physical dissipation is sufficiently high. And so, the numerical instability cannot be observed. This compensation is observed in Simo [68], during the time integration of motions of plastic materials. In the same reference, a non-conserving time integration algorithm is compared with a total linear and total angular momentum conserving algorithm. By using numerical simulations, the author concludes that the latter is more stable than the non-conserving time integrator. Hence, the relevance of momentum conserving time integration algorithms is verified also for dissipative materials.

This expected compensation of algorithmically produced energy is not observed in each case. In Meng & Laursen [69], it is described that a not sufficiently high internal dissipation of a plastic material leads to an energy blow-up with subsequent numerical instability. However, this blow-up behaviour is avoided by using an energy consistent time integration algorithm, which is an algorithm fulfilling exactly the discrete energy balance. In the conservative case, the energy is conserved, and in the dissipative case, the approximated physical dissipation leads to a prescribed energy loss. In this paper, algorithms for the additive as well as multiplicative plasticity with isotropic hardening are presented. In Noels et al. [70], a variational formulation with incremental potentials according to Ortiz & Stainier [71] allows the construction of a conserving time integrator for elastoplasticity, which is based on the discrete derivative approach for hyperelastic materials according to Gonzalez [10]. The procedure in Noels et al. [70] is not restricted to isotropic hardening. In Noels et al. [72], these authors introduce numerical dissipation for high-frequency numerical modes using this variational formulation, and arrive at a first-order accurate time integrator which also conserve the total linear and total angular momentum. The introduction of controllable numerical dissipation by remaining total linear and total angular momentum conservation is motivated by the energy consistent integrator in Armero [73], which is based on the schemes in Armero & Romero [30, 31] for nonlinear elastodynamics. However, in Noels et al. [72], the numerical dissipation is not only in the additional term of the discrete derivative involved, but also in the analytical derivative at the midpoint strain. In Armero & Zambrana-Rojas [74], a volume-preserving energy-momentum scheme for isochoric multiplicative plasticity is presented, in order to preserve exactly the plastic volume for isochoric plastic models. This time integrator is based on the scheme in Armero [73]. In Armero [75], this energy-dissipating momentum-conserving time integration algorithm is adjusted to assumed strain finite elements in space, which are constructed for nearly incompressible material responses. In all these references, the discrete derivative approach is applied, which also leads to an energy consistent material-point method for dynamic finite deformation plasticity in Love & Sulsky [76]. The material-point-method is an extension of the particle-in-cell method, in which particles are interpreted as material points. Alternatively, in Mohr et al. [77] and Mohr [78], energy consistent time integration algorithms for finite elasto-plasto dynamics are presented, which base on a finite element method in time. In these References, it is also shown that, using a first order accurate algorithm for updating the plastic internal variables, we obtain an order reduction of a higher-order time integration method as soon as plastic deformations occur. A remedy of this formal disadvantage could be to consider elastoplasticity from the viewpoint of a differential algebraic system. For infinitesimal elastoplasticity, this is done in Papadopoulos & Taylor [79] and Büttner & Simeon [80], respectively.

The mentioned energy consistent time integration algorithms for elastoplastic materials are based on the assumption of hyperelastic constitutive laws for the elastic behaviour. In this plasticity concept, the inelastic deformation is determined by a flow rule, and the stress is subsequently derived from the hyperelastic strain energy function (see Simo & Ortiz [81]). An older procedure is based on hypoelastic stress formulations, in which the stress follows from the time integration of a stress rate equation. However, the configuration in which the considered stress tensor is defined draw a distinction. In the current configuration, for example, we have to approximate objective stress rate tensors (see Pinsky et al. [82]). By means of a discrete form pertaining to such an objective stress rate tensor, energy consistent algorithms for dynamic finite deformation hypoelasticity are designed in Noels et al. [83,84]. The difference between these algorithms lies in the accuracy order of the stress rate approximation. In the former reference, the approximation is of first order accurate, where in the latter, a second order accurate stress rate approximation is used.

Since we consider in the present work an internal dissipation of a viscoelastic material law and a dissipation arising from a classical heat conduction by means of Fourier's law, we give an overview about algorithms for calculating deformations of these dissipative materials. However, beside intermediate results of the present authors in Groß & Betsch [85, 86] for the dynamic finite deformation viscoelasticity, in Groß & Betsch [87] for the dynamic finite deformation classical thermoelasticity, and in Groß & Betsch [88–91] for nonlinear thermo-viscoelastodynamics, there are no references known to the present authors, which are concerned with the simulation of corresponding dynamic problems with energy consistent algorithms. Mostly the approach of introducing numerical dissipation is applied. In contrast, for the non-dissipative non-classical theory of thermoelasticity according to Green & Naghdi [92], an energy consistent time integration algorithm is presented in Bargmann [93]. This algorithm is also based on a finite element approximation in space and time (see also Bargmann and Steinmann [94, 95]).

In nonlinear viscoelasticity, for a long time, inelastic stresses are determined by means of approximated time integrals. These integrals follow directly from the older representation by means of functionals, or indirect from the newer representation by means of internal variables (see Haupt [96]). The concept of internal variables for viscoelastic materials is already known from Green & Tobolsky [97], and is newly taken up in Lubliner [98]. However, this concept is increasingly used in numerical implementations only since Simo [99]. Here, the internal variable plays the role of an non-equilibrium stress tensor, which is determined by an evolution equation similar to that in the linear theory. In Holzapfel [100], the evolution of the non-equilibrium stress determines an internal variable of strain-type. The formulation presented in Le Tallec et al. [101] is based totally on a strain-type internal variable, however, the corresponding evolution equation is also derived from the linear theory. The constitutive law in Reese & Govindjee [102] is also based on internal variables of strain-type. The evolution equations, however, are here not deduced from the linear theory, wherefore they allow material states far away from the thermodynamic equilibrium state. The evolution equations in this reference have the same structure as a plastic flow rule. Therefore, the time integration is performed by using algorithms known from elastoplasticity. For example, the exponential mapping algorithm is established for finite isotropic elastoplasticity (see Simo [68], Weber & Anand [103] and Miehe & Stein [104]). In the latter references, this algorithm is based on a spectral decomposition of the considered tensors. However, in Miehe [105], the exponential map algorithm is applied to anisotropic multiplicative elastoplasticity by avoiding the spectral decomposition of the argument tensors. For this reason, the exponential mapping algorithm is appropriate to constitutive laws for rubber-like polymers based on principal stretches (compare the material in Ogden [106]). However, the time integration with this algorithm is at most first order accurate. For obtaining a higher order of accuracy, we have to apply more general methods for solving ordinary differential equations (see Reese [107]). Since the time evolution of internal variables are associated with different time scales, the corresponding differential equations are numerically stiff, and require robust time integration algorithms. Owing to the better stability, implicit time integrators are preferred to explicit schemes. In particular, implicit time integration algorithms with numerical damping, as the implicit Euler method, is used frequently (see Le Tallec et al. [101]). Another approach for improving the robustness is the application of an adaptive time step size control (see Reese [107] and Diebels et al. [108]). The corresponding error estimate is based on a comparison of the solution of two time integrators with distinct orders of accuracy. For instance, Runge-Kutta methods are applied, which are not restricted in their accuracy order (compare Hairer et al. [109] and Hairer & Wanner [110]). The mentioned implicit Euler method is an element of the class of implicit Runge-Kutta methods. The consideration of the viscous evolution equation together with a semi-discrete static boundary value problem leads to a differential algebraic system of equations (see Kirchner & Simeon [111], for instance). These most stiff systems of equations are often solved by using BDF methods. The implicit Euler method, for example, is the first order BDF method (see Ascher & Petzold [112] and Brenan et al. [113]). For this reason, higher order BDF methods are used for integrating viscous evolution equations in time, in order to realise an adaptive time step size control. In Kirchner & Simeon [111], a viscous material model for small strain is considered. For large strains, the differential algebraic approach is applied in Hartmann [114]. However, the time integration is taken over by diagonal implicit Runge-Kutta methods. These methods are also considered to be robust, however, in addition, they have advantages for efficiency and implementation purposes (compare Ellsiepen & Hartmann [115]).

In classical thermoelasticity, the temperature is considered as additional independent variable. This is well-founded by the observability of the temperature, and by the fulfillment of the axiom of causality of constitutive equations (see Eringen [116]). As additional equation to the balance of mechanical energy, the balance of internal energy or the balance of entropy is used. The finite element method approximates the independent temperature field by spatial trial functions. After the spatial discretisation, we therefore obtain a coupled system of ordinary differential equations (compare Oden [117]). Methods for solving these coupled equations apply the monolithic or the partitioned solution strategy (see Wood [6]). A monolithic solution is mostly obtained by applying an implicit time integration algorithm, as the generalised midpoint rule, together with a simultaneous solving of the resulting algebraic system of equations. As solution strategy for the algebraic system is applied a direct method or a staggered method (see Argyris & Doltsinis [118] and Argyris et al. [119]). Partitioned solution strategies are introduced in order to improve the numerical effort, solving many degrees of freedom. For example, special time integration methods leading to uncoupled semi-discrete equations are combined with an explicit extrapolation of the coupling terms. However, according to Park & Felippa [120], this extrapolation leads to conditionally stable algorithms. In Simo & Miehe [121], a split of the elliptic operator of the coupled field equations according to the fractional step method (see Yanenko [122]) is performed. By means of this operator splitting technique, the problem is solved sequently in an isothermal mechanical and a purely thermal phase. Thus, the equations of motion are solved with constant temperature, and the energy equation during a fixed position. The time integration is performed by means of the already mentioned first order accurate implicit Euler method, since the total operator split is a first order accurate approximation. The algorithm pertaining to this so-called isothermal split, however, is solely unconditionally stable in the sense of linear stability. However, this is not sufficient for highly nonlinear problems. For this reason, the problem in Armero & Simo [123] is solved in an adiabatic mechanical phase and in a purely thermal phase. Hence, the motion is now calculated at constant entropy. But, the condition of a constant entropy leads to a necessary iteration procedure on the element level. This adiabatic split is also nonlinear stable in the sense of Lyapunov. The improved stability is also confirmed in Miehe [124] and Holzapfel & Simo [125], solving problems with entropic thermoelastic materials. On the other hand, a stability procedure for the isothermal split is given in Farhat et al. [126]. In a direct comparison of the monolithic and the partitioned solution strategy for strong coupled problems, which means relatively high thermal expansion coefficients, for instance, is found that the former strategy leads to better results (see Reese [107]). This is also concluded in Ibrahimbegovic et al. [127], wherein a covariant formulation of thermoelasticity is presented. There are two reasons for this. Solving a strong coupled problem sequently in split phases, first, the number of iterations is, in the worst case, nearly twice the number of iterations pertaining to the natural monolithic strategy, and second, there is possibly a great deviation of both solutions. This deviation would lead necessarily to an iterative refinement or a decrease of the time step size. In these cases, the partitioned solution strategy is therefore no more efficient, and it is not worth to accept the low accuracy order of the algorithm. On the other hand, an advantage of the partitioned solution strategy is the possible usage of different time step sizes in the two phases. In this way, different time scales in the temperature and the displacement can be considered already during the time integration. However, since we aim at higher-order accurate algorithms also appropriate for strong coupled problems, we apply a monolithic solution strategy using a Newton-Raphson method with consistent tangent. We determine the displacement and the temperature increment in the iterative solution procedure sequently in an efficient way, in order to avoid large algebraic systems of equations.

The consideration of thermal effects, as heating of the material after being deformed (Gough-Joule effect, see Miehe [128])) or changes in the body temperature arising from internal dissipation, is especially for viscous materials as polymers of importance. Therefore, viscoelastic material models are often extended to temperature dependent viscoelastic behaviour. The viscoelastic material model in the already mentioned reference Holzapfel [100] is extended in Holzapfel & Simo [129] to such thermal effects. In both references, the time evolution of a strain-like viscous internal variable is calculated by means of a linear non-equilibrium stress rate equation. The modelling by means of a nonlinear strain rate equation (see Reese &

Govindjee [102]) is used in Reese & Govindjee [130] for simulating thermo-viscoelastic materials. Accordingly, in order to calculate motions of thermo-viscoelastic materials, the local iterative solution procedure pertaining to the viscoelasticity has to be applied on the element level, and the global iterative solution procedure of a thermoelastic problem is used on the global level. However, in the entropy evolution equation, there is additionally an entropy term arising from the internal dissipation of the viscous material law.

1.2. Outline

The outline of the paper is as follows. In Section 2, we define our problem of continuum motions of a viscoelastic body, under inclusion of the coupling of thermal and mechanical fields. Thereby, we use the Lagrangian description of continuum motions. We start with mathematical preliminaries, which explain the used notation. In order to display the tensors, and the equations in which they are included, we use a mixed form of a symbolic notation and an index notation. This notation inherits the advantages of both notations. Namely, the possible identification of the whole tensor in the equation, however, with avoiding many shorthand notions for chaining these tensors. Moreover, this notation simplifies later the transition to the matrix notation in the implementation. Further, in the light of Marsden & Hughes [131] and Abraham et al. [132], we reveal the distinction of tangent and cotangent vectors by subscript and superscript indices, and use different symbols for the corresponding different sets. Especially, when introducing the viscoelastic material model and the spatial discretisation, this simplifies to retain the clarity in which space or set the quantities are defined. Recall the mentioned necessary distinction in the approximation of rate equations with respect to the current or the reference configuration. Although, we are only concerned with rectangular coordinates, the distinction between tangent and cotangent vectors in the general sense are necessary for explaining which time discretisations are consistent with the applicable energy function. For example, the considered boundary conditions have an influence on the defined energy function, and thus on the energy consistent time discretisation. We already apply this notation to the mathematical definition of all the concerned terms, such as reference and current configuration, deformation and motion and many others (compare Ciarlet [133]), in order to bring the reader close to this notation and the corresponding perspective. In spite of the theoretical purposes of the notation for deriving the finite element method, the used tensor notation is geared to the common matrix notation, which is used in the implementation of the algorithm. After defining the physical quantities related with the Lagrangian description of continuum motions, we also introduce in Section 2 the governing evolution and constitutive equations, and define the strong form of the corresponding initial boundary value problem. This section is closed by deriving the conservation laws and the energy-based stability estimate of the strong form, whose fulfillment is an aim of the Galerkin finite element method.

In Section 3, we derive the weak formulation of the initial boundary value problem straight forward by using the defined energy function. Thus, it is guaranteed that the Galerkin finite element method, derived in Section 4, satisfies the stability estimate. Here, we consciously discretise at first in time and then in space. The idee is to argue that we calculate time curves of fields over a bounded domain, and we therefore approximate first the time curves of the fields and then the fields themselves. In this way, we arrive in Section 5 at an already known temporal approximation of the strain evolution, called assumed strain approximation in time, which is unaffected by rigid body motions according to Groß et al. [16] and Groß [35]. In this section, we also derive additional terms of the weak forms pertaining to the equations of motion and the thermal evolution equation, which lead to the exact energy consistency and the nonlinear stability in the sense of Lyapunov also in the discrete case.

Section 6 then shows by means of numerical simulations that the modifications in Section 5 do not affect the accuracy order of the finite element method, but improve the stability. These motions are initiated by initial conditions in order to verify the stability estimate as well as the conservation laws. Additionally, we show simulations with mechanical and thermal excitation by means of boundary conditions, which are also incorporated energy consistently.

In an appendix, we give details about our implementation of the algorithm. First, we derive in Section A the discrete initial boundary value problem, which includes the nonlinear algebraic system of equations, solved by the numerical solution procedure. Since we solve the problem by using Newton-Raphson methods with consistent tangent matrices, we linearise this system of equations in Section B. Here, we also introduce physically motivated convergence criteria for the Newton-Raphson methods, which take the energy consistency of the finite element method into account. In Section C, we show the physical and numerical applicability of the used Neo-Hookean material model, called Simo-Taylor material, for the present numerical problem. The appendix is concluded by Section D, which deduces an analytical solution of an approximate problem, used for interpreting the numerical results.

2. PROBLEM DEFINITION

We consider arbitrary motions of a continuum body consisting of viscoelastic material, and take the coupling of thermal and mechanical fields into account. We start by introducing all the necessary quantities related with dynamic deformations of thermally extended viscoelastic material, and all the necessary balance laws of continuum mechanics. Thereby, we restrict us to the Lagrangian description. Then, we introduce the considered constitutive equations for the entropy flux arising from conduction of heat, and the viscous internal variable formulation. We arrive at a system of coupled nonlinear partial differential equations, representing an initial boundary value problem. We show that, under certain circumstances, the time evolution of this problem fulfills conservation laws and a stability estimate.

2.1. Lagrangian description of continuum motions

We are interested in the time evolution of positions of certain particles pertaining to a continuum body, during a prescribed time interval. Therefore, we consider in this paper continuum mechanics in dependence of the initial positions of these particles, which means their Lagrangian description (see Holzapfel [135] and references therein). This preliminary section introduces the necessary quantities by emphasising the notion of tangent vectors at curves and the corresponding cotangent vectors. This point of view is used below for deriving the energy consistent time integration algorithms. We thereby use a notation, which simplifies to retain the clarity in which of the many spaces or sets the used tensors are defined. We begin this section by introducing the mathematical concept of a continuum, inspired by Marsden & Hughes [131], Abraham et al. [132] and Bertram [134], which models the body itself and its ambient space.

2.1.1. Mathematical preliminaries. Let $\mathbb{R}$ denote the set of real numbers, and $1 \leqslant n_{\mathrm{dim}} \leqslant 3$ be a positive natural number. We denote by $\mathscr{A}$ the set of columns $\boldsymbol{a} = [a^1, \ldots, a^{n_{\mathrm{dim}}}]$, where the entries $a^i \in \mathbb{R}$ denote real numbers. Since $\mathscr{A}$ is a real vector space, the element $\boldsymbol{a} \in \mathscr{A}$ is called a

$$\begin{tikzcd}[column sep=huge, row sep=huge]
\mathscr{A} \arrow[r, "\boldsymbol{A}"'] \arrow[r, phantom, ""] & \mathscr{A} \arrow[l, dashed, bend right=20, "(\boldsymbol{A}^*)^T"'] \arrow[l, dotted, bend left=40, "\boldsymbol{A}^{-1}"] \arrow[d, "\boldsymbol{\delta}"] \\
\mathscr{A}^* \arrow[u, "\boldsymbol{\delta}^{-1}"] \arrow[r, "\boldsymbol{A}^*"] & \mathscr{A}^* \arrow[l, dashed, bend left=20, "\boldsymbol{A}^T"]
\end{tikzcd}$$

Figure 2.1. A linear mapping $\boldsymbol{A}$ between two vectors in the ambient space $\mathscr{A}$ possesses an inverse $\boldsymbol{A}^{-1}$, and a transpose $\boldsymbol{A}^T$ as well as a dual mapping $\boldsymbol{A}^*$ on the dual ambient space $\mathscr{A}^*$.

column vector. The vector space $\mathscr{A}$ models a continuum with respect to the Euclidean reference frame. The origin of this frame is given by the zero vector $\boldsymbol{o} = [0, \ldots, 0]$ of $\mathscr{A}$. Since a continuum body $\mathscr{B} \subset \mathscr{A}$ is considered as a connected subspace of the continuum, the space $\mathscr{A}$ denotes the ambient space of the body.

We associate with the space $\mathscr{A}$ a symmetric and positive-definite matrix $\boldsymbol{\delta}$. The entries of this matrix are the usual Kronecker symbols δ_{ij}, $i, j \in \mathscr{N}_{sd} = \{1, \ldots, n_{\mathrm{dim}}\}$. This matrix defines an inner product on $\mathscr{A}$ by the relation

$$[\boldsymbol{a}, \boldsymbol{b}] = [\boldsymbol{a}]^i \delta_{ij} [\boldsymbol{b}]^j \tag{2.1}$$

Summation on repeated indices is understood. By using this inner product, we define the Euclidean norm $\|\boldsymbol{a}\|$ of the column $\boldsymbol{a}$ by the expression $\sqrt{[\boldsymbol{a}, \boldsymbol{a}]}$. Moreover, Equation (2.1) defines a row vector $\boldsymbol{a}^* = [a_1 \ldots a_{n_{\mathrm{dim}}}]$, whose entries $[\boldsymbol{a}]_j$ are given by the real numbers $[\boldsymbol{a}]^i \delta_{ij}$. This row vector $\boldsymbol{a}^*$ is called the covector corresponding to the column vector $\boldsymbol{a}$. By using this definition, the inner product on the vector space $\mathscr{A}$ can be viewed as a pairing

$$\langle \boldsymbol{a}^*, \boldsymbol{b} \rangle = [\boldsymbol{a}^*]_j [\boldsymbol{b}]^j \tag{2.2}$$

of columns $\boldsymbol{b} \in \mathscr{A}$ and rows $\boldsymbol{a}^*$. Thus, a covector is an element in the space $\mathbb{L}(\mathscr{A}, \mathbb{R})$ of all linear maps of $\mathscr{A}$ to $\mathbb{R}$, called the dual space $\mathscr{A}^*$ of the ambient space, and the matrix $\boldsymbol{\delta}$ is a mapping from the ambient space

$\mathscr{A}$ to its dual space. Since the matrix $\boldsymbol{\delta}$ is positive-definite, the identities $\delta^{ik}\delta_{kj}[\boldsymbol{a}]^j = [\boldsymbol{a}]^i$defines a symmetric and positive-definite matrix $\boldsymbol{\delta}^{-1}$ on the dual space $\mathscr{A}^*$ with the Kronecker symbols δ^{ij} as entries. By the relation

$$[\boldsymbol{a}^*, \boldsymbol{b}^*] = [\boldsymbol{a}^*]_i \delta^{ij} [\boldsymbol{b}^*]_j \tag{2.3}$$

we denote the corresponding inner product of two row vectors $\boldsymbol{a}^*, \boldsymbol{b}^* \in \mathscr{A}^*$ in the dual space of the ambient space. Likewise, the matrix $\boldsymbol{\delta}^{-1}$ denotes a mapping from the dual space $\mathscr{A}^*$ to the ambient space itself.

A linear mapping or tensor $\boldsymbol{A} \in \mathbb{L}(\mathscr{A}, \mathscr{A})$ on the ambient space maps column vectors to column vectors, and is defined by the relation

$$[\boldsymbol{A}(\boldsymbol{a})]^i = [\boldsymbol{A}]^i{}_j \, [\boldsymbol{a}]^j \tag{2.4}$$

where the real numbers $[\boldsymbol{A}]^i{}_j \in \mathbb{R}$ denote the entries of the square matrix corresponding to this linear map. The first index denotes the row and the second index the column of the matrix. The sum of the entries on the main diagonal of linear maps $\boldsymbol{A} \in \mathbb{L}(\mathscr{A}, \mathscr{A})$ defines the trace

$$\operatorname{tr}(\boldsymbol{A}) = [\boldsymbol{A}]^i{}_i \in \mathbb{R} \tag{2.5}$$

If the matrix corresponding to $\boldsymbol{A}$ is positive-definite, then there is an inverse $(\boldsymbol{A})^{-1}$. Its matrix entries $[(\boldsymbol{A})^{-1}]^k{}_i$ are defined by the equations $[(\boldsymbol{A})^{-1}]^k{}_i [\boldsymbol{A}]^i{}_j = [\boldsymbol{I}]^k{}_j$, where the linear mapping $\boldsymbol{I} \in \mathbb{L}(\mathscr{A}, \mathscr{A})$ denotes the identity matrix with the Kronecker symbols $\delta^k{}_j$ as entries. The matrix corresponding to the transpose $(\boldsymbol{A})^T \in \mathbb{L}(\mathscr{A}^*, \mathscr{A}^*)$ of the linear map $\boldsymbol{A}$ is defined by the relation

$$[\boldsymbol{a}^*]_i \, [\boldsymbol{A}]^i{}_j [\boldsymbol{b}]^j = [\boldsymbol{b}]^j \, [(\boldsymbol{A})^T]_j{}^i [\boldsymbol{a}^*]_i \tag{2.6}$$

with the covector $\boldsymbol{a}^* \in \mathscr{A}^*$ and the vector $\boldsymbol{b} \in \mathscr{A}$. By this definition, the matrix associated with this transpose emanates from the matrix of $\boldsymbol{A}$ by interchanging the rows and the columns. A further mapping $\boldsymbol{A}^*$ in the linear space $\mathbb{L}(\mathscr{A}^*, \mathscr{A}^*)$, which we call the dual mapping of $\boldsymbol{A}$ (see Figure 2.1), can be defined by a matrix product with $\boldsymbol{\delta}$ and its inverse, given by

$$[\boldsymbol{A}^*]_k{}^i = \delta_{ki}[\boldsymbol{A}]^i{}_j \delta^{jl} \tag{2.7}$$

Analogous to vectors, a pairing $\langle \boldsymbol{A}, \boldsymbol{B}^* \rangle$ of a mapping $\boldsymbol{A}$ in the linear space $\mathbb{L}(\mathscr{A}, \mathscr{A})$ and the dual mapping of a second mapping $\boldsymbol{B} \in \mathbb{L}(\mathscr{A}, \mathscr{A})$ defines an inner product on this linear space. Then, the squared norm $\|\boldsymbol{A}\|^2$ of a linear map $\boldsymbol{A}$ on the ambient space coincides with the inner product $[\boldsymbol{A}, \boldsymbol{A}]$ of this mapping with itself. The inner product is defined as

$$[\boldsymbol{A}, \boldsymbol{B}] = [\boldsymbol{A}]^i{}_j [(\boldsymbol{B}^*)^T]^j{}_i \tag{2.8}$$

We denote by ϵ_{ijk} the permutation or Levi-Civita symbol. It coincides with one for even permutations of (i, j, k), with minus one for odd permutations and zero elsewhere. We introduce the bilinear vector product of two column vectors $\boldsymbol{a}, \boldsymbol{b} \in \mathscr{A}$ by the components $\epsilon_{ijk}[\boldsymbol{a}]^j[\boldsymbol{b}]^k$. By using the vector product, the triple scalar product of three column vectors is defined as

$$[\boldsymbol{a}, \boldsymbol{b}, \boldsymbol{c}] = \epsilon_{ijk}[\boldsymbol{a}]^j[\boldsymbol{b}]^k[\boldsymbol{c}]^i \tag{2.9}$$

for any three column vectors $\boldsymbol{a}, \boldsymbol{b}, \boldsymbol{c}$ in the ambient space. According to the mentioned properties of the permutation symbol, each triple scalar product coincides with the product of its even permutated arguments, and with the negative product of its odd permutated arguments. It vanishes for at least two equal arguments. The permutation tensor is a linear mapping

$$[\boldsymbol{\epsilon}(\boldsymbol{T})]_i = \epsilon_{ijk}[\boldsymbol{T}]^{jk} \tag{2.10}$$

relating uniquely to each skew-symmetric tensor $\boldsymbol{T} \in \mathbb{L}(\mathscr{A}^*, \mathscr{A})$, with the property $\boldsymbol{T} = -(\boldsymbol{T})^T$, a row vector $\boldsymbol{\epsilon}$ in the dual space $\mathscr{A}^*$ of the ambient space. However, a symmetric tensor $\boldsymbol{S} \in \mathbb{L}(\mathscr{A}^*, \mathscr{A})$, with the property $\boldsymbol{S} = (\boldsymbol{S})^T$, is mapped to the zero vector $\boldsymbol{o} = (0, \dots, 0)$ of the ambient space.

2.1.2. The reference configuration. Let the set $\mathscr{T}$ denote the time interval $[t_0, T] \subset \mathbb{R}_+$ of interest. We consider a continuum body $\mathscr{B}$ at initial time $t_0 \in \mathscr{T}$ as an bounded open set $\mathscr{B}_0$ in the ambient space $\mathscr{A}$ with a piecewise smooth boundary $\partial\mathscr{B}_0$. Points $\boldsymbol{X}$ in this so-called reference configuration are

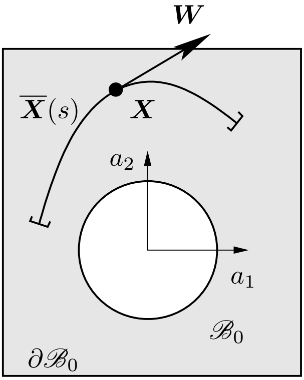

Figure 2.2. A curve $\overline{\boldsymbol{X}}(s)$ through any point $\boldsymbol{X}$ in the reference configuration $\mathscr{B}_0$ and a tangent vector $\boldsymbol{W} \in T_X\mathscr{B}_0$ in the corresponding tangent space at this curve.

thus identified by column vectors

$$\boldsymbol{X} = [X^1, \ldots, X^{n_{\mathrm{dim}}}] \in \mathscr{B}_0 \tag{2.11}$$

A (topological) curve $\overline{\boldsymbol{X}}(s)$, connecting points in $\mathscr{B}_0$ such that $\overline{\boldsymbol{X}}(0)$ coincides with a fixed point $\boldsymbol{X} \in \mathscr{B}_0$, is a subset of the reference configuration (see Figure 2.2). A tangent vector $\boldsymbol{W}$ at this curve in the point $\boldsymbol{X}$ is a column vector $[W^1, \ldots, W^{n_{\mathrm{dim}}}]$ in the ambient space $\mathscr{A}$, defined by the components

$$[\boldsymbol{W}]^A = \left.\frac{\mathrm{d}}{\mathrm{d}s}\right|_{s=0} [\overline{\boldsymbol{X}}(s)]^A \tag{2.12}$$

The vector $\boldsymbol{W}$ lies in a space $T_X\mathscr{B}_0$ of column vectors, which are tangent to all curves $\overline{\boldsymbol{X}}(s)$ at the point $\boldsymbol{X}$ in $\mathscr{B}_0$. This set is called the tangent space. The union of the tangent spaces to $\mathscr{B}_0$ at all points $\boldsymbol{X} \in \mathscr{B}_0$ is called the tangent bundle $T\mathscr{B}_0$.

We are able to define a length scale for tangent vectors by using the inner product on the ambient space, which means

$$[\boldsymbol{W}, \boldsymbol{V}] = [\boldsymbol{W}]^A \, \delta_{AB} \, [\boldsymbol{V}]^B \tag{2.13}$$

for any two tangent vectors $\boldsymbol{W}$ and $\boldsymbol{V}$ in $T_X\mathscr{B}_0$. This inner product defines a linear mapping $\boldsymbol{W}^*$ in the dual space $\mathbb{L}(T_X\mathscr{B}_0, \mathbb{R})$ corresponding to the tangent space $T_X\mathscr{B}_0$. This dual space is called the cotangent space $T_X^*\mathscr{B}_0$. Each cotangent vector $\boldsymbol{W}^*$ coincides with a row vector $[W_1 \ldots W_{n_{\text{dim}}}]$. The entries W_B coincide with the real numbers $W^A\,\delta_{AB}$. The bundle space of the cotangent space is denoted by $T^*\mathscr{B}_0$. We obtain a pairing $\langle \boldsymbol{W}^*, \boldsymbol{V} \rangle$ of arbitrary tangent vectors $\boldsymbol{V}$ and cotangent vectors $\boldsymbol{W}^*$ by using the dual pairing corresponding to the ambient space.

2.1.3. The current configuration. The bounded open set $\mathscr{B}_t \subset \mathscr{A}$ denotes the current configuration of the continuum body at fixed time $t \in \mathscr{T}$. Points $\boldsymbol{x}$ in $\mathscr{B}_t$ are designated by column vectors $[x^1, \ldots, x^{n_{\text{dim}}}]$. The set $\mathscr{B}_t$ possesses a piecewise smooth boundary $\partial\mathscr{B}_t$, on which we prescribe positions $\boldsymbol{x}$ on a part $\partial_x\mathscr{B}_t$.

A curve $\overline{\boldsymbol{x}}(s)$ in $\mathscr{B}_t$, which fulfils the given boundary conditions and coincides for $\overline{\boldsymbol{x}}(0)$ with the fixed point $\boldsymbol{x}$, is a subset of this current configuration. The tangent vector in the space $T_x\mathscr{B}_t$ at the curve $\overline{\boldsymbol{x}}(s)$ in the point $\boldsymbol{x}$ is given by the components

$$[\boldsymbol{w}]^a = \left.\frac{\mathrm{d}}{\mathrm{d}s}\right|_{s=0} [\overline{\boldsymbol{x}}(s)]^a \tag{2.14}$$

The corresponding tangent bundle is denoted by $T\mathscr{B}_t$. Accordingly, a tangent vector $\boldsymbol{w}$ at $\mathscr{B}_t$ coincides with a column vector $[w^1, \ldots, w^{n_{\text{dim}}}]$ in the ambient space $\mathscr{A}$. The inner product $[\boldsymbol{w}, \boldsymbol{v}]$ of arbitrary two tangent vectors $\boldsymbol{w}$ and $\boldsymbol{v}$ in $T_x\mathscr{B}_t$ arises from the inner product on the ambient space. Likewise, this inner product defines a cotangent space $T_x^*\mathscr{B}_t$ at the current position $\boldsymbol{x} \in \mathscr{B}_t$, including cotangent vectors

$$[\boldsymbol{w}^*]_b = [\boldsymbol{w}]^a\,\delta_{ab} \tag{2.15}$$

The matrix corresponding to such cotangent vectors is a row vector $[w_1 \ldots w_{n_{\text{dim}}}]$ in the dual space $\mathscr{A}^*$. The inner product defines, in turn, a pairing $\langle \boldsymbol{w}^*, \boldsymbol{v} \rangle$ of arbitrary tangent vectors $\boldsymbol{v}$ and cotangent vectors $\boldsymbol{w}^*$ in terms of the pairing on the ambient space.

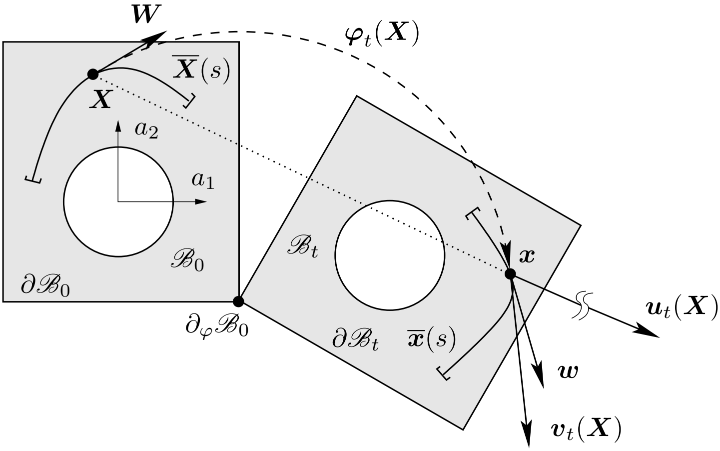

Figure 2.3. The current configuration $\mathscr{B}_t$ with the curve $\overline{\boldsymbol{x}}(s)$ through the point $\boldsymbol{x} \in \mathscr{B}_t$ and the corresponding tangent vector $\boldsymbol{w} \in T_x\mathscr{B}_t$. Further elements of this tangent space are the deformation velocity $\boldsymbol{v}_t(\boldsymbol{X})$ as tangent vector at the motion $\boldsymbol{\varphi}(t)$ and the displacement vector $\boldsymbol{u}_t(\boldsymbol{X})$ as tangent vector at the displacement curve.

2.1.4. Deformation and motion. A smooth injective and orientation preserving mapping $\boldsymbol{\varphi}_t : \mathscr{B}_0 \to \mathscr{B}_t$ of the reference configuration $\mathscr{B}_0$ to a current configuration $\mathscr{B}_t$ is called a deformation field of $\mathscr{B}_0$ (see Ciarlet [133]). The image $\boldsymbol{\varphi}_t(\mathscr{B}_0)$ coincides with the current configuration $\mathscr{B}_t$ of the continuum body. The entries x^a of the column vector $\boldsymbol{x} \in \mathscr{B}_t$ at fixed time $t \in \mathscr{T}$ are given by

$$[\boldsymbol{x}]^a = [\boldsymbol{\varphi}_t(\boldsymbol{X})]^a \tag{2.16}$$

We assume that, for all times $t \in \mathscr{T}$, the positions $\boldsymbol{x}$ on the boundary $\partial_x\mathscr{B}_t$ coincide with the points $\boldsymbol{X}$ on the so-called Dirichlet boundary $\partial_\varphi\mathscr{B}_0 \subset \partial\mathscr{B}_0$. A motion is a time curve $\boldsymbol{\varphi}(t)$, which coincides for a fixed time $t \in \mathscr{T}$ with a deformation field $\boldsymbol{\varphi}_t$ of the body (see Figure 2.3).

2.1.5. Displacement and velocity. Suppose a smooth curve $\overline{\boldsymbol{\varphi}}_t(s)$ of deformation fields, defined such that the Dirichlet boundary condition is satisfied and $\overline{\boldsymbol{\varphi}}_t(0)$ coincides with a fixed deformation field $\boldsymbol{\varphi}_t$. Then, a tangent field $\boldsymbol{\nu}_t : \mathscr{B}_0 \to T\mathscr{B}_t$ at this curve in $\boldsymbol{\varphi}_t$ is defined locally by the components

$$[\boldsymbol{\nu}_t(\boldsymbol{X})]^a = \left.\frac{\mathrm{d}}{\mathrm{d}s}\right|_{s=0} [\overline{\boldsymbol{\varphi}}_t(\boldsymbol{X})(s)]^a \qquad \forall \boldsymbol{X} \in \mathscr{B}_0 \tag{2.17}$$

where the mapping $\overline{\boldsymbol{\varphi}}_t(\boldsymbol{X})(s)$ denotes the trajectory for any point $\boldsymbol{X} \in \mathscr{B}_0$. A curve $\overline{\boldsymbol{\varphi}}_t(s)$ satisfies the Dirichlet boundary condition if each trajectory $\overline{\boldsymbol{\varphi}}_t(\boldsymbol{X})(s)$ coincides with $\boldsymbol{X}$ for all points $\boldsymbol{X} \in \partial_\varphi\mathscr{B}_0$ and for all curve parameter $s \in \mathbb{R}$.

For example, the trajectories $\boldsymbol{\varphi}_t(\boldsymbol{X}) + s(\boldsymbol{\varphi}_t(\boldsymbol{X}) - \boldsymbol{X})$ defines such a curve. The corresponding tangent field $\boldsymbol{u}_t$ at this curve is defined by

$$\boldsymbol{u}_t : \mathscr{B}_0 \ni \boldsymbol{X} \mapsto \boldsymbol{\varphi}_t(\boldsymbol{X}) - \boldsymbol{X} \in T_x\mathscr{B}_t \tag{2.18}$$

which is called displacement field. Hence, a tangent field $\boldsymbol{\nu}_t$ at an admissible curve $\overline{\boldsymbol{\varphi}}_t(s)$ vanishes at the Dirichlet boundary $\partial_\varphi\mathscr{B}_0$.

A further example of a curve $\overline{\boldsymbol{\varphi}}_t(s)$ is the time curve $\boldsymbol{\varphi}_{t+s}$, wherein s denotes a time difference. This curve satisfies the given time-independent Dirichlet boundary condition. According to the chain rule of differentiation, the tangent field at this time curve at the deformation field $\boldsymbol{\varphi}_t$ for a fixed time $t \in \mathscr{T}$ reads

$$\boldsymbol{v}_t : \mathscr{B}_0 \ni \boldsymbol{X} \mapsto \dot{\boldsymbol{\varphi}}_t(\boldsymbol{X}) \in T_x\mathscr{B}_t \tag{2.19}$$

where the dot denotes the partial time derivative. We call this mapping the Lagrangian deformation velocity field of the body, and refer to the curve $\boldsymbol{v}(t)$ as the velocity of the motion.

2.1.6. Momentum and kinetic energy. Based on the inner product corresponding to the ambient space, there is an inner product of arbitrary two tangent fields $\boldsymbol{\omega}_t$ and $\boldsymbol{\nu}_t$, which is given by

$$[\boldsymbol{\omega}_t, \boldsymbol{\nu}_t] = \int_{\mathscr{B}_0} [\rho_0(\boldsymbol{X})\, \boldsymbol{\omega}_t(\boldsymbol{X}), \boldsymbol{\nu}_t(\boldsymbol{X})] = \int_{\mathscr{B}_0} \rho_0(\boldsymbol{X})\, [\boldsymbol{\omega}_t(\boldsymbol{X})]^a\, \delta_{ab}\, [\boldsymbol{\nu}_t(\boldsymbol{X})]^b \tag{2.20}$$

where $\rho_0 : \mathscr{B}_0 \to \mathbb{R}_+$ denotes the density field in the reference configuration. The corresponding squared norm $\|\boldsymbol{\omega}_t\|^2$ is given by the expression $[\boldsymbol{\omega}_t, \boldsymbol{\omega}_t]$.

Hence, a cotangent field $\boldsymbol{\omega}_t^\star$ corresponding to the tangent field $\boldsymbol{\omega}_t$ in the deformation field $\boldsymbol{\varphi}_t$ can be defined by the components

$$[\boldsymbol{\omega}_t^\star(\boldsymbol{X})]_a = \rho_0(\boldsymbol{X})\,[\boldsymbol{\omega}_t^*(\boldsymbol{X})]_a \tag{2.21}$$

for any $\boldsymbol{X} \in \mathscr{B}_0$. By means of the inner product, we obtain a dual pairing $\langle \boldsymbol{\omega}_t^\star, \boldsymbol{\nu}_t \rangle$ of this cotangent field with a tangent field $\boldsymbol{\nu}_t$ at the deformation field $\boldsymbol{\varphi}_t$. Thus, in this context, we obtain the Lagrangian momentum field $\boldsymbol{\pi}_t$, defined by the components

$$[\boldsymbol{\pi}_t(\boldsymbol{X})]_a = [\boldsymbol{v}_t^\star(\boldsymbol{X})]_a \tag{2.22}$$

as the cotangent field corresponding to the Lagrangian deformation velocity field (compare Simo et al. [136]). Further, we refer to the curve $\boldsymbol{\pi}(t)$ as the momentum of the motion.

On the basis of the norm $\|\boldsymbol{v}_t\|$ of the Lagrangian deformation velocity field at fixed time $t \in \mathscr{T}$, the kinetic energy of the continuum body is defined by

$$\mathcal{T}(t) = \frac{1}{2}\|\boldsymbol{v}_t\|^2 = \frac{1}{2}\int_{\mathscr{B}_0} \rho_0(\boldsymbol{X})\,[\boldsymbol{v}_t(\boldsymbol{X})]^a\,\delta_{ab}\,[\boldsymbol{v}_t(\boldsymbol{X})]^a = \frac{1}{2}\,\langle \boldsymbol{v}_t^\star, \boldsymbol{v}_t \rangle \tag{2.23}$$

and can be viewed as a time curve during a motion $\boldsymbol{\varphi}(t)$ in the time interval of interest. Thus, the kinetic energy is based directly on the pairing of the Lagrangian deformation velocity field with its cotangent vector.

2.1.7. The deformation gradient field. The relation between a curve $\overline{\boldsymbol{X}}(s)$ at a point $\boldsymbol{X}$ in the reference configuration and the corresponding curve $\overline{\boldsymbol{x}}(s)$ in the current configuration is given by the deformation mapping. Consequently, the chain rule of differentiation implies the relations

$$[\boldsymbol{w}]^a = \frac{\partial[\boldsymbol{\varphi}_t(\boldsymbol{X})]^a}{\partial X^A}\,[\boldsymbol{W}]^A = [\partial_X \boldsymbol{\varphi}_t(\boldsymbol{X})]^a{}_A\,[\boldsymbol{W}]^A \tag{2.24}$$

of the components pertaining to the corresponding tangent vectors. The reals $[\partial_X \boldsymbol{\varphi}_t(\boldsymbol{X})]^a{}_A$ coincide with the components $[\mathrm{D}\boldsymbol{\varphi}_t(\boldsymbol{X})]^a{}_A$ of the Frèchet derivative $\mathrm{D}\boldsymbol{\varphi}_t : \mathscr{B}_0 \to \mathbb{L}(T\mathscr{B}_0, T\mathscr{B}_t)$ pertaining to the deformation $\boldsymbol{\varphi}_t$ at fixed time $t \in \mathscr{T}$ (see Figure 2.4).

$$\begin{tikzcd}[row sep=large, column sep=huge]
T\mathscr{B}_0 \arrow[r, shift right, "\boldsymbol{F}_t"'] \arrow[d, shift left, "\boldsymbol{C}_t"] & T\mathscr{B}_t \arrow[l, dashed, shift right, "\boldsymbol{F}_t^{-1}"'] \arrow[d, shift right, "\boldsymbol{\delta}"'] \\
T^*\mathscr{B}_0 \arrow[u, dashed, shift left, "\boldsymbol{C}_t^{-1}"] \arrow[r, dashed, shift right, "\boldsymbol{F}_t^{-T}"'] & T^*\mathscr{B}_t \arrow[l, shift right, "\boldsymbol{F}_t^{T}"'] \arrow[u, dashed, shift right, "\boldsymbol{\delta}^{-1}"']
\end{tikzcd}$$

Figure 2.4. The deformation gradient field $\boldsymbol{F}_t$ and the right Cauchy-Green tensor field $\boldsymbol{C}_t$ as linear mappings between bundle spaces.

The volume element V_X at any point $\boldsymbol{X} \in \mathscr{B}_0$ is mapped by the non-negative Jacobian determinant

$$J_t(\boldsymbol{X}) = \det(\mathrm{D}\boldsymbol{\varphi}_t(\boldsymbol{X})) > 0 \tag{2.25}$$

to the volume element V_x at the point $\boldsymbol{x} \in \mathscr{B}_t$, which indicates the local impenetrability of matter. Consequently, the tensor $\mathrm{D}\boldsymbol{\varphi}_t(\boldsymbol{X})$ at any $\boldsymbol{X} \in \mathscr{B}_0$ is positive-definite, and an element of the general linear group $\mathbb{GL}_+(T_X\mathscr{B}_0, T_x\mathscr{B}_t)$. The Lagrangian field $\mathrm{D}\boldsymbol{\varphi}_t$ is designated as the deformation gradient field $\boldsymbol{F}_t$, which means

$$[\boldsymbol{F}_t(\boldsymbol{X})]^a{}_A = [\partial_X \boldsymbol{\varphi}_t(\boldsymbol{X})]^a{}_A \tag{2.26}$$

Since for any point $\boldsymbol{X} \in \mathscr{B}_0$ at fixed time $t \in \mathscr{T}$ the deformation gradient $\boldsymbol{F}_t(\boldsymbol{X})$ is a positive-definite tensor, there exists a uniquely defined inverse $(\boldsymbol{F}_t(\boldsymbol{X}))^{-1}$. This tensor coincides with the Frèchet derivative $\mathrm{D}(\boldsymbol{\varphi}_t^{-1})(\boldsymbol{x})$ of the inverse deformation with $\boldsymbol{x} = \boldsymbol{\varphi}_t(\boldsymbol{X})$. Hence, the inverse deformation gradient field is given by the components

$$[(\boldsymbol{F}_t(\boldsymbol{X}))^{-1}]^B{}_a = [\mathrm{D}(\boldsymbol{\varphi}_t^{-1})(\boldsymbol{\varphi}_t(\boldsymbol{X}))]^B{}_a = [\partial_x(\boldsymbol{\varphi_t}^{-1})(\boldsymbol{\varphi}_t(\boldsymbol{X}))]^B{}_a \tag{2.27}$$

The Frèchet derivative $\mathrm{D}\boldsymbol{v}_t : \mathscr{B}_0 \to \mathbb{GL}_+(T\mathscr{B}_0, T\mathscr{B}_t)$ of the Lagrangian deformation velocity field $\boldsymbol{v}_t$ at time $t \in \mathscr{T}$ is called the Lagrangian deformation velocity gradient field. According to Clairaut's theorem, partial derivatives commute, and $\mathrm{D}\boldsymbol{v}_t$ coincides with the time rate of change $\dot{\boldsymbol{F}}_t$ of the deformation gradient field. Hence, we obtain

$$[\mathrm{D}\boldsymbol{v}_t(\boldsymbol{X})]^a{}_A = [\partial_X \boldsymbol{v}_t(\boldsymbol{X})]^a{}_A = [\partial_X \dot{\boldsymbol{\varphi}}_t(\boldsymbol{X})]^a{}_A = \overset{\cdot}{\overline{[\partial_X \boldsymbol{\varphi}_t(\boldsymbol{X})]^a{}_A}} = [\dot{\boldsymbol{F}}_t(\boldsymbol{X})]^a{}_A \tag{2.28}$$

Considering the time curve $\boldsymbol{F}_{t+s}$ at a fixed time $t \in \mathscr{T}$, the mapping $\dot{\boldsymbol{F}}_t$ is a tangent field at the deformation gradient field according to the chain rule of differentiation.

2.1.8. The right Cauchy-Green tensor field. The deformation gradient relates the vector $\boldsymbol{w}$ in the tangent space at the current configuration to the tangent vector $\boldsymbol{W}$ at the reference configuration. The squared length $\|\boldsymbol{w}\|^2$ of the tangent vector $\boldsymbol{w}$ therefore can be written as

$$\|\boldsymbol{w}\|^2 = [\boldsymbol{w}^*]_a [\boldsymbol{w}]^a = [\boldsymbol{w}^*]_a \, [\boldsymbol{F}_t(\boldsymbol{X})]^a{}_A [\boldsymbol{W}]^A \tag{2.29}$$

by taking Equations (2.24) and (2.26) into account. Next, we substitute the tangent vector $\boldsymbol{W}$ for the cotangent vector $\boldsymbol{w}^*$ by recalling that the transpose $(\boldsymbol{F}_t(\boldsymbol{X}))^T$ of the deformation gradient is a tensor of the cotangent space $T_x^*\mathscr{B}_t$ to the cotangent space $T_X^*\mathscr{B}_0$. We arrive at

$$\|\boldsymbol{w}\|^2 = [\boldsymbol{W}]^A \, [(\boldsymbol{F}_t(\boldsymbol{X}))^T]_A{}^a \delta_{ab} \, [\boldsymbol{F}_t(\boldsymbol{X})]^b{}_B [\boldsymbol{W}]^B = [\boldsymbol{W}]^A \, [\boldsymbol{C}_t(\boldsymbol{X})]_{AB} [\boldsymbol{W}]^B \tag{2.30}$$

This symmetric positive-definite tensor $\boldsymbol{C}_t(\boldsymbol{X})$ in the set $\mathbb{S}_+(T_X\mathscr{B}_0, T_X^*\mathscr{B}_0)$ expresses the length of a tangent vector $\boldsymbol{w} \in T_x\mathscr{B}_t$ by means of the corresponding Lagrangian tangent vector $\boldsymbol{W} \in T_X\mathscr{B}_0$, and is called the right Cauchy-Green tensor. The corresponding inverse tensor $(\boldsymbol{C}_t(\boldsymbol{X}))^{-1}$ is uniquely defined by the components

$$[(\boldsymbol{C}_t(\boldsymbol{X}))^{-1}]^{AB} = [(\boldsymbol{F}_t(\boldsymbol{X}))^{-1}]^A{}_a \, \delta^{ab} \, [(\boldsymbol{F}_t(\boldsymbol{X}))^{-T}]_b{}^B \tag{2.31}$$

We refer to the field $\boldsymbol{C}_t : \mathscr{B}_0 \to \mathbb{S}_+(T\mathscr{B}_0, T^*\mathscr{B}_0)$ as the right Cauchy-Green tensor field. By means of the curve $\boldsymbol{C}_{t+s}$ at time $t \in \mathscr{T}$, we identify the time derivative $\dot{\boldsymbol{C}}_t$ of the right Cauchy-Green tensor field as a tangent field, which we call the Lagrangian strain velocity field.

Recalling that the stretch λ denotes the length of change of tangent vectors, the squared stretch reads

$$\lambda^2 = \|\boldsymbol{w}\|^2 - \|\boldsymbol{W}\|^2 = [\boldsymbol{W}]^A \left\{[\boldsymbol{C}_t(\boldsymbol{X})]_{AB} - [\boldsymbol{\delta}]_{AB}\right\} [\boldsymbol{W}]^B = 0 \tag{2.32}$$

on a rigid body motion, which means the right Cauchy-Green tensor field coincides with the metric tensor in the ambient space.

Taking the definition of the right Cauchy-Green tensor in Equation (2.30) into account, the Jacobian determinant is written by the determinant of the right Cauchy-Green tensor as

$$J_t(\boldsymbol{X}) = \sqrt{\det(\boldsymbol{C}_t(\boldsymbol{X}))} \tag{2.33}$$

Furthermore, by introducing the symmetric right Cauchy-Green tensor field $\boldsymbol{C}_t$ as argument of the elastic potential energy function, the elastic material model is frame-indifferent in the sense that, its free energy is left-invariant under the (left-) action of the rotation group $\mathbb{SO}(\mathscr{A}, \mathscr{A})$ of the ambient space on the deformation gradient field (for more details see Simo et al. [137]).

2.1.9. The Lagrangian temperature field. We regard the absolute temperatures $\Theta_t(\boldsymbol{X})$ of each point $\boldsymbol{X} \in \mathscr{B}_0$ at time $t \in \mathscr{T}$ as elements of the temperature set $\mathscr{H}_t \subset \mathbb{R}_+$. The Lagrangian temperature field is denoted by the mapping

$$\Theta_t : \mathscr{B}_0 \ni \boldsymbol{X} \mapsto \Theta_t(\boldsymbol{X}) \in \mathscr{H}_t \tag{2.34}$$

We assume a piecewise smooth boundary $\partial_\Theta \mathscr{B}_0 \subset \partial \mathscr{B}_0$ on which temperatures $\Theta_t(\boldsymbol{X})$ for all points $\boldsymbol{X} \in \partial_\Theta \mathscr{B}_0$ at all times $t \in \mathscr{T}$ coincide with the constant temperature Θ_∞ in the ambient space (see Figure 2.5).

In the temperature set, there is defined a curve $\Theta_t(\overline{\boldsymbol{X}}(s))$ by means of the curve $\overline{\boldsymbol{X}}(s) \subset \mathscr{B}_0$. Since this curve is defined such that $\overline{\boldsymbol{X}}(0)$ coincides with a fixed point $\boldsymbol{X}$, the chain rule of differentiation implies

$$\vartheta_t(\boldsymbol{X}) \doteq \frac{\mathrm{d}}{\mathrm{d}s}\bigg|_{s=0} \Theta_t(\overline{\boldsymbol{X}}(s)) = [\partial_X \Theta_t(\boldsymbol{X})]_A [\boldsymbol{W}]^A = [\mathrm{D}\,\Theta_t(\boldsymbol{X})]_A [\boldsymbol{W}]^A \tag{2.35}$$

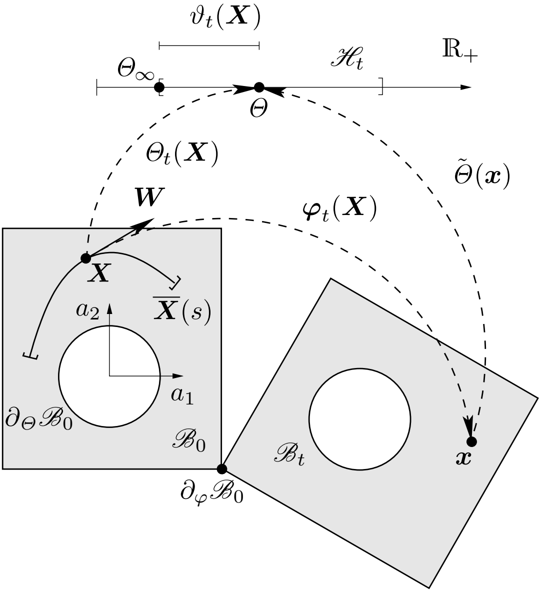

Figure 2.5. The mappings from the configurations of a deformed body $\mathscr{B}$ into the temperature set $\mathscr{H}_t$, and a corresponding tangent vector $\vartheta_t(\boldsymbol{X})$ associated with a tangent vector $\boldsymbol{W}$ in the tangent space at the point $\boldsymbol{X}$ in the reference configuration.

between the element $\vartheta_t(\boldsymbol{X})$ in the tangent space $T_\Theta\mathscr{H}_t$ at the temperature curve and the vector $\boldsymbol{W}$ in the tangent space $T_X\mathscr{B}_0$. The row vector $\mathrm{D}\,\Theta_t(\boldsymbol{X})$ lies in the cotangent space $T_X^*\mathscr{B}_0$. Taking relation (2.35) into account, we identify a tangent vector $\vartheta_t(\boldsymbol{X})$ at all points $\boldsymbol{X}$ on the Dirichlet boundary $\partial_\Theta\mathscr{B}_0$ as zero. The Frèchet derivative

$$\mathrm{D}\,\Theta_t : \mathscr{B}_0 \ni \boldsymbol{X} \mapsto \mathrm{D}\,\Theta_t(\boldsymbol{X}) \in T_X^*\mathscr{B}_0 \tag{2.36}$$

of the Lagrangian temperature field is called the Lagrangian temperature gradient field at fixed time $t \in \mathscr{T}$.

We obtain a curve $\overline{\Theta}_t(s)$ of temperature fields, which fulfills the boundary condition $\Theta_t(\boldsymbol{X}) = \Theta_\infty$ at all points $\boldsymbol{X} \in \partial_\Theta\mathscr{B}_0$ for all curve parameter $s \in \mathbb{R}$, by means of the temperature trajectories $\Theta_t(\boldsymbol{X}) + s\,(\Theta_t(\boldsymbol{X}) - \Theta_\infty)$.

$$\begin{tikzcd}
T\mathscr{B}_0 \arrow[d, dashed, shift left, "\boldsymbol{C}_t"] & \mathscr{V} \arrow[l, "\boldsymbol{T}_t^{-1}"] \arrow[d, dashed, shift right, "\tilde{\boldsymbol{c}}_t"'] \\
T^*\mathscr{B}_0 \arrow[u, shift left, "\boldsymbol{\Gamma}_t^{-1}"] \arrow[r, dashed, "\boldsymbol{T}_t^{-T}"] & \mathscr{V}^* \arrow[u, shift right, "\boldsymbol{\delta}^{-1}"']
\end{tikzcd}$$

Figure 2.6. The viscous transformation tensor field $\boldsymbol{T}_t$ and the deformation-dependent metric tensor field $\tilde{\boldsymbol{c}}_t$ are linear mappings with respect to the tangent space $T\mathscr{B}_0$ at the reference configuration and the subspace $\mathscr{V}$ of the ambient space. The internal variable $\boldsymbol{\Gamma}_t$ can be viewed as a kind of right Cauchy-Green tensor on the reference configuration.

The tangent vector at such a temperature trajectory is given by

$$\vartheta_t(\boldsymbol{X}) = \left.\frac{\mathrm{d}}{\mathrm{d}s}\right|_{s=0} \Theta_{t,s}(\boldsymbol{X}) = \Theta_t(\boldsymbol{X}) - \Theta_\infty \tag{2.37}$$

Hence, the mapping $\vartheta_t : \boldsymbol{X} \ni \mathscr{B}_0 \mapsto \Theta(\boldsymbol{X}) - \Theta_\infty$ is a tangent field at the curve $\overline{\Theta}_t(s)$, to which we refer to as the Lagrangian relative temperature field of the body.

On the other hand, the time curve Θ_{t+s} also satisfies the time-independent temperature boundary condition. Therefore, the Lagrangian temperature velocity $\dot{\Theta}_t(\boldsymbol{X})$ is a tangent vector for all $\boldsymbol{X} \in \mathscr{B}_0$, and the Lagrangian temperature velocity field $\dot{\Theta}_t$ is a tangent field.

2.1.10. The Lagrangian internal variable field. For describing viscous behaviour, we introduce an invertible tensor $\boldsymbol{T}_t(\boldsymbol{X})$ of the tangent space $T_X\mathscr{B}_0$ to a subspace $\mathscr{V}_X \subset \mathscr{A}$ as internal variable. In order to obtain a viscoelastic material model, this transformation shall not change the elastic properties of the material (compare Noll [138] as well as Bertram [139–141]). Therefore, we carry the right Cauchy-Green tensor $\boldsymbol{C}_t(\boldsymbol{X})$ in the argument of its free energy to the vector space $\mathscr{V}_X$ by the push-forward

$$[(\boldsymbol{T}_t(\boldsymbol{X}))^{-T}]_\alpha{}^A\,[\boldsymbol{C}_t(\boldsymbol{X})]_{AB}\,[(\boldsymbol{T}_t(\boldsymbol{X}))^{-1}]^B{}_\beta = [\tilde{\boldsymbol{c}}_t(\boldsymbol{X})]_{\alpha\beta} \tag{2.38}$$

while Greek indices refer to the space $\mathscr{V}_X$ (compare Figure 2.6). We obtain the deformation-dependent metric tensor $\tilde{\boldsymbol{c}}_t(\boldsymbol{X}) \in \mathbb{S}_+(\mathscr{V}_X, \mathscr{V}_X^*)$ for vectors in the space $\mathscr{V}_X$ as argument of the free energy.

On the other hand, the matrix corresponding to this metric tensor and the matrix of the tensor $\boldsymbol{\Lambda}_t(\boldsymbol{X})$ in the linear space $\mathbb{L}(T_X^*\mathscr{B}_0, T_X^*\mathscr{B}_0)$, given by the components

$$[\boldsymbol{\Lambda}_t(\boldsymbol{X})]_C{}^A = [\boldsymbol{C}_t(\boldsymbol{X})]_{CB}\,[(\boldsymbol{\Gamma}_t(\boldsymbol{X}))^{-1}]^{BA} \tag{2.39}$$

where

$$[(\boldsymbol{\Gamma}_t(\boldsymbol{X}))^{-1}]^{BA} = [(\boldsymbol{T}_t(\boldsymbol{X}))^{-1}]^B{}_\beta\,\delta^{\beta\alpha}\,[(\boldsymbol{T}_t(\boldsymbol{X}))^{-T}]_\alpha{}^A \tag{2.40}$$

has equal invariants (see Miehe [142], Betsch & Stein [143] and Betsch & Steinmann [144]). Hence, the symmetric tensor $\boldsymbol{\Gamma}_t(\boldsymbol{X})$ in the set $\mathbb{S}_+(T_X\mathscr{B}_0, T_X^*\mathscr{B}_0)$ can be viewed as a viscous internal variable for an isotropic material, because its free energy depends only on the invariants of its tensorial arguments. The symmetric tensor $\boldsymbol{\Gamma}_t(\boldsymbol{X})$ can be interpreted as a kind of right Cauchy-Green tensor according to its positive definiteness

$$[\boldsymbol{W}]^A[\boldsymbol{\Gamma}_t(\boldsymbol{X})]_{AB}[\boldsymbol{W}]^B = [\boldsymbol{T}_t(\boldsymbol{X})]^\alpha{}_A[\boldsymbol{W}]^A\,\delta_{\alpha\beta}\,[\boldsymbol{T}_t(\boldsymbol{X})]^\beta{}_B[\boldsymbol{W}]^B \geqslant 0 \tag{2.41}$$

for any vector $\boldsymbol{W}$ in the tangent space $T_X\mathscr{B}_0$. We consider the internal variables $\boldsymbol{\Gamma}_t(\boldsymbol{X})$ pertaining to all points $\boldsymbol{X} \in \mathscr{B}_0$ at a fixed time $t \in \mathscr{T}$ as a subspace $\mathscr{S}_t$ of the linear space $\mathbb{S}_+(T_X\mathscr{B}_0, T_X^*\mathscr{B}_0)$. We refer to the set $\mathscr{S}_t$ as the internal variable set.

In the end, we obtain the potential energy function

$$\mathcal{U}^{\text{int}}(t) = \int_{\mathscr{B}_0} \Psi_t(\boldsymbol{X}) = \int_{\mathscr{B}_0} \Psi(\boldsymbol{\Lambda}_t(\boldsymbol{X}), \Theta_t(\boldsymbol{X})) \tag{2.42}$$

and the associated free energy $\Psi : \mathbb{L}(T_X^*\mathscr{B}_0, T_X^*\mathscr{B}_0) \times \mathscr{H}_t \to \mathbb{R}$. Using the symmetric tensor field $\boldsymbol{\Gamma}_t$ as internal variable, the potential energy function is also frame-indifferent in the sense that the free energy Ψ is left-invariant under the (left-) action of the rotation group $\mathbb{SO}(\mathscr{A}, \mathscr{A})$ on the viscous transformation field $\boldsymbol{T}_t$.

Note also that a symmetric internal variable does not require the specification of an inelastic spin tensor by an additional condition as in Armero [73]. Considering the curve $\boldsymbol{\Gamma}_{t+s}$ with the time difference s as curve

$$\begin{tikzcd}[column sep=huge, row sep=huge]
T\mathscr{B}_0 \arrow[r, dashed, "\boldsymbol{F}_t"] & T\mathscr{B}_t \\
T^*\mathscr{B}_0 \arrow[u, dashed, "\boldsymbol{S}_t"] \arrow[ur, "\boldsymbol{P}_t"] \arrow[r, shift right=1.5, "\boldsymbol{P}_t^*"'] & T^*\mathscr{B}_t \arrow[u, "\boldsymbol{\delta}^{-1}"'] \arrow[ul, dashed, "\boldsymbol{P}_t^T"'] \arrow[l, dashed, shift right=1.5, "\boldsymbol{F}_t^T"']
\end{tikzcd}$$

Figure 2.7. The first Piola-Kirchhoff stress tensor field $\boldsymbol{P}_t$ can be written by the second Piola-Kirchhoff stress tensor field $\boldsymbol{S}_t$ and the deformation gradient $\boldsymbol{F}_t$, or by means of the covariant first Piola-Kirchhoff stress tensor field $\boldsymbol{P}_t^*$ and the inverse metric tensor $\boldsymbol{\delta}^{-1}$ corresponding to the current configuration.

parameter, the corresponding tangent field coincides for all $\boldsymbol{X} \in \mathscr{B}_0$ with the internal variable velocity $\dot{\boldsymbol{\Gamma}}_t(\boldsymbol{X})$. We refer to the tangent field $\dot{\boldsymbol{\Gamma}}_t$ as the Lagrangian internal variable velocity field.

2.1.11. Stress and entropy. We consider the directional derivative of the free energy at the point $\boldsymbol{X} \in \mathscr{B}_0$ along the continuous time curve $\Psi_{t+s}(\boldsymbol{X})$, and obtain the time rate of change

$$\dot{\Psi}_t(\boldsymbol{X}) = \frac{\partial \Psi_t(\boldsymbol{X})}{\partial \Gamma_{AB}} \, [\dot{\boldsymbol{\Gamma}}_t(\boldsymbol{X})]_{AB} + \frac{\partial \Psi_t(\boldsymbol{X})}{\partial C_{AB}} \, [\dot{\boldsymbol{C}}_t(\boldsymbol{X})]_{AB} + \frac{\partial \Psi_t(\boldsymbol{X})}{\partial \Theta} \, \dot{\Theta}_t(\boldsymbol{X}) \tag{2.43}$$

Since $\dot{\boldsymbol{\Gamma}}_t(\boldsymbol{X})$, $\dot{\boldsymbol{C}}_t(\boldsymbol{X})$ and $\dot{\Theta}_t(\boldsymbol{X})$ are tangent vectors and the free energy is a real number, the righthand side of Equation (2.43) defines a dual pairing of tangent vectors with their corresponding cotangent vectors.

First, the negative partial derivative of the free energy with respect to the internal variable $\boldsymbol{\Gamma}_t(\boldsymbol{X})$ defines a cotangent vector

$$[\boldsymbol{\Upsilon}_t(\boldsymbol{X})]^{AB} = -\frac{\partial \Psi(\boldsymbol{\Lambda}_t(\boldsymbol{X}), \Theta_t(\boldsymbol{X}))}{\partial \Gamma_{AB}} \tag{2.44}$$

which we term Lagrangian non-equilibrium stress tensor. The corresponding field $\boldsymbol{\Upsilon}_t$ is a cotangent field at the internal variable field.

Similarly, twice the partial derivative of the free energy with respect to the right Cauchy-Green tensor $\boldsymbol{C}_t(\boldsymbol{X})$ represents a cotangent vector $\boldsymbol{S}_t(\boldsymbol{X})$ in the linear space $\mathbb{S}(T_X^*\mathscr{B}_0, T_X\mathscr{B}_0)$, which denotes the second Piola-Kirchhoff stress tensor. The corresponding dual pairing designates the stress power

$$\mathcal{P}^{\text{int}}(t) = \int_{\mathscr{B}_0} p_t^{\text{int}}(\boldsymbol{X}) = \int_{\mathscr{B}_0} \frac{\partial \Psi_t(\boldsymbol{X})}{\partial C_{AB}} \, [\dot{\boldsymbol{C}}_t(\boldsymbol{X})]_{AB} = \frac{1}{2} \int_{\mathscr{B}_0} [\boldsymbol{S}_t(\boldsymbol{X})]^{AB} \, [\dot{\boldsymbol{C}}_t(\boldsymbol{X})]_{AB} \tag{2.45}$$

at time $t \in \mathscr{T}$ done by the second Piola-Kirchhoff stress tensor field. Therefore, the second Piola-Kirchhoff stress tensor field $\boldsymbol{S}_t$ is called energy-conjugated to the half of the strain velocity field $\dot{\boldsymbol{C}}_t$. By using the chain rule of differentiation, the density $p_t^{\text{int}}(\boldsymbol{X})$ of the stress power can be also written as

$$p_t^{\text{int}}(\boldsymbol{X}) = [\boldsymbol{S}_t(\boldsymbol{X})]^{BA} \, [\boldsymbol{R}_t(\boldsymbol{X})]_{BA} = [\boldsymbol{P}_t^*(\boldsymbol{X})]_a{}^A \, [\dot{\boldsymbol{F}}_t(\boldsymbol{X})]^a{}_A \tag{2.46}$$

where

$$[\boldsymbol{R}_t(\boldsymbol{X})]_{BA} = [(\boldsymbol{F}_t(\boldsymbol{X}))^T]_B{}^c \delta_{ca} [\dot{\boldsymbol{F}}_t(\boldsymbol{X})]^a{}_A \tag{2.47}$$

We refer to $\boldsymbol{R}_t(\boldsymbol{X})$ as elastic deformation rate tensor, and to the cotangent vector $\boldsymbol{P}_t^*(\boldsymbol{X})$ in the linear space $\mathbb{L}(T_X^*\mathscr{B}_0, T_x^*\mathscr{B}_t)$ as covariant first Piola-Kirchhoff stress tensor (compare Miehe [145]).

On the other hand, a cotangent vector corresponding to the negative Lagrangian temperature velocity $\dot{\Theta}_t(\boldsymbol{X}) \in T_\Theta\mathscr{H}_t$ is the Lagrangian entropy

$$\eta_t(\boldsymbol{X}) = -\frac{\partial \Psi(\boldsymbol{\Lambda}_t(\boldsymbol{X}), \Theta_t(\boldsymbol{X}))}{\partial \Theta} \tag{2.48}$$

which is an element in the linear space $\mathbb{L}(T_\Theta\mathscr{H}_t, \mathbb{R})$ or the cotangent space $T_\Theta^*\mathscr{H}_t$, respectively. The corresponding field is a cotangent field at the temperature field Θ_t of the body.

2.2. Lagrangian description of the governing equations

The motion $\boldsymbol{\varphi}(t)$ of the body and the temperature evolution curve $\Theta(t)$ are determined by a system of evolution equations in local or strong form. These equations emanate from the balance laws of continuum dynamics, postulated in integral or spatially weak form. We also prefer the Lagrangian description of these balance laws.

For more details see the recent references Haupt [96] and Holzapfel [135], as well as the classical references Truesdell & Toupin [146] and Malvern [147], for instance.

2.2.1. The mechanical evolution equation. Let us start by postulating the balance of mechanical energy of the continuum body, written as the equation

$$\dot{\mathcal{T}} + \mathcal{P}^{\text{int}} = \mathcal{P}^{\text{ext}} \tag{2.49}$$

and relating the rate of change of the kinetic energy $\mathcal{T}(t)$ with the stress power $\mathcal{P}^{\text{int}}(t)$, done by the stress field, and the external mechanical power $\mathcal{P}^{\text{ext}}(t)$, done by the acting forces. We neglect a prescribed body force density field on the reference configuration. In the Lagrangian description this balance equation then reads

$$\int_{\mathscr{B}_0} \rho_0(\boldsymbol{X})[\boldsymbol{v}_t^*(\boldsymbol{X})]_a \, [\dot{\boldsymbol{v}}_t(\boldsymbol{X})]^a + \int_{\mathscr{B}_0} [\boldsymbol{P}_t^*(\boldsymbol{X})]_a{}^A [\dot{\boldsymbol{F}}_t(\boldsymbol{X})]^a{}_A = \int_{\partial\mathscr{B}_0} [\boldsymbol{v}_t^*(\boldsymbol{X})]_a \, [\boldsymbol{t}_t(\boldsymbol{X})]^a \tag{2.50}$$

where the surface force field $\boldsymbol{t}_t : \partial\mathscr{B}_0 \to T\mathscr{B}_t$ represents the first Piola-Kirchhoff traction vector field. According to the Piola-Kirchhoff theorem, the components of the Piola-Kirchhoff traction vector at each point $\boldsymbol{X} \in \partial\mathscr{B}_0$ is connected with the outward normal field $\boldsymbol{N}_0 : \partial\mathscr{B}_0 \to T^*\mathscr{B}_0$ on the reference configuration by the relation

$$[\boldsymbol{t}_t(\boldsymbol{X})]^a = [\boldsymbol{P}_t(\boldsymbol{X})]^{aA} \, [\boldsymbol{N}_0(\boldsymbol{X})]_A = \delta^{ab} \, [\boldsymbol{P}_t^*(\boldsymbol{X})]_b{}^A \, [\boldsymbol{N}_0(\boldsymbol{X})]_A \tag{2.51}$$

The first Piola-Kirchhoff stress tensor field $\boldsymbol{P}_t : \mathscr{B}_0 \to \mathbb{L}(T^*\mathscr{B}_0, T\mathscr{B}_t)$ follows from the covariant first Piola-Kirchhoff stress tensor field $\boldsymbol{P}_t^*$ by the inverse metric in the current configuration (compare Figure 2.7). Thus, the righthand side in Equation (2.50) takes the form

$$\int_{\partial\mathscr{B}_0} [\boldsymbol{v}_t^*(\boldsymbol{X})]_a \, [\boldsymbol{P}_t(\boldsymbol{X})]^{aA} \, [\boldsymbol{N}_0(\boldsymbol{X})]_A = \int_{\partial\mathscr{B}_0} [\boldsymbol{N}_0(\boldsymbol{X})]_A \, [(\boldsymbol{P}_t(\boldsymbol{X}))^T]^{Aa} [\boldsymbol{v}_t^*(\boldsymbol{X})]_a \tag{2.52}$$

where Equation (2.6) for the transposed mapping has been applied to the first Piola-Kirchhoff stress tensor. The application of Gauss' divergence theorem then transforms the boundary integral (2.52) to a volume integral. Since the velocity vector $\boldsymbol{v}_t$ and the first Piola-Kirchhoff stress tensor $\boldsymbol{P}_t$ both depends on the point $\boldsymbol{X} \in \mathscr{B}_0$, we obtain

$$\begin{aligned} \int_{\mathscr{B}_0} \frac{\partial[(\boldsymbol{P}_t(\boldsymbol{X}))^T]^{Aa}[\boldsymbol{v}_t^*(\boldsymbol{X})]_a}{\partial X^A} = & \int_{\mathscr{B}_0} [\boldsymbol{v}_t^*(\boldsymbol{X})]_a \, [\partial_X \boldsymbol{P}_t(\boldsymbol{X})]^{aA}{}_A + \\ & + \int_{\mathscr{B}_0} [\boldsymbol{P}_t^*(\boldsymbol{X})]_a{}^A \, [\dot{\boldsymbol{F}}_t(\boldsymbol{X})]^a{}_A \end{aligned} \tag{2.53}$$

after employing Equation (2.28) for the Lagrangian velocity gradient. We substitute Equation (2.53) for the righthand side of Equation (2.50). In this way, the terms associated with the stress power annihilate each other. Noting the definitions of the Lagrangian momentum field in Equation (2.22) and of the covariant first Piola-Kirchhoff stress tensor, the localisation theorem implies the relation

$$\left([\dot{\boldsymbol{\pi}}_t(\boldsymbol{X})]_a - [\partial_X \boldsymbol{P}_t^*(\boldsymbol{X})]_a{}^A{}_A\right) [\boldsymbol{v}_t(\boldsymbol{X})]^a = 0 \tag{2.54}$$

Note that the tangent vector $\boldsymbol{v}_t(\boldsymbol{X}) \in T_x\mathscr{B}_t$ at the point $\boldsymbol{\varphi}_t(\boldsymbol{X}) \in \mathscr{B}_t$ at fixed time $t \in \mathscr{T}$ has to be arbitrary for any point $\boldsymbol{X}$ in the reference configuration. Taking the definition of the Lagrangian deformation velocity field into account, for any point $\boldsymbol{X} \in \mathscr{B}_0$ and $a \in \mathscr{N}_{sd}$, we thus arrive at the partial differential equation system

$$\boxed{\begin{array}{rcl} [\dot{\boldsymbol{\varphi}}_t(\boldsymbol{X})]^a & = & [\boldsymbol{v}_t(\boldsymbol{X})]^a \\ [\dot{\boldsymbol{\pi}}_t(\boldsymbol{X})]_a & = & [\partial_X \boldsymbol{P}_t^*(\boldsymbol{X})]_a{}^A{}_A \end{array}} \tag{2.55}$$

which represents the local form of the equations of motion in the Lagrangian setting.

2.2.2. The thermal evolution equation. Now, we consider the case in which thermal power $\mathcal{Q}(t)$ is introduced in the continuum by a heat surface density field $Q_t : \partial\mathscr{B}_0 \to \mathbb{R}$ on the boundary of the body, which means

$$\mathcal{Q}(t) = \int_{\partial\mathscr{B}_0} Q_t(\boldsymbol{X}) \tag{2.56}$$

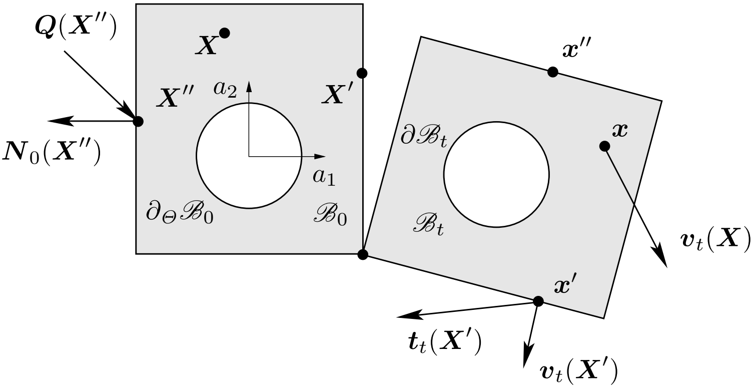

Figure 2.8. The Piola-Kirchhoff heat flux field $\boldsymbol{Q}$ is pointwise projected by the inward normal field $-\boldsymbol{N}_0$ on the boundary of the reference configuration. The first Piola-Kirchhoff traction vector field $\boldsymbol{t}_t(\boldsymbol{X}')$ follows via a linear mapping from the normal field $\boldsymbol{N}_0$ of the reference configuration.

According to Stokes' heat flux theorem, the heat surface density field Q_t is defined by a Piola-Kirchhoff heat flux field $\boldsymbol{Q}_t : \mathscr{B}_0 \to T\mathscr{B}_0$ via an inward normal projection (see Figure 2.8) at a point $\boldsymbol{X} \in \partial\mathscr{B}_0$ on the boundary, that is

$$Q_t(\boldsymbol{X}) = -[\boldsymbol{N}_0(\boldsymbol{X})]_A \, [\boldsymbol{Q}_t(\boldsymbol{X})]^A \tag{2.57}$$

The postulate accounting for heat transfer is the second law of thermodynamics. The corresponding state variable is the Lagrangian entropy field η_t. In the Lagrangian setting, this balance law postulates a non-negative total production of entropy $\tilde{\mathcal{D}}(t)$, defined by

$$\tilde{\mathcal{D}} := \dot{\mathcal{S}} - \tilde{\mathcal{Q}} \geqslant 0, \tag{2.58}$$

where $\mathcal{S}(t)$ denotes the entropy possessed by the entire continuum body, and the entropy input in the body has been designated by the mapping $\tilde{\mathcal{Q}}(t)$. Neglecting an entropy source density field, the entropy input $\tilde{\mathcal{Q}}$ is solely related to the Piola-Kirchhoff heat flux field $\boldsymbol{Q}_t$ via the assumed entropy flux

$$[\boldsymbol{H}_t(\boldsymbol{X})]^A = \frac{1}{\Theta_t(\boldsymbol{X})} \, [\boldsymbol{Q}_t(\boldsymbol{X})]^A \tag{2.59}$$

(compare Hutter [148]). We postulate the local production of entropy $\tilde{D}_t(\boldsymbol{X})$ for a point $\boldsymbol{X} \in \mathscr{B}_0$ associated with the total production of entropy $\tilde{\mathcal{D}}(t)$ by the relation $D_t^{\mathrm{tot}}(\boldsymbol{X})/\Theta_t(\boldsymbol{X})$, where $D_t^{\mathrm{tot}}(\boldsymbol{X})$ denotes the total dissipation in the point $\boldsymbol{X} \in \mathscr{B}_0$. The Lagrangian form of the second law of thermodynamics then reads

$$\int_{\mathscr{B}_0} \frac{D_t^{\mathrm{tot}}(\boldsymbol{X})}{\Theta_t(\boldsymbol{X})} = \int_{\mathscr{B}_0} \dot{\eta}_t(\boldsymbol{X}) + \int_{\partial\mathscr{B}_0} [\boldsymbol{N}_0(\boldsymbol{X})]_A \, [\boldsymbol{H}_t(\boldsymbol{X})]^A \geqslant 0 \tag{2.60}$$

As next step, we apply Gauss' divergence theorem to the boundary integral in Equation (2.60). In this way, the boundary integral can be related to the associated vector field in $\mathscr{B}_0$. Since the Piola-Kirchhoff heat flux $\boldsymbol{Q}_t$ and the body temperature field Θ_t both depend on the point $\boldsymbol{X} \in \mathscr{B}_0$, the product rule of partial differentiation leads to

$$\begin{aligned} \int_{\mathscr{B}_0} [\partial_X \boldsymbol{H}_t(\boldsymbol{X})]^A{}_A = \int_{\mathscr{B}_0} \frac{1}{\Theta_t(\boldsymbol{X})} [\partial_X \boldsymbol{Q}_t(\boldsymbol{X})]^A{}_A - \\ - \int_{\mathscr{B}_0} \frac{1}{\Theta_t(\boldsymbol{X})} \, [\mathrm{D}\,\Theta_t(\boldsymbol{X})]_A \, [\boldsymbol{H}_t(\boldsymbol{X})]^A \end{aligned} \tag{2.61}$$

The dual paring $[\mathrm{D}\,\Theta_t(\boldsymbol{X})]_A \, [\boldsymbol{H}_t(\boldsymbol{X})]^A$ in the second term of Equation (2.61) is by definition the negative dissipation $D_t^{\mathrm{cdu}}(\boldsymbol{X})$ arising from conduction of heat in a point $\boldsymbol{X} \in \mathscr{B}_0$. The sum of this dissipation and the internal dissipation $D_t^{\mathrm{int}}(\boldsymbol{X})$ of the material coincides with the total dissipation. Hence, the terms associated with $D_t^{\mathrm{cdu}}(\boldsymbol{X})$ annihilate each other. We arrive at the entropy balance

$$-\int_{\mathscr{B}_0} \frac{1}{\Theta_t(\boldsymbol{X})} \, [\partial_X \boldsymbol{Q}_t(\boldsymbol{X})]^A{}_A + \int_{\mathscr{B}_0} \frac{D_t^{\mathrm{int}}(\boldsymbol{X})}{\Theta_t(\boldsymbol{X})} = \int_{\mathscr{B}_0} \dot{\eta}_t(\boldsymbol{X}) \geqslant 0 \tag{2.62}$$

The left hand side of inequality (2.62) gives an equation for the time evolution of the total entropy. The localisation theorem implies a local form determining the time evolution curve $\eta(t)$ of the Lagrangian entropy field η_t. For all points

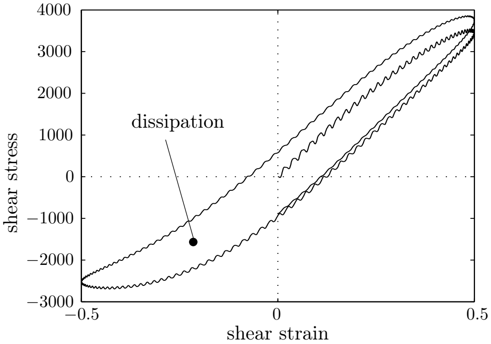

Figure 2.9. Numerically determined stress-strain hysteresis loop during a cyclic shear loading of a visco-elastic material by taking into account the inertia of the specimen.

$\boldsymbol{X}$ in the reference configuration $\mathscr{B}_0$, we obtain the evolution equation

$$\boxed{\dot{\eta}_t(\boldsymbol{X}) = -\frac{1}{\Theta_t(\boldsymbol{X})}\left\{[\partial_X \boldsymbol{Q}_t(\boldsymbol{X})]^A{}_A - D_t^{\mathrm{int}}(\boldsymbol{X})\right\}} \tag{2.63}$$

Recall that the first and the second term on the righthand side of this equation denotes the entropy input arising from conduction of heat and the internal production of entropy, respectively.

2.2.3. The constitutive equations. The entropy evolution is restricted by postulating a non-negative total dissipation D_t^{tot}. This postulate can be satisfied by the conditions of a non-negative dissipation D_t^{cdu} arising from conduction of heat, and a non-negative internal dissipation D_t^{int}.

The former condition is always satisfied for Fourier's law of isotropic heat conduction (see Holzapfel [135]), which defines the components of the Piola-Kirchhoff heat flux for each point $\boldsymbol{X} \in \partial\mathscr{B}_0$ by the matrix product

$$\begin{aligned} [\boldsymbol{Q}_t(\boldsymbol{X})]^A &= -[\boldsymbol{K}_t(\boldsymbol{X})]^{AB}[\mathrm{D}\,\Theta_t(\boldsymbol{X})]_B \\ &= -k_0\, J_t(\boldsymbol{X})\,[(\boldsymbol{C}_t(\boldsymbol{X}))^{-1}]^{AB}[\mathrm{D}\,\Theta_t(\boldsymbol{X})]_B \end{aligned} \tag{2.64}$$

with an isotropic Lagrangian conductivity tensor $\boldsymbol{K}_t(\boldsymbol{X}) \in \mathbb{S}_+(T^*\mathscr{B}_0, T\mathscr{B}_0)$. The real number $k_0 > 0$ denotes a constant conductivity of the continuum body in each direction. Fourier's law of heat condution can be also viewed as potential relation with respect to a heat flux potential (see Simo [149]). The dissipation $D_t^{\mathrm{cdu}}(\boldsymbol{X})$ arising from conduction of heat at the point $\boldsymbol{X} \in \mathscr{B}_0$ is non-negative according to the positive definiteness of the inverse right Cauchy-Green tensor, which means

$$\begin{aligned}
&[\boldsymbol{W}^*]_A\, [(\boldsymbol{C}_t(\boldsymbol{X}))^{-1}]^{AB}\, [\boldsymbol{W}^*]_B = \\
&\qquad = [(\boldsymbol{F}_t(\boldsymbol{X}))^{-T}]_a{}^A\, [\boldsymbol{W}^*]_A\, \delta^{ab}\, [(\boldsymbol{F}_t(\boldsymbol{X}))^{-T}]_b{}^B\, [\boldsymbol{W}^*]_B \geqslant 0
\end{aligned} \tag{2.65}$$

for any cotangent vector $\boldsymbol{W}^* \in T_X^*\mathscr{B}_0$.

On the other hand, the non-negative internal dissipation is a restriction for the constitutive equation pertaining to the Lagrangian non-equilibrium stress tensor $\boldsymbol{\Upsilon}_t(\boldsymbol{X})$. We derive this relation by using the balance of thermal energy determining the rate of change of the internal energy $\mathcal{E}(t)$ of the body. Hence, we postulate

$$\dot{\mathcal{E}} = \mathcal{P}^{\mathrm{int}} + \mathcal{Q} \tag{2.66}$$

Combining Equation (2.66) and Equation (2.49), we obtain the balance of total energy or first law of thermodynamics. In this work, we neglect a heat source density field with respect to the reference configuration. Accordingly, in the Lagrangian description, the balance of total energy reads

$$\int_{\mathscr{B}_0} [\dot{\boldsymbol{\pi}}_t(\boldsymbol{X})]_a\, [\boldsymbol{v}_t(\boldsymbol{X})]^a + \dot{e}_t(\boldsymbol{X}) = \int_{\partial\mathscr{B}_0} [\boldsymbol{v}_t^*(\boldsymbol{X})]_a\, [\boldsymbol{t}_t(\boldsymbol{X})]^a - \int_{\partial\mathscr{B}_0} [\boldsymbol{N}_0(\boldsymbol{X})]_A\, [\boldsymbol{Q}_t(\boldsymbol{X})]^A \tag{2.67}$$

where $e_t(\boldsymbol{X})$ denotes the internal energy density in the reference configuration. The left hand side denotes the time rate of change $\dot{\mathcal{H}}$ of the total energy. In the righthand side of Equation (2.67), we apply Gauss' divergence theorem and employ the implications (2.53) of the Piola-Kirchhoff theorem. We obtain the time rate of change

$$\dot{\mathcal{H}} = \int_{\mathscr{B}_0} [\partial_X \boldsymbol{P}_t^*(\boldsymbol{X})]_a{}^A{}_A\, [\boldsymbol{v}_t(\boldsymbol{X})]^a + \int_{\mathscr{B}_0} [\boldsymbol{P}_t^*(\boldsymbol{X})]_a{}^A\, [\dot{\boldsymbol{F}}_t(\boldsymbol{X})]^a{}_A - \int_{\mathscr{B}_0} [\partial_X \boldsymbol{Q}_t(\boldsymbol{X})]^A{}_A \tag{2.68}$$

Then, we take Equation (2.55.2) into account, and apply the localisation theorem. After eliminating the divergence of the Piola-Kirchhoff heat flux field $\boldsymbol{Q}_t$ by the entropy evolution Equation (2.63), we arrive at the Clausius-Planck inequality

$$D_t^{\mathrm{int}}(\boldsymbol{X}) = \Theta_t(\boldsymbol{X})\,\dot{\eta}_t(\boldsymbol{X}) - \dot{e}_t(\boldsymbol{X}) + [\boldsymbol{P}_t^*(\boldsymbol{X})]_a{}^A\,[\dot{\boldsymbol{F}}_t(\boldsymbol{X})]^a{}_A \geqslant 0 \tag{2.69}$$

We define the internal energy density $e_t(\boldsymbol{X})$ by the Legendre transform of the free energy $\Psi_t(\boldsymbol{X})$ with respect to the Lagrangian temperature $\Theta_t(\boldsymbol{X})$. The internal energy is then given as the associated energy function

$$e_t(\boldsymbol{X}) = \Theta_t(\boldsymbol{X})\,\eta_t(\boldsymbol{X}) + \Psi_t(\boldsymbol{X}) \tag{2.70}$$

According to Equation (2.46), the last term on the righthand side of Equation (2.69) denotes the density $p_t^{\mathrm{int}}(\boldsymbol{X})$ of the stress power. Employing Equation (2.70) in Equation (2.69), the internal dissipation takes the form

$$D_t^{\mathrm{int}}(\boldsymbol{X}) = p_t^{\mathrm{int}}(\boldsymbol{X}) - \eta_t(\boldsymbol{X})\,\dot{\Theta}_t(\boldsymbol{X}) - \dot{\Psi}_t(\boldsymbol{X}) \geqslant 0 \tag{2.71}$$

Now, we combine Equation (2.71) with the rate of change of the free energy density $\Psi_t(\boldsymbol{X})$ in Equation (2.43). After employing the definitions of the Lagrangian entropy and the Lagrangian non-equilibrium stress, given by Equations (2.48) and (2.44), respectively, we obtain

$$D_t^{\mathrm{int}}(\boldsymbol{X}) = [\boldsymbol{\Upsilon}_t(\boldsymbol{X})]^{AB}\,[\dot{\boldsymbol{\Gamma}}_t(\boldsymbol{X})]_{AB} = [\boldsymbol{M}_t(\boldsymbol{X})]_A{}^B\,[\boldsymbol{L}_t(\boldsymbol{X})]^A{}_B \geqslant 0 \tag{2.72}$$

where

$$[\boldsymbol{L}_t(\boldsymbol{X})]^A{}_B = \frac{1}{2}\,[\boldsymbol{\Gamma}_t^{-1}(\boldsymbol{X})]^{AC}[\dot{\boldsymbol{\Gamma}}_t(\boldsymbol{X})]_{CB} \tag{2.73}$$

denotes a viscous deformation rate tensor $\boldsymbol{L}_t(\boldsymbol{X}) \in \mathbb{L}(T_X\mathscr{B}_0, T_X\mathscr{B}_0)$ with respect to the tangent space at the reference configuration. The corresponding dual mapping $\boldsymbol{M}_t(\boldsymbol{X})$ in the set $\mathbb{L}(T_X^*\mathscr{B}_0, T_X^*\mathscr{B}_0)$ denotes the energy-conjugated stress tensor field. According to Equation (2.42), the considered isotropic free energy function depends directly on the invariants of the matrix $\boldsymbol{\Lambda}_t(\boldsymbol{X})$. After taking into account the representation in terms of these invariants, we find the relation

$$[\boldsymbol{M}_t(\boldsymbol{X})]_A{}^B = 2\,[\boldsymbol{\Gamma}_t(\boldsymbol{X})]_{AC}\,[\boldsymbol{\Upsilon}_t(\boldsymbol{X})]^{CB} = [\boldsymbol{C}_t(\boldsymbol{X})]_{AC}\,[\boldsymbol{S}_t(\boldsymbol{X})]^{CB} \tag{2.74}$$

by using the chain rule of differentiation.

Accordingly, the stress tensor $\boldsymbol{M}_t(\boldsymbol{X})$ denotes the Mandel stress tensor. Since this tensor represents an isotropic tensor function with respect to the unsymmetric tensor $\boldsymbol{\Lambda}_t(\boldsymbol{X})$ (compare Equation (C.48)), the Mandel stress tensor represents a consistent stress measure for the considered inelastic isotropic material (compare the conditions for the frame-indifferent response function of an isotropic material in Ciarlet [133]). Consequently, the deformation rate tensor $\boldsymbol{L}_t(\boldsymbol{X})$, in turn, denotes a consistent deformation rate measure for the present viscoelastic material.

Characteristic for a viscous material is a closed stress-strain hysteresis loop during a cyclic shear loading (see Reese & Govindjee [102] and Kaliske [150]). The included area of this loop is proportional to a consistent viscous strain rate measure. Since this included area indicates the free energy loss during the deformation (see Figure 2.9), we arrive at a viscous strain rate dependent internal dissipation. This material behaviour can be modelled by introducing a viscosity tensor (see Reese [107]), which maps a consistent viscous strain rate tensor linear on the energy-conjugated stress tensor. Hence, we assume the relation

$$[\boldsymbol{M}_t(\boldsymbol{X})]_A{}^B = [\mathbb{V}_t(\boldsymbol{X})]_A{}^B{}_C{}^D\;[\boldsymbol{L}_t(\boldsymbol{X})]^C{}_D \tag{2.75}$$

where $\mathbb{V}_t(\boldsymbol{X})$ denotes a fourth order viscosity tensor. Since the most viscous materials behave quite differently in bulk and shear (see Holzapfel & Simo [125] for rubber-like solids), we split the viscosity tensor in a volumetric and a deviatoric projection. We relate the former part with a volumetric viscosity parameter $V_{\mathrm{vol}} > 0$ and the latter with a deviatoric viscosity parameter $V_{\mathrm{dev}} > 0$. Without loss of generality, we restrict us to constant viscosity parameters, which leads to a constant viscosity tensor. In order to arrive from the viscous deformation rate tensor $\boldsymbol{L}_t(\boldsymbol{X})$ at the set $\mathbb{L}(T^*_X\mathscr{B}_0, T^*_X\mathscr{B}_0)$, we determine the volumetric part of its transpose. We obtain

$$[\boldsymbol{M}_t(\boldsymbol{X})]_A{}^B = \left(V_{\mathrm{vol}} - \frac{2\,V_{\mathrm{dev}}}{n_{\mathrm{dim}}}\right)\mathrm{tr}(\boldsymbol{L}_t(\boldsymbol{X}))\,\delta_A{}^B + 2\,V_{\mathrm{dev}}\,[(\boldsymbol{L}_t(\boldsymbol{X}))^T]_A{}^B \tag{2.76}$$

In an isotropic hyperelastic response, the material parameter V_{vol} and V_{dev} would correspond to the bulk and shear modulus, respectively. Taking this duality into account, the parenthesis in the first term then denotes a first 'viscous' Lamé parameter, which has to be positive, as the first Lamé parameter in hyperelasticity. Employing the assumed Mandel stress tensor field (2.76) in Equation (2.74), arising from the Clausius-Plank inequality, we arrive at the ordinary differential equation

$$\boxed{[\boldsymbol{\Upsilon}_t(\boldsymbol{X})]^{AD} = [\boldsymbol{\Sigma}_t(\boldsymbol{X})]^{AD}} \tag{2.77}$$

where

$$[\boldsymbol{\Sigma}_t]^{AD} = \frac{1}{2}\left(V_{\mathrm{vol}} - \frac{2\,V_{\mathrm{dev}}}{n_{\mathrm{dim}}}\right)\mathrm{tr}(\boldsymbol{L}_t)\,[(\boldsymbol{\Gamma}_t)^{-1}]^{AD} - \frac{V_{\mathrm{dev}}}{2}\,[\dot{\overline{(\boldsymbol{\Gamma}_t)^{-1}}}]^{AD} \tag{2.78}$$

denotes a viscous stress tensor. Note that in Le Tallec et al. [101] a similar evolution equation is deduced by a different approach. Equation (2.77) determines the time evolution of the internal variable field at each point $\boldsymbol{X}$ in the reference configuration. For a shorter description, we have taken into account the time derivative of the definition of an inverse matrix applied to the internal variable field, which leads to the relation

$$[\dot{\overline{(\boldsymbol{\Gamma}_t(\boldsymbol{X}))^{-1}}}]^{AD} = -[(\boldsymbol{\Gamma}_t(\boldsymbol{X}))^{-1}]^{AB}\,[\dot{\boldsymbol{\Gamma}}_t(\boldsymbol{X})]_{BC}\,[(\boldsymbol{\Gamma}_t(\boldsymbol{X}))^{-1}]^{CD} \tag{2.79}$$

However, the consideration of the inverse $(\boldsymbol{\Gamma}_t(\boldsymbol{X}))^{-1}$ as a new internal variable would not be advantageous for solving Equation (2.77), because it is not possible to transform both sides of the evolution equation, such that they depend only on $(\boldsymbol{\Gamma}_t(\boldsymbol{X}))^{-1}$. One side of the equation every depends directly on the internal variable.

As last step, we have to verify that the internal dissipation, given by Equation (2.72), is non-negative when solving the time evolution. We begin by multiplying the first term on the righthand side of Equation (2.78) with $\dot{\boldsymbol{\Gamma}}_t(\boldsymbol{X})$ from the right, and arrive at

$$\left(V_{\mathrm{vol}} - \frac{2\,V_{\mathrm{dev}}}{n_{\mathrm{dim}}}\right)\{\mathrm{tr}(\boldsymbol{L}_t(\boldsymbol{X}))\}^2 \geqslant 0 \tag{2.80}$$

by taking Equation (2.73) into account. Since the parenthesis is already defined to be positive, the entire term is non-negative. Then, we consider the second term on the righthand side of the internal variable evolution equation. We take the explicit representation (2.79) pertaining to the time derivative of the inverse internal variable field into account, and obtain

$$-[\dot{\overline{(\boldsymbol{\Gamma}_t)^{-1}}}]^{AD}\,[\dot{\boldsymbol{\Gamma}}_t]_{AD} = [(\boldsymbol{\Gamma}_t)^{-1}]^{AB}\,[\dot{\boldsymbol{\Gamma}}_t]_{BC}\,[(\boldsymbol{\Gamma}_t)^{-1}]^{CD}[\dot{\boldsymbol{\Gamma}}_t]_{DA} \tag{2.81}$$

The idea is, now, to transform the righthand side into a squared norm of a well-defined viscous strain rate tensor, which is obviously non-negative (compare Le Tallec et al. [101]). Since the viscous internal variable tensor is symmetric and positive definite, we are able to apply the square-root theorem on it (see Gurtin [151]). In this way, we obtain the viscous strain rate tensor

$$[\boldsymbol{D}_t(\boldsymbol{X})]^{AD} = \frac{1}{2}[(\boldsymbol{\Gamma}_t(\boldsymbol{X}))^{-\frac{1}{2}}]^{AB}\,[\dot{\boldsymbol{\Gamma}}_t(\boldsymbol{X})]_{BC}\,[(\boldsymbol{\Gamma}_t(\boldsymbol{X}))^{-\frac{1}{2}}]^{CD} \tag{2.82}$$

Bearing this definition in mind, the righthand side of Equation (2.81) leads to the squared norm of the viscous strain rate tensor, which is non-negative for all times in consideration of the positive deviatoric viscosity. In summary, the internal dissipation is thus non-negative and takes the form

$$D_t^{\text{int}}(\boldsymbol{X}) = \left(V_{\text{vol}} - \frac{2\,V_{\text{dev}}}{n_{\text{dim}}}\right)\{\text{tr}(\boldsymbol{L}_t(\boldsymbol{X}))\}^2 + 2V_{\text{dev}}\,\|\boldsymbol{D}_t(\boldsymbol{X})\|^2 \geqslant 0 \tag{2.83}$$

Hence, the parenthesis has to also be defined positive in order to fulfill the Clausius-Plank inequality at any material point $\boldsymbol{X} \in \mathscr{B}_0$ for all times. Note that we have shown, in this way, that the trace of the square product of the viscous deformation rate tensor is non-negative, which means

$$[\boldsymbol{L}_t(\boldsymbol{X})]^B{}_A\,[\boldsymbol{L}_t(\boldsymbol{X})]^A{}_B = \text{tr}\left(\{\boldsymbol{L}_t(\boldsymbol{X})\}^2\right) = \|\boldsymbol{D}_t(\boldsymbol{X})\|^2 \geqslant 0 \tag{2.84}$$

We have to show this relation, if we use the Mandel stress tensor in Equation (2.76) directly in Equation (2.72). Using the abstract notation of the Mandel stress tensor field in Equation (2.75), the internal dissipation can

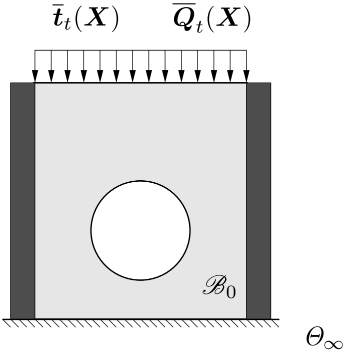

Figure 2.10. In the considered problem, the boundary conditions allow for a fixed support and an uninsulated part (bottom) as well as for a traction load and a heat transfer (top). A given vanishing Piola-Kirchhoff heat flux on the boundary $\partial_Q\mathscr{B}_0$ corresponds to an insulated boundary (left and right).

be written as

$$D_t^{\text{int}}(\boldsymbol{X}) = [\boldsymbol{L}_t(\boldsymbol{X})]^A{}_B \; [\mathbb{V}_t(\boldsymbol{X})]_A{}^B{}_C{}^D \; [\boldsymbol{L}_t(\boldsymbol{X})]^C{}_D \tag{2.85}$$

where the used constant viscosity tensor only introduce the transposed volumetric and the deviatoric projection of the viscous deformation rate tensor.

2.3. Strong form of the initial boundary value problem

The coupled differential equation system, given by Equations (2.55), (2.63) and (2.77), is generally supplemented by conditions on the boundary $\partial\mathscr{B}_0$ of the reference configuration (see Figure 2.10). We assume that this boundary is divided into two disjoint parts for each of the partial differential equations (2.55) and (2.63). First, Equations (2.55) are supplemented by the mechanical boundary conditions

$$\begin{aligned} \boldsymbol{\varphi}_t(\boldsymbol{X}) &= \boldsymbol{X} && \text{for all} \quad (t,\boldsymbol{X}) \in \mathscr{T} \times \partial_\varphi\mathscr{B}_0 \\ \boldsymbol{t}_t(\boldsymbol{X}) &= \bar{\boldsymbol{t}}_t(\boldsymbol{X}) && \text{for all} \quad (t,\boldsymbol{X}) \in \mathscr{T} \times \partial_T\mathscr{B}_0 = \mathscr{T} \times (\partial\mathscr{B}_0 \setminus \partial_\varphi\mathscr{B}_0) \end{aligned} \tag{2.86}$$

specifying the deformation $\boldsymbol{\varphi}_t(\boldsymbol{X})$ and the Piola-Kirchhoff traction vector $\boldsymbol{t}_t(\boldsymbol{X})$ for all points $\boldsymbol{X}$ on the corresponding boundary of the body. In analogy, we assume thermal boundary conditions for Equation (2.63), which prescribe the Lagrangian temperature $\Theta_t(\boldsymbol{X})$ and the Piola-Kirchhoff heat flux $\boldsymbol{Q}_t(\boldsymbol{X})$ as

$$\begin{aligned} \Theta_t(\boldsymbol{X}) &= \Theta_\infty(\boldsymbol{X}) \quad \text{for all} \quad (t,\boldsymbol{X}) \in \mathscr{T} \times \partial_\Theta \mathscr{B}_0 \\ \boldsymbol{Q}_t(\boldsymbol{X}) &= \overline{\boldsymbol{Q}}_t(\boldsymbol{X}) \quad \text{for all} \quad (t,\boldsymbol{X}) \in \mathscr{T} \times \partial_Q \mathscr{B}_0 = \mathscr{T} \times (\partial\mathscr{B}_0 \setminus \partial_\Theta \mathscr{B}_0) \end{aligned} \tag{2.87}$$

Along with the following initial conditions, we arrive at an initial boundary value problem for the deformation $\boldsymbol{\varphi}_t$ and the corresponding Lagrangian deformation velocity field $\boldsymbol{v}_t$ as well as the Lagrangian temperature field Θ_t. However, we obtain an initial value problem for the viscous internal variable field $\boldsymbol{\Gamma}_t$. We assume

$$\begin{aligned} \boldsymbol{\varphi}_{t_0}(\boldsymbol{X}) &= \boldsymbol{X} & \Theta_{t_0}(\boldsymbol{X}) &= \Theta_0(\boldsymbol{X}) \\ \boldsymbol{v}_{t_0}(\boldsymbol{X}) &= \boldsymbol{v}_0(\boldsymbol{X}) & \boldsymbol{\Gamma}_{t_0}(\boldsymbol{X}) &= \boldsymbol{\delta} \end{aligned} \tag{2.88}$$

for all points $\boldsymbol{X} \in \mathscr{B}_0 \backslash \partial\mathscr{B}_0$. The initial condition for the viscous evolution equation arises from defining the reference configuration at $t = t_0$ as equilibrium state of the viscous evolution. In fact, we define the reference configuration as equilibrium state of a total time evolution related with vanishing external loads, vanishing relative temperatures as well as vanishing velocities. Finally, the initial conditions

$$\boldsymbol{\pi}_{t_0}(\boldsymbol{X}) = \rho_0(\boldsymbol{X})\,\boldsymbol{v}_0(\boldsymbol{X}) \qquad \eta_{t_0}(\boldsymbol{X}) = -\frac{\partial \Psi(\boldsymbol{I}^*, \Theta_0(\boldsymbol{X}))}{\partial \Theta} \tag{2.89}$$

for all points $\boldsymbol{X} \in \mathscr{B}_0 \backslash \partial\mathscr{B}_0$ specify the momentum evolution and the entropy evolution, where the mapping $\boldsymbol{I}^* \in \mathbb{L}(\mathscr{A}^*, \mathscr{A}^*)$ denotes the shifter with the entries ${\delta_A}^B$ in the corresponding matrix.

2.3.1. The conservation laws. According to the theorem of Emmy Noether, the equations of motion have a first integral, under certain circumstances, if there exists at a fixed time $t \in \mathscr{T}$ a continuous variation curve $\overline{\boldsymbol{\varphi}}_t(s)$ of deformation fields, which coincides for $s = 0$ with a fixed deformation field

$\boldsymbol{\varphi}_t$ and is compatible with given boundary conditions as well as preserves the associated symmetry function

$$\mathcal{K}(t) = \frac{1}{2}\int_{\mathscr{B}_0} \rho_0(\boldsymbol{X})\, [\dot{\boldsymbol{\varphi}}_t(\boldsymbol{X})]^a\, \delta_{ab}\, [\dot{\boldsymbol{\varphi}}_t(\boldsymbol{X})]^b - \int_{\mathscr{B}_0} W(\boldsymbol{\varphi}_t(\boldsymbol{X})) \tag{2.90}$$

The strain energy function $W(\boldsymbol{\varphi}_t(\boldsymbol{X}))$ coincides for each point $\boldsymbol{X} \in \mathscr{B}_0$ with the free energy $\Psi(\boldsymbol{\Lambda}_t(\boldsymbol{X}), \Theta_t(\boldsymbol{X}))$ of the material, for a fixed Lagrangian temperature $\Theta_t(\boldsymbol{X})$ and a fixed Lagrangian internal variable tensor $\boldsymbol{\Gamma}_t(\boldsymbol{X})$. The symmetry function $\mathcal{K}(t)$ at fixed time $t \in \mathscr{T}$ is preserved on the variation curve $\overline{\boldsymbol{\varphi}}_t(s)$, if it coincides with the symmetry function $\mathcal{K}_s(t)$ associated with any deformation field on the variation curve. Hence, the symmetry function does not depend on the curve parameter s, which means the directional derivative of the function $\mathcal{K}_s(t)$ at $s = 0$ vanish (see also Kuypers [152] and Groß [35]). We begin by determining the directional derivative of the first term of the function $\mathcal{K}_s(t)$ along the continuous variation curve $\overline{\boldsymbol{\varphi}}_t(s)$, and obtain

$$\frac{1}{2}\int_{\mathscr{B}_0} \frac{\mathrm{d}}{\mathrm{d}s}\bigg|_{s=0} \rho_0(\boldsymbol{X})\, [\dot{\overline{\boldsymbol{\varphi}}}_t(\boldsymbol{X})(s)]^a\, \delta_{ab}\, [\dot{\overline{\boldsymbol{\varphi}}}_t(\boldsymbol{X})(s)]^b = \int_{\mathscr{B}_0} [\boldsymbol{\pi}_t(\boldsymbol{X})]_a\, [\dot{\boldsymbol{\nu}}_t(\boldsymbol{X})]^a \tag{2.91}$$

where $\boldsymbol{\nu}_t(\boldsymbol{X})$ denotes the tangent vector at the variation curve $\overline{\boldsymbol{\varphi}}_t(s)$ in the point $\boldsymbol{\varphi}_t(\boldsymbol{X}) \in \mathscr{B}_t$. Here, we have taken into account that the time derivative and the derivative with respect to the curve parameter s at fixed time commute. The derivative of the last term with respect to the curve parameter at $s = 0$ is given by

$$-\int_{\mathscr{B}_0} \frac{\mathrm{d}}{\mathrm{d}s}\bigg|_{s=0} W(\overline{\boldsymbol{\varphi}}_t(\boldsymbol{X})(s)) = -\int_{\mathscr{B}_0} [\boldsymbol{P}^*_t(\boldsymbol{X})]_a{}^A\, [\partial_X \boldsymbol{\nu}_t(\boldsymbol{X})]^a{}_A \tag{2.92}$$

On the right hand side of Equation (2.92), we take the product rule of the partial derivative with respect to the coordinates X^A into account, and obtain a similar relation as in Equation (2.53). Then, we also apply Gauss' divergence theorem on the left hand side of this relation, and employ the mechanical Neumann boundary condition, given by Equation (2.86.2). The directional derivative of the symmetry function $\mathcal{K}_s(t)$ along the continuous variation curve

$\overline{\boldsymbol{\varphi}}_t(s)$ then takes the form

$$\left.\frac{\mathrm{d}}{\mathrm{d}s}\right|_{s=0} \mathcal{K}_s(t) = \int_{\mathscr{B}_0} [\boldsymbol{\pi}_t(\boldsymbol{X})]_a \, [\dot{\boldsymbol{\nu}}_t(\boldsymbol{X})]^a + \int_{\mathscr{B}_0} [\partial_X \boldsymbol{P}^*_t(\boldsymbol{X})]_a{}^A{}_A \, [\boldsymbol{\nu}_t(\boldsymbol{X})]^a - \\ - \int_{\partial\mathscr{B}_0} [\bar{\boldsymbol{t}}_t(\boldsymbol{X})]^a \, [\boldsymbol{\nu}^*_t(\boldsymbol{X})]_a \tag{2.93}$$

In the second term on the right hand side of Equation (2.93), we employ the local form of the second equation of motion, given by Equation (2.55.2). The first and the second term can be now combined by taking the product rule of the partial time differentiation into account. Since Equation (2.93) has to vanish if the symmetry function is preserved, we obtain the balance equation

$$\dot{\mathcal{I}}(t) = \int_{\partial\mathscr{B}_0} [\bar{\boldsymbol{t}}_t(\boldsymbol{X})]^a \, [\boldsymbol{\nu}^*_t(\boldsymbol{X})]_a \tag{2.94}$$

where

$$\mathcal{I}(t) = \int_{\mathscr{B}_0} [\boldsymbol{\pi}_t(\boldsymbol{X})]_a \, [\boldsymbol{\nu}_t(\boldsymbol{X})]^a \tag{2.95}$$

denotes the first integral associated with the continuous variation curve $\overline{\boldsymbol{\varphi}}_t(s)$. Thus, this balance law yields a conservation law for a motion under equilibriated external loads $\bar{\boldsymbol{t}}_t(\boldsymbol{X}) = \boldsymbol{o}$ for all points $\boldsymbol{X}$ on the boundary $\partial_T\mathscr{B}_0$ at any time $t \in \mathscr{T}$ of the time interval of interest. Examples for first integrals of the kind of Equation (2.95) are the total linear and the total angular momentum function, as can be seen in the following paragraphs.

The differential equations of the initial boundary value problem under equilibriated external loads $\bar{\boldsymbol{t}}_t(\boldsymbol{X}) = \boldsymbol{o}$ for all points $\boldsymbol{X} \in \partial_T\mathscr{B}_0$ at any time $t \in \mathscr{T}$ and with an empty Dirichlet boundary $\partial_\varphi\mathscr{B}_0$ yields conservation of the total linear momentum function

$$\mathcal{L}(t) = \int_{\mathscr{B}_0} [\boldsymbol{\pi}_t(\boldsymbol{X})]_a \, [\boldsymbol{\xi}_0]^a \tag{2.96}$$

The vector $\boldsymbol{\xi}_0 \in \mathscr{A}$ is arbitrary, fixed in the ambient space, and thus time-independent (see also Armero [73]). The vector $\boldsymbol{\xi}_0$ denotes the fixed direction vector of a virtual translation of the body at fixed time $t \in \mathscr{T}$ (see Figure 2.11).

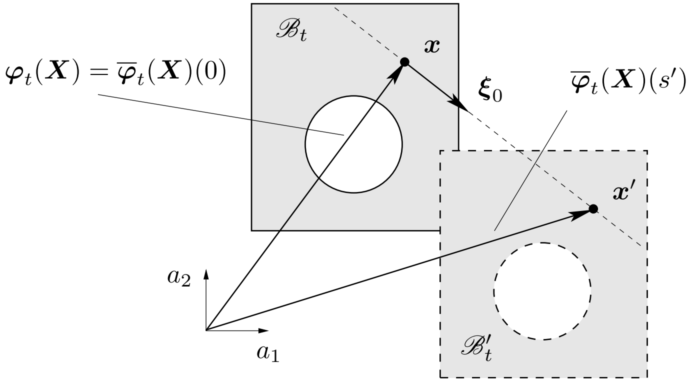

Figure 2.11. The current configuration $\mathscr{B}_t$ is virtually translated in the configuration $\mathscr{B}'_t$ at fixed time. The tangent vector at the virtual translation curve $\overline{\boldsymbol{\varphi}}_t(\boldsymbol{X})(s)$ through the point $\boldsymbol{x} \in \mathscr{B}_t$ is given by the direction vector $\boldsymbol{\xi}_0$ of the virtual translation.

This translation can be written as a smooth curve $\overline{\boldsymbol{\varphi}}_t(s)$ of deformation fields, defined locally by the relation $\boldsymbol{\varphi}_t(\boldsymbol{X}) + s\boldsymbol{\xi}_0$ for each point $\boldsymbol{X} \in \mathscr{B}_0$. According to Equation (2.17), the components

$$[\boldsymbol{\nu}_0(\boldsymbol{X})]^a = [\boldsymbol{\xi}_0]^a \qquad\qquad \forall \boldsymbol{X} \in \mathscr{B}_0 \tag{2.97}$$

define the tangent field at this virtual translation curve. We verify the balance of total linear momentum by using the fundamental theorem of calculus corresponding to the total linear momentum function, and obtain the relation

$$\mathcal{L}(T) - \mathcal{L}(t_0) = \int_{\mathscr{T}} \dot{\mathcal{L}}(t) = \int_{\mathscr{T}} \int_{\mathscr{B}_0} [\dot{\boldsymbol{\pi}}_t(\boldsymbol{X})]_a \, [\boldsymbol{\xi}_0]^a \tag{2.98}$$

Then, we employ Cauchy's first equation of motion (2.55.2) in the righthand side of this equation for each point $\boldsymbol{X} \in \mathscr{B}_0$. After using the definition of a transposed tensor, the volume integral is transformed such that

$$\int_{\mathscr{B}_0}[\partial_X \boldsymbol{P}^*_t(\boldsymbol{X})]_a{}^A{}_A\,[\boldsymbol{\xi}_0]^a = \int_{\mathscr{B}_0}[\boldsymbol{\xi}^*_0]_a\,[\partial_X\boldsymbol{P}_t(\boldsymbol{X})]^{aA}{}_A = \int_{\mathscr{B}_0}\frac{\partial[(\boldsymbol{P}_t(\boldsymbol{X}))^T]^{Aa}[\boldsymbol{\xi}^*_0]_a}{\partial X^A} \tag{2.99}$$

where the vector $\boldsymbol{\xi}^*_0 = \boldsymbol{\nu}^*_0(\boldsymbol{X}) \in T^*_x\mathscr{B}_t$ designates the cotangent vector corresponding to the tangent vector (2.97) at the virtual translation curve. Using Gauss' divergence theorem together with the Piola-Kirchhoff theorem, the mechanical boundary condition (2.86.2) leads to

$$\int_{\partial_T\mathscr{B}_0}[\boldsymbol{N}_0(\boldsymbol{X})]_A\,[(\boldsymbol{P}_t(\boldsymbol{X}))^T]^{Aa}\,[\boldsymbol{\xi}^*_0]_a \quad = \quad \int_{\partial_T\mathscr{B}_0}[\boldsymbol{\xi}^*_0]_a\,[\bar{\boldsymbol{t}}_t(\boldsymbol{X})]^a \tag{2.100}$$

With regard to the assumed vanishing loads $\bar{\boldsymbol{t}}_t(\boldsymbol{X}) = \boldsymbol{o}$ for each point $\boldsymbol{X} \in \partial_T\mathscr{B}_0$ at all times $t \in \mathscr{T}$, we arrive at the conservation of the total linear momentum function in the sense that $\mathcal{L}(t_0) = \mathcal{L}(T)$ for any fixed tangent vector $\boldsymbol{\xi}_0 \in T_x\mathscr{B}_t$. According to the arbitrariness of the vector $\boldsymbol{\xi}_0$, the components

$$[\boldsymbol{L}(t)]_a = \int_{\mathscr{B}_0}[\boldsymbol{\pi}_t(\boldsymbol{X})]_a \tag{2.101}$$

of the total linear momentum $\boldsymbol{L}(t)$ at any time $t \in \mathscr{T}$ are constants of the motion.

On the other hand, the total angular momentum function $\mathcal{J}(t)$ is a second first integral about the origin of the ambient space, supposing identical circumstances. This function is defined by

$$\mathcal{J}(t) = \int_{\mathscr{B}_0}\epsilon_{abc}\delta^{cd}\,[\boldsymbol{\varphi}_t(\boldsymbol{X})]^b\,[\boldsymbol{\pi}_t(\boldsymbol{X})]_d[\boldsymbol{\xi}_0]^a \tag{2.102}$$

The fixed vector $\boldsymbol{\xi}_0$ represents the axial vector, that is the direction vector of the rotation axis, pertaining to a virtual rotation of the body at fixed time $t \in \mathscr{T}$ around the origin of the ambient space (see Figure 2.12). Such a virtual rotation is a circular curve $\overline{\boldsymbol{\varphi}}_t(s)$ with the radius $\|\boldsymbol{\varphi}_t(\boldsymbol{X})\|$ for each point $\boldsymbol{X} \in \mathscr{B}_0$. Consequently, the axial vector $\boldsymbol{\xi}_0$ is a vector going through the centre of the circle, and being perpendicular to each radius vector $\overline{\boldsymbol{\varphi}}_t(\boldsymbol{X})(s)$ and the corresponding tangent vector $\mathrm{d}\overline{\boldsymbol{\varphi}}_t(\boldsymbol{X})(s)/\,\mathrm{d}s$ at any position s on the circle. Thus, we obtain the relation

$$\left[\frac{\mathrm{d}\overline{\boldsymbol{\varphi}}_t(\boldsymbol{X})(s)}{\mathrm{d}s}\right]^a = \delta^{ab}\epsilon_{bcd}\,[\boldsymbol{\xi}_0]^c\,[\overline{\boldsymbol{\varphi}}_t(\boldsymbol{X})(s)]^d = [\bar{\boldsymbol{\xi}}_0]^a{}_d\,[\overline{\boldsymbol{\varphi}}_t(\boldsymbol{X})(s)]^d \tag{2.103}$$

which represents an ordinary differential equation with respect to s. The mapping $\bar{\boldsymbol{\xi}}_0$ associated with the axial vector $\boldsymbol{\xi}_0$ denotes the spin tensor in the rotation group $\mathbb{SO}(\mathscr{A},\mathscr{A})$ corresponding to the ambient space. Evaluating Equation (2.103) at $s = 0$, we obtain the tangent field $\boldsymbol{\nu}_t$ at the virtual rotation curve, given by the matrix entries

$$[\boldsymbol{\nu}_t(\boldsymbol{X})]^a = [\bar{\boldsymbol{\xi}}_0]^a{}_d\,[\boldsymbol{\varphi}_t(\boldsymbol{X})]^d \tag{2.104}$$

The explicit function of the curve $\overline{\boldsymbol{\varphi}}_t(s)$ follows from solving the ordinary differential Equation (2.103) associated with the initial condition $\overline{\boldsymbol{\varphi}}_t(0) = \boldsymbol{\varphi}_t$. The solution $\overline{\boldsymbol{\varphi}}_t(\boldsymbol{X})(s)$ of this equation coincides with the mapping $\exp(s\,\bar{\boldsymbol{\xi}}_0)\,\boldsymbol{\varphi}_t(\boldsymbol{X}) \in \mathscr{A}$, where the linear mapping exp denotes the matrix exponential map in the ambient space. The balance of total angular momentum follows from the fundamental theorem of calculus

$$\begin{aligned}\mathcal{J}(T) - \mathcal{J}(t_0) = \int_{\mathscr{T}}\int_{\mathscr{B}_0} &\epsilon_{abc}\delta^{cd}\,[\dot{\boldsymbol{\varphi}}_t(\boldsymbol{X})]^b\,[\boldsymbol{\pi}_t(\boldsymbol{X})]_d\,[\boldsymbol{\xi}_0]^a + \\ &+\epsilon_{abc}\delta^{cd}\,[\boldsymbol{\varphi}_t(\boldsymbol{X})]^b\,[\dot{\boldsymbol{\pi}}_t(\boldsymbol{X})]_d\,[\boldsymbol{\xi}_0]^a\end{aligned} \tag{2.105}$$

Employing Equations (2.55) for each $\boldsymbol{X} \in \mathscr{B}_0$ and recalling Equation (2.22) as definition of the Lagrangian momentum field, the first volume integral on the righthand side vanishes due to the properties of the permutation symbol. The last volume integral yields

$$\begin{aligned}&\int_{\mathscr{B}_0} \epsilon_{abc}\delta^{cd}\,[\boldsymbol{\varphi}_t(\boldsymbol{X})]^b\,[\partial_X \boldsymbol{P}_t^*(\boldsymbol{X})]_d{}^A{}_A\,[\boldsymbol{\xi}_0]^a = \\ &\qquad = \int_{\mathscr{B}_0} \epsilon_{cab}\,[\boldsymbol{\xi}_0]^a\,[\boldsymbol{\varphi}_t(\boldsymbol{X})]^b\,[\partial_X \boldsymbol{P}_t(\boldsymbol{X})]^{cA}{}_A\end{aligned} \tag{2.106}$$

by taking into account the equality of the permutation symbol for even permutations. Furthermore, by using the product rule of partial differentiation with respect to the Lagrangian coordinates $\{X^A\}$, this integral can be written as

$$\int_{\mathscr{B}_0} \frac{\partial\left\{\epsilon_{cab}\,[\boldsymbol{\xi}_0]^a\,[\boldsymbol{\varphi}_t(\boldsymbol{X})]^b\,[\boldsymbol{P}_t(\boldsymbol{X})]^{cA}\right\}}{\partial X^A} - \epsilon_{cab}\,[\boldsymbol{\xi}_0]^a\,[\partial_X\boldsymbol{\varphi}_t(\boldsymbol{X})]^b{}_A\,[\boldsymbol{P}_t(\boldsymbol{X})]^{cA} \tag{2.107}$$

Now, we convert the last term of Equation (2.107). First, we employ Equation (2.26) for the deformation gradient. Then, we transform the first Piola-Kirchhoff stress tensor into the second Piola-Kirchhoff stress tensor, according to Equation (2.46). Hence, the last term takes the form

$$\int_{\mathscr{B}_0} \epsilon_{abc}\,[\boldsymbol{\xi}_0]^a\,[\boldsymbol{F}_t(\boldsymbol{X})]^c{}_B\,[\boldsymbol{S}_t(\boldsymbol{X})]^{BA}\,[(\boldsymbol{F}_t(\boldsymbol{X}))^T]_A{}^b = \int_{\mathscr{B}_0} \epsilon_{abc}\,[\boldsymbol{\xi}_0]^a\,[(\boldsymbol{\tau}_t(\boldsymbol{X}))^T]^{bc} \tag{2.108}$$

where the tensor $\boldsymbol{\tau}_t(\boldsymbol{X}) \in \mathbb{S}_+(T^*_X\mathscr{B}_t, T_X\mathscr{B}_t)$ denotes the symmetric Kirchhoff stress tensor, defined for each point $\boldsymbol{X} \in \mathscr{B}_0$ in the reference configuration by the components

$$[\boldsymbol{\tau}_t(\boldsymbol{X})]^{ab} = [\boldsymbol{F}_t(\boldsymbol{X})]^a{}_A\,[\boldsymbol{S}_t(\boldsymbol{X})]^{AB}\,[(\boldsymbol{F}_t(\boldsymbol{X}))^T]_B{}^b \tag{2.109}$$

Hence, Equation (2.108) vanishes according to the properties of the permutation tensor in Equation (2.10). Next, we apply to the first term in Equation (2.107) Gauss' divergence theorem, and employ the Piola-Kirchhoff traction vector according to the Piola-Kirchhoff theorem. According to the boundary condition (2.86.2), this term takes the form

$$\int_{\partial_T\mathscr{B}_0} [\boldsymbol{N}_0(\boldsymbol{X})]_A\,[(\boldsymbol{P}_t(\boldsymbol{X}))^T]^{Ac}\,[\boldsymbol{\nu}^*_t(\boldsymbol{X})]_c = \int_{\partial_T\mathscr{B}_0} [\boldsymbol{\nu}^*_t(\boldsymbol{X})]_c\,[\bar{\boldsymbol{t}}_t(\boldsymbol{X})]^c \tag{2.110}$$

where the vector $\boldsymbol{\nu}^*_t(\boldsymbol{X}) \in T^*_x\mathscr{B}_t$ denotes the cotangent vector corresponding to the tangent vector at the virtual rotation curve, given by Equation (2.104). Since the assumed loads vanish for each point $\boldsymbol{X} \in \partial_T\mathscr{B}_0$ on the traction boundary at all times $t \in \mathscr{T}$, we obtain a conserved total angular momentum function, in the sense that $\mathcal{J}(t_0) = \mathcal{J}(T)$ for an arbitrary time interval $\mathscr{T}$ of interest. Hence, further constants of the motion are the components of the

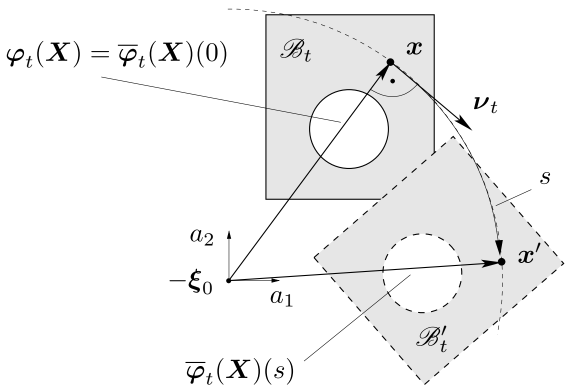

Figure 2.12. The current configuration $\mathscr{B}_t$ is virtually rotated in the configuration $\mathscr{B}'_t$ at fixed time. The tangent vector $\boldsymbol{\nu}_t \in T_x\mathscr{B}_t$ at the virtual rotation curve $\overline{\boldsymbol{\varphi}}_t(\boldsymbol{X})(s)$ through the point $\boldsymbol{x} \in \mathscr{B}_t$ is perpendicular to the corresponding position vector and the axial vector $\boldsymbol{\xi}_0$ of the virtual rotation.

total angular momentum $\boldsymbol{J}(t)$, given by

$$[\boldsymbol{J}(t)]_a = \int_{\mathscr{B}_0} \epsilon_{abc}\delta^{cd}\,[\boldsymbol{\varphi}_t(\boldsymbol{X})]^b\,[\boldsymbol{\pi}_t(\boldsymbol{X})]_d \tag{2.111}$$

Note that the just mentioned curves $\overline{\boldsymbol{\varphi}}_t(s)$ represent one-parameter groups of diffeomorphisms arising from actions of the Lie groups $\mathscr{A}$ and $\mathbb{SO}(\mathscr{A}, \mathscr{A})$, respectively. The tangent fields $\boldsymbol{\nu}_t$ at these curves are therefore called the infinitesimal generator of these actions (see Marsden & Ratiu [153]).

Summing up, the total linear momentum $\boldsymbol{L}(t)$ and the total angular momentum $\boldsymbol{J}(t)$ is conserved for vanishing loads, if the body can be virtually translated or rotated, respectively.

2.3.2. The nonlinear stability estimate. The equilibrium state of the body is a fix point of its time evolution equations. If there exists a corresponding Lyapunov function, this equilibrium is stable in the sense of Lyapunov (see Hahn [154]). Therefore, stability of nonlinear equilibria is often phrased in terms of an 'a priori' estimate arising from a Lyapunov-like function. For the considered time evolution equations, there exists such a function, which allows for a stability estimate (compare Gurtin [155] and Simo [156]).

In this estimate, it is possible to incorporate a *conservative* Piola-Kirchhoff traction vector $\bar{\boldsymbol{t}}_t(\boldsymbol{X})$ for all points $\boldsymbol{X} \in \partial_T \mathscr{B}_0$, which is derived via the directional derivative

$$\dot{\mathcal{U}}^{\text{ext}}(t) = \int_{\partial_T \mathscr{B}_0} [\mathrm{D}V^{\text{ext}}(\boldsymbol{u}_t(\boldsymbol{X}))]_a \, [\dot{\boldsymbol{\varphi}}_t(\boldsymbol{X})]^a =: -\int_{\partial_T \mathscr{B}_0} [\bar{\boldsymbol{t}}_t^*(\boldsymbol{X})]_a \, [\dot{\boldsymbol{\varphi}}_t(\boldsymbol{X})]^a \tag{2.112}$$

of a potential energy $\mathcal{U}^{\text{ext}}(t)$ along the time curve $\gamma_t(s) = \mathcal{U}^{\text{ext}}(t+s)$. The density function $V^{\text{ext}} : T_x \mathscr{B}_t \to \mathbb{R}$ denotes the corresponding potential. We consider the thermal Neumann boundary $\partial_Q \mathscr{B}_0 = \emptyset$ in the absence of heat sources, which means an adiabatic process with a non-decreasing total entropy according to Equation (2.58). We define the Lyapunov-like function

$$\mathcal{V}(t) = \mathcal{T}(t) + \mathcal{U}^{\text{int}}(t) + \mathcal{U}^{\text{ext}}(t) + \int_{\mathscr{B}_0} \eta_t(\boldsymbol{X}) \, \vartheta_t(\boldsymbol{X}) \tag{2.113}$$

In the following, we refer to the sum of the potential energy function $\mathcal{U}^{\text{int}}(t)$ and the volume integral as relative internal energy $\hat{\mathcal{E}}(t)$. According to the tangent fields ϑ_t and $\boldsymbol{u}_t$, as well as a free energy Ψ vanishing at ambient temperature and initial position, the Lyapunov-like function vanish in the equilibrium state at ambient temperature. The fundamental theorem of calculus leads to the equation

$$\begin{aligned} \mathcal{V}(T) - \mathcal{V}(t_0) = \int_{\mathscr{T}} \int_{\mathscr{B}_0} & [\dot{\boldsymbol{\pi}}_t(\boldsymbol{X})]_a \, [\boldsymbol{v}_t(\boldsymbol{X})]^a + \dot{\eta}_t(\boldsymbol{X}) \, \vartheta_t(\boldsymbol{X}) + \eta_t(\boldsymbol{X}) \, \dot{\Theta}_t(\boldsymbol{X}) + \\ & + \int_{\mathscr{T}} \int_{\mathscr{B}_0} \dot{\Psi}_t(\boldsymbol{X}) - \int_{\mathscr{T}} \int_{\partial_T \mathscr{B}_0} [\bar{\boldsymbol{t}}_t^*(\boldsymbol{X})]_a \, [\dot{\boldsymbol{\varphi}}_t(\boldsymbol{X})]^a \end{aligned} \tag{2.114}$$

where in the first term of Equation (2.114) the definition of the Lagrangian momentum field $\boldsymbol{\pi}_t$ has been employed.

Now, we employ Equations (2.55) in the first and in the last term, and bear in mind the product rule of partial differentiation with respect to the point $\boldsymbol{X} \in \mathscr{B}_0$. In this way, the first term reads

$$\int_{\mathscr{B}_0} [\dot{\boldsymbol{\pi}}_t(\boldsymbol{X})]_a \, [\boldsymbol{v}_t(\boldsymbol{X})]^a = \mathcal{P}^{\text{ext}}(t) - \mathcal{P}^{\text{int}}(t) \tag{2.115}$$

after applying Gauss' divergence theorem together with the Piola-Kirchhoff theorem and the mechanical boundary condition (2.86.2) to the volume integral. Since terms associated with the stress power and the external mechanical power annihilate each other, and likewise the terms with the time derivative of the temperature, we arrive at the stability estimate

$$\mathcal{V}(T) - \mathcal{V}(t_0) = \int_{\mathscr{T}} \int_{\mathscr{B}_0} \dot{\eta}_t(\boldsymbol{X})\, \vartheta_t(\boldsymbol{X}) - [\boldsymbol{\Upsilon}_t(\boldsymbol{X})]^{AB}\, [\dot{\boldsymbol{\Gamma}}(\boldsymbol{X})]_{AB} \tag{2.116}$$

Now, we consider the thermal evolution. We employ the strong form of the entropy evolution equation in the first term on the righthand side of Equation (2.116). The product rule of partial differentiation leads to a volume integral, which we transform into a boundary integral by applying Gauss' divergence theorem. Then, we employ in this boundary integral the Piola-Kirchhoff heat flux according to Equation (2.87.2). We obtain the relation

$$\int_{\mathscr{B}_0} \dot{\eta}_t(\boldsymbol{X})\, \vartheta_t(\boldsymbol{X}) = -\int_{\mathscr{B}_0} \frac{\Theta_\infty}{\Theta_t(\boldsymbol{X})}\, D_t^{\mathrm{tot}}(\boldsymbol{X}) + \int_{\mathscr{B}_0} D_t^{\mathrm{int}}(\boldsymbol{X}) + \int_{\partial_Q \mathscr{B}_0} \frac{\vartheta_t(\boldsymbol{X})}{\Theta_t(\boldsymbol{X})}\, \overline{Q}_t(\boldsymbol{X}) \tag{2.117}$$

where we denoted by $\overline{Q}_t$ the heat surface density field associated with the Piola-Kirchhoff heat flux $\overline{\boldsymbol{Q}}_t$ on the thermal Neumann boundary. The last term in this equation vanishes due to the assumed thermal Neumann boundary $\partial_Q \mathscr{B}_0 = \emptyset$.

As last step, we introduce in the last term of Equation (2.116) the evolution equation for the viscous internal variable. According to Equation (2.83), this term coincides with the negative internal dissipation, and it remains the stability estimate

$$\boxed{\mathcal{V}(T) - \mathcal{V}(t_0) = -\int_{\mathscr{T}} \int_{\mathscr{B}_0} \frac{\Theta_\infty}{\Theta_t(\boldsymbol{X})}\, D_t^{\mathrm{tot}}(\boldsymbol{X}) \leqslant 0} \tag{2.118}$$

for the thermo-viscoelastic evolution of the continuum body $\mathscr{B}$ in the arbitrary time interval $\mathscr{T}$ of interest (compare the estimates in Armero & Simo [123] and Laursen [157] as well as in Holzapfel & Simo [125]).

3. WEAK FORMULATION OF THE PROBLEM

Usually, the spatially weak formulation of the considered evolution equations is derived from its strong form by introducing a class of test functions, which vanish on the Dirichlet boundary of the body. A second common way is to use a variational principle with certain independent variables. In this connection note that the authors of Antman & Osborn [158] show that the weak form of the equations of motion can be also derived by precisely formulated versions of integral laws of motion. On the temporal test functions, there are mostly no requirements provided. Some exceptions are Hansbo [159] and Betsch & Steinmann [63, 65–67] as well as Groß et al. [16], where the temporal test functions are chosen subject to energy conservation.

Here, we generalise this approach, and view the fulfillment of the stability estimate (2.118) as constraint for the temporal test functions. The idea is to derive the weak forms of the evolution equations directly from the Lyapunov-like function (2.113), in order to fulfill the stability estimate (2.118) by the weak formulation of the time evolution. Since this function represents the total energy of the body relative to the equilibrium state of the material, we choose the temporal test functions so that the weak forms link the corresponding energy terms together. In this way, the discrete form of the balance principles are directly related with the residual equations solved in the iterative solution procedure. This leads to further advantages, which we utilise in solving the discrete problem.

We begin by determining the directional derivative of the kinetic energy $\mathcal{T}$ along the continuous time curve $\gamma_t(s) = \mathcal{T}(t + s)$. Subsequently, the fundamental theorem of calculus leads to the balance equation

$$\mathcal{T}(T) - \mathcal{T}(t_0^+) = \int_{\mathscr{T}} \frac{\mathrm{d}}{\mathrm{d}s}\bigg|_{s=0} \mathcal{T}(t+s) = \int_{\mathscr{T}} \int_{\mathscr{B}_0} [\dot{\boldsymbol{\pi}}_t(\boldsymbol{X})]_a \, [\boldsymbol{v}_t(\boldsymbol{X})]^a \tag{3.1}$$

where

$$\mathcal{T}(t_0^+) = \lim_{s \to 0^+} \mathcal{T}(t_0 + s) \qquad \text{and} \qquad \mathcal{T}(T) = \lim_{s \to 0^+} \mathcal{T}(T - s) \tag{3.2}$$

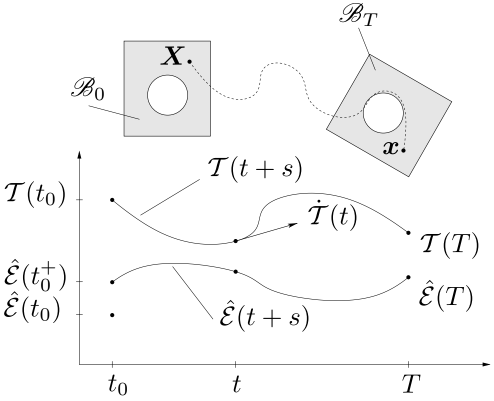

Figure 3.1. The continuous curve $\mathcal{T}(t+s)$ connects the kinetic energy $\mathcal{T}(t_0)$ of the reference configuration $\mathscr{B}_0$ with the kinetic energy $\mathcal{T}(T)$ of the final configuration $\mathscr{B}_T$. However, the lower bound of the continuous relative internal energy curve $\hat{\mathcal{E}}(t+s)$ does not coincide with the energy $\hat{\mathcal{E}}(t_0)$ of the reference configuration.

denote the kinetic energies at the lower and upper bound of the time curve, respectively (see Figure 3.1). Note that the vector field $\dot{\boldsymbol{\pi}}_t$ at any time $t \in \mathscr{T}$ is tangent to a continuous variation curve $\boldsymbol{\gamma}_t(s) = \boldsymbol{\pi}_{t+s}$. We employ Equation (2.55.1) in the righthand side of Equation (3.1), and obtain the identity

$$\int_{\mathscr{T}} \int_{\mathscr{B}_0} [\dot{\boldsymbol{\pi}}_t(\boldsymbol{X})]_a \, [\boldsymbol{v}_t(\boldsymbol{X})]^a = \int_{\mathscr{T}} \int_{\mathscr{B}_0} [\dot{\boldsymbol{\pi}}_t(\boldsymbol{X})]_a \, [\dot{\boldsymbol{\varphi}}_t(\boldsymbol{X})]^a \tag{3.3}$$

The time curve $\boldsymbol{\gamma}_t$ do not violate a vanishing conjugated momentum at the time-independent Dirichlet boundary nor a constant initial value, so that the corresponding tangent vectors vanish. Hence, the tangent vector $\dot{\boldsymbol{\pi}}_t$ represents an admissible test function for the weak form

$$\boxed{\int_{\mathscr{T}} \int_{\mathscr{B}_0} [\delta\dot{\boldsymbol{\pi}}_t(\boldsymbol{X})]_a \, [\dot{\boldsymbol{\varphi}}_t(\boldsymbol{X})]^a = \int_{\mathscr{T}} \int_{\mathscr{B}_0} [\delta\dot{\boldsymbol{\pi}}_t(\boldsymbol{X})]_a \, [\boldsymbol{v}_t(\boldsymbol{X})]^a} \tag{3.4}$$

determining a continuous weak motion $\boldsymbol{\varphi}(t)$. Consequently, the initial condition of the motion and the assumed Dirichlet boundary can be fulfilled exactly. Employing the first space-time weak equation of motion (3.4) in

Equation (3.1), we obtain

$$\mathcal{T}(T) - \mathcal{T}(t_0^+) = \int_{\mathscr{T}} \int_{\mathscr{B}_0} [\dot{\boldsymbol{\pi}}_t(\boldsymbol{X})]_a \, [\dot{\boldsymbol{\varphi}}_t(\boldsymbol{X})]^a \tag{3.5}$$

Next, we employ Equation (2.55.2) in the righthand side of Equation (3.5). Integration by part then leads to a volume integral, which we transform in a boundary integral by using Gauss' divergence theorem. Noticing the Piola-Kirchhoff theorem (2.52) and the mechanical boundary conditions (2.86), we arrive at

$$\begin{aligned} \int_{\mathscr{T}} \int_{\mathscr{B}_0} [\dot{\boldsymbol{\pi}}_t(\boldsymbol{X})]_a \, [\dot{\boldsymbol{\varphi}}_t(\boldsymbol{X})]^a = \int_{\mathscr{T}} \int_{\partial_T \mathscr{B}_0} [\bar{\boldsymbol{t}}_t^*(\boldsymbol{X})]_a \, [\dot{\boldsymbol{\varphi}}_t(\boldsymbol{X})]^a - \\ - \int_{\mathscr{T}} \int_{\mathscr{B}_0} [\boldsymbol{P}_t^*(\boldsymbol{X})]_a{}^A \, [\partial_X \dot{\boldsymbol{\varphi}}_t(\boldsymbol{X})]^a{}_A \end{aligned} \tag{3.6}$$

Note that the vector field $\dot{\boldsymbol{\varphi}}_t$ at any time $t \in \mathscr{T}$ is tangent to the continuous variation curve $\boldsymbol{\gamma}_t(s) = \boldsymbol{\varphi}_{t+s}$ of deformation fields. Since the Dirichlet boundary nor the initial value are violated by this curve, the vector field $\dot{\boldsymbol{\varphi}}_t$ represents an admissible test function. Accordingly, we determine a continuous weak momentum $\boldsymbol{\pi}(t)$ with the weak form

$$\boxed{\begin{aligned} \int_{\mathscr{T}} \int_{\mathscr{B}_0} [\dot{\boldsymbol{\pi}}_t(\boldsymbol{X})]_a \, [\delta\dot{\boldsymbol{\varphi}}_t(\boldsymbol{X})]^a = \int_{\mathscr{T}} \int_{\partial_T \mathscr{B}_0} [\bar{\boldsymbol{t}}_t^*(\boldsymbol{X})]_a \, [\delta\dot{\boldsymbol{\varphi}}_t(\boldsymbol{X})]^a - \\ - \int_{\mathscr{T}} \int_{\mathscr{B}_0} [\boldsymbol{P}_t^*(\boldsymbol{X})]_a{}^A \, [\partial_X (\delta\dot{\boldsymbol{\varphi}}_t(\boldsymbol{X}))]^a{}_A \end{aligned}} \tag{3.7}$$

Hence, the initial kinetic energy $\mathcal{T}(t_0)$ and the kinetic energy $\mathcal{T}(t_0^+)$ at the lower bound of the time curve coincide. Nevertheless, the time evolution $\boldsymbol{P}^*(t)$ of the covariant first Piola-Kirchhoff stress tensor field is, for the time being, only related with the field $\boldsymbol{P}^*(t_0^+)$. The weak form (3.7) leads to the kinetic energy balance

$$\mathcal{T}(T) - \mathcal{T}(t_0) = \int_{\mathscr{T}} \int_{\partial_T \mathscr{B}_0} [\bar{\boldsymbol{t}}_t^*(\boldsymbol{X})]_a \, [\dot{\boldsymbol{\varphi}}_t(\boldsymbol{X})]^a - \int_{\mathscr{T}} \mathcal{P}^{\text{int}}(t) \tag{3.8}$$

where Equation (2.28) has been taken into account. For a conservative Piola-Kirchhoff traction vector field, the integrand of the first term on the righthand side of Equation (3.8) coincides with the time integral of the negative directional derivative (2.112). Since the weak motion is continuous, the initial potential energy $\mathcal{U}^{\text{ext}}(t_0)$ and the energy $\mathcal{U}^{\text{ext}}(t_0^+)$ at the lower bound of the time curve coincide. By using the fundamental theorem of calculus, Equation (3.8) takes the form

$$\mathcal{T}(T) + \mathcal{U}^{\text{ext}}(T) - \mathcal{T}(t_0) - \mathcal{U}^{\text{ext}}(t_0) = -\int_{\mathscr{T}} \mathcal{P}^{\text{int}}(t) \tag{3.9}$$

As next step, we calculate the directional derivative of the relative internal energy along the continuous time curve $\gamma_t(s) = \hat{\mathcal{E}}(t+s)$, and apply the fundamental theorem of calculus. The relative internal energies $\hat{\mathcal{E}}(t_0^+)$ and $\hat{\mathcal{E}}(T)$ denote the energies at the lower and upper bound of the time curve, respectively. Noticing the definitions of the cotangent vectors corresponding to the free energy, we obtain the balance equation

$$\hat{\mathcal{E}}(T) - \hat{\mathcal{E}}(t_0^+) = \int_{\mathscr{T}} \mathcal{P}^{\text{int}}(t) + \int_{\mathscr{T}} \int_{\mathscr{B}_0} \dot{\eta}_t(\boldsymbol{X})\, \vartheta_t(\boldsymbol{X}) - [\boldsymbol{\Upsilon}_t(\boldsymbol{X})]^{AB}\, [\dot{\boldsymbol{\Gamma}}_t(\boldsymbol{X})]_{AB} \tag{3.10}$$

The Lagrangian relative temperature field is tangent to the variation curve $\gamma_t(s) = \Theta_t + s\,\vartheta_t$ of the fixed temperature field Θ_t. This curve does not violate the fixed ambient temperature Θ_∞ at the thermal Dirichlet boundary. Hence, the Lagrangian relative temperature field is an admissible test function for Equation (2.63) at fixed time $t \in \mathscr{T}$ in the time interval of interest. We therefore combine this equation with the first term on the righthand side of Equation (3.10), and arrive at

$$\begin{aligned} \int_{\mathscr{T}} \int_{\mathscr{B}_0} \dot{\eta}_t(\boldsymbol{X})\, \vartheta_t(\boldsymbol{X}) &= \int_{\mathscr{T}} \int_{\partial_Q \mathscr{B}_0} \frac{\vartheta_t(\boldsymbol{X})}{\Theta_t(\boldsymbol{X})}\, \overline{Q}_t(\boldsymbol{X}) + \\ &+ \int_{\mathscr{T}} \int_{\mathscr{B}_0} \frac{\Theta_\infty}{\Theta_t(\boldsymbol{X})}\, [\partial_X \vartheta_t(\boldsymbol{X})]_A\, [\boldsymbol{H}_t(\boldsymbol{X})]^A + \frac{\vartheta_t(\boldsymbol{X})}{\Theta_t(\boldsymbol{X})}\, D_t^{\text{int}}(\boldsymbol{X}) \end{aligned} \tag{3.11}$$

after integration by part and applying Gauss' divergence theorem, as well as employing the thermal boundary condition (2.87.2). Since the relative

Lagrangian temperature field ϑ_t at any time $t \in \mathscr{T}$ vanish solely at the thermal Dirichlet boundary, the temperature variation curve $\gamma_t(s)$ generally varies the temperature field Θ_{t_0} at initial time t_0. Consequently, we obtain a jump

$$[\![\Theta_{t_0}]\!] = \Theta_{t_0} - \Theta_0 \tag{3.12}$$

in the temperature time evolution at initial time t_0, wherefore the initial condition for the Lagrangian temperature field cannot be fulfilled exactly. According to the definition of the Lagrangian entropy field, we also get a jump $[\![\eta_{t_0}]\!]$ in the entropy time evolution. Thus, the relative internal energy $\hat{\mathcal{E}}(t_0^+)$ differs from the initial value $\hat{\mathcal{E}}(t_0)$. However, by introducing Equation (3.10) in the identity

$$\hat{\mathcal{E}}(T) - \hat{\mathcal{E}}(t_0) = \hat{\mathcal{E}}(T) - \hat{\mathcal{E}}(t_0^+) + \hat{\mathcal{E}}(t_0^+) - \hat{\mathcal{E}}(t_0) = \left[\!\!\left[\hat{\mathcal{E}}(t_0)\right]\!\!\right] + \hat{\mathcal{E}}(T) - \hat{\mathcal{E}}(t_0^+) \tag{3.13}$$

we arrive at the energy difference between the upper bound $\hat{\mathcal{E}}(T)$ and the initial value $\hat{\mathcal{E}}(t_0)$. Now, we add Equation (3.9), Equation (3.10) and Equation (3.13). Since terms associated with the stress power annihilate each other, we obtain the balance equation

$$\mathcal{V}(T) - \mathcal{V}(t_0) = \left[\!\!\left[\hat{\mathcal{E}}(t_0)\right]\!\!\right] + \int_{\mathscr{T}} \int_{\mathscr{B}_0} \dot{\eta}_t(\boldsymbol{X})\, \vartheta_t(\boldsymbol{X}) - [\,\boldsymbol{\Upsilon}_t(\boldsymbol{X})]^{AB}\, [\dot{\boldsymbol{\Gamma}}_t(\boldsymbol{X})]_{AB} \tag{3.14}$$

We want to derive from this balance equation a weak form of the entropy evolution equation. Thereby, the initial condition associated with the temperature has to be enforced weakly by a so-called trace term (see Cockburn [38]). We have to deduce a trace term, which fulfills the balance in Equation (3.14). We start by recalling the density $\hat{e}_t(\boldsymbol{X})$ of the relative internal energy, given by the expression

$$\hat{e}_t(\boldsymbol{X}) = \eta_t(\boldsymbol{X})\, \vartheta_t(\boldsymbol{X}) + \Psi_t(\boldsymbol{X}) \tag{3.15}$$

The energy jump in the balance Equation (3.14) then leads to a jump $[\![\hat{e}_{t_0}(\boldsymbol{X})]\!]$ in the density for all points $\boldsymbol{X} \in \mathscr{B}_0$. We assume that this jump coincides with the trace term $\vartheta_{t_0}(\boldsymbol{X})\, \hat{\eta}_{t_0}(\boldsymbol{X})$, where $\hat{\eta}_{t_0}(\boldsymbol{X})$ is an unknown entropy trace. We search for the smallest entropy trace, which fulfills this constraint. Hence, we determine the trace $\hat{\eta}_{t_0}(\boldsymbol{X})$ by minimising the Lagrange function

$$F(\hat{\eta}_{t_0}(\boldsymbol{X}), \lambda(\boldsymbol{X})) = \frac{1}{2}\, \hat{\eta}^2_{t_0}(\boldsymbol{X}) + \lambda(\boldsymbol{X}) \left\{ \vartheta_{t_0}(\boldsymbol{X})\, \hat{\eta}_{t_0}(\boldsymbol{X}) - [\![\hat{e}_{t_0}(\boldsymbol{X})]\!] \right\} \tag{3.16}$$

where $\lambda(\boldsymbol{X})$ denotes the associated Lagrange multiplier. According to the Euler-Lagrange equation corresponding to the entropy trace, $\hat{\eta}_{t_0}(\boldsymbol{X})$ coincides with $-\lambda(\boldsymbol{X})\, \vartheta_{t_0}(\boldsymbol{X})$. Employing this relation in the Euler-Lagrange equation corresponding to the Lagrange multiplier, the energy jump term reads

$$\left[\!\!\left[\hat{\mathcal{E}}(t_0) \right]\!\!\right] = \int_{\mathscr{B}_0} [\![\hat{e}_{t_0}(\boldsymbol{X})]\!] = \int_{\mathscr{B}_0} \hat{\eta}_{t_0}(\boldsymbol{X})\, \vartheta_{t_0}(\boldsymbol{X}) = \int_{\mathscr{B}_0} \frac{[\![\hat{e}_{t_0}(\boldsymbol{X})]\!]}{\vartheta_{t_0}(\boldsymbol{X})}\, \vartheta_{t_0}(\boldsymbol{X}) \tag{3.17}$$

Now, we consider the entropy trace as function of the temperature $\Theta_{t_0}(\boldsymbol{X})$, and apply L'Hôpital's rule. In this way, we realise that the limit of this fraction, as $\Theta_{t_0}(\boldsymbol{X})$ approaches Θ_∞, is zero as for the density jump $[\![\hat{e}_{t_0}(\boldsymbol{X})]\!]$ alone. Since the density jump vanishes at ambient temperature Θ_∞, we have not introduced a singularity in this way. Thus, Equation (3.14) can be written as

$$\begin{aligned} \mathcal{V}(T) - \mathcal{V}(t_0) = \int_{\mathscr{B}_0} \frac{[\![\hat{e}_{t_0}(\boldsymbol{X})]\!]}{\vartheta_{t_0}(\boldsymbol{X})}\, \vartheta_{t_0}(\boldsymbol{X}) + \\ + \int_{\mathscr{T}} \int_{\mathscr{B}_0} \dot{\eta}_t(\boldsymbol{X})\, \vartheta_t(\boldsymbol{X}) - [\boldsymbol{\Upsilon}_t(\boldsymbol{X})]^{AB}\, [\dot{\boldsymbol{\Gamma}}_t(\boldsymbol{X})]_{AB} \end{aligned} \tag{3.18}$$

The first and the second term of this equation include the relative Lagrangian temperature as test function. These terms are therefore related to the space-time weak form of the entropy evolution equation. Taking Equation (3.11) into account, we obtain the weak form

$$\boxed{\begin{aligned} \int_{\mathscr{B}_0} \frac{[\![\hat{e}_{t_0}(\boldsymbol{X})]\!]}{\vartheta_{t_0}(\boldsymbol{X})}\, \delta\Theta_{t_0}(\boldsymbol{X}) + \int_{\mathscr{T}} \int_{\mathscr{B}_0} \dot{\eta}_t(\boldsymbol{X})\, \delta\Theta_t(\boldsymbol{X}) = \int_{\mathscr{T}} \int_{\partial_Q \mathscr{B}_0} \frac{\delta\Theta_t(\boldsymbol{X})}{\Theta_t(\boldsymbol{X})}\, \overline{Q}_t(\boldsymbol{X}) + \\ + \int_{\mathscr{T}} \int_{\mathscr{B}_0} \frac{\Theta_\infty}{\Theta_t(\boldsymbol{X})}\, [\partial_X(\delta\Theta_t(\boldsymbol{X}))]_A\, [\boldsymbol{H}_t(\boldsymbol{X})]^A + \delta\Theta_t(\boldsymbol{X})\, \frac{D^{\text{int}}_t(\boldsymbol{X})}{\Theta_t(\boldsymbol{X})} \end{aligned}} \tag{3.19}$$

The mapping $\delta\Theta_{t_0}$ varies the Lagrangian temperature field Θ_{t_0} at the limit from above. Bearing in mind the vanishing thermal Neumann boundary in conjunction with the stability estimate (2.118), a comparison of this weak form with the first two terms on the righthand side of Equation (3.18) yields the balance

$$\begin{aligned} \mathcal{V}(T) - \mathcal{V}(t_0) = &-\int_{\mathscr{T}} \int_{\mathscr{B}_0} \frac{\Theta_\infty}{\Theta_t(\boldsymbol{X})} D_t^{\text{tot}}(\boldsymbol{X}) + \\ &+ \int_{\mathscr{T}} \int_{\mathscr{B}_0} D_t^{\text{int}}(\boldsymbol{X}) - [\boldsymbol{\varUpsilon}_t(\boldsymbol{X})]^{AB} \, [\dot{\boldsymbol{\varGamma}}_t(\boldsymbol{X})]_{AB} \end{aligned} \tag{3.20}$$

in which the definition of the dissipation arising from conduction of heat has been used.

The last step is a weak formulation of Equation (2.77). Here, we go a different way as for the former time evolution equations. We determine the viscous internal variable at each considered point $\boldsymbol{X} \in \mathscr{B}_0$. That is possible, because the viscous internal variable evolution is only a coupled initial value problem. Employing Equation (2.77) in the last term of Equation (3.20), we obtain the temporally weak equation

$$\boxed{\int_{\mathscr{T}} [\boldsymbol{\varUpsilon}_t(\boldsymbol{X})]^{AD} \, [\delta\dot{\boldsymbol{\varGamma}}_t(\boldsymbol{X})]_{AD} = \int_{\mathscr{T}} [\boldsymbol{\varSigma}_t(\boldsymbol{X})]^{AD} \, [\delta\dot{\boldsymbol{\varGamma}}_t(\boldsymbol{X})]_{AD}} \tag{3.21}$$

wherein the test function $\delta\dot{\boldsymbol{\varGamma}}_t(\boldsymbol{X})$ is a tangent vector at the variation curve $\gamma_t(\boldsymbol{X})(s) = \boldsymbol{\varGamma}_{t+s}(\boldsymbol{X})$ in the internal variable set. Since this variation curve does not violate a constant value at initial time t_0 for all $\boldsymbol{X} \in \mathscr{B}_0$, the initial condition of the internal variable at any point $\boldsymbol{X} \in \mathscr{B}_0$ can be satisfied exactly. Hence, the time evolution of the viscous internal variable is continuous. Equation (3.21) leads to the identity

$$\int_{\mathscr{T}} \int_{\mathscr{B}_0} [\boldsymbol{\varUpsilon}_t(\boldsymbol{X})]^{AF} \, [\dot{\boldsymbol{\varGamma}}_t(\boldsymbol{X})]_{AF} = \int_{\mathscr{T}} \int_{\mathscr{B}_0} D_t^{\text{int}}(\boldsymbol{X}) \tag{3.22}$$

relating the last term on the righthand side of Equation (3.20) to the internal dissipation, given by Equation (2.83). Note that we employ a temporally weak equation at each integration point in the reference configuration. According to Equations (3.20) and (3.22), we arrive at the ‘a priori’ stability estimate.

4. FINITE ELEMENT APPROXIMATION

First, we perform a finite-dimensional approximation of the considered time evolutions. This leads to a temporal finite element approximation. Then, we obtain a finite-dimensional approximation of the Lagrangian fields at fixed time by introducing a spatial finite element approximation. Here, we incorporate the boundary conditions on the fields over the continuum body.

Note that we approximate the flow of the dynamical system on the ambient space $\mathscr{A}$ before we approximate the considered subset $\mathscr{B}_0 \subset \mathscr{A}$ in the ambient space. The reason is that we calculate time curves of fields over a bounded domain. Therefore, we approximate first the time curves of the fields and subsequently the fields themselves. That leads to the mentioned assumed strain approximation in time, which reproduce exactly the vanishing strains in a rigid body motion (see Groß et al. [16] and Groß [35]).

In this way, we arrive at a space-time finite element approximation, which is consistent with the 'a priori' stability estimate. A detailed description of nonlinear finite element methods for solids can be found in Hughes [160], Belytschko et al. [161] and Oden [162].

4.1. Temporal finite element approximation

We introduce a partition of the time interval $\mathscr{T} = [t_0, T]$ of interest into $m_{el} \geqslant 1$ disjoint sub-intervals $\mathscr{T}^n$, $n \in \mathscr{M}_{el} = \{1, \ldots, m_{el}\}$, such that the union of all sub-intervals coincides with $\mathscr{T}$. This partition is related with a mesh $t_0 = t^1 < t^2 < \ldots < t^{m_{el}} < t^{m_{el}+1} = T$ of time points. We refer to a sub-interval $\mathscr{T}^n = [t^n, t^{n+1}]$ as the n-th time element. We consider time nodes $t_i^n < t_k^n \in \mathscr{T}^n$, where $i < k \in \mathscr{M}_{en} = \{1, \ldots, m_{en}\}$, distributed such that $t_1^n = t^n$ and $t_{m_{en}}^n = t^{n+1}$ denote the boundaries of the n-th time element (see Figure 4.1). The difference $h^n = t_{m_{en}}^n - t_1^n$ then designates the time step size. By the transformation

$$\tau^n(\alpha) = \sum_{i=1}^{m_{en}} M^i(\alpha)\, t_i^n \qquad \alpha \in [0, 1] \tag{4.1}$$

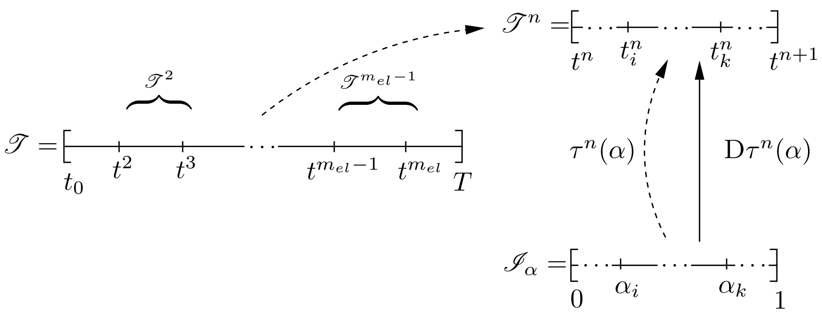

Figure 4.1. The time interval of interest $\mathscr{T}$ is partitioned in sub-intervals $\mathscr{T}^n$, which are related with time nodes. By introducing a transformation $\tau^n(\alpha)$, a parent domain $\mathscr{I}_\alpha$ is mapped on such a sub-interval.

we map a temporal parent domain $\mathscr{I}_\alpha = [0,1]$ on a time element $\mathscr{T}^n$. Accordingly, the time nodes $\alpha_k \in \mathscr{I}_\alpha$, $k \in \mathscr{M}_{en}$, on the parent domain are mapped to the time nodes $t_k^n = \tau^n(\alpha_k)$ by the transformation (4.1). The shape functions $M^i(\alpha)$ denote Lagrange polynomials on the parent domain, satisfying the condition $M^i(\alpha_k) = \delta_k{}^i$. Since we restrict ourselves to an equidistant distribution of the time nodes t_k^n on the n-th time element, there remains the transformation

$$\tau^n(\alpha) = (1-\alpha)\, t_1^n + \alpha\, t_{m_{en}}^n \tag{4.2}$$

The partition of $\mathscr{T}$ divides the time integrals of the space-time weak forms into a sum of m_{el} sub-integrals with respect to the time elements $\mathscr{T}^n$. We get n coupled systems of weak forms determining the time evolutions on the time elements $\mathscr{T}^n$. By using the time transformation (4.2), we transform each time element to the parent domain. For each $n \in \mathscr{M}_{el}$, we obtain the weak form

$$\int_{\mathscr{I}_\alpha}\int_{\mathscr{B}_0} [\delta\dot{\boldsymbol{\pi}}_\alpha^n(\boldsymbol{X})]_a\, [\dot{\boldsymbol{\varphi}}_\alpha^n(\boldsymbol{X})]^a = \int_{\mathscr{I}_\alpha}\int_{\mathscr{B}_0} [\delta\dot{\boldsymbol{\pi}}_\alpha^n(\boldsymbol{X})]_a\, [\boldsymbol{v}_\alpha^n(\boldsymbol{X})]^a \tag{4.3}$$

of the first space-time weak equation of motion. We have used the substitution rule together with the identity $\mathrm{D}\tau^n(\alpha) = h^n$ for relating the time integration to the parent domain on both sides. The mapping $\boldsymbol{\varphi}_\alpha^n = [\boldsymbol{\varphi}|_{\mathscr{T}^n} \circ \tau^n](\alpha)$

designates a deformation field $\boldsymbol{\varphi}_t$ at any time point $\mathscr{T}^n \ni t = \tau^n(\alpha)$ on the n-th time element, parameterised by the transformation (4.2). The field $\boldsymbol{v}_\alpha^n$ denotes the corresponding Lagrangian deformation velocity field at the same time point. We approximate the corresponding time evolutions, such that

$$\boldsymbol{\varphi}_\alpha^n(\boldsymbol{X}) = \sum_{i=1}^{m_{en}} M^i(\alpha)\,\boldsymbol{\varphi}_{\alpha_i}^n(\boldsymbol{X}) \qquad \text{and} \qquad \boldsymbol{v}_\alpha^n(\boldsymbol{X}) = \sum_{i=1}^{m_{en}} M^i(\alpha)\,\boldsymbol{v}_{\alpha_i}^n(\boldsymbol{X}) \tag{4.4}$$

by applying the same shape functions as for the transformation (4.1). In this way, we obtain an isoparametric finite element approximation in time. We have to apply the chain rule of differentiation for calculating the time derivatives in Equation (4.3). The first space-time weak equation of motion for the time element $\mathcal{T}^n$, $n \in \mathscr{M}_{el}$, then takes the form

$$\boxed{\frac{1}{h^n}\int_{\mathscr{I}_\alpha}\int_{\mathscr{B}_0}[\delta\mathring{\boldsymbol{\pi}}_\alpha^n(\boldsymbol{X})]_a\,[\mathring{\boldsymbol{\varphi}}_\alpha^n(\boldsymbol{X})]^a = \int_{\mathscr{I}_\alpha}\int_{\mathscr{B}_0}[\delta\mathring{\boldsymbol{\pi}}_\alpha^n(\boldsymbol{X})]_a\,[\boldsymbol{v}_\alpha^n(\boldsymbol{X})]^a} \tag{4.5}$$

where the symbol $\circ$ indicates the partial derivative of a time evolution $\hat{\boldsymbol{\varphi}}|_{\mathscr{T}^n}(\tau^n(\alpha),\boldsymbol{X})$ with respect to α. Note that we do not multiply both sides with h^n, because then the weak form no longer relates virtual energy to virtual work, but with the time step size weighted virtual energy and work. However, that the weak equations of motion exactly relate virtual energy to virtual work is used later for solving the problem. We approximate the time evolution of the tangent fields $\delta\mathring{\boldsymbol{\pi}}_\alpha^n$ on the parent domain $\mathscr{I}_\alpha$, pertaining to the Lagrangian momentum field on the n-th time element, such that

$$\delta\mathring{\boldsymbol{\pi}}_\alpha^n(\boldsymbol{X}) = \sum_{j=1}^{m_{eq}} \tilde{M}^j(\alpha)\,\delta\boldsymbol{\pi}_{\tilde{\alpha}_j}^n(\boldsymbol{X}) \tag{4.6}$$

with $\delta\mathring{\boldsymbol{\pi}}_{\alpha_1}^n(\boldsymbol{X}) = \boldsymbol{o}$ for all points $\boldsymbol{X} \in \mathscr{B}_0$. The shape functions $\tilde{M}^j(\alpha)$ denote Lagrange polynomials on the parent domain, satisfying the condition $\tilde{M}^j(\tilde{\alpha}_l) = \delta_l{}^j$, with $j, l \in \mathscr{M}_{eq} = \{1, \ldots, m_{eq}\}$. The points $\tilde{\alpha}_l$ designate test notes on the parent domain. Note that the number m_{eq} of these test notes coincides with $m_{en} - 1$, because they support a velocity field approximation. Since the variation at the initial time node $t_1^n = \tau^n(\alpha_1)$ vanishes, the initial condition $\boldsymbol{\pi}^n_{\alpha_1} = \boldsymbol{\pi}_{t^{n-1}_{m_{en}}}$ is fulfilled exactly.

On the other hand, according to Equation (3.7), we obtain for each time element $\mathcal{T}^n$, $n \in \mathscr{M}_{el}$, the space-time weak form

$$\boxed{\begin{aligned}\frac{1}{h^n}\int_{\mathscr{I}_\alpha}\int_{\mathscr{B}_0}[\mathring{\boldsymbol{\pi}}^n_\alpha(\boldsymbol{X})]_a\,[\delta\mathring{\boldsymbol{\varphi}}^n_\alpha(\boldsymbol{X})]^a = \int_{\mathscr{I}_\alpha}\int_{\partial_T\mathscr{B}_0}[\bar{\boldsymbol{t}}^{*,n}_\alpha(\boldsymbol{X})]_a\,[\delta\mathring{\boldsymbol{\varphi}}^n_\alpha(\boldsymbol{X})]^a -& \\ -\int_{\mathscr{I}_\alpha}\int_{\mathscr{B}_0}[\boldsymbol{P}^{*,n}_\alpha(\boldsymbol{X})]_a{}^A\,[\partial_X(\delta\mathring{\boldsymbol{\varphi}}^n_\alpha(\boldsymbol{X}))]^a{}_A&\end{aligned}} \tag{4.7}$$

by using the substitution rule and the constant Frèchet derivative of the transformation (4.2). Further, the chain rule has been used for the time differentiation of the approximations. We approximate the Lagrangian momentum field $\boldsymbol{\pi}^n_\alpha(\boldsymbol{X})$ on the basis of Equations (2.22) and (4.4). The time evolution corresponding to the tangent field $\delta\mathring{\boldsymbol{\varphi}}^n_\alpha$ pertaining to the deformation during the n-th time element is again directly approximated on the parent domain. Hence, we obtain the approximations

$$\boldsymbol{\pi}^n_\alpha(\boldsymbol{X}) = \sum_{i=1}^{m_{en}} M^i(\alpha)\,\boldsymbol{\pi}^n_{\alpha_i}(\boldsymbol{X}) \qquad \text{and} \qquad \delta\mathring{\boldsymbol{\varphi}}^n_\alpha(\boldsymbol{X}) = \sum_{j=1}^{m_{eq}} \tilde{M}^j(\alpha)\,\delta\boldsymbol{\varphi}^n_{\tilde{\alpha}_j}(\boldsymbol{X}) \tag{4.8}$$

with $\delta\mathring{\boldsymbol{\varphi}}^n_{\alpha_1}(\boldsymbol{X}) = \boldsymbol{o}$ for all $\boldsymbol{X} \in \mathscr{B}_0$.

Now, we formulate the space-time weak Equation (3.11) with respect to the parent domain. We transform the integrals by using the substitution rule and the Frèchet derivative of the transformation (4.2). Subsequently, we apply the chain rule to the time differentiation of the approximation $\eta^n_\alpha(\boldsymbol{X})$ pertaining to the Lagrangian entropy field on the n-th time element $\mathcal{T}^n$. For each $n \in \mathscr{M}_{el}$, we obtain the space-time weak equation

$$\begin{aligned}\int_{\mathscr{I}_\alpha}\int_{\mathscr{B}_0}\mathring{\eta}^n_\alpha(\boldsymbol{X})\,\vartheta^n_\alpha(\boldsymbol{X}) = h^n\int_{\mathscr{I}_\alpha}\int_{\partial_Q\mathscr{B}_0}\frac{\vartheta^n_\alpha(\boldsymbol{X})}{\varTheta^n_\alpha(\boldsymbol{X})}\,\overline{Q}^n_\alpha(\boldsymbol{X}) +& \\ +h^n\int_{\mathscr{I}_\alpha}\int_{\mathscr{B}_0}\frac{\varTheta_\infty}{\varTheta^n_\alpha(\boldsymbol{X})}\,[\partial_X\vartheta^n_\alpha(\boldsymbol{X})]_A\,[\boldsymbol{H}^n_\alpha(\boldsymbol{X})]^A + \frac{\vartheta^n_\alpha(\boldsymbol{X})}{\varTheta^n_\alpha(\boldsymbol{X})}\,D^{\text{int},n}_\alpha(\boldsymbol{X})&\end{aligned} \tag{4.9}$$

From the outset, we considered the Lagrangian entropy field as state variable, on which the thermal time evolution equation is based. Therefore, we approximate the time evolution of the Lagrangian entropy field, and the time evolution of the Lagrangian temperature field in the exact same manner. We arrive at

$$\eta^n_\alpha(\boldsymbol{X}) = \sum_{i=1}^{m_{en}} M^i(\alpha)\, \eta^n_{\alpha_i}(\boldsymbol{X}) \qquad \text{and} \qquad \varTheta^n_\alpha(\boldsymbol{X}) = \sum_{i=1}^{m_{en}} M^i(\alpha)\, \varTheta^n_{\alpha_i}(\boldsymbol{X}) \tag{4.10}$$

Note that this temporal entropy approximation goes with the time approximation of the nonlinear energy equation in Holzapfel & Simo [125]. In this way, we approximate the time evolution of the Lagrangian entropy field in the time interval of interest before we approximate the Lagrangian entropy field in the ambient space. The test space for Equation (4.9) has to include the time evolutions of the relative Lagrangian temperature field ϑ^n_α. Consequently, we obtain the approximation

$$\delta\varTheta^n_\alpha(\boldsymbol{X}) = \sum_{i=1}^{m_{en}} M^i(\alpha)\, \delta\varTheta^n_{\alpha_i}(\boldsymbol{X}) \tag{4.11}$$

which only vanish at the boundary $\partial_\varTheta \mathscr{B}_0$. Hence, the initial condition for the Lagrangian temperature field cannot be fulfilled exactly, and the temperature $\varTheta^n_{\alpha_1}$ generally differ from the initial value for the temperature evolution on the time element. In analogy to Equation (3.19), we incorporate the corresponding jump in an energy consistent way. We obtain

$$\boxed{\begin{aligned} \int_{\mathscr{B}_0} \frac{\llbracket \hat{e}^n_{\alpha_1}(\boldsymbol{X}) \rrbracket}{\vartheta^n_{\alpha_1}(\boldsymbol{X})}\, \delta\varTheta^n_{\alpha_1}(\boldsymbol{X}) + \int_{\mathscr{I}_\alpha} \int_{\mathscr{B}_0} \mathring{\eta}^n_\alpha(\boldsymbol{X})\, \delta\varTheta^n_\alpha(\boldsymbol{X}) &= \int_{\mathscr{I}_\alpha} \int_{\partial_Q \mathscr{B}_0} h^n \frac{\delta\varTheta^n_\alpha(\boldsymbol{X})}{\varTheta^n_\alpha(\boldsymbol{X})}\, \overline{Q}^n_\alpha(\boldsymbol{X}) \\ + h^n \int_{\mathscr{I}_\alpha} \int_{\mathscr{B}_0} \frac{\varTheta_\infty}{\varTheta^n_\alpha(\boldsymbol{X})}\, [\partial_X(\delta\varTheta^n_\alpha(\boldsymbol{X}))]_A\, [\boldsymbol{H}^n_\alpha(\boldsymbol{X})]^A &+ \delta\varTheta^n_\alpha(\boldsymbol{X})\, \frac{D^{\mathrm{int},n}_\alpha(\boldsymbol{X})}{\varTheta^n_\alpha(\boldsymbol{X})} \end{aligned}} \tag{4.12}$$

for each $\mathcal{T}^n$, $n \in \mathscr{M}_{el}$, with respect to the parent domain. On each time element, the initial condition of the temperature is incorporated by the jump $\llbracket \hat{e}^n_{\alpha_1}(\boldsymbol{X}) \rrbracket$ of the relative internal energy density.

At last, we perform an isoparametric approximation for the time evolution of the pointwise determined Lagrangian internal variable field $\boldsymbol{\varGamma}^n_\alpha$ on the parent domain. According to Equation (3.21), the corresponding test space has to include the time evolution of the internal variable velocity field $\overset{\circ}{\boldsymbol{\varGamma}}{}^n_\alpha$ with respect to the parent domain. We arrive at

$$\boldsymbol{\varGamma}^n_\alpha(\boldsymbol{X}) = \sum_{i=1}^{m_{en}} M^i(\alpha)\, \boldsymbol{\varGamma}^n_{\alpha_i}(\boldsymbol{X}) \qquad \text{and} \qquad \delta\overset{\circ}{\boldsymbol{\varGamma}}{}^n_\alpha(\boldsymbol{X}) = \sum_{j=1}^{m_{eq}} \tilde{M}^j(\alpha)\, \delta\boldsymbol{\varGamma}^n_{\tilde{\alpha}_j}(\boldsymbol{X}) \tag{4.13}$$

with $\delta\overset{\circ}{\boldsymbol{\varGamma}}{}^n_{\alpha_1}(\boldsymbol{X}) = \boldsymbol{O}^*$ due to the continuity, where $\boldsymbol{O}^*$ denotes the matrix corresponding to the zero element in the linear space $\mathbb{L}(\mathscr{A}, \mathscr{A}^*)$. First, we divide each integral of Equation (3.21) into m_{el} sub-integrals. Then, we apply the substitution rule to the time integrals and the chain rule of differentiation to the time derivatives. Either in the light of the constant Frèchet derivative of the transformation (4.2). For each $n \in \mathscr{M}_{el}$ and $\boldsymbol{X} \in \mathscr{B}_0$, we obtain the temporally weak form

$$\boxed{\begin{aligned} &\int_{\mathscr{I}_\alpha} [\boldsymbol{\varUpsilon}^n_\alpha(\boldsymbol{X})]^{AD}\, [\delta\overset{\circ}{\boldsymbol{\varGamma}}{}^n_\alpha(\boldsymbol{X})]_{AD} = -\int_{\mathscr{I}_\alpha} \frac{V_{\mathrm{dev}}}{2\, h^n}\, [\overset{\circ}{\overline{(\boldsymbol{\varGamma}^n_\alpha(\boldsymbol{X}))^{-1}}}]^{AD}\, [\delta\overset{\circ}{\boldsymbol{\varGamma}}{}^n_\alpha(\boldsymbol{X})]_{AD} + \\ &\qquad + \frac{1}{2}\int_{\mathscr{I}_\alpha} \left(V_{\mathrm{vol}} - \frac{2\, V_{\mathrm{dev}}}{n_{\mathrm{dim}}} \right) \mathrm{tr}(\boldsymbol{L}^n_\alpha(\boldsymbol{X}))\, [(\boldsymbol{\varGamma}^n_\alpha(\boldsymbol{X}))^{-1}]^{AD}\, [\delta\overset{\circ}{\boldsymbol{\varGamma}}{}^n_\alpha(\boldsymbol{X})]_{AD} \end{aligned}} \tag{4.14}$$

where

$$[\boldsymbol{L}^{n,e}_\alpha(\boldsymbol{X})]^A{}_C = \frac{1}{2\, h^n} [(\boldsymbol{\varGamma}^{n,e}_\alpha(\boldsymbol{X}))^{-1}]^{AB} [\overset{\circ}{\boldsymbol{\varGamma}}{}^{n,e}_\alpha(\boldsymbol{X})]_{BC} \tag{4.15}$$

designates the approximated viscous deformation rate tensor during the n-th time interval.

In order to obtain a unique interpolation of the temporal test nodes at each temporal quadrature point, a family of m shape functions has to be evaluated at exactly m distinct quadrature points. Since we approximate the test function associated with Equation (4.12) with one Lagrange polynomial more as compared to the other weak forms, we have to use one quadrature point more. Therefore, in the following, we endue the symbol $\mathscr{I}_\alpha$ of the time integration domain associated with Equation (4.12) with the suffix η to refer to this different number of quadrature points.

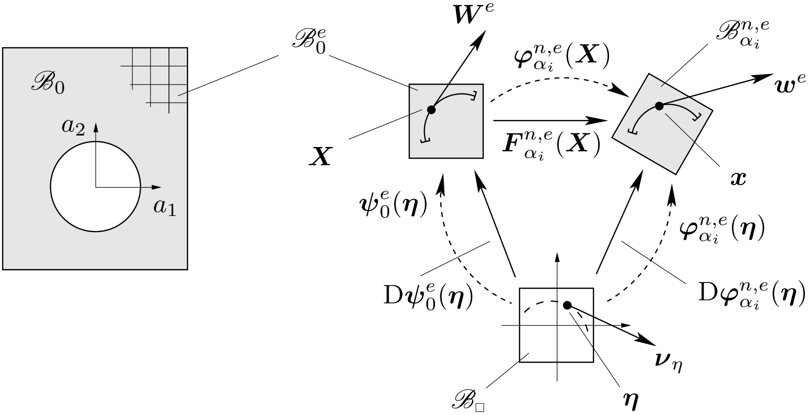

Figure 4.2. The reference configuration $\mathscr{B}_0$ is partitioned into disjoint sub-domains $\mathscr{B}_0^e$. A parent domain $\mathscr{B}_\square$ is mapped on each sub-domain in the reference configuration and on the corresponding sub-domain $\mathscr{B}_{\alpha_i}^{n,e}$ in the current configuration.

4.2. Spatial finite element approximation

We consider a partition of the reference configuration $\mathscr{B}_0$ into $n_{el} \geqslant 1$ disjoint sub-domains $\mathscr{B}_0^e$, $e \in \mathscr{N}_{el} = \{1, \dots, n_{el}\}$, called the e-th element of $\mathscr{B}_0$, such that the union of all these spatial elements, in turn, is given by $\mathscr{B}_0$. Each element $\mathscr{B}_0^e$ is defined by spatial element nodes ${}^a\boldsymbol{X}^e$, $a \in \mathscr{N}_{en}^e = \{1, \dots, n_{en}\}$. Element nodes, which lie on the mechanical Dirichlet boundary, are indicated by index sets $\mathscr{N}_\varphi^e = \{a \in \mathscr{N}_{en}^e | {}^a\boldsymbol{X}^e \in \partial_\varphi \mathscr{B}_0\}$. We introduce a spatial parent domain $\mathscr{B}_\square$ (see Figure 4.2), of which each point $\boldsymbol{\eta} \in \mathscr{B}_\square$ is mapped on a point $\boldsymbol{X}$ in the spatial element $\mathscr{B}_0^e$ by the transformation

$$\boldsymbol{\psi}_0^e(\boldsymbol{\eta}) = \sum_{a \in \mathscr{N}_{en}^e} N_a(\boldsymbol{\eta})\, {}^a\boldsymbol{X}^e \tag{4.16}$$

The shape functions $N_a(\boldsymbol{\eta})$ on the parent domain are Lagrange polynomials. The conditions $N_a(\boldsymbol{\eta}^b) = \delta^b{}_a$, $a, b \in \mathscr{N}_{en}^e$, provides that the nodes $\boldsymbol{\eta}^b \in \mathscr{B}_\square$ in the spatial parent domain are mapped to the spatial element nodes ${}^b\boldsymbol{X}^e = \boldsymbol{\psi}_0^e(\boldsymbol{\eta}^b)$. In the isoparametric concept, the spatial parent domain $\mathscr{B}_\square$ is mapped on the corresponding deformed spatial element $\mathscr{B}_{\alpha_i}^{n,e}$ in the current configuration at the time node $t_i^n = \tau^n(\alpha_i)$ by

$$\boldsymbol{\varphi}_{\alpha_i}^{n,e}(\boldsymbol{\eta}) = \sum_{a \in \mathscr{N}_{en}^e \setminus \mathscr{N}_\varphi^e} N_a(\boldsymbol{\eta})\, {}^a\boldsymbol{x}_{\alpha_i}^{n,e} + \sum_{b \in \mathscr{N}_\varphi^e} N_b(\boldsymbol{\eta})\, {}^b\boldsymbol{X}^e \tag{4.17}$$

analogously to Equation (4.16). The last sum arises from the boundary condition (2.86.1). Equation (4.17) is defined to coincide with the composition $\boldsymbol{\varphi}_{\alpha_i}^{n,e}(\boldsymbol{X}) \circ \boldsymbol{\psi}_0^e(\boldsymbol{\eta})$, so that $\boldsymbol{\varphi}_{\alpha_i}^{n,e}(\boldsymbol{\eta})$ approximates the deformation $\boldsymbol{\varphi}_{\alpha_i}^{n,e}(\boldsymbol{X})$ of the point $\boldsymbol{X} \in \mathscr{B}_0^e$ at the time node $t_i^n \in \mathscr{T}^n$ on the spatial parent domain.

Hence, a material curve in the e-th spatial element is related to a curve in the spatial parent domain by Equation (4.16). Differentiation with respect to the curve parameter implies the relation

$$[\boldsymbol{W}^e]^A = [\mathrm{D}\boldsymbol{\psi}_0^e(\boldsymbol{\eta})]^A{}_i\, [\boldsymbol{\nu}_\eta]^i \tag{4.18}$$

between the tangent vector $\boldsymbol{W}^e \in T_X\mathscr{B}_0^e$ at a point $\boldsymbol{X} \in \mathscr{B}_0^e$ and the tangent vector $\boldsymbol{\nu}_\eta \in T_\eta\mathscr{B}_\square$ at a point $\boldsymbol{\eta} \in \mathscr{B}_\square$.

On the other hand, the Jacobian matrix $\mathrm{D}\boldsymbol{\varphi}_{\alpha_i}^{n,e}(\boldsymbol{\eta})$ maps the tangent vector $\boldsymbol{\nu}_\eta$ on a tangent vector $\boldsymbol{w}^e \in T_x\mathscr{B}_{\alpha_i}^{n,e}$ at a point $\boldsymbol{x} \in \mathscr{B}_{\alpha_i}^{n,e}$ in the current configuration. Multiplying Equation (4.18) with the inverse Jacobian $(\mathrm{D}\boldsymbol{\psi}_0^e)^{-1}$, the deformation gradient

$$[\boldsymbol{F}_{\alpha_i}^{n,e}(\boldsymbol{\eta})]^a{}_A = [\mathrm{D}\boldsymbol{\varphi}_{\alpha_i}^{n,e}(\boldsymbol{\eta})]^a{}_i\, [(\mathrm{D}\boldsymbol{\psi}_0^e)^{-1}(\boldsymbol{\eta})]^i{}_A \tag{4.19}$$

maps the tangent vector $\boldsymbol{W}^e$ on the tangent vector $\boldsymbol{w}^e$. The index i indicates the coordinates in the spatial parent domain.

The volume element V_X^e at the point $\boldsymbol{X} \in \mathscr{B}_0^e$ in the e-th spatial element is defined by the triple scalar product $[\boldsymbol{W}_1^e, \boldsymbol{W}_2^e, \boldsymbol{W}_3^e]$ of tangent vectors at three curves, crossing each other in $\boldsymbol{X} \in \mathscr{B}_0^e$. This volume element is mapped by the Jacobian determinant

$$J_0^e(\boldsymbol{\eta}) \equiv \det(\mathrm{D}\boldsymbol{\psi}_0^e(\boldsymbol{\eta})) = \frac{\det(\mathrm{D}\boldsymbol{\varphi}_{\alpha_i}^{n,e}(\boldsymbol{\eta}))}{J_{\alpha_i}^{n,e}(\boldsymbol{\eta})} \tag{4.20}$$

to the volume element V_η at the point $\boldsymbol{\eta} \in \mathscr{B}_\square$ in the spatial parent domain.

Now, the partition of $\mathscr{B}_0$ divides the spatial integrals in the space-time weak forms into a sum of n_{el} sub-integrals with respect to the spatial elements $\mathscr{B}_0^e$, $e \in \mathscr{N}_{el}$. Transforming each material point $\boldsymbol{X} \in \mathscr{B}_0^e$ to the spatial parent domain by the mapping $\boldsymbol{\psi}_0^e$, Equation (4.5) takes the form

$$\boxed{\frac{1}{h^n}\int_{\mathscr{I}_\alpha}\int_{\mathscr{B}_\square}[\delta\mathring{\boldsymbol{\pi}}_\alpha^{n,e}(\boldsymbol{\eta})]_a\,[\mathring{\boldsymbol{\varphi}}_\alpha^{n,e}(\boldsymbol{\eta})]^a J_0^e(\boldsymbol{\eta}) = \int_{\mathscr{I}_\alpha}\int_{\mathscr{B}_\square}[\delta\mathring{\boldsymbol{\pi}}_\alpha^{n,e}(\boldsymbol{\eta})]_a\,[\boldsymbol{v}_\alpha^{n,e}(\boldsymbol{\eta})]^a J_0^e(\boldsymbol{\eta})} \tag{4.21}$$

for all $(n,e) \in \mathscr{M}_{el} \times \mathscr{N}_{el}$. The velocity field $\boldsymbol{v}_{\alpha_i}^{n,e}$ is a tangent field of the motion at the time node $\alpha_i \in \mathscr{I}_\alpha$, and the test field $\delta\boldsymbol{\pi}_{\tilde{\alpha}_j}^{n,e}$ is a tangent field at a variation of the cotangent field $\boldsymbol{\pi}_{\tilde{\alpha}_j}^{n,e}$ at the deformation field. With exception of the different boundary conditions, tangent and cotangent fields at the deformation field are approximated as the deformation field itself. Hence, we obtain

$$\boldsymbol{v}_{\alpha_i}^{n,e}(\boldsymbol{\eta}) = \sum_{a\in\mathscr{N}_{en}^e\setminus\mathscr{N}_\varphi^e} N_a(\boldsymbol{\eta})\,{}^a\boldsymbol{v}_{\alpha_i}^{n,e} \qquad \text{and} \qquad \delta\boldsymbol{\pi}_{\tilde{\alpha}_j}^{n,e}(\boldsymbol{\eta}) = \sum_{a\in\mathscr{N}_{en}^e\setminus\mathscr{N}_\varphi^e} \rho_0^e(\boldsymbol{\eta})\,N_a(\boldsymbol{\eta})\,{}^a\delta\boldsymbol{v}_{\tilde{\alpha}_j}^{n,e} \tag{4.22}$$

according to the Dirichlet boundary conditions, where $\rho_0^e(\boldsymbol{\eta}) = [\rho_0|_{\mathscr{B}_0^e} \circ \boldsymbol{\psi}_0^e](\boldsymbol{\eta})$ denotes the density of the element $\mathscr{B}_0^e$.

To account for the mechanical Neumann boundary $\partial_T\mathscr{B}_0$ of the reference configuration, we define the index set $\mathscr{N}_T^e = \{a \in \mathscr{N}_{en}^e | {}^a\boldsymbol{X}^e \in \partial_T\mathscr{B}_0^e\}$, which includes the nodes on the Neumann boundary of the element $\mathscr{B}_0^e$. Then, we introduce a transformation

$$\bar{\boldsymbol{\psi}}_0^e(\bar{\eta}) = \sum_{a\in\mathscr{N}_T^e} \bar{N}_a(\bar{\eta})\,{}^a\boldsymbol{X}^e \tag{4.23}$$

from a parent domain $\partial\mathscr{B}_\square$ to the e-th (Neumann) boundary element $\partial_T\mathscr{B}_0^e$. The shape functions $\bar{N}_a(\bar{\eta})$ are Lagrange polynomials on the parent domain, satisfying the condition $\bar{N}_a(\bar{\eta}^b) = \delta^b{}_a$. Therefore, nodes $\bar{\eta}^b \in \partial\mathscr{B}_\square$ are mapped to nodes ${}^b\boldsymbol{X}^e = \bar{\boldsymbol{\psi}}_0^e(\bar{\eta}^b)$ on a boundary element $\partial_T\mathscr{B}_0^e$.

After dividing up the spatial integrals in Equation (4.7), the transformations (4.16) and (4.23) to the parent domains provides the weak form

$$\boxed{\begin{aligned}\frac{1}{h^n}\int_{\mathscr{I}_\alpha}\int_{\mathscr{B}_\square}[\mathring{\boldsymbol{\pi}}_\alpha^{n,e}(\boldsymbol{\eta})]_a\,[\delta\mathring{\boldsymbol{\varphi}}_\alpha^{n,e}(\boldsymbol{\eta})]^a J_0^e(\boldsymbol{\eta}) = &\int_{\mathscr{I}_\alpha}\int_{\partial\mathscr{B}_\square}[\bar{\boldsymbol{t}}_\alpha^{*,n,e}(\bar{\eta})]_a\,[\delta\mathring{\boldsymbol{\varphi}}_\alpha^{n,e}(\bar{\eta})]^a \bar{J}_0^e(\bar{\eta}) - \\ &-\int_{\mathscr{I}_\alpha}\int_{\mathscr{B}_\square}[\boldsymbol{P}_\alpha^{*,n,e}(\boldsymbol{\eta})]_a{}^A\,[\partial_X(\delta\mathring{\boldsymbol{\varphi}}_\alpha^{n,e}(\boldsymbol{\eta}))]^a{}_A J_0^e(\boldsymbol{\eta})\end{aligned}} \tag{4.24}$$

for all $(n,e) \in \mathscr{M}_{el} \times \mathscr{N}_{el}$. The mapping $\bar{J}_0^e(\bar{\eta}) = \det(\mathrm{D}\bar{\boldsymbol{\psi}}_0^e(\bar{\eta}))$ denotes the Jacobian determinant of the transformation (4.23). The Lagrangian momentum field $\boldsymbol{\pi}_{\alpha_i}^{n,e}$ at the node $\alpha_i \in \mathscr{I}_\alpha$ is a cotangent field at the deformation field, whereas the test field $\delta\boldsymbol{\varphi}_{\tilde{\alpha}_j}^{n,e}$ is a tangent field at the deformation field. Hence, we approximate these fields in an analogous manner as in Equation (4.22).

However, under the boundary integral sign on the righthand side of Equation (4.24), this spatial approximation of the test field $\delta\boldsymbol{\varphi}_{\tilde{\alpha}_j}^{n,e}$ is reduced to an approximation of the variations at the boundary nodes, using the boundary shape functions on the spatial parent domain. For simplicity, we restrict us to boundary loadings with deformation-independent directions, which exclude a pressure boundary loading as treated in Simo et al. [163]. Further, we assume that the time course of the Piola-Kirchhoff traction vector field $\bar{\boldsymbol{t}}_\alpha^{n,e}$ is given. Thus, we only approximate the spatial distribution, and obtain

$$\bar{\boldsymbol{t}}_\alpha^{n,e}(\bar{\eta}) = \sum_{a\in\mathscr{N}_T^e}\bar{N}_a(\bar{\eta})\,{}^a\boldsymbol{t}_\alpha^{n,e} \qquad \text{and} \qquad \delta\boldsymbol{\varphi}_{\tilde{\alpha}_j}^{n,e}(\bar{\eta}) = \sum_{a\in\mathscr{N}_T^e}\bar{N}_a(\bar{\eta})\,{}^a\delta\boldsymbol{x}_{\tilde{\alpha}_j}^{n,e} \tag{4.25}$$

The vectors ${}^a\boldsymbol{t}_\alpha^{n,e}$ denote the traction on the boundary nodes.

In the last term on the righthand side of Equation (4.24), we have to determine the gradient with respect to a material point $\boldsymbol{X} \in \mathscr{B}_0^e$. Analogous to the relation for the deformation gradient in Equation (4.19), the gradient of the test function reads

$$[\partial_X(\delta\mathring{\boldsymbol{\varphi}}_\alpha^{n,e}(\boldsymbol{\eta}))]^a{}_A = [\mathrm{D}(\delta\mathring{\boldsymbol{\varphi}}_\alpha^{n,e})(\boldsymbol{\eta})]^a{}_i\,[(\mathrm{D}\boldsymbol{\psi}_0^e)^{-1}(\boldsymbol{\eta})]^i{}_A \tag{4.26}$$

Now, we define index sets $\mathscr{N}_\Theta^e = \{a \in \mathscr{N}_{en}^e | {}^a\boldsymbol{X}^e \in \partial_\Theta\mathscr{B}_0^e\}$ to indicate the nodes on the thermal Dirichlet boundary $\partial_\Theta\mathscr{B}_0$, and index sets $\mathscr{N}_Q^e = \{a \in \mathscr{N}_{en}^e | {}^a\boldsymbol{X}^e \in \partial_Q\mathscr{B}_0^e\}$ to designate nodes on the thermal Neumann boundary $\partial_Q\mathscr{B}_0$. Taking the partition of $\mathscr{B}_0$ into account, and relating spatial integrals to the corresponding parent domains, Equation (4.12) reads

$$\boxed{\begin{aligned}&\int_{\mathscr{B}_\square}\frac{\llbracket\hat{e}^{n,e}_{\alpha_1}(\boldsymbol{\eta})\rrbracket}{\vartheta^{n,e}_{\alpha_1}(\boldsymbol{\eta})}\;\delta\Theta^{n,e}_{\alpha_1}(\boldsymbol{\eta})\,J^e_0(\boldsymbol{\eta})+\int_{\mathscr{I}^\eta_\alpha}\int_{\mathscr{B}_\square}\mathring{\eta}^{n,e}_\alpha(\boldsymbol{\eta})\,\delta\Theta^{n,e}_\alpha(\boldsymbol{\eta})\,J^e_0(\boldsymbol{\eta})=\\&=\int_{\mathscr{I}^\eta_\alpha}\int_{\mathscr{B}_\square}h^n\Big\{\Theta_\infty[\partial_X(\delta\Theta^{n,e}_\alpha(\boldsymbol{\eta}))]_A\frac{[\boldsymbol{H}^{n,e}_\alpha(\boldsymbol{\eta})]^A}{\Theta^{n,e}_\alpha(\boldsymbol{\eta})}+\delta\Theta^{n,e}_\alpha(\boldsymbol{\eta})\frac{D^{\mathrm{int},n,e}_\alpha(\boldsymbol{\eta})}{\Theta^{n,e}_\alpha(\boldsymbol{\eta})}\Big\}\;J^e_0(\boldsymbol{\eta})+\\&\qquad+h^n\int_{\mathscr{I}^\eta_\alpha}\int_{\partial\mathscr{B}_\square}\frac{\delta\Theta^{n,e}_\alpha(\bar{\eta})}{\Theta^{n,e}_\alpha(\bar{\eta})}\,\overline{Q}^{n,e}_\alpha(\bar{\eta})\,\bar{J}^e_0(\bar{\eta})\end{aligned}}\tag{4.27}$$

for all $(n,e)\in\mathscr{M}_{el}\times\mathscr{N}_{el}$. The geometric approximation of the thermal Neumann boundary coincides with that of the mechanical Neumann boundary. According to the isoparametric concept, the approximation of the Lagrangian temperature field $\Theta^{n,e}_\alpha$ on the e-th spatial element during the time interval $\mathscr{T}^n$ is given by

$$\Theta^{n,e}_{\alpha_i}(\boldsymbol{\eta})=\sum_{a\in\mathscr{N}^e_{en}\setminus\mathscr{N}^e_\Theta}N_a(\boldsymbol{\eta})\,{}^a\Theta^{n,e}_{\alpha_i}+\sum_{b\in\mathscr{N}^e_\Theta}N_b(\boldsymbol{\eta})\,\Theta_\infty\tag{4.28}$$

where the constant ambient temperature Θ_∞ on the thermal Dirichlet boundary has been taken into account. We approximate the Lagrangian entropy field $\eta^{n,e}_{\alpha_i}$ and the test field $\delta\Theta^{n,e}_{\alpha_i}$ at the nodes in the parent domain in compliance with their definitions as cotangent and tangent field, respectively. We define

$$\eta^{n,e}_{\alpha_i}(\boldsymbol{\eta})=-\frac{\partial\Psi(\boldsymbol{\Lambda}^{n,e}_{\alpha_i}(\boldsymbol{\eta}),\,\Theta^{n,e}_{\alpha_i}(\boldsymbol{\eta}))}{\partial\Theta}\qquad\text{and}\qquad\delta\Theta^{n,e}_{\alpha_i}(\boldsymbol{\eta})=\sum_{a\in\mathscr{N}^e_{en}\setminus\mathscr{N}^e_\Theta}N_a(\boldsymbol{\eta})\,{}^a\delta\Theta^{n,e}_{\alpha_i}\tag{4.29}$$

According to Equation (2.39), the spatial approximation of the tensor $\boldsymbol{\Lambda}^{n,e}_{\alpha_i}(\boldsymbol{\eta})$ in the e-th spatial element at the time nodes in the parent domain follows from the spatial approximation $\boldsymbol{C}^{n,e}_{\alpha_i}(\boldsymbol{\eta})$ of the right Cauchy-Green tensor field and the locally determined tensor field $\boldsymbol{\Gamma}^{n,e}_{\alpha_i}(\boldsymbol{\eta})$. The approximation of the right Cauchy-Green tensor at the time nodes, in turn, follows from the push-forward operation

$$[\boldsymbol{C}^{n,e}_{\alpha_i}(\boldsymbol{\eta})]_{AB} = [(\mathrm{D}\boldsymbol{\psi}^e_0(\boldsymbol{\eta}))^{-T}]_A{}^k\,[\boldsymbol{C}^{n,e,\square}_{\alpha_i}(\boldsymbol{\eta})]_{kl}\,[(\mathrm{D}\boldsymbol{\psi}^e_0(\boldsymbol{\eta}))^{-1}]^l{}_B \tag{4.30}$$

where

$$[\boldsymbol{C}^{n,e,\square}_{\alpha_i}(\boldsymbol{\eta})]_{kl} = [(\mathrm{D}\boldsymbol{\varphi}^{n,e}_{\alpha_i}(\boldsymbol{\eta}))^T]_k{}^a\delta_{ab}[\mathrm{D}\boldsymbol{\varphi}^{n,e}_{\alpha_i}(\boldsymbol{\eta})]^b{}_l \tag{4.31}$$

denotes the right Cauchy-Green tensor with respect to the spatial parent domain.

We restrict us to a heat surface density field $\overline{Q}^{n,e}_{\alpha}$ on the thermal Neumann boundary $\partial_Q\mathscr{B}^e_0$, which is also given directly in dependence of the time $\alpha \in \mathscr{I}_\alpha$. Another possible Neumann boundary condition is a convective heat exchange on the boundary, which depends linear on the Lagrangian relative temperature field (see Wriggers et al. [164]). We define inward normal projections ${}^aQ^e_\alpha$ of the heat flux at the nodes of the boundary element, and approximate their spatial distribution. Likewise, we approximate the test field on this boundary. We obtain the distributions

$$\overline{Q}^{n,e}_{\alpha}(\overline{\eta}) = \sum_{a\in\mathscr{N}^e_Q}\bar{N}_a(\overline{\eta})^aQ^{n,e}_\alpha \qquad \text{and} \qquad \delta\Theta^{n,e}_{\alpha_i}(\overline{\eta}) = \sum_{a\in\mathscr{N}^e_Q}\bar{N}_a(\overline{\eta})\,{}^a\delta\Theta^{n,e}_{\alpha_i} \tag{4.32}$$

along the corresponding element boundary.

Since we determine the Lagrangian internal variable field $\boldsymbol{\Gamma}^{n,e}_\alpha$ at the considered points $\boldsymbol{\eta} \in \mathscr{B}_\square$ in the spatial parent domain, we desist from a spatial approximation. The temporally weak form

$$\boxed{\begin{aligned}\int_{\mathscr{I}_\alpha}[\boldsymbol{\Upsilon}^{n,e}_\alpha(\boldsymbol{\eta})]^{AD}\,[\delta\mathring{\boldsymbol{\Gamma}}^{n,e}_\alpha(\boldsymbol{\eta})]_{AD} = -\int_{\mathscr{I}_\alpha}\frac{V_{\mathrm{dev}}}{2\,h^n}\,\overset{\circ}{\overline{[(\boldsymbol{\Gamma}^{n,e}_\alpha(\boldsymbol{\eta}))^{-1}}}]^{AD}\,[\delta\mathring{\boldsymbol{\Gamma}}^{n,e}_\alpha(\boldsymbol{\eta})]_{AD} + \\ +\frac{1}{2}\int_{\mathscr{I}_\alpha}\left(V_{\mathrm{vol}} - \frac{2\,V_{\mathrm{dev}}}{n_{\mathrm{dim}}}\right)\mathrm{tr}(\boldsymbol{L}^{n,e}_\alpha(\boldsymbol{\eta}))\,[(\boldsymbol{\Gamma}^{n,e}_\alpha(\boldsymbol{\eta}))^{-1}]^{AD}\,[\delta\mathring{\boldsymbol{\Gamma}}^{n,e}_\alpha(\boldsymbol{\eta})]_{AD}\end{aligned}} \tag{4.33}$$

is thus solved on the parent domain of each spatial element $\mathscr{B}^e_0$, $e \in \mathscr{N}_{el}$, in the reference configuration.

5. TIME APPROXIMATION OF THE CONSTITUTIVE FIELDS

In order that the conservation laws and the stability estimate are also valid in the discrete setting, we have to supplement the weak forms. One reason is that both properties are based on the exact fulfillment of the fundamental theorem of calculus. However, using solely numerical quadrature, this is generally not possible. Furthermore, we have to guarantee that terms, which annihilate in the exactly integrated stability estimate, still annihilate with numerical time integration.

First, we consider the directional derivative of the approximated total linear momentum function along the continuous time curve $\boldsymbol{\gamma}_t^n(s) = \mathcal{L}(t+s)$ in the n-th time element. Time integration leads to

$$\int_{\mathscr{T}^n} \frac{\mathrm{d}}{\mathrm{d}s}\bigg|_{s=0} \mathcal{L}(t+s) = \sum_{e=1}^{n_{el}} \int_{\mathscr{I}_\alpha} \int_{\mathscr{B}_\square} [\mathring{\boldsymbol{\pi}}_\alpha^{n,e}(\boldsymbol{\eta})]_a \, [\boldsymbol{\xi}_0]^a \, J_0^e(\boldsymbol{\eta}) \tag{5.1}$$

If we employ the time approximation (4.8) corresponding to the Lagrangian momentum field, the time integration concerns only the temporal shape functions. Since this time integrals can be computed exactly with the recommended m_{eq}-point Gaussian quadrature, the fundamental theorem of calculus is fulfilled. The left hand side of Equation (5.1) therefore coincides with $\mathcal{L}(t^{n+1}) - \mathcal{L}(t^n)$.

On the righthand side, we bear in mind the equations of motion in order to verify conservation. First, the vector $\boldsymbol{\xi}_0 \in \mathscr{A}$ is fixed in the ambient space and hence time-independent. Nevertheless, it can be rewritten as

$$[\boldsymbol{\xi}_0]^a = \sum_{j=1}^{m_{eq}} \sum_{a=1}^{n_{el}} \tilde{M}^j(\alpha)\, N_a(\boldsymbol{\eta})\, [\boldsymbol{\xi}_0]^a \tag{5.2}$$

because both sums separately coincide with one due to the completeness condition of the Lagrange polynomials. Thus, the constant direction vector $\boldsymbol{\xi}_0$ is an admissible test function $\delta\mathring{\boldsymbol{\varphi}}_\alpha^{n,e}(\boldsymbol{\eta})$ of Equation (4.24). According to the absence of Dirichlet and Neumann boundary conditions, the righthand side of Equation (5.1) then coincides with

$$-h^n \sum_{e=1}^{n_{el}} \int_{\mathscr{I}_\alpha} \int_{\mathscr{B}_\square} [\boldsymbol{P}_\alpha^{*,n,e}(\boldsymbol{\eta})]_a{}^A \, [\partial_X \boldsymbol{\xi}_0]^a{}_A J_0^e(\boldsymbol{\eta}) = 0 \tag{5.3}$$

Thus, we obtain total linear momentum conservation for an arbitrary approximation of the covariant first Piola-Kirchhoff stress tensor and for an arbitrary time step size.

On the other hand, the directional derivative of the approximated total angular momentum function along the continuous time curve $\boldsymbol{\gamma}_t^n(s) = \mathcal{J}(t+s)$ in the n-th time element leads to

$$\begin{aligned}\int_{\mathscr{T}^n} \frac{\mathrm{d}}{\mathrm{d}s}\bigg|_{s=0} \mathcal{J}(t+s) = &\sum_{e=1}^{n_{el}} \int_{\mathscr{I}_\alpha} \int_{\mathscr{B}_\square} \epsilon_{abc} \delta^{cd} [\boldsymbol{\xi}_0]^a [\mathring{\boldsymbol{\varphi}}_\alpha^{n,e}(\boldsymbol{\eta})]^b [\boldsymbol{\pi}_\alpha^{n,e}(\boldsymbol{\eta})]_d J_0^e(\boldsymbol{\eta}) + \\ &+ \sum_{e=1}^{n_{el}} \int_{\mathscr{I}_\alpha} \int_{\mathscr{B}_\square} \epsilon_{abc} \delta^{cd} [\boldsymbol{\xi}_0]^a [\boldsymbol{\varphi}_\alpha^{n,e}(\boldsymbol{\eta})]^b [\mathring{\boldsymbol{\pi}}_\alpha^{n,e}(\boldsymbol{\eta})]_d J_0^e(\boldsymbol{\eta})\end{aligned} \tag{5.4}$$

After employing the time approximations (4.4) and (4.8), the fundamental theorem of calculus with respect to $\mathcal{J}(t)$ is fulfilled, because the time integrals associated with the temporal shape functions can be calculated exactly, using the m_{eq}-point Gaussian quadrature. The left hand side of Equation (5.4) therefore coincides with the difference $\mathcal{J}(t^{n+1}) - \mathcal{J}(t^n)$.

In order to show the conservation, we have to employ Equation (4.21) in the first term to the right. However, in Equation (5.4), the corresponding test function is not interpolated by the Lagrange polynomials $\{\tilde{M}^j(\alpha)\}_{j=1}^{m_{eq}}$ at the temporal test nodes $\tilde{\alpha}_j$, $j = 1, \ldots, m_{eq}$. Therefore, we determine nodal values $\boldsymbol{\pi}_{\tilde{\alpha}_j}^{n,e}(\boldsymbol{\eta})$ associated with the temporal test nodes by solving the linear equations

$$\sum_{j=1}^{m_{eq}} \tilde{M}^j(\tilde{\xi}_k) \boldsymbol{\pi}_{\tilde{\alpha}_j}^{n,e}(\boldsymbol{\eta}) = \sum_{i=1}^{m_{en}} M^i(\tilde{\xi}_k) \boldsymbol{\pi}_{\alpha_i}^{n,e}(\boldsymbol{\eta}) \qquad (k = 1, \ldots, m_{eq}) \tag{5.5}$$

where the values $\tilde{\xi}_k$, $k = 1, \ldots, m_{eq}$, denote quadrature points. The Haar matrix $[\tilde{M}^j(\tilde{\xi}_k)]_{j,k=1}^{m_{eq}}$ is invertible, if the quadrature points are distinct (for a proof see Groß et al. [16] and Groß [35]). Hence, the exactly m_{eq} quadrature points, which are already recommended for obtaining a unique interpolation at the temporal test nodes, are important for the total angular momentum balance. Due to Equation (4.21), the first term on the righthand side of Equation (5.4) thus takes the form

$$h^n \int_{\mathscr{I}_\alpha} \int_{\mathscr{B}_\square} \{\rho_0^e(\boldsymbol{\eta})\, \epsilon_{abc}[\boldsymbol{\xi}_0]^a [\boldsymbol{v}_\alpha^{n,e}(\boldsymbol{\eta})]^c\}\, [\boldsymbol{v}_\alpha^{n,e}(\boldsymbol{\eta})]^b J_0^e(\boldsymbol{\eta}) \tag{5.6}$$

by taking the definition of the Lagrangian momentum field into account. According to the skew-symmetry of the permutation symbol, this term vanishes independent of the time step size. In order to employ Equation (4.24) in the second term of Equation (5.4), we determine nodal values $\boldsymbol{\varphi}_{\tilde{\alpha}_j}^{n,e}(\boldsymbol{\eta})$ associated with the temporal test nodes by a corresponding linear system of the form given in Equation (5.5). Then, the second term reads

$$-h^n \int_{\mathscr{I}_\alpha} \int_{\mathscr{B}_\square} [\boldsymbol{P}_\alpha^{*,n,e}(\boldsymbol{\eta})]_d{}^A \, \frac{\partial \left\{\delta^{dc}\, \epsilon_{abc}[\boldsymbol{\xi}_0]^a [\boldsymbol{\varphi}_\alpha^{n,e}(\boldsymbol{\eta})]^b\right\}}{\partial X^A}\, J_0^e(\boldsymbol{\eta}) \tag{5.7}$$

Since the vector $\boldsymbol{\xi}_0 \in \mathscr{A}$ is fixed in space, the partial derivative with respect to the point $\boldsymbol{X} \in \mathscr{B}_0$ is only related to the deformation $\boldsymbol{\varphi}_\alpha^{n,e}(\boldsymbol{\eta})$. Taking the definitions of the deformation gradient $\boldsymbol{F}_\alpha^{n,e}(\boldsymbol{\eta})$ and of the Kirchhoff stress tensor $\boldsymbol{\tau}_\alpha^{n,e}(\boldsymbol{\eta})$ into account, the second term of Equation (5.4) is given by

$$h^n \int_{\mathscr{I}_\alpha} \int_{\mathscr{B}_\square} \epsilon_{acb}[\boldsymbol{\xi}_0]^a [\boldsymbol{\tau}_\alpha^{n,e}(\boldsymbol{\eta})]^{cb} J_0^e(\boldsymbol{\eta}) \tag{5.8}$$

Accordingly, a symmetric approximation of the Kirchhoff stress tensor in conjunction with the skew-symmetry of the permutation symbol leads to the annihilation of the sums in Equation (5.8), independent of the time step size. Since both terms of Equation (5.4) vanish, we obtain total angular momentum conservation for any time step size.

Now, we consider the directional derivative of the approximated kinetic energy along the continuous time curve $\gamma_t^n(s) = \mathcal{T}(t+s)$ in the n-th time element. Time integration leads to

$$\int_{\mathscr{T}^n} \frac{\mathrm{d}}{\mathrm{d}s}\bigg|_{s=0} \mathcal{T}(t+s) = \sum_{e=1}^{n_{el}} \int_{\mathscr{I}_\alpha}\int_{\mathscr{B}_\square} [\mathring{\boldsymbol{\pi}}^{n,e}_{\alpha}(\boldsymbol{\eta})]_a \, [\boldsymbol{v}^{n,e}_{\alpha}(\boldsymbol{\eta})]^a J^e_0(\boldsymbol{\eta}) \tag{5.9}$$

After substituting Equation (4.4) and (4.8) for the velocity and the momentum, respectively, the time integration concerns only the temporal shape functions. The fundamental theorem of calculus is therefore fulfilled exactly by the m_{eq}-point Gaussian quadrature, and the left side of Equation (5.9) coincides with the difference $\mathcal{T}(t^{n+1}) - \mathcal{T}(t^n)$.

Since the derivative $\mathring{\boldsymbol{\pi}}^{n,e}_{\alpha}(\boldsymbol{\eta})$ is an admissible test function for Equation (4.21), the righthand side of Equation (5.9) takes the form

$$\frac{1}{h^n} \sum_{e=1}^{n_{el}} \int_{\mathscr{I}_\alpha}\int_{\mathscr{B}_\square} [\mathring{\boldsymbol{\pi}}^{n,e}_{\alpha}(\boldsymbol{\eta})]_a \, [\mathring{\boldsymbol{\varphi}}^{n,e}_{\alpha}(\boldsymbol{\eta})]^a J^e_0(\boldsymbol{\eta}) \tag{5.10}$$

Moreover, the derivative $\mathring{\boldsymbol{\varphi}}^{n,e}_{\alpha}(\boldsymbol{\eta})$ of the deformation approximation lies in the test space of Equation (4.24). Therefore, we are able to relate Equation (5.10) to this weak form. Since the fundamental theorem of calculus with respect to $\mathcal{T}(t)$ is satisfied, Equation (5.9) in conjunction with the weak equations of motion leads to the kinetic energy balance

$$\begin{aligned} \mathcal{T}(t^{n+1}) - \mathcal{T}(t^n) = {} & \sum_{e=1}^{n_{el}} \int_{\mathscr{I}_\alpha}\int_{\partial\mathscr{B}_\square} [\bar{\boldsymbol{t}}^{*,n,e}_{\alpha}(\overline{\eta})]_a \, [\mathring{\boldsymbol{\varphi}}^{n,e}_{\alpha}(\overline{\eta})]^a \bar{J}^e_0(\overline{\eta}) - \\ & - \sum_{e=1}^{n_{el}} \int_{\mathscr{I}_\alpha}\int_{\mathscr{B}_\square} [\boldsymbol{P}^{*,n,e}_{\alpha}(\boldsymbol{\eta})]_a{}^A \, [\mathring{\boldsymbol{F}}^{n,e}_{\alpha}(\boldsymbol{\eta})]^a{}_A J^e_0(\boldsymbol{\eta}) \end{aligned} \tag{5.11}$$

Considering again a conservative Piola-Kirchhoff traction vector, the first term on the righthand side of Equation (5.11) can be expressed by the Frèchet derivative of the density function $V^{\mathrm{ext}}(\boldsymbol{u}^{n,e}_{\alpha}(\overline{\eta}))$. In order to fulfil the corresponding fundamental theorem of calculus, the Piola-Kirchhoff traction vector has to be at most linear in the displacement $\boldsymbol{u}^{n,e}_{\alpha}(\overline{\eta})$, as the Lagrangian deformation velocity in Equation (5.9). If this condition is satisfied, the first term reads

$$-\mathcal{U}^{\mathrm{ext}}(t^{n+1}) + \mathcal{U}^{\mathrm{ext}}(t^{n}) = \sum_{e=1}^{n_{el}} \int_{\mathscr{I}_\alpha} \int_{\partial \mathscr{B}_\square} [\bar{\boldsymbol{t}}_\alpha^{*,n,e}(\overline{\eta})]_a \, [\mathring{\boldsymbol{\varphi}}_\alpha^{n,e}(\overline{\eta})]^a \, \bar{J}_0^e(\overline{\eta}) \tag{5.12}$$

Now, we determine the directional derivative of the relative internal energy along a continuous time curve $\boldsymbol{\gamma}_t^n(s) = \hat{\mathcal{E}}(t+s)$ in the n-th time element. At the time integration of this derivative, we bear in mind the different quadrature rules in the discrete setting, which is indicted by the suffix c at the symbol $\mathscr{I}_\alpha$ of the time integral. Noticing the definitions of all the cotangent vectors pertaining to the free energy, we obtain the relation

$$\begin{aligned}\int_{\mathscr{I}_\alpha^c} \int_{\mathscr{B}_\square} \frac{\mathrm{d}}{\mathrm{d}s}\bigg|_{s=0} \hat{e}_{\alpha+s}^{n,e}(\boldsymbol{\eta}) \, J_0^e(\boldsymbol{\eta}) = \int_{\mathscr{I}_\alpha^\eta} \int_{\mathscr{B}_\square} \mathring{\eta}_\alpha^{n,e}(\boldsymbol{\eta}) \, \vartheta_\alpha^{n,e}(\boldsymbol{\eta}) \, J_0^e(\boldsymbol{\eta}) + \\ + \int_{\mathscr{I}_\alpha} \int_{\mathscr{B}_\square} \Big\{ [\boldsymbol{P}_\alpha^{*,n,e}(\boldsymbol{\eta})]_a{}^A \, [\mathring{\boldsymbol{F}}_\alpha^{n,e}(\boldsymbol{\eta})]^a{}_A - [\boldsymbol{\Upsilon}_\alpha^{n,e}(\boldsymbol{\eta})]^{AB} \, [\mathring{\boldsymbol{\Gamma}}_\alpha^{n,e}(\boldsymbol{\eta})]_{AB} \Big\} \, J_0^e(\boldsymbol{\eta})\end{aligned} \tag{5.13}$$

for all $(n, e) \in \mathscr{M}_{el} \times \mathscr{N}_{el}$. In this equation, the free energy depends on the mapping $\boldsymbol{C}_\alpha^n = [\boldsymbol{C}|_{\mathscr{T}^n} \circ \tau^n](\alpha)$, which designates the right Cauchy-Green tensor field during the n-th time element at any time point $\alpha \in \mathscr{I}_\alpha$ in the temporal parent domain. We approximate the time evolution of the corresponding right Cauchy-Green tensor $\boldsymbol{C}_\alpha^{n,e}(\boldsymbol{\eta})$, and the time evolution of the deformation gradient $\boldsymbol{F}_\alpha^{n,e}(\boldsymbol{\eta})$ pertaining to the e-th spatial element, such that

$$\boldsymbol{C}_\alpha^{n,e}(\boldsymbol{\eta}) = \sum_{i=1}^{m_{en}} M^i(\alpha) \, \boldsymbol{C}_{\alpha_i}^{n,e}(\boldsymbol{\eta}) \qquad \text{and} \qquad \boldsymbol{F}_\alpha^{n,e}(\boldsymbol{\eta}) = \sum_{i=1}^{m_{en}} M^i(\alpha) \, \boldsymbol{F}_{\alpha_i}^{n,e}(\boldsymbol{\eta}) \tag{5.14}$$

Note that with these independent time approximations, the time evolution of the stress power in Equation (2.45) does not exactly coincide with the time evolution of the stress power in Equation (2.46). The reason is that a dependence of the time evolution of the right Cauchy Green tensor from the time evolution of the deformation gradient is the assumption for the transformation of the second Piola-Kirchhoff tensor in Equation (2.46). However, after a numerical time integration, the distance of both stress powers lies in the order of the quadrature error. Since the stress power density, determined by the weak equations of motion, coincides with the stress power density in Equation (2.46), we use in the second equation of motion, the right Cauchy Green tensor only in the argument of the free energy. Further, through the linearity of the deformation gradient field in the deformation field, the time approximation of the deformation gradient can be traced back to the time approximation of the deformation.

The time integration of the directional derivative in Equation (5.13) is, in general, not computable exactly. Therefore, we have to enforce the fundamental theorem of calculus with respect to $\hat{e}_\alpha^{n,e}(\boldsymbol{\eta})$. Analogous to the construction of the jump term (3.17), we formulate a corresponding constraint, given by

$$\begin{aligned}\mathcal{G}_S(\hat{\boldsymbol{S}}_\alpha^{n,e}(\boldsymbol{\eta})) = \hat{e}_{\alpha_{men}}^{n,e}(\boldsymbol{\eta}) - \hat{e}_{\alpha_1}^{n,e}(\boldsymbol{\eta}) - \int_{\mathscr{I}_\alpha^c} \frac{\mathrm{d}}{\mathrm{d}s}\bigg|_{s=0} \hat{e}_{\alpha+s}^{n,e}(\boldsymbol{\eta}) \; - \\ - \int_{\mathscr{I}_\alpha} [\hat{\boldsymbol{S}}_\alpha^{n,e}(\boldsymbol{\eta})]^{BA} \, [\boldsymbol{R}_\alpha^{n,e}(\boldsymbol{\eta})]_{BA}\end{aligned} \tag{5.15}$$

where

$$[\boldsymbol{R}_\alpha^{n,e}(\boldsymbol{\eta})]_{BA} = [(\boldsymbol{F}_\alpha^{n,e}(\boldsymbol{\eta}))^T]_B{}^b \delta_{ba} [\mathring{\boldsymbol{F}}_\alpha^{n,e}(\boldsymbol{\eta})]^a{}_A \tag{5.16}$$

in analogy to the elastic deformation rate tensor defined in Equation (2.47). In this constraint, the stress power density is consciously formulated as in Equation (2.46), because, as just mentioned, that is the stress power determined by the weak equations of motion. Since we need a symmetric approximation of the Kirchhoff stress tensor for retaining total angular momentum conservation, we determine a trace tensor $\hat{\boldsymbol{S}}_\alpha^{n,e}(\boldsymbol{\eta})$ corresponding to the second Piola-Kirchhoff stress tensor. We also obtain an isoperimetrical minimisation problem associated with the Lagrange functional

$$\mathcal{F}_S(\hat{\boldsymbol{S}}_\alpha^{n,e}(\boldsymbol{\eta}), \lambda(\boldsymbol{\eta})) = \lambda(\boldsymbol{\eta}) \, \mathcal{G}_S(\hat{\boldsymbol{S}}_\alpha^{n,e}(\boldsymbol{\eta})) + \frac{1}{2} \int_{\mathscr{I}_\alpha} [\hat{\boldsymbol{S}}_\alpha^{*,n,e}(\boldsymbol{\eta})]_{AB} \, [\hat{\boldsymbol{S}}_\alpha^{n,e}(\boldsymbol{\eta})]^{AB} \tag{5.17}$$

where the star indicates the corresponding dual map (compare Mohr et al. [77], Bargmann [93] and Groß [35]). Applying the time approximation of the right Cauchy-Green tensor in Equation (5.14), the stress trace tensor coincides with

$\lambda(\boldsymbol{\eta})\,\mathring{\boldsymbol{C}}_{\alpha}^{*,n,e}(\boldsymbol{\eta})$. We obtain the Lagrange multiplier by employing this stress trace tensor in the vanishing Gâteaux derivative with respect to $\lambda(\boldsymbol{\eta})$. We arrive at the weak term

$$\boxed{-\int_{\mathscr{B}_{\square}} \frac{\mathcal{G}_S(\boldsymbol{O})}{\displaystyle\int_{\mathscr{I}_{\alpha}} [\mathring{\boldsymbol{C}}_{\alpha}^{*,n,e}(\boldsymbol{\eta})]^{BA}\,[\boldsymbol{R}_{\alpha}^{n,e}(\boldsymbol{\eta})]_{BA}} \int_{\mathscr{I}_{\alpha}} [\mathring{\boldsymbol{C}}_{\alpha}^{*,n,e}(\boldsymbol{\eta})]^{BA}\,[\delta\boldsymbol{R}_{\alpha}^{n,e}(\boldsymbol{\eta})]_{BA} J_0^e(\boldsymbol{\eta})} \tag{5.18}$$

where

$$[\delta\boldsymbol{R}_{\alpha}^{n,e}(\boldsymbol{\eta})]_{BA} = [(\boldsymbol{F}_{\alpha}^{n,e}(\boldsymbol{\eta}))^T]_B{}^b \delta_{ba} [\partial_X(\delta\mathring{\boldsymbol{\varphi}}_{\tilde{\alpha}}^{n,e}(\boldsymbol{\eta}))]^a{}_A \tag{5.19}$$

and $\boldsymbol{O}$ denotes the matrix corresponding to the zero element in the linear space $\mathbb{L}(\mathscr{A}^*, \mathscr{A})$. We add the weak term (5.18) on the righthand side of Equation (4.24). This additional term in Equation (4.24) annihilates the stress power in Equation (5.11) independent of the quadrature rule, and introduces the relative internal energy density behind the jump. We obtain the kinetic energy balance

$$\begin{aligned} \mathcal{V}(t^{n+1}) - \mathcal{T}(t^n) - \mathcal{U}^{\text{ext}}(t^n) = \sum_{e=1}^{n_{el}} \int_{\mathscr{B}_{\square}} \left\{ \hat{e}_{\alpha_1}^{n,e}(\boldsymbol{\eta}) + \int_{\mathscr{I}_{\alpha}^{\eta}} \mathring{\eta}_{\alpha}^{n,e}(\boldsymbol{\eta})\, \vartheta_{\alpha}^{n,e}(\boldsymbol{\eta}) \right\} J_0^e(\eta) - \\ - \sum_{e=1}^{n_{el}} \int_{\mathscr{I}_{\alpha}} \int_{\mathscr{B}_{\square}} [\boldsymbol{\Upsilon}_{\alpha}^{n,e}(\boldsymbol{\eta})]^{AB}\, [\mathring{\boldsymbol{\Gamma}}_{\alpha}^{n,e}(\boldsymbol{\eta})]_{AB}\, J_0^e(\boldsymbol{\eta}) \end{aligned} \tag{5.20}$$

Recall that we arrive at the stability estimate (2.118) by the assumption that the time integrals of the internal dissipation in Equation (3.19) and (3.22) are identical. In the discrete setting, however, we have to enforce this property owing to the different quadrature rules. Consequently, we formulate a constraint for a viscosity trace tensor in Equation (3.19), given by

$$\begin{aligned} \mathcal{G}_V(\hat{\mathbb{V}}_{\alpha}^{n,e}(\boldsymbol{\eta})) = \int_{\mathscr{I}_{\alpha}} D_{\alpha}^{\text{int},n,e}(\boldsymbol{\eta}) - \int_{\mathscr{I}_{\alpha}^{\eta}} D_{\alpha}^{\text{int},n,e}(\boldsymbol{\eta}) - \\ - \int_{\mathscr{I}_{\alpha}^{\eta}} \frac{\vartheta_{\alpha}^{n,e}}{\Theta_{\alpha}^{n,e}} [\boldsymbol{L}_{\alpha}^{n,e}(\boldsymbol{\eta})]^A{}_C\, [\hat{\mathbb{V}}_{\alpha}^{n,e}(\boldsymbol{\eta})]_A{}^C{}_D{}^F\, [\boldsymbol{L}_{\alpha}^{n,e}(\boldsymbol{\eta})]^D{}_F \end{aligned} \tag{5.21}$$

where the approximated viscous deformation rate tensor (4.15) on the e-th spatial element during the n-th time interval already includes the reciprocal time step size arising from the finite element transformation (4.2). We search for a viscosity trace tensor minimising the augmented Lagrange functional

$$\mathcal{F}_V(\hat{\mathbb{V}}^{n,e}_\alpha(\boldsymbol{\eta}), \lambda(\boldsymbol{\eta})) = \lambda(\boldsymbol{\eta})\, \mathcal{G}_V(\hat{\mathbb{V}}^{n,e}_\alpha(\boldsymbol{\eta})) + \frac{1}{2}\int_{\mathscr{I}^\eta_\alpha} [\hat{\mathbb{V}}^{*,n,e}_\alpha(\boldsymbol{\eta})]^A{}_C{}^D{}_F [\hat{\mathbb{V}}^{n,e}_\alpha(\boldsymbol{\eta})]_A{}^C{}_D{}^F \tag{5.22}$$

where the star denotes the corresponding dual mapping. The viscosity trace tensor arises from a vanishing Gâteaux derivative associated with a viscosity curve. Then, we employ the viscosity trace tensor in the vanishing Gâteaux derivative with respect to the Lagrange multiplier. By introducing this viscosity trace tensor in Equation (2.83), we arrive at the integral

$$\boxed{h^n \int_{\mathscr{B}_\square} \frac{\displaystyle\int_{\mathscr{I}_\alpha} D^{\mathrm{int},n,e}_\alpha(\boldsymbol{\eta}) - \int_{\mathscr{I}^\eta_\alpha} D^{\mathrm{int},n,e}_\alpha(\boldsymbol{\eta})}{\displaystyle\int_{\mathscr{I}^\eta_\alpha} \left\{ \frac{\vartheta^{n,e}_\alpha(\boldsymbol{\eta})}{\Theta^{n,e}_\alpha(\boldsymbol{\eta})} \|\boldsymbol{L}^{n,e}_\alpha(\boldsymbol{\eta})\|^2 \right\}^2} \int_{\mathscr{I}^\eta_\alpha} \frac{\delta\Theta^{n,e}_\alpha(\boldsymbol{\eta})}{\vartheta^{n,e}_\alpha(\boldsymbol{\eta})} \left\{ \frac{\vartheta^{n,e}_\alpha(\boldsymbol{\eta})}{\Theta^{n,e}_\alpha(\boldsymbol{\eta})} \|\boldsymbol{L}^{n,e}_\alpha(\boldsymbol{\eta})\|^2 \right\}^2 J^e_0(\boldsymbol{\eta})} \tag{5.23}$$

This weak term is added on the righthand side of Equation (4.27). After employing the relative temperature field as admissible test function in the now supplemented Equation (4.27), we get at the balance equation

$$\begin{aligned} \int_{\mathscr{B}_\square} \left\{ \hat{e}^{n,e}_{\alpha_1}(\boldsymbol{\eta}) + \int_{\mathscr{I}^\eta_\alpha} \mathring{\eta}^{n,e}_\alpha(\boldsymbol{\eta})\, \vartheta^{n,e}_\alpha(\boldsymbol{\eta}) \right\} J^e_0(\boldsymbol{\eta}) = \int_{\mathscr{B}_\square} \hat{e}^e_{t_n}(\boldsymbol{\eta})\, J^e_0(\boldsymbol{\eta}) - \\ -h^n \int_{\mathscr{I}^\eta_\alpha} \int_{\mathscr{B}_\square} \frac{\Theta_\infty}{\Theta^{n,e}_\alpha(\boldsymbol{\eta})}\, D^{\mathrm{tot},n,e}_\alpha(\boldsymbol{\eta})\, J^e_0(\boldsymbol{\eta}) + h^n \int_{\mathscr{B}_\square} \int_{\mathscr{I}_\alpha} D^{\mathrm{int},n,e}_\alpha(\boldsymbol{\eta})\, J^e_0(\boldsymbol{\eta}) \end{aligned} \tag{5.24}$$

of the relative internal energy pertaining to the e-th space element, wherein the energy density $\hat{e}^e_{t_n}(\boldsymbol{\eta})$ denotes the element energy at the initial time of the n-th time element, and $D^{\mathrm{tot},n,e}_\alpha(\boldsymbol{\eta})$ denotes the total dissipation in the e-th spatial element at any time point $\alpha \in \mathscr{I}_\alpha$. A comparison with the kinetic energy balance (5.20) leads to the balance equation

$$\begin{aligned}\mathcal{V}(t^{n+1}) - \mathcal{V}(t^n) = -h^n \sum_{e=1}^{n_{el}} \int_{\mathscr{I}_\alpha^n} \int_{\mathscr{B}_\square} \frac{\Theta_\infty}{\Theta_\alpha^{n,e}(\boldsymbol{\eta})}\, D_\alpha^{\mathrm{tot},n,e}(\boldsymbol{\eta})\, J_0^e(\boldsymbol{\eta}) + \\ + \sum_{e=1}^{n_{el}} \int_{\mathscr{B}_\square} \int_{\mathscr{I}_\alpha} \Big\{ h^n\, D_\alpha^{\mathrm{int},n,e}(\boldsymbol{\eta}) - [\,\boldsymbol{\Upsilon}_\alpha^{n,e}(\boldsymbol{\eta})]^{AB}\, [\mathring{\boldsymbol{\Gamma}}_\alpha^{n,e}(\boldsymbol{\eta})]_{AB} \Big\} J_0^e(\boldsymbol{\eta})\end{aligned} \tag{5.25}$$

pertaining to the Lyapunov-like function.

Due to the finite element approximation of the spatially weak forms, we solve the temporally weak internal variable evolution in Equation (4.33) at the considered points $\boldsymbol{\eta} \in \mathscr{B}_\square$ in the spatial parent domain. We employ the time derivative $\mathring{\boldsymbol{\Gamma}}_\alpha^n(\boldsymbol{\eta})$ as admissible test function, and obtain the relation

$$\begin{aligned}\int_{\mathscr{I}_\alpha} [\,\boldsymbol{\Upsilon}_\alpha^{n,e}(\boldsymbol{\eta})]^{AD}\, [\mathring{\boldsymbol{\Gamma}}_\alpha^{n,e}(\boldsymbol{\eta})]_{AD} = -\int_{\mathscr{I}_\alpha} \frac{V_{\mathrm{dev}}}{2\, h^n}\, [\overset{\circ}{\overline{\{\boldsymbol{\Gamma}_\alpha^{n,e}(\boldsymbol{\eta})\}^{-1}}}]^{AD}\, [\mathring{\boldsymbol{\Gamma}}_\alpha^{n,e}(\boldsymbol{\eta})]_{AD} + \\ + \int_{\mathscr{I}_\alpha} \left(V_{\mathrm{vol}} - \frac{2\, V_{\mathrm{dev}}}{n_{\mathrm{dim}}} \right) \{\mathrm{tr}(\boldsymbol{L}_\alpha^{n,e})(\boldsymbol{\eta})\}^2\end{aligned} \tag{5.26}$$

According to Equation (2.83), the integrand on the righthand side of Equation (5.26) coincides with the internal dissipation $h_n\, D_\alpha^{\mathrm{int},n,e}(\boldsymbol{\eta})$ in the e-th spatial element during the n-th time element. Therefore, the last sum on the righthand side of Equation (5.25) vanishes, and we arrive at the stability estimate

$$\boxed{\mathcal{V}(t^{n+1}) - \mathcal{V}(t^n) = -h^n \sum_{e=1}^{n_{el}} \int_{\mathscr{I}_\alpha^n} \int_{\mathscr{B}_\square} \frac{\Theta_\infty}{\Theta_\alpha^{n,e}(\boldsymbol{\eta})}\, D_\alpha^{\mathrm{tot},n,e}(\boldsymbol{\eta})\, J_0^e(\boldsymbol{\eta}) \leqslant 0} \tag{5.27}$$

which coincides with Equation (2.118). Recall that in the discrete setting, we apply the Gaussian quadrature rule. Hence, the existing time integrals associated with the temporal shape functions are calculated exactly, which is important for the conservation laws and for the kinetic energy and external energy balance as verified. The stability estimate (5.27) is fulfilled independent of the order of the temporal shape functions.

6. REPRESENTATIVE NUMERICAL SIMULATIONS

We now verify the characteristic properties of the finite element method. First, we show the consistency of the time approximations by verifying the expected order of accuracy in time. A time approximation to a quantity is m-th order accurate if the term $\mathcal{O}((h^n)^m)$ in the temporal Taylor expansion of the quantity is correctly reproduced. Hence, the order of accuracy of a finite element method in time follows from the quadrature rule with the lowest order of accuracy. In this work, this is the m_{eq}-point Gaussian quadrature rule in the equations of motion and the viscous evolution equation, which is $2m_{eq}$-th order accurate.

Second, we verify the predicted conservation laws and stability properties of the finite element method. For this purpose, we consider a free flying body with an uninsulated part on the boundary. We close this section with simulations subject to suspensions associated with dynamic traction and heat flux loads. Here, we show that external power is incorporated consistently with the energy balance equations.

6.1. Consistency of the inherently energy consistent method

We start by demonstrating the consistency of the non-standard right Cauchy-Green tensor approximation in time, given by Equation (5.14), to which is referred to as assumed strain approximation in time (see Betsch & Steinmann [66]). We verify the order of accuracy in time by means of the relative L_2-error of the primary variables. Further, we demonstrate the inherently energy consistency with this time approximation by determining the order of accuracy in time of the energy balance in Equation (5.27).

Recall that the finite element method without the additional terms (5.18) and (5.23) in the weak forms is inherently energy consistent, which means this method fulfills Equation (5.27) up to the accuracy of the used Gaussian quadrature rule. Hence, the expression

$$\mathcal{V}(t^{n+1}) - \mathcal{V}(t^n) + h^n \sum_{e=1}^{n_{el}} \sum_{l=1}^{m_{eq}+1} \int_{\mathscr{B}_\square} \frac{\Theta_\infty}{\Theta^{n,e}_{\hat{\alpha}_l}(\boldsymbol{\eta})} \, D^{\mathrm{tot},n,e}_{\hat{\alpha}_l}(\boldsymbol{\eta}) \, J_0^e(\boldsymbol{\eta}) \, w_{\hat{\alpha}_l} \tag{6.1}$$

is of order $\mathcal{O}((h^n)^{2\,m_{eq}+2})$, where $\hat{\alpha}_l$ denote the Gauss points in time and $w_{\hat{\alpha}_l}$ denote the corresponding quadrature weights.

The assumed strain approximation in time arises from a temporal approximation before an interpolation over spatial nodes is performed. We indicate the finite element method with this approximation by the shorthand notation mhG(m_{eq}) method, where the number m_{eq} coincide with the polynomial order of the shape functions M^i in the time finite elements. In contrast to the assumed strain approximation in time, the standard right Cauchy-Green tensor approximation is given by

$$[\boldsymbol{C}_\alpha^{n,e}(\boldsymbol{\eta})]_{AB} = [(\mathrm{D}\boldsymbol{\psi}_0^e(\boldsymbol{\eta}))^{-T}]_A{}^k\,[\boldsymbol{C}_\alpha^{n,e,\square}(\boldsymbol{\eta})]_{kl}\,[(\mathrm{D}\boldsymbol{\psi}_0^e)^{-1}(\boldsymbol{\eta})]^l{}_B \tag{6.2}$$

where

$$[\boldsymbol{C}_\alpha^{n,e,\square}(\boldsymbol{\eta})]_{kl} = [(\mathrm{D}\boldsymbol{\varphi}_\alpha^{n,e}(\boldsymbol{\eta}))^T]_k{}^a\delta_{ab}[\mathrm{D}\boldsymbol{\varphi}_\alpha^{n,e}(\boldsymbol{\eta})]^b{}_l \tag{6.3}$$

denotes the right Cauchy-Green tensor with respect to the spatial parent domain at any time point $\alpha \in \mathscr{I}_\alpha$ in the temporal parent domain. The Jacobian matrix $\mathrm{D}\boldsymbol{\varphi}_\alpha^{n,e}(\boldsymbol{\eta})$ follows from a spatial approximation of the deformation mapping $\boldsymbol{\varphi}_\alpha^{n,e}(\boldsymbol{\eta})$ at any time in the temporal parent domain analogous to Equation (4.17), and a subsequent temporal approximation of the trajectories ${}^a\boldsymbol{x}_\alpha^{n,e}$ pertaining to the spatial nodes as in Equation (4.4). We obtain the equation

$$\mathrm{D}\boldsymbol{\varphi}_\alpha^{n,e}(\boldsymbol{\eta}) = \sum_{i=1}^{m_{en}} \sum_{a\in\mathscr{N}_{en}^e\setminus\mathscr{N}_\varphi^e} \mathrm{D}N_a(\boldsymbol{\eta})\,M^i(\alpha)\,{}^a\boldsymbol{x}_{\alpha_i}^{n,e} + \sum_{b\in\mathscr{N}_\varphi^e} \mathrm{D}N_b(\boldsymbol{\eta})\,{}^b\boldsymbol{X}^e \tag{6.4}$$

which also results from the temporal approximation (4.4) and a subsequent spatial approximation (4.17) owing to the linearity in the space-time nodal values ${}^a\boldsymbol{x}_{\alpha_i}^{n,e}$ of the current configuration. Accordingly, the standard right Cauchy-Green tensor approximation arise from a spatial interpolation before a temporal interpolation is done, in contrast to the assumed strain approximation in time. We indicate the inherently energy consistent finite element method associated with the standard right Cauchy-Green tensor approximation by the shorthand notation hG(m_{eq}) method.

6.1.1. The finite element L_2-error. The order of accuracy in time coincides with the slope of the curves, resulting from plotting the local solution error against the corresponding time step size in double logarithmic scale. Therefore, we determine the relative L_2-error of the deformation field, the Lagrangian velocity field and the Lagrangian temperature field on a current configuration $\mathscr{B}_T$ at a fixed time T. In general, the relative L_2-error e_{φ_t} of a Lagrangian vector field $\boldsymbol{\varphi}_t : \mathscr{B}_0 \to \mathscr{B}_t$ at the time $t \in \mathscr{T}$ with reference to the vector field $\overline{\boldsymbol{\varphi}}_t : \mathscr{B}_0 \to \mathscr{B}_t$ is defined via the L_2-norm $\| \cdot \|_2$ by the expression

$$\boxed{e_{\varphi_t} = \frac{\|\boldsymbol{\varphi}_t - \overline{\boldsymbol{\varphi}}_t\|_2}{\|\overline{\boldsymbol{\varphi}}_t\|_2}} \tag{6.5}$$

The L_2-norm $\|\boldsymbol{\Phi}_t\|_2$ of any Lagrangian vector field $\boldsymbol{\Phi}_t : \mathscr{B}_0 \to \mathscr{B}_t$ at the time $t \in \mathscr{T}$ in the time interval of interest is a natural norm for Lagrangian vector fields in infinite-dimensional vector spaces associated with weak forms (compare Gonzalez [165]). The definition reads

$$\|\boldsymbol{\Phi}_t\|_2 = \sqrt{\int_{\mathscr{B}_0} [\boldsymbol{\Phi}_t(\boldsymbol{X})]^c \, \delta_{cd} \, [\boldsymbol{\Phi}_t(\boldsymbol{X})]^d} \tag{6.6}$$

Since we use a spatial finite element approximation of a Lagrangian field in analogy to Equation (4.17), the spatial integration is concerned only with the spatial Lagrangian shape functions $N_a(\boldsymbol{\eta})$, included in the area element matrix blocks

$$\mathsf{H}^e_{ab} = \int_{\mathscr{B}_\square} N_a(\boldsymbol{\eta}) \, N_b(\boldsymbol{\eta}) \, J^e_0(\boldsymbol{\eta}) \qquad\qquad a, b \in \mathscr{N}^e_{en} \tag{6.7}$$

Hence, the L_2-norm of the Lagrangian vector field $\boldsymbol{\Phi}_t$ is reduced to a weighted Euclidean norm of the corresponding spatial nodal values ${}^a\boldsymbol{z}^e_t$. We arrive at the L_2-norm of the spatial finite element approximation pertaining to the Lagrangian vector field $\boldsymbol{\Phi}_t : \mathscr{B}_0 \to \mathscr{B}_t$ by the summation

$$\|\boldsymbol{\Phi}_t\|_2 = \sqrt{\sum_{e \in \mathscr{N}_{el}} \sum_{a,b \in \mathscr{N}^e_{en}} [{}^a\boldsymbol{z}^{*,e}_t]_c \, (\mathsf{H}^e_{ab} [\boldsymbol{I}]^c{}_d) \, [{}^a\boldsymbol{z}^e_t]^d} \tag{6.8}$$

The sums over the element nodes can be expressed by matrix products after combining the spatial element nodes in element vectors z^e and $\mathsf{z}^{*,e}$, respectively, and the area element matrix blocks in an area element matrix H^e. The parenthesis in Equation (6.8) then coincides with the Kronecker product of the area element matrix H^e and the identity matrix $\boldsymbol{I}$ of column vectors in the ambient space. We obtain

$$\|\boldsymbol{\Phi}_t\|_2 = \left(\mathop{\mathsf{A}}_{e \in \mathscr{N}_{el}} \mathsf{z}_t^{*,e} \left[\mathsf{H}^e \otimes \boldsymbol{I} \right] \mathsf{z}_t \right)^{1/2} \tag{6.9}$$

We transform this local matrix form on each element $e \in \mathscr{N}_{el}$ into a global matrix form for the entire body by assembling all spatial element matrices to global matrices. We obtain a global nodal column vector z_t and a global nodal row vector z_t^*. Finally, a global area matrix H occurs, such that the L_2-norm of the spatial approximated Lagrangian vector field $\boldsymbol{\Phi}_t$ is given by

$$\boxed{\|\boldsymbol{\Phi}_t\|_2 = \sqrt{\mathsf{z}_t^* \left[\mathsf{H} \otimes \boldsymbol{I} \right] \mathsf{z}_t}} \tag{6.10}$$

The L_2-norm of a Lagrangian scalar field $\theta_t : \mathscr{B}_0 \to \mathbb{R}$ as the Lagrangian temperature field can be calculated analogously, except that the Kronecker product with the identity matrix $\boldsymbol{I}$ has to be dropped.

6.1.2. The numerical example. We compare the order of accuracy pertaining to the hG(m_{eq}) and the mhG(m_{eq}) method by means of the following numerical example: A small polymeric plate consisting of the Neo-Hookean material described in Appendix C, with the edge length 0.1 m and the density ρ_0 of $8.93\,\mathrm{kg/m^2}$. The Lamé constants in the free energy function are given by $\mu = 7.5\,\mathrm{J/m^2}$ and $\lambda = 30\,\mathrm{J/m^2}$, respectively. In the thermal part of the free energy, the thermal expansion coefficient of the material is set to $\beta = 10^{-4}\,\mathrm{K^{-1}}$ and the specific heat capacity of the body amounts to $c = 100\,\mathrm{J/m^2K}$. In the heat conduction term of the entropy evolution, the constant specific thermal conductivity is chosen to be $k_0 = 10\,\mathrm{W/K}$. The deviatoric and volumetric viscosity is set to $V_{\text{dev}} = 10000\,\mathrm{Js/m^2}$ and $V_{\text{vol}} = 50000\,\mathrm{Js/m^2}$, respectively. The temperature of the bottom of the plate coincides with the ambient temperature, however, the remainder of the body is heated about 10 K. The

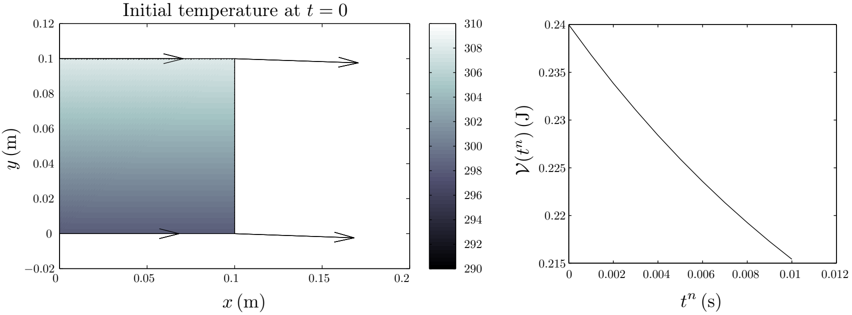

Figure 6.1. On the left, the reference configuration of a small polymeric plate, discretised by one four node Lagrange element, is depicted. The arrows shows the initial velocities of the nodes. The colour in the element indicates the interpolation of the initial temperature at the nodes in Kelvin. On the right, the relative total energy $\mathcal{V}(t)$, determined with quartic finite elements in time ($m_{eq} = 4$) and a time step size $h^n = 1\,\mathrm{ms}$, is plotted versus the time interval $\mathscr{T} = [0, 10\,\mathrm{ms}]$ of interest.

motion is initiated by an initial velocity field with the components

$$[\boldsymbol{v}_0(\boldsymbol{X})]^a = 2\,\frac{\mathrm{m}}{\mathrm{s}}\,\delta^{a1} - 0.7\,\frac{1}{\mathrm{s}}\,\delta^{ab}\epsilon_{b3c}[\boldsymbol{X}]^c \tag{6.11}$$

and is simulated during the time interval $\mathscr{T} = [0, T]$ with $T = 10\mathrm{ms}$ (see Figure 6.1). The plate is moving freely in a two-dimensional continuum with ambient temperature Θ_∞ of 298.15 K.

For this motion, we determine the L_2-error corresponding to the deformation field $\boldsymbol{\varphi}_T$, the velocity field $\boldsymbol{v}_T$ and the temperature field Θ_T at the final time T with reference to a calculation with quartic finite elements in time ($m_{eq} = 4$) and a time step size $h^n = 1\mathrm{ms}$. Since the deformation field and the velocity field is determined by a continuous Galerkin (cG) method with Gaussian quadrature of accuracy $\mathcal{O}((h^n)^{2\,m_{eq}})$, we obtain the accuracy orders 2, 4 and 6 (see Figure 6.2). With these approximated fields, we calculate a temperature field approximation of the same order of accuracy. However, the discrete energy balance in Equation (6.1) shows the accuracy $\mathcal{O}((h^n)^{2\,m_{eq}+1})$ of the quadrature rule in the entropy evolution equation with the orders 3, 5 and 7 (see Figure 6.3). A comparison of the curves in Figure 6.2 and Figure 6.3 shows the consistency of the assumed strain approximation given

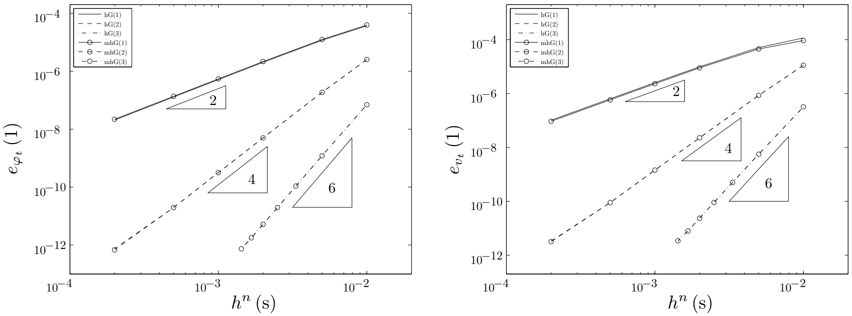

Figure 6.2. On the left, the relative L_2-errors of the deformation field $\boldsymbol{\varphi}_T$ at the final time $T = 10\,\mathrm{ms}$ is plotted versus the time step sizes h^n used for the calculations. On the right, the relative L_2-error of the corresponding velocity field $\boldsymbol{v}_T$ is depicted as function of the time step size. The reference solution is calculated with quartic finite elements in time ($m_{eq} = 4$) and a time step size $h^n = 1\,\mathrm{ms}$.

by Equation (5.14) in the considered time approximation. Neither the orders of accuracy of the time approximation nor the inherently energy consistency of the weak forms is violated.

6.2. Consistency of the exactly energy consistent method

The finite element method in this work is energy consistent by adding the additional terms (5.18) and (5.23) in the weak forms. We designate this enhanced finite element method by the shorthand notation ehG(m_{eq}) method. The number m_{eq} specify the polynomial order of the temporal shape functions for the primary variables. We verify the order of accuracy of the exactly energy consistent method by using a similar numerical example as in Section 6.1. We consider the free flight of a large polymeric plate with an edge length 1m during the time interval $\mathscr{T} = [0, T]$ of interest with a final time $T = 0.1$s. The motion is initiated by the initial velocity field given by Equation (6.11). The polymeric plate consists of the material specified in Section 6.1.

In Figure 6.4 to the left, the approximated initial velocity field is depicted by the velocities at the spatial nodes. We determine the relative L_2-error pertaining to the deformation field $\boldsymbol{\varphi}_T$, the Lagrangian velocity field $\boldsymbol{v}_T$ as well as the Lagrangian temperature field Θ_T in the current configuration at the final time T. The reference solution is determined by quartic finite elements

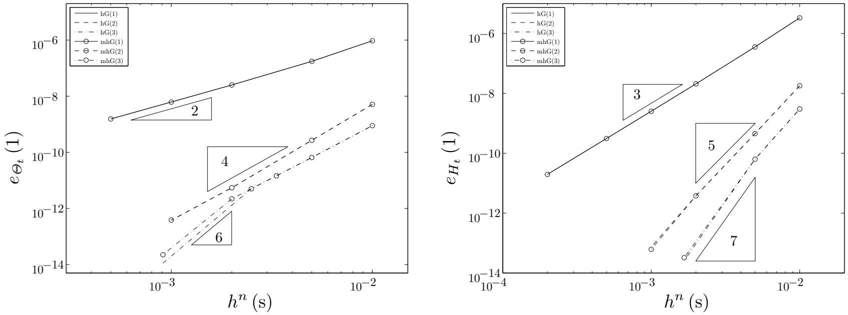

Figure 6.3. On the left, the relative L_2-error of the temperature field Θ_T at the final time $T = 10\,\mathrm{ms}$ is plotted as function of the time step size h^n, used for the calculation. On the right, the corresponding relative L_2-error of the energy balance in Equation (5.27) is depicted. The reference solution is calculated with quartic finite elements in time ($m_{eq} = 4$) and a time step size $h^n = 1\,\mathrm{ms}$.

in time ($m_{eq} = 4$) and a small time step size $h^n = 1\mathrm{ms}$. The right plot in Figure 6.4 shows the final configuration and the Lagrangian velocity field pertaining to the reference solution.

The left diagram in Figure 6.5 shows the associated relative total energy during the time interval of interest. The order of accuracy of the methods coincide with the slope of the curves in the L_2-error plots. Owing to the accuracy of the Gaussian quadrature rule in the equations of motion, we obtain the order $2m_{eq}$ of the time approximation. The L_2-error plot of the deformation field in Figure 6.5, as well as the error curves pertaining to the Lagrangian velocity and Lagrangian temperature field in Figure 6.6, corroborate this theoretical result.

6.3. Conservation laws and stability properties

In this section, we verify the robustness of the time integration algorithms with respect to large constant time step sizes throughout the calculation, as well as with respect to time step size changes. The spatial mesh is thereby hold fixed. Large time steps are desirable for effective long time simulations, and time step size changes appear in time-adaptive time stepping schemes, for instance. In order to verify the total linear and total angular momentum conservation, we consider a translational and rotational free motion of a continuum body

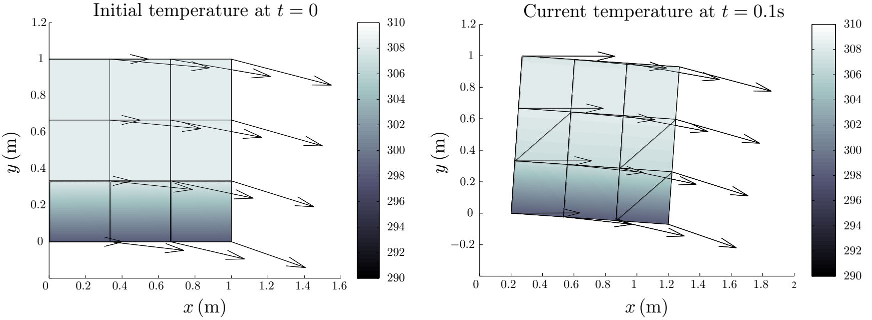

Figure 6.4. On the left, the reference configuration of the polymeric plate, discretised by nine four node Lagrange elements, is depicted. The arrows show the initial velocities of the nodes, and the colour in the spatial elements indicates the interpolation of the temperature at the corresponding element nodes in Kelvin. On the right, the current configuration of the plate at time $T = 100\,\mathrm{ms}$, determined with quartic finite elements in time ($m_{eq} = 4$) and a time step size $h^n = 1\,\mathrm{ms}$, is shown.

without mechanical loads. We are able to verify also the stability estimate in Equation (5.27), because we neglect thermal loads.

6.3.1. The numerical example. We consider a free flying ring, consisting of the Neo-Hookean material described in Appendix C. The inner radius of the ring is $R_i = 0.5\,\mathrm{m}$ and the outer radius is given by $R_a = 1.5\,\mathrm{m}$. We orientate the material properties to a polyurethane elastomer. The density ρ_0 of the material is $30\,\mathrm{kg/m^2}$, and the first and second Lamé constant in the Neo-Hookean free energy function is chosen to be $\mu = 7500\,\mathrm{J/m^2}$ and $\lambda = 30000\,\mathrm{J/m^2}$, respectively. The thermal expansion coefficient of the material is set to $\beta = 10^{-4}\,\mathrm{K}^{-1}$ and the specific heat capacity of the ring amounts to $c = 1500\,\mathrm{J/m^2K}$. The heat conduction in the ring is determined by the constant specific thermal conductivity $k_0 = 0.02\,\mathrm{W/K}$. The deviatoric viscosity is set to $V_{\mathrm{dev}} = 10000\,\mathrm{Js/m^2}$ and the volumetric viscosity amounts to $V_{\mathrm{vol}} = 50000\,\mathrm{Js/m^2}$. The motion is initiated by an initial velocity field with components given by

$$[\boldsymbol{v}_0(\boldsymbol{X})]^a = 20\,\frac{\mathrm{m}}{\mathrm{s}}\,\delta^{a1} - 7\,\frac{1}{\mathrm{s}}\,\delta^{ab}\epsilon_{b3c}[\boldsymbol{X}]^c \tag{6.12}$$

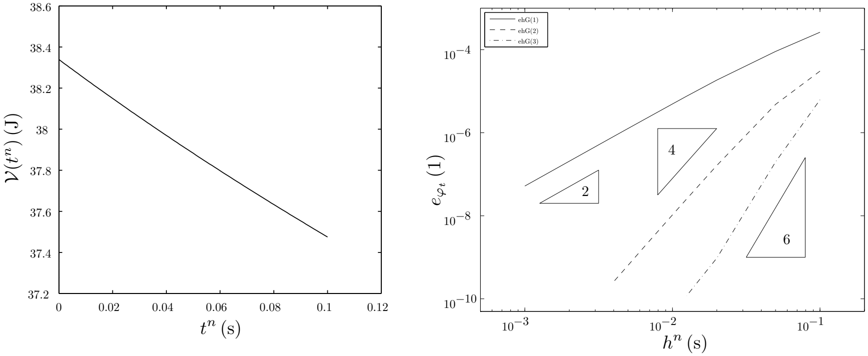

Figure 6.5. On the left, the relative total energy $\mathcal{V}(t)$ of the reference solution, determined by quartic finite elements in time ($m_{eq} = 4$) and a time step size $h^n = 1\,\mathrm{ms}$, is plotted versus the time interval $\mathscr{T} = [0, 0.1\,\mathrm{s}]$ of interest. On the right, the relative L_2-errors of the deformation field $\boldsymbol{\varphi}_T$ at the final time $T = 0.1\,\mathrm{s}$ is depicted as function of the time step size.

The temperature Θ_∞ in the ambient space of the two-dimensional continuum body amounts 298.15 K. The temperature at a small portion of the outer side of the ring coincides with the ambient temperature, which means this is the only uninsulated part of the ring. However, the remainder of the ring is heated about 10K.

6.3.2. The heat flux projection. Arising from the uninsulated part of the ring, a Lagrangian temperature gradient field acts on the reference configuration from the outset. According to Equation (2.64), we obtain on $\mathscr{B}_0$ a Lagrangian heat flux at any time $t \in \mathscr{T}$ with the components

$$[\boldsymbol{Q}_t(\boldsymbol{X})]^A = -k_0\, J_t(\boldsymbol{X})\, [(\boldsymbol{C}_t(\boldsymbol{X}))^{-1}]^{AB} [\mathrm{D}\,\Theta_t(\boldsymbol{X})]_B \tag{6.13}$$

in each point $\boldsymbol{X} \in \mathscr{B}_0$. After performing the spatial finite element approximation, the Lagrangian heat flux is given at the spatial Gauss points of the entropy evolution equation. In order to depict the Lagrangian heat flux on the ring as smooth vector field by vector arrows at the nodes, we project all element heat fluxes $\boldsymbol{Q}_t^e(\boldsymbol{\eta})$ at the spatial Gauss points onto the corresponding spatial element nodes by using a global least square minimisation with the

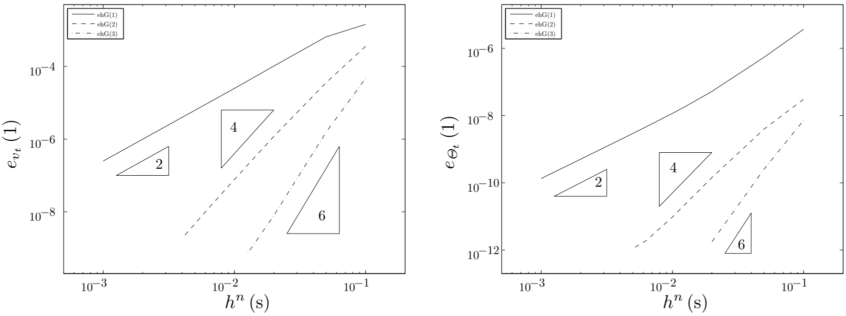

Figure 6.6. On the left, the relative L_2-errors of the Lagrangian velocity field $\boldsymbol{v}_T$ at the final time $T = 0.1\,\mathrm{s}$ is plotted versus the corresponding time step sizes used for the calculations. The right diagram shows the relative L_2-error pertaining to the Lagrangian temperature field Θ_T as function of the time step size. The reference solution is calculated with quartic finite elements in time ($m_{eq} = 4$) and a time step size $h^n = 1\,\mathrm{ms}$.

Lagrange functional

$$\mathcal{F}_Q(\widehat{\boldsymbol{Q}}_t) = \frac{1}{2}\sum_{e\in\mathscr{N}_{el}}\int_{\mathscr{B}_\square}\left[[\overset{e}{\widehat{\boldsymbol{Q}}}_t(\boldsymbol{\eta})]^A - [\boldsymbol{Q}^e_t(\boldsymbol{\eta})]^A\right]\left[[\overset{*,e}{\widehat{\boldsymbol{Q}}}_t(\boldsymbol{\eta})]_B - [\boldsymbol{Q}^{*,e}_t(\boldsymbol{\eta})]_B\right] J^e_0(\boldsymbol{\eta}) \tag{6.14}$$

where $\overset{e}{\widehat{\boldsymbol{Q}}}_t(\boldsymbol{\eta})$ denotes the projected element heat flux, interpolating nodal vectors ${}^a\overset{e}{\widehat{\boldsymbol{Q}}}_t$ over the entire finite element $e \in \mathscr{N}_{el}$. This procedure is entered into the literature as patch recovery technique (see Denzer et al. [166] and Zienkiewicz & Zhu [167] for more details). We interpolate the element heat flux just as the primary variables, which means

$$[\overset{e}{\widehat{\boldsymbol{Q}}}_t(\boldsymbol{\eta})]^A = \sum_{a\in\mathscr{N}^e_{en}} N_a(\boldsymbol{\eta})\,[{}^a\overset{e}{\widehat{\boldsymbol{Q}}}_t]^A \tag{6.15}$$

Applying in Equation (6.14) the directional derivative to the unknown projected element heat flux $\overset{e}{\widehat{\boldsymbol{Q}}}_t(\boldsymbol{\eta})$ in direction of a variation $\delta\overset{e}{\widehat{\boldsymbol{Q}}}_t(\boldsymbol{\eta})$ of the projected element heat flux, the corresponding weak Euler-Lagrange equations take the form

$$\sum_{e\in\mathscr{N}_{el}} \sum_{a,b\in\mathscr{N}_{en}^e} [{}^b\delta\widehat{\boldsymbol{Q}}_t^{*,e}]_A \left(\mathsf{H}_{ba}^e [\boldsymbol{I}]^A{}_B\right) [{}^a\widehat{\boldsymbol{Q}}_t^e]^B = \sum_{e\in\mathscr{N}_{el}} \sum_{b\in\mathscr{N}_{en}^e} [{}^b\delta\widehat{\boldsymbol{Q}}_t^{*,e}]_A \, [{}_b\widetilde{\boldsymbol{Q}}_t^e]^A \tag{6.16}$$

where the variation of the projected element heat flux is approximated as the projected element heat flux itself. Since, on the left hand side, the spatial integration is concerned only with the spatial Lagrangian shape functions, we also obtain the area element matrix blocks in Equation (6.7). On the right hand side, the shorthand notation

$$[{}_b\widetilde{\boldsymbol{Q}}_t^e]^A = \int_{\mathscr{B}_\square} N_b(\boldsymbol{\eta})\,[\boldsymbol{Q}_t^e(\boldsymbol{\eta})]^A \tag{6.17}$$

denotes the assignment of the element heat flux to any spatial element node $b \in \mathscr{N}_{en}^e$. As next step, we substitute matrix products for the distinct summations. We start with the summation over the tensor components. Then, we express the summation over the element nodes by a matrix product of block matrices. In this way, we arrive at the discrete weak forms

$$\delta\widehat{\mathbf{Q}}_t^{*,e}\left[(\mathbf{H}^e \otimes \boldsymbol{I})\,\widehat{\mathbf{Q}}_t^e - \widetilde{\mathbf{Q}}_t^e\right] = 0 \tag{6.18}$$

for each spatial element $e \in \mathscr{N}_{el}$. After the assembling procedure, we obtain a column vector $\widehat{\mathbf{Q}}_t$ and a row vector $\delta\widehat{\mathbf{Q}}_t^*$, including the projected heat flux and its variations, respectively, at the spatial nodes of the reference configuration. The element heat fluxes $\widetilde{\mathbf{Q}}_t^e$ leads to a global column vector $\widetilde{\mathbf{Q}}_t$, and the area element matrices coalesce to the global area matrix $\mathbf{H}$ of the ring. According to the fundamental lemma of calculus of variations, we obtain a linear algebraic system

$$\boxed{(\mathbf{H} \otimes \boldsymbol{I})\,\widehat{\mathbf{Q}}_t = \widetilde{\mathbf{Q}}_t} \tag{6.19}$$

which we solve for the unknown nodal heat fluxes by using the Gaussian elimination method. Among the projected Lagrangian heat flux at initial time $t = 0$, this projection allows to show the Lagrangian heat flux in the reference configuration of the ring at each temporal Gauss point of the entropy evolution equation in the considered sub-interval $\mathscr{T}^n$.

6.3.3. The second order tensor field projection. Similarly, we depict the norm of any Lagrangian second order tensor field, given at the points $\boldsymbol{X} \in \mathscr{B}_0$, by means of colours in the reference or current configuration, respectively. For example, we illustrate the first Piola-Kirchhoff stress tensor field $\boldsymbol{P}_t$ by colours in the reference configuration. Since the finite element method furnishes a Lagrangian stress field locally at spatial Gauss points, we project all these tensors onto the corresponding spatial element nodes also by a global least square minimisation.

As first step, we transform the considered second order tensor field at each point $\boldsymbol{X} \in \mathscr{B}_0$ in a column vector. For the first Piola-Kirchhoff stress tensor $\boldsymbol{P}_t(\boldsymbol{X})$ in the case of a two-dimensional ambient space, we obtain

$$\mathsf{P}_t(\boldsymbol{X}) = \big[[\boldsymbol{P}_t(\boldsymbol{X})]^{11}, [\boldsymbol{P}_t(\boldsymbol{X})]^{21}, [\boldsymbol{P}_t(\boldsymbol{X})]^{12}, [\boldsymbol{P}_t(\boldsymbol{X})]^{22}\big] \tag{6.20}$$

Then, we perform the corresponding global least square minimisation of the spatial finite element approximation as for the heat flux projection. We substitute matrix products for each summation and assemble the discrete weak forms. After applying the fundamental lemma of calculus of variations, we arrive at the linear algebraic system

$$\boxed{[(\mathsf{H} \otimes \boldsymbol{I}) \otimes \boldsymbol{I}]\, \widehat{\mathsf{P}}_t = \widetilde{\mathsf{P}}_t} \tag{6.21}$$

where the global column vectors $\widehat{\mathsf{P}}_t$ and $\widetilde{\mathsf{P}}_t$ includes the unknown values of the tensor components at the spatial nodes, and the spatially averaged tensor components defined on the element level analogous to Equation (6.17), respectively.

In order to depict the projected tensor field by colours in the element, we determine a norm of the tensor field. However, we first split up the tensor field additively in a spherical part and a deviatoric part, because a temperature change only leads to a volume change. We show the spectral norm $|||\cdot|||$ of the nodal tensors

$$\operatorname{sph}({}^{A}\widetilde{\boldsymbol{P}}_t) = \frac{\operatorname{tr}({}^{A}\widetilde{\boldsymbol{P}}_t)}{n_{\mathrm{dim}}}\,\boldsymbol{I} \qquad \text{and} \qquad \operatorname{dev}({}^{A}\widetilde{\boldsymbol{P}}_t) = {}^{A}\widetilde{\boldsymbol{P}}_t - \operatorname{sph}({}^{A}\widetilde{\boldsymbol{P}}_t) \tag{6.22}$$

in the global numbering $\boldsymbol{A} \in \mathscr{N}_{no}$ as colours in the finite elements. In the case of the spherical part, the spectral norm simply coincides with the trace divided by the space dimension. By using this projection, we show projected second order tensor fields of the ring at the initial time $t_0 = 0$ as well as at each temporal Gauss point of the second equation of motion in the considered sub-interval $\mathscr{T}^n$.

6.3.4. The inherently energy consistent method. We start the stability investigation with the hG method, and use linear finite elements in time, for instance. We discretise the ring by 416 four-node Lagrange elements (see Hueck & Wriggers [168] for implementational aspects) and totally 448 spatial nodes. For simplicity, we use the same mesh for the mechanical as well as for the thermal Lagrangian fields. The time step size h^n is chosen to be 10 ms throughout the calculation. For the iterative solution procedure described in Appendix B, we prescribe the global tolerance $\mathsf{tol} = 10^{-6}\,\mathrm{J}$, and the local iteration is stopped if the tolerance tolevo is gone bellow $10^{-9}\ \mathrm{J/m^2}$. The initial configurations of the ring at time $t_0 = 0$ is shown in Figure 6.7. At initial time, the reference configuration to the right and its current configuration to the left coincide. In the reference configuration, the colour designates the spectral norm of the spherical part of the projected first Piola-Kirchhoff stress tensor, and the vector arrows depict the projected first Piola-Kirchhoff heat flux. The stress vanishes due to the assumed Neo-Hookean free energy. In the current configuration, the colour indicates the initial temperature 308.15 K of the ring. The vector arrows at the spatial nodes indicate the initial Lagrangian velocity field, which results from a superposition of a translation in horizontal direction and a rotation about the centre of mass (see Equation (6.12)). That implies the instantaneous centre of rotation at the lowest point of the ring. On the uninsulated part of the ring (see right side of the ring), the initial temperature is given by the ambient temperature Θ_∞ of 298.15 K. Hence, we obtain a temperature gradient field at the spatial nodes of the corresponding elements. In the reference configuration, a projected first Piola-Kirchhoff heat flux is the consequence of this temperature gradient field.

Figure 6.8 shows the current configurations pertaining to the first total rotation of the ring. Owing to the low heat conduction compared to the specific heat capacity of the ring, the small uninsulated portion gives rise to a slowly decreasing temperature level. This is observable in Figure 6.9, where time evolutions of the calculations are depicted. The time evolution of the primary unknowns pertain to a spatial node A at the outside of the ring opposite the uninsulated portion. The temperature oscillates around a decreasing level, till an abrupt temperature jump arise at time $t^n = 1.39\,\mathrm{s}$. At this time point, the global Newton-Raphson method is not gone bellow the prescribed tolerance tol. Further, we realise high-frequent oscillations in the time evolution of the temperature and the corresponding velocity, especially after the time $t^n = 1.39\,\mathrm{s}$. However, not in the time evolution of the corresponding position. We also see that the hG(1) method calculates a relative total energy, which oscillates around a decreasing energy level. The decreasing energy level is mainly based on the viscous dissipation, and these unphysical local energy rises are associated with a local increase of the non-negative viscous dissipation. However, an energy rise would mean a negative physical dissipation, which is not the case. Hence, the hG(1) method produce negative numerical dissipation. The time evolution of the relative total energy ends in a blow up behaviour at time $t^n = 1.47\,\mathrm{s}$, as the global Newton-Raphson method is not gone bellow the prescribed tolerance for the second time. Nevertheless, the total linear and total angular momentum is conserved in all time steps. This oscillating relative total energy is associated with an oscillating first Piola-Kirchhoff stress field, which is shown in Figure 6.10. We see the reference configurations of the time interval at the beginning of the motion, in which the total dissipation reaches the highest value. The colour denotes the spectral norm of the spherical part pertaining to the corresponding projected first Piola-Kirchhoff stress tensor. The stress reaches a maximum value at the inner radius and a minimum value at the outer radius. However, we obtain spurious radial stress waves at these time points at which the hG(1) method is diverged, which is shown in Figure 6.11. In the time step, where the energy additionally blows up (the plot to the left), there is observable a particularly high-frequent wave in front of the uninsulated portion on the righthand side of the ring. In this figure, we also depict the absolute value of four residual equations versus time. First, we observe the violation of the stability estimate in Equation (2.118). The reason is that on each time element the time integral of the directional derivative of the relative internal energy along a continuous time curve does not coincide exactly with the difference of the corresponding energies at the time nodes. Hence, relative total energy is produced and annihilated algorithmically, which leads to the oscillations in the time evolution of the relative total energy. Then, we show the time evolution pertaining to the absolute value of the global mechanical residual

$G_{\mathrm{mech}}(\mathscr{Z};\tilde{\mathsf{x}}^{*,n})$ in Appendix B. This residual equation coincides with the kinetic energy balance in Equation (5.11), which, in turn, is the time averaged balance of mechanical energy of the ring. Since the time integral of the kinetic energy rate is evaluated exactly by the applied Gaussian quadrature rule in time, the peaks in this time evolution probably arise from an interpolation error in the temporal quadrature of the associated dual pairing of the free energy. In the kinetic energy balance, the dual pairing denotes the stress power. That would explain why at the same time points peaks in the absolute value of the thermal residual $G_{\mathrm{ther}}(\mathscr{Z};\mathsf{u}^{*,n})$ appear. Because, in the thermal residual, there is also a dual pairing of the free energy involved, that is the dual pairing corresponding to the Lagrangian entropy field. The first four peaks in these time evolutions does not lead to a divergence according to the global convergence criterion in Equation (B.99). But the last two peaks correspond to the divergence at the time $t^n = 1.39\,\mathrm{s}$ and the blow up at time $t^n = 1.47\,\mathrm{s}$, respectively. In contrast, the time evolution of the spatially assembled and integrated residual equation

$$\left| \sum_{e=1}^{n_{el}} \int_{\mathscr{B}_\square} G_{\mathrm{visc}}(\mathscr{Z};\tilde{\tilde{\mathsf{i}}}^{*,n,e}(\boldsymbol{\eta}))\, J_0^e(\boldsymbol{\eta}) \right| = 0 \tag{6.23}$$

pertaining to the local mechanical residual are even of the order of the local tolerance tolevo, which is only claimed at each spatial Gauss point. Thus, the prescribed global tolerance tol lies between the convergence criterion and the sum of the absolute values of each Galerkin form, which is possible due to the triangle relation for the convergence criterion, given by

$$\begin{aligned} &\left| G_{\mathrm{ther}}(\mathscr{Z};\mathsf{u}^{*,n}) + G_{\mathrm{mech}}(\mathscr{Z};\tilde{\mathsf{x}}^{*,n}) - \sum_{e=1}^{n_{el}} \int_{\mathscr{B}_\square} G_{\mathrm{visc}}(\mathscr{Z};\tilde{\tilde{\mathsf{i}}}^{*,n,e}(\boldsymbol{\eta}))\, J_0^e(\boldsymbol{\eta}) \right| \leqslant \mathsf{tol} \leqslant \\ &\leqslant |\, G_{\mathrm{ther}}(\mathscr{Z};\mathsf{u}^{*,n}) \,| + |\, G_{\mathrm{mech}}(\mathscr{Z};\tilde{\mathsf{x}}^{*,n}) \,| + \left| \sum_{e=1}^{n_{el}} \int_{\mathscr{B}_\square} G_{\mathrm{visc}}(\mathscr{Z};\tilde{\tilde{\mathsf{i}}}^{*,n,e}(\boldsymbol{\eta}))\, J_0^e(\boldsymbol{\eta}) \right| \end{aligned} \tag{6.24}$$

The mentioned interpolation error in the temporal quadrature has different algebraic signs in the global mechanical and the thermal residual. Therefore, in the convergence criterion, this error does not appear. Referring to the global convergence criterion in Equation (B.99), we found that this criterion identifies unphysical numerical results as spurious stress waves, before the resulting blow up behaviour occurs.

The divergence of the hG(1) method appear to be associated with spurious stress waves at the time points of divergence. Therefore, we modify the approximation of the second Piola-Kirchhoff stress tensor by substituting the assumed strain approximation in Equation (5.14) for the standard right Cauchy-Green tensor approximation in Equation (6.2). We obtain the mhG method, which is now compared to the hG method. We also apply linear finite elements in time and bilinear finite elements in space, for instance. We consider the same motion with the same time step size h^n of $10\,\mathrm{ms}$ throughout the calculation. The first distinctive feature of the mhG(1) method in comparison to the hG(1) method is that the simulation runs over the time points $t^n = 1.39\,\mathrm{s}$ and $t^n = 1.47\,\mathrm{s}$, at which the hG(1) method is not converged. Ultimately, we stop the calculation at time $t^n = 5\,\mathrm{s}$, since the mhG(1) method calculates the initiated motion of the ring without numerical problems.

Looking at the time evolutions of the primary unknowns in Figure 6.12, we realise no major differences in comparison to the time evolutions of the hG(1) method before it diverged. However, we obtain a distinct behaviour in the time evolution of the relative total energy, because, in Figure 6.13, we see no further local energy rises. The relative total energy is steady decreasing with variable speed, and approaches asymptotically towards a constant value associated with a purely elastic behaviour of the material at ambient temperature. The speed of the energy decrease depends mainly on the dissipated internal energy $\mathcal{D}^{\mathrm{int},n}$ of the entire ring on each time element $\mathscr{T}^n$, which can be directly calculated by the weak form of the viscous evolution equation, according to the energy consistent approximation (see Equation (B.51)). Hence, we obtain

$$\mathcal{D}^{\mathrm{int},n} = \int_{\mathscr{T}^n} \int_{\mathscr{B}_0} D_t^{\mathrm{int}}(\boldsymbol{X}) = \sum_{e \in \mathscr{N}_{el}} \int_{\mathscr{B}_\square} \tilde{\mathbf{i}}^{*,n,e}(\boldsymbol{\eta})\, \mathbf{z}^{n,e}(\boldsymbol{\eta}) \tag{6.25}$$

We depict this energy loss versus the corresponding time points t^n also in this figure. We realise that the steps in the time evolution of the relative total energy corresponds to the minima of the dissipated internal energy. On the other hand, it can be seen that both the total linear and total angular momentum are not affected by the assumed strain approximation. This more physically meaningful time evolution of the relative total energy arise from the better fulfilled stability estimate, see Figure 6.14. Moreover, in opposition to the constant violation of the stability estimate by the hG(1) method, the mhG(1) method fulfils the stability estimate better and better the lower the dissipated internal energy is. There is also a distinction in the time evolution of the global mechanical Galerkin form. Whereas the hG(1) method fulfills this Galerkin form in the range of 10^{-11} J, however, with sporadic high peaks, the mhG(1) method fulfills the global mechanical Galerkin form throughout in the range of the Newton-Raphson tolerance tol. The reason is that the mhG(1) method need predominantly two global Newton-Raphson iterations per time step, and the hG(1) method three iterations. Hence, we save CPU time. Since we have not modified the spatial approximation of the stress field by using the assumed strain approximation in time, the stress distribution over the ring corresponding to the mhG(1) method looks like that of the hG(1) method, see Figure 6.15.

Regarding a node A at the outside of the ring opposite the uninsulated portion, in Figure 6.16, we see a relative smooth time evolution of the projected first Piola-Kirchhoff stress calculated by the mhG(1) method, however, a superposed high-frequency mode in the time evolution of the hG(1) method. This superposed high-frequency mode is especially distinct near the time point $t^n = 1.39\,\mathrm{s}$ of the first divergence. Accordingly, the assumed strain approximation in time affects the temporal approximation of the second Piola-Kirchhoff stress, and reduces a spurious high-frequency solution in the time evolution of the first Piola-Kirchhoff stress field. This leads to a more robust mhG method concerning a constant time step size throughout the simulation. As next step, we investigate the behaviour of the mhG method after changing the time step size during the simulation. We calculate with a time step size h^n of 10 ms till the time $t^n = 2.5\,\mathrm{s}$, and afterwards, we choose a time step size of 62.5 ms.

In Figure 6.17, we see time evolutions of the ring pertaining to the node A at the outside of the ring opposite the uninsulated portion. By using the small time step size at the beginning, we see the relative high frequency of the temperature oscillations with an approximate period of 125 ms. Changing the time step size to the higher value of 62.5 ms, we obtain a temporal aliasing according to the Nyquist criterion, because the time step size is not smaller the half period. Consequently, the high frequent oscillation cannot be reproduced by the time integrator. At the time point $t^n = 3.25\,\mathrm{s}$, the mhG(1) method diverge the first time and calculates an abrupt decay in the temperature evolution. The period of the oscillation pertaining to the velocity and the position of approximate 940 ms in consequence of the initiated rotation can be also reproduced with the higher time step size. The second divergence of the mhG(1) method at time $t^n = 3.4375\,\mathrm{s}$ finally leads to a blow up in the time evolution of the relative total energy. Before blowing up, however, the relative total energy decays owing to the temperature decay after the first divergence at time $t^n = 3.25\,\mathrm{s}$. In spite of the divergences, the total linear momentum is conserved, however, the total angular momentum shows a jump in the third component after the second divergence.

Figure 6.18 includes the time evolution of the dissipated internal energy before and after the time step size change. Since the approximation error of the time integration dependents on the time step size h^n, the dissipated internal energy $\mathcal{D}^{\mathrm{int},n}$, given by Equation (6.25), increases with a greater time step, however decrease with increasing simulation time as before the time step size change. Only at the first divergence at time $t^n = 3.25\,\mathrm{s}$, we obtain an abrupt energy increase, and at time $t^n = 3.4375\,\mathrm{s}$, a blow up of the dissipated internal energy goes with the second divergence. This temporal behaviour is reflected in the stability estimate, given by Equation (2.118), because in the considered motion, the dissipated internal energy dominates in the stability estimate. This time step size dependent approximation error of the time integration is also the reason for the higher values of Equation (6.23), associated with the local mechanical Galerkin form. However, these absolute values are even of the order of the absolute value of the local tolerance $\mathsf{tolevo} = 10^{-9}\,\mathrm{J/m^2}$, associated with the criterion for the convergence of the spatially local viscous evolution equation, given by Equation (B.51). The convergence criterion of the global iterative solution procedure in Equation (B.99) is associated directly with the relative internal energy balance and not with the kinetic energy balance. Therefore, a converged solution allows a small exceedance of the global tolerance $\mathsf{tol} = 10^{-6}\,\mathrm{J}$ by the absolute value of the global mechanical residual, see the time point $t^n = 140\,\mathrm{ms}$. The last two peaks correspond to the divergence of the mhG(1) method at the time points $t^n = 3.25\,\mathrm{s}$ and time $t^n = 3.4375\,\mathrm{s}$. On the other hand, it is remarkable that a greater time step size with a greater approximation error in the time integration can leads to a visibly smaller absolute value of the global mechanical residual. Recall that the distinction between solving the local mechanical Galerkin form and the global mechanical Galerkin form lies in the effect of the spatial quadrature associated with the given spatial discretisation. Whereas the local mechanical Galerkin

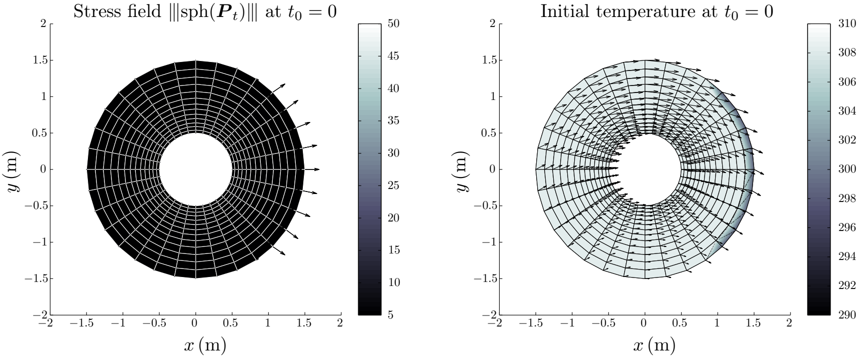

Figure 6.7. Initial configurations of the ring at $t_0 = 0$ with an uninsulated portion on its righthand side. In the reference configuration to the left, the initial projected heat flux is depicted by vector arrows at the spatial nodes in Joule per square meter. The colour denotes the spectral norm of the spherical part of the projected first Piola-Kirchhoff stress tensor field. In the current configuration to the right, the colour indicates the initial temperature field in Kelvin, and the vector arrows at the spatial nodes designate the initial velocity field.

form is solved at each spatial quadrature point without an influence of a spatial quadrature, the global mechanical Galerkin form consists of spatially integrated virtual energy terms. Thus, it seems that the greater time step size h^n of 62.5 ms goes better with the spatial mesh of the ring. Since we used for the Lagrangian temperature field the same spatial discretisation as for the deformation field, and in the thermal Galerkin form the same spatial quadrature as in the global mechanical Galerkin form, we observe this effect also in the thermal Galerkin form. However, the absolute value of the thermal residual is always below the global tolerance tol of 10^{-6}J. We also show the time evolution of the projected first Piola-Kirchhoff stress pertaining to the node A at the outside of the ring opposite the uninsulated portion. We see, this time evolution pertaining to the outside of the ring is not conspicuously modified after changing the time step size. Only the aliasing by virtue of the larger time step is observable. However, in Figure 6.19, it can be seen that the projected first Piola-Kirchhoff stress at the inside of the ring increases with increasing simulation time. Moreover, we observe an increasing radial stress wave with progressing simulation time till the mhG(1) method at time $t = 3.4062$ s ultimately diverge.

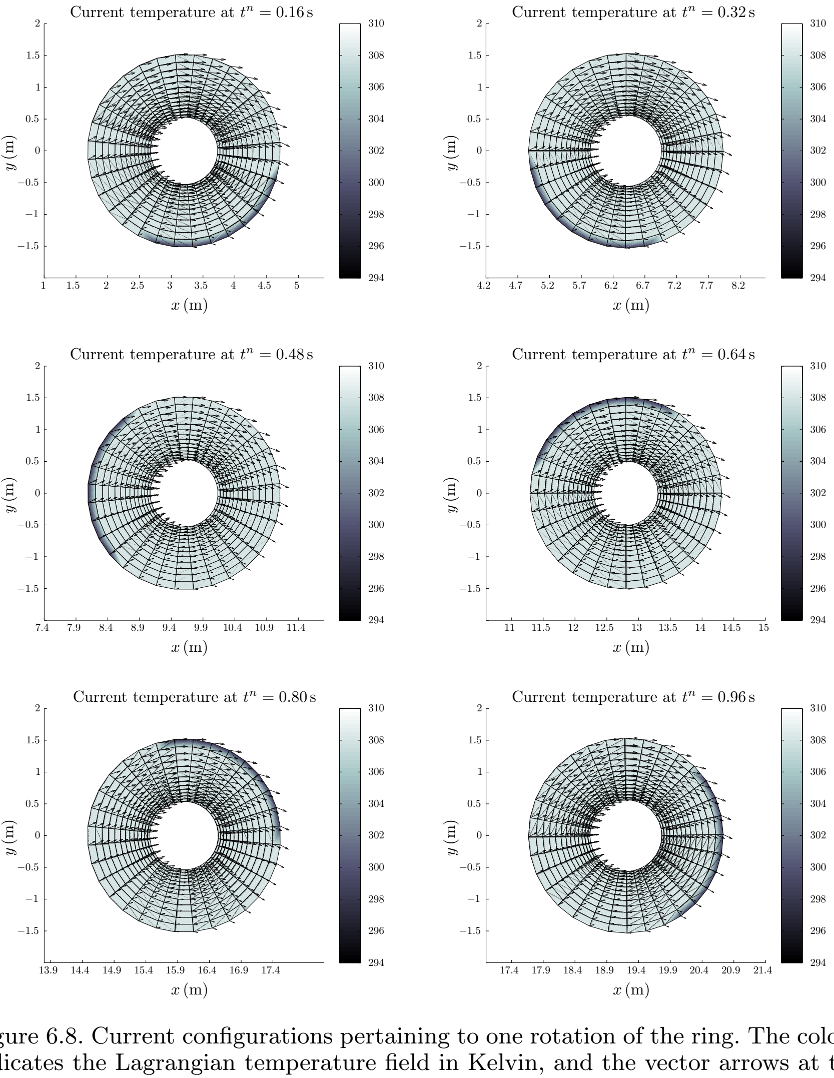

Figure 6.8. Current configurations pertaining to one rotation of the ring. The colour indicates the Lagrangian temperature field in Kelvin, and the vector arrows at the spatial nodes designate the Lagrangian velocity field. The motion is calculated by the hG method with linear finite elements in time and bilinear finite elements in space. The time step size h^n is chosen to be 10 ms throughout the simulation.

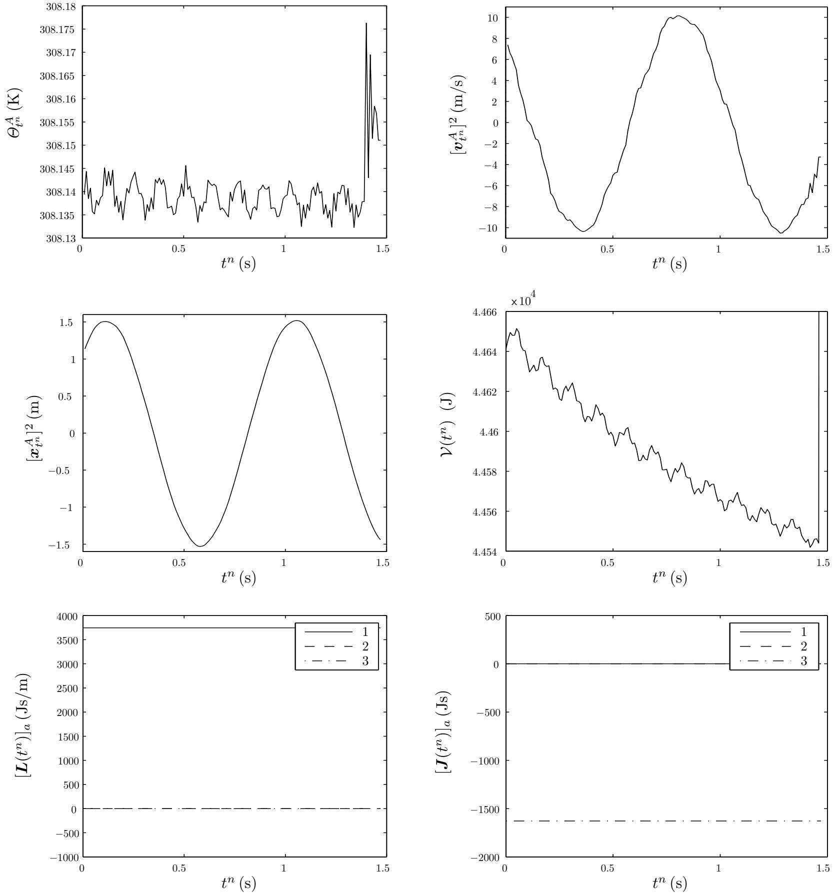

Figure 6.9. Time evolutions pertaining to the motion of the ring, calculated by the hG(1) method with linear finite elements in time and bilinear finite elements in space. The time step size h^n is equal to 10 ms throughout the calculation. First, the temperature, the vertical velocity and the vertical position pertaining to a node A at the outside of the ring opposite the uninsulated portion is depicted versus time t^n. Second, the figure shows the time evolutions of the relative total energy as well as of the components of the total linear and total angular momentum, respectively. The legends in the last row indicate the components a of the momenta.

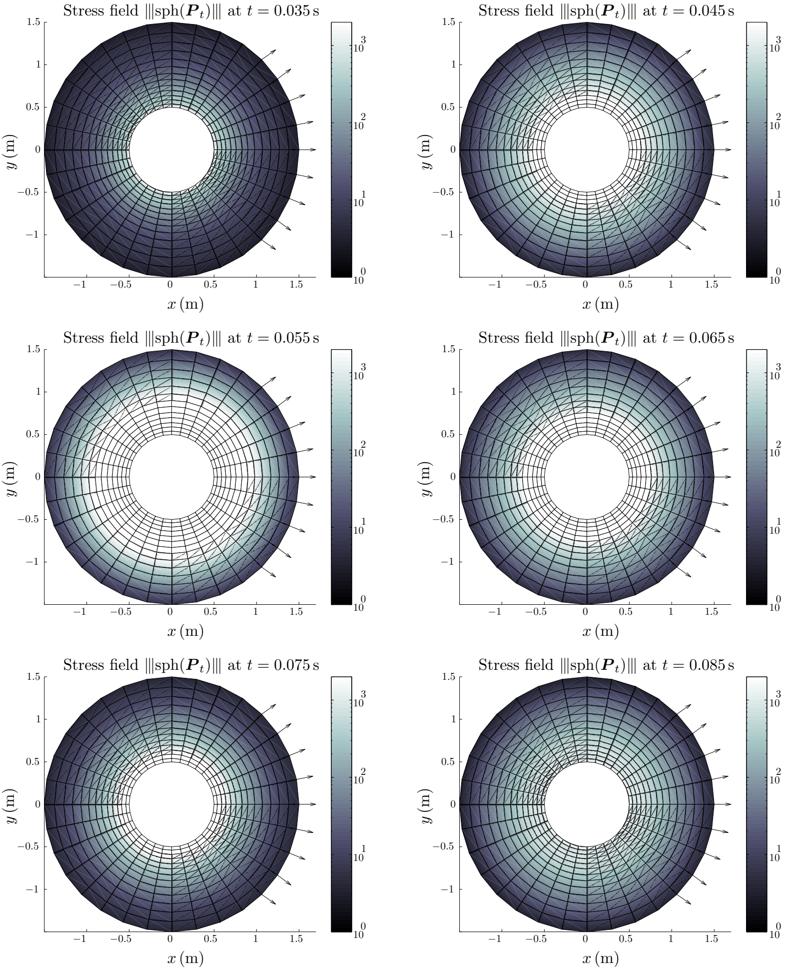

Figure 6.10. Reference configurations pertaining to the motion of the ring. The colour indicates the spectral norm of the spherical part pertaining to the projected first Piola-Kirchhoff stress field in Joule per square meter, and the vector arrows at the spatial nodes designate the projected Piola-Kirchhoff heat flux. The motion is calculated by the hG(1) method with linear finite elements in time and bilinear finite elements in space. The time step size h^n is chosen to be 10 ms throughout the simulation.

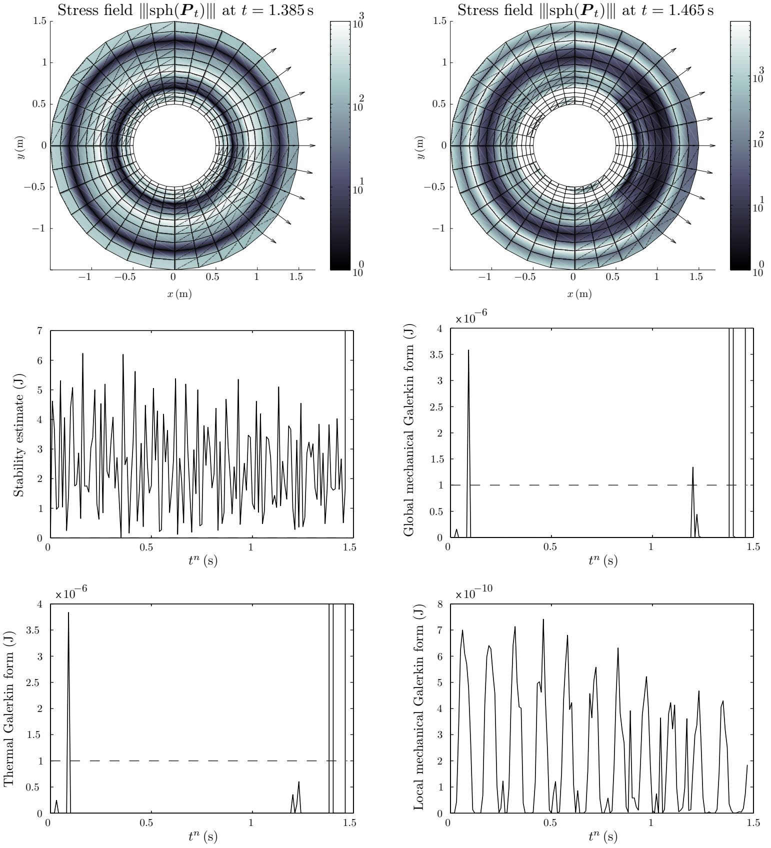

Figure 6.11. The reference configurations pertaining to the two time points, whose calculation led to the divergence of the hG(1) method with linear finite elements in time and bilinear finite elements in space (first row). The colour indicates the spectral norm of the spherical part pertaining to the projected first Piola-Kirchhoff stress field in Joule per square meter, and the vector arrows at the spatial nodes designate the projected Piola-Kirchhoff heat flux. The time step size is given by $h^n = 10\,\text{ms}$ throughout the calculation. In the second row on the left hand side, the absolute value of the residual of Equation (2.118) is depicted. The remainder diagrams show the absolute values of the Galerkin forms in Appendix B versus the corresponding time points t^n. The dashed lines indicate the used tolerance tol of the global Newton-Raphson method.

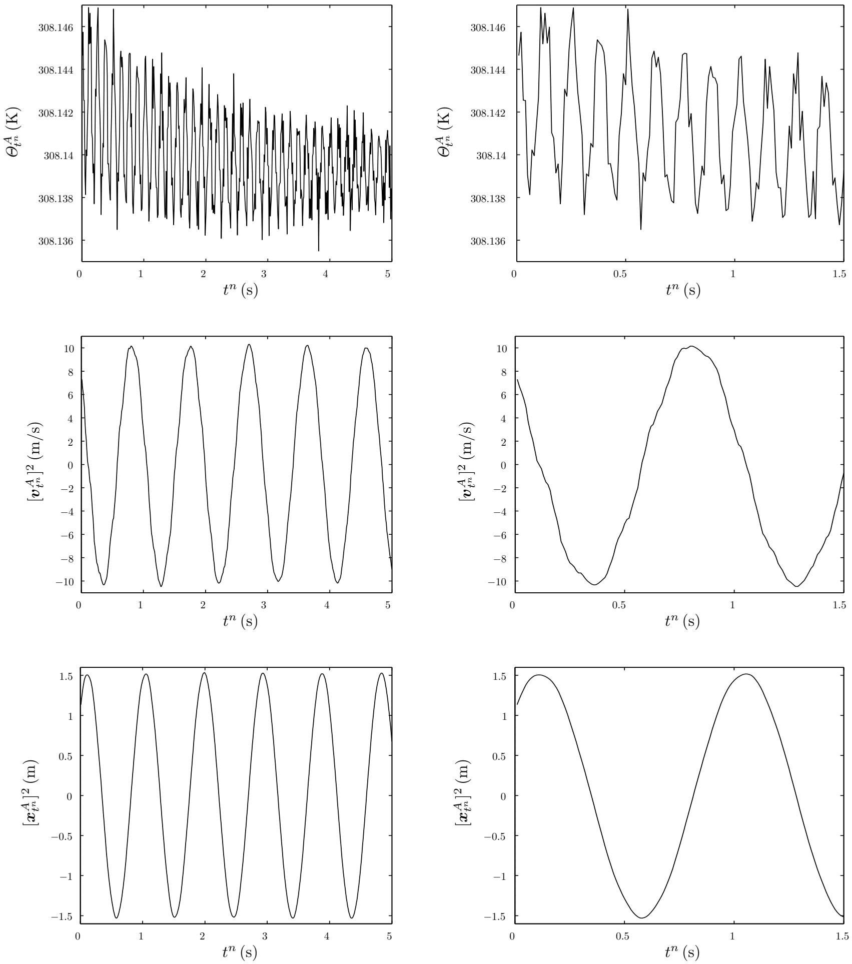

Figure 6.12. Time evolutions pertaining to the motion of the ring, calculated by the mhG(1) method with linear finite elements in time and bilinear finite elements in space. The time step size h^n is equal to 10 ms throughout the calculation. The plots show the temperature, the vertical velocity and the vertical position pertaining to the node A at the outside of the ring opposite the uninsulated portion versus the corresponding time points t^n.

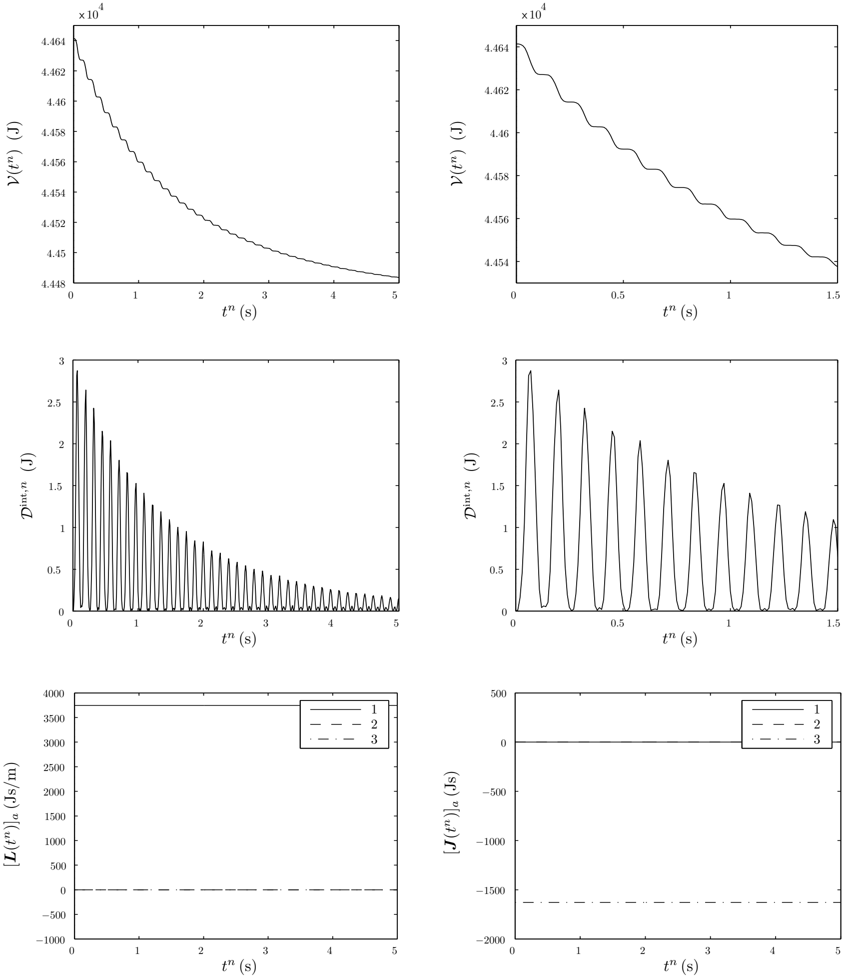

Figure 6.13. Time evolutions pertaining to the motion of the ring, calculated by the mhG(1) method with linear finite elements in time and bilinear finite elements in space. The time step size h^n is equal to 10 ms throughout the simulation. The plots show the relative total energy $\mathcal{V}(t^n)$ (first row), and the dissipated internal energy $\mathcal{D}^{\text{int},n}$ (second row) versus the time points t^n. The last row shows the total linear and total angular momentum components versus the same time points.

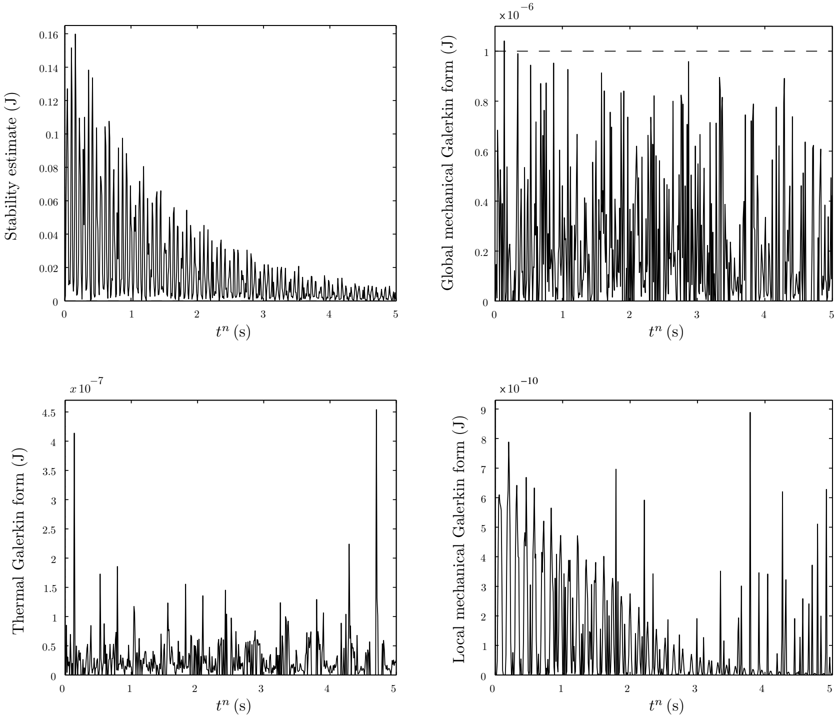

Figure 6.14. Time evolutions pertaining to the motion of the ring, calculated by the mhG(1) method with linear finite elements in time and bilinear finite elements in space. The time step size h^n is equal to 10 ms throughout the simulation. In the first row on the left hand side, the absolute value of the residual of Equation (2.118) is depicted. The remainder plots show the absolute values of the Galerkin forms in Appendix B versus the corresponding time points t^n. The dashed line indicates the used tolerance tol of the global Newton-Raphson method.

6.3.5. The exactly energy consistent method. The robustness of the inherently energy consistent finite element method with respect to a large constant time step size is increased by applying the assumed strain approximation in time in the argument of the free energy function as well as in the Lagrangian conductivity tensor. The assumed strain approximation in time improves the time evolution of the first Piola-Kirchhoff stress tensor,

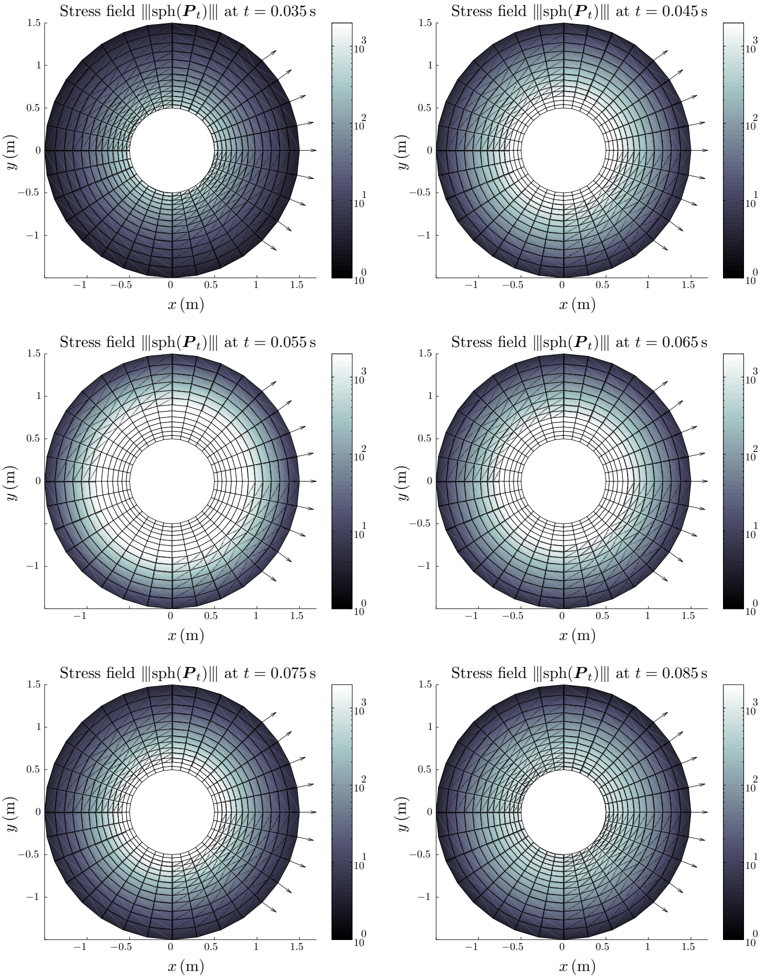
Stress field $|||\mathrm{sph}(\boldsymbol{P}_t)|||$ at $t = 0.035\,\mathrm{s}$

Stress field $|||\mathrm{sph}(\boldsymbol{P}_t)|||$ at $t = 0.045\,\mathrm{s}$

Stress field $|||\mathrm{sph}(\boldsymbol{P}_t)|||$ at $t = 0.055\,\mathrm{s}$

Stress field $|||\mathrm{sph}(\boldsymbol{P}_t)|||$ at $t = 0.065\,\mathrm{s}$

Stress field $|||\mathrm{sph}(\boldsymbol{P}_t)|||$ at $t = 0.075\,\mathrm{s}$

Stress field $|||\mathrm{sph}(\boldsymbol{P}_t)|||$ at $t = 0.085\,\mathrm{s}$

Figure 6.15. Reference configurations pertaining to the motion of the ring. The colour indicates the spectral norm of the spherical part pertaining to the projected first Piola-Kirchhoff stress field in Joule per square meter, and the vector arrows at the spatial nodes designate the projected Piola-Kirchhoff heat flux. The motion is calculated by the mhG(1) method with linear finite elements in time and bilinear finite elements in space. The time step size h^n is chosen to be $10\,\mathrm{ms}$ throughout the simulation.

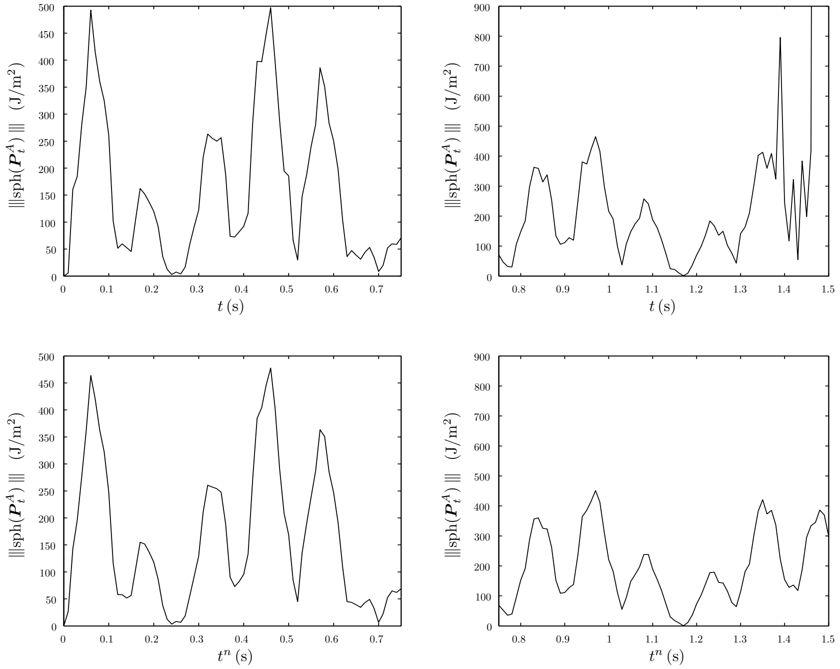

Figure 6.16. Time evolution of the projected first Piola-Kirchhoff stress pertaining to the node A at the outside of the ring opposite the uninsulated portion. The simulations are done by the hG(1) method (first row) and the mhG(1) method (last row), respectively, with linear finite elements in time and bilinear finite elements in space. The time step size h^n is chosen to be 10 ms throughout the calculation.

however, does not avoid the formation of high spurious stress waves in radial direction of the ring after changing the time step size. These spurious stress waves are especially distinctive when the mhG method diverges. Therefore, in order to improve the robustness with respect to time step size changes, we modify also the spatial approximation of the first Piola-Kirchhoff stress tensor field by keeping the total linear and total angular momentum conserved. Furthermore, since we observe a blow up of the dissipated internal energy, we modify the viscosity in the entropy evolution equation. For these purposes, we introduce the enhanced virtual work and the enhanced virtual viscous

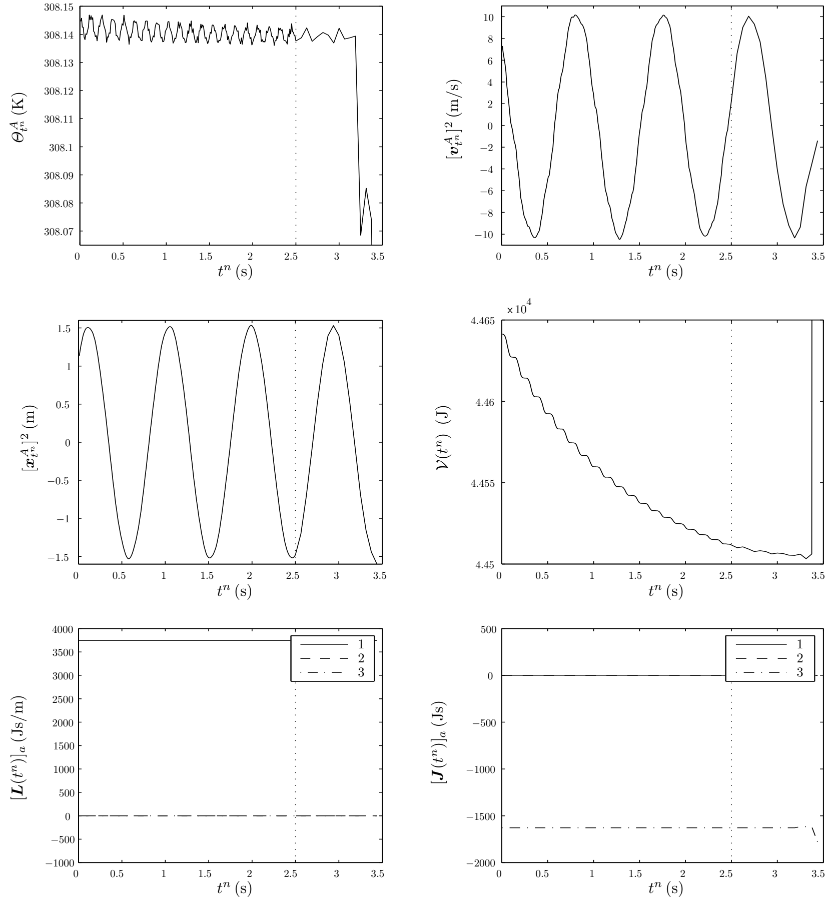

Figure 6.17. Time evolutions pertaining to the motion of the ring, calculated by the mhG(1) method with linear finite elements in time and bilinear finite elements in space. The time step size h^n is equal to 10 ms till the time $t^n = 2.5$ s, and afterwards 62.5 ms. The dotted line designates the time step size change. First, the temperature, the vertical velocity and the vertical position pertaining to the node A at the outside of the ring opposite the uninsulated portion is depicted versus time t^n. Second, the time evolutions of the relative total energy as well as of the components of the total linear and total angular momentum are shown. The legends in the last row indicate the components a of the momenta.

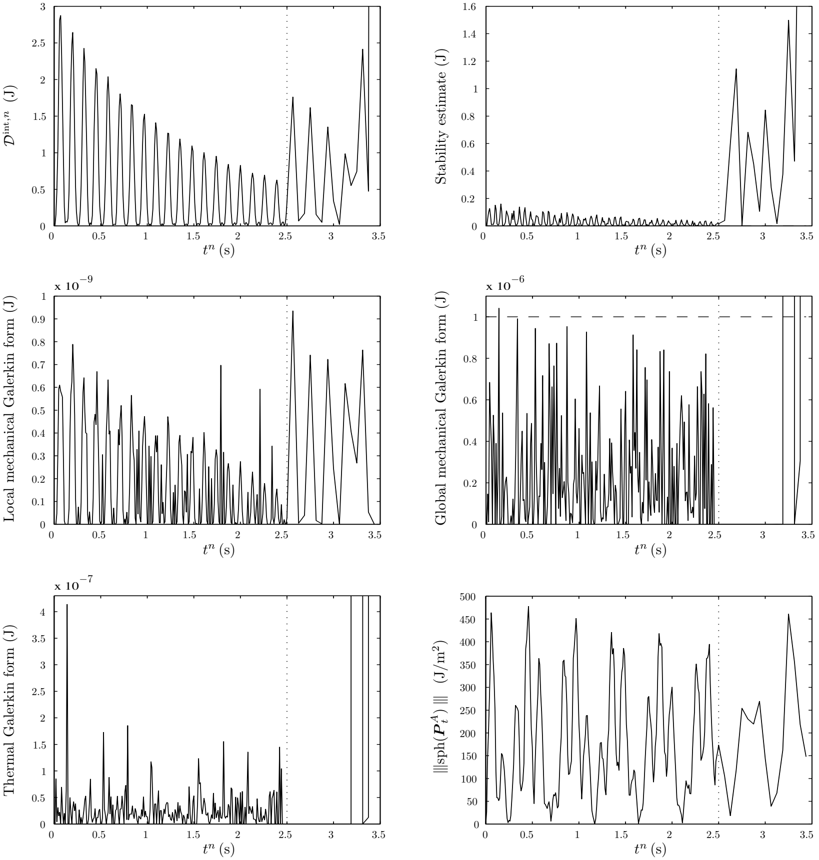

Figure 6.18. Time evolutions pertaining to the motion of the ring, calculated by the mhG(1) method with linear finite elements in time and bilinear finite elements in space. The time step size h^n is equal to 10 ms till the time $t^n = 2.5$ s, and afterwards 62.5 ms. The dotted lines designate the time step size change. In the first row, the dissipated internal energy and the absolute value of the residual of Equation (2.118) is depicted. The remainder plots, but the last to the right in the third row, show the absolute values of the Galerkin forms in Appendix B versus the corresponding time points t^n. In the last plot, the time evolution of the projected first Piola-Kirchhoff stress pertaining to the node A at the outside of the ring opposite the uninsulated portion is displayed.

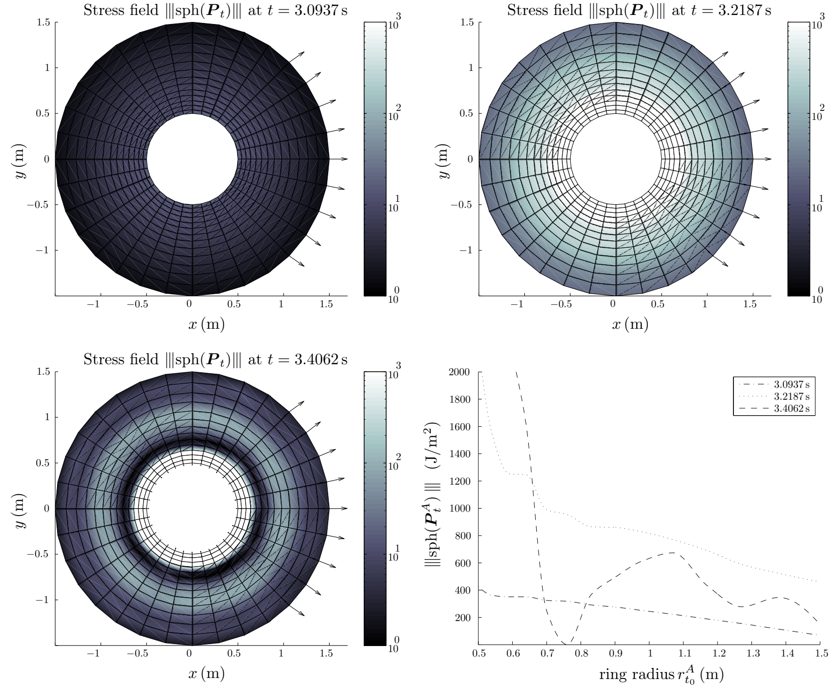

Figure 6.19. Reference configurations pertaining to three time points after the time point $t^n = 2.5\,\mathrm{s}$ where the time step size is changed from $10\,\mathrm{ms}$ to $62.5\,\mathrm{ms}$. The simulation is done by the mhG(1) method with linear finite elements in time and bilinear finite elements in space. The colour indicates the spectral norm of the spherical part pertaining to the projected first Piola-Kirchhoff stress field in Joule per square meter. The vector arrows at the spatial nodes designate the projected Piola-Kirchhoff heat flux. On the ordinate of the plot in the bottom right corner, the stress norm pertaining to nodes A on a radial line is indicated, which ends at a node on the outside of the ring opposite the uninsulated portion. The corresponding radial positions in the reference configuration at time $t_0 = 0$ are shown on the abscissa.

dissipation, derived in Section 5 from the view point of energy consistency. We arrive at the exactly energy consistent ehG method, which we now apply for simulating the free flight of the ring. More precisely, the simulation based on the ehG(1) method with linear finite elements in time and bilinear finite elements in space. Again, we compute in time steps of $10\,\mathrm{ms}$ till the time $t^n = 2.5\,\mathrm{s}$, and afterwards, we set the time step size to $62.5\,\mathrm{ms}$. The ehG(1) method calculates the initiated motion of the ring without numerical problems, and runs over the time points $t^n = 3.25\,\mathrm{s}$ and time $t^n = 3.4375\,\mathrm{s}$ at which the mhG(1) method is diverged. Therefore, we ultimately stop the calculation after five seconds.

In Figure 6.20, we show the discrete time evolution of the temperature pertaining to the node A at the outside of the ring, opposite the uninsulated portion. In the time interval $[0, 2.5\,\mathrm{s}]$, where the small time step size $h^n = 10\,\mathrm{ms}$ is used, the temperature decreases more than using the greater time step size of $62.5\,\mathrm{ms}$ afterwards. The reason is, according to the exactly fulfilled stability estimate, the total dissipated energy on the righthand side of Equation (6.1) depends on the error of the used numerical time integration rule. On the other hand, the temporal aliasing in the temperature evolution after changing the time step size does not lead to convergence problems. In the time evolution of the corresponding nodal velocity and position, there are hardly any changes after changing the time step size. Since the time evolution of the velocity and position is not affected by high-frequent modes, we occasionally realise the cutting of maxima and minima only. The reduced total dissipation is also observable in the time evolution of the relative total energy, when we compare the slope of this time curve. Further, owing to the exactly fulfilled stability estimate, spurious node-to-node oscillations in the relative total energy course are avoided at the time points where the internal dissipation is minimal. The dissipated energy is thus really non-negative. In this figure, the time evolution of the total linear and total angular momentum is also depicted. We see, the modified stress further satisfies the conservation laws, since we enhanced the second Piola-Kirchhoff stress tensor in order to retain the symmetry of the Kirchhoff stress tensor.

In Figure 6.21, the time evolution of the internal dissipation also shows the dependence on the approximation error of the time integration rule. However, the ehG method is stable, and therefore, the internal dissipation decreases with increasing time, also after the time step size change. We also observe the fulfillment of the stability estimate during the total simulation time. The convergence criterion requires a maximal absolute value of $\mathsf{tol} = 10^{-6}\mathrm{J}$. Again, the residual equation associated with the local mechanical Galerkin form is fulfilled, since its absolute values are even of the order of the local tolerance $\mathsf{tolevo} = 10^{-9}\mathrm{J/m^2}$. As the convergence criterion requires the fulfillment of the stability estimate, a converged solution allows a small exceedance of the tolerance tol by the global mechanical Galerkin form and by the thermal Galerkin form. The thermal Galerkin form of the ehG(1) method is again better fulfilled with the greater time step size. Also interesting is that the greater time step size leads to a smaller spectral norm of the spherical part of the first Piola-Kirchhoff stress tensor. A possible conclusion is, in turn, that the greater time step size goes better with the spatial mesh.

In Figure 6.22, we show the reference configurations determined by the ehG(1) method for the purpose of comparison with the mhG(1) method. Recall, at the last time point, the mhG(1) method is diverged. We see, the modified spatial stress approximation by means of the enhanced stress tensor avoids distinctive overstresses at the inner ring, and high spurious stress waves. However, depicting the spectral norm of the spherical part pertaining to the projected first Piola-Kirchhoff stress tensor on a radial line, we identify small spurious stress waves in the radius interval $[0.5\,\mathrm{m}, \sim 0.86\,\mathrm{m}]$. The stress distribution in the disjoint interval $]\sim 0.86\,\mathrm{m}, 1.5\,\mathrm{m}]$ is smooth.

In Figure 6.23, it is shown by the plot in the upper left corner, that these spurious stress waves are also present before the time step size has been changed. We compare the numerical results with the closed-form analytical solution pertaining to the steady-state stress distribution of a free rotating linear elastic ring in the linearised theory (see Appendix D). We see the corresponding stress distribution in the stress plots as solid lines. The bottom solid line depicts the radial stress distribution, and the upper solid line the spectral norm of the spherical part pertaining to the linearised Cauchy stress tensor. We recognise that the waves lie approximately in the radius interval $[R_i, \sqrt{R_i R_a}]$ between the vertical solid lines, in which the linearised radial stress decrease. The waves are also present in the radial distribution of the spectral norm of the spherical part pertaining to the projection of the Euler-Almansi strain tensor

$$[\boldsymbol{e}_t(\boldsymbol{X})]_{ab} = [(\boldsymbol{F}_t(\boldsymbol{X}))^{-T}]_a{}^A\,[\boldsymbol{E}_t(\boldsymbol{X})]_{AB}\,[(\boldsymbol{F}_t(\boldsymbol{X}))^{-1}]^B{}_b \qquad (6.26)$$

which is defined as the push-forward of the Green-Lagrange strain tensor $\boldsymbol{E}_t(\boldsymbol{X})$, defined by Equation (D.12), at each point $\boldsymbol{X} \in \mathscr{B}_0$ in the reference configuration. Here, it is noticeable that between the vertical lines the Euler-Almansi strain decrease, and the waviness in this interval is increasing as the slope of the Euler-Almansi strain distribution increases. The circles in the plots indicate the grid points of the spatial mesh which is used for the ring as hitherto in this paper. The corresponding grid point distribution is stretched in radial direction toward the outer radius (compare the radial grid point distributions). These spurious waves are reminiscent of the spurious note-to-note oscillations appearing in steady and unsteady convection-dominated transport problems (see Donea & Huerta [169] and Eriksson et al. [36], for instance). In these problems, a to course mesh in relation to high material parameters leads to decaying non-physical oscillations, downhill in the descending interval of the solution, after a steeply ascending interval (compare the first shown Euler-Almansi distribution). In our problem, the operative material parameter for the spurious waves in the strain and stress distributions is the second Lamé constant λ in the volumetric free energy (see Appendix C). For a given spatial mesh, the higher this penalty parameter is the higher the spurious waves. Otherwise, in relation to a given second Lamé constant, we obtain high spurious waves using a to course mesh in the radius interval between the vertical lines. This shows the calculation of the ring with an equally-spaced radial grid point distribution. On the other hand, a finer spatial mesh in the inner region of the ring leads to less waves. In the comparison of the radial grid point distributions of these three spatial meshes, the different markers goes with the markers in the corresponding stress and strain plots.

Finally, in Figure 6.24, we show a simulation of the ring with a lower second Lamé constant of $\lambda = 3000\,\mathrm{J/m^2}$, and with the initial mesh denoted by the circles. We see, the distribution is also more smooth.

6.4. Energy consistent incorporated Neumann boundaries

In Section 2.3, we also specify so-called Neumann boundary conditions on the initial boundary value problem. That means Piola-Kirchhoff traction loads for all points $\boldsymbol{X}$ on the boundary $\partial_T\mathscr{B}_0$ of the continuum body, leading to an added term in the weak form of the second equation of motion, and a Piola-Kirchhoff heat flux on the boundary $\partial_Q\mathscr{B}_0$ of the body, incorporated in the weak form of the entropy evolution equation (see Section 3). The Piola-Kirchhoff traction vector causes an external mechanical power $\mathcal{P}^{\mathrm{ext}}(t)$, which is added in the balance of mechanical energy of the body. According to the inherently energy consistent finite element approximation, this balance equation coincide with the global mechanical Galerkin form $G_{\mathrm{mech}}(\mathscr{Z};\tilde{\mathbf{x}}^{*,n})$ at the variations $\tilde{\mathbf{x}}^{*,n}$ arising from the rate of change of the deformation field.

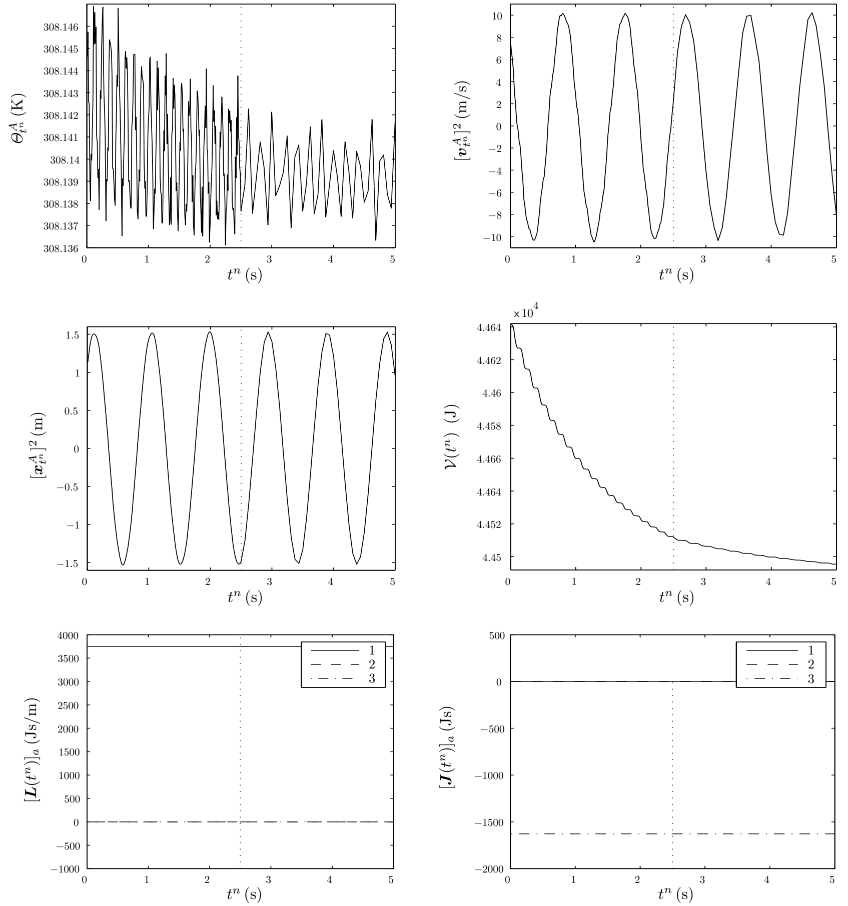

Figure 6.20. Time evolutions pertaining to the motion of the ring, calculated by the ehG(1) method with linear finite elements in time and bilinear finite elements in space. The time step size h^n is equal to 10 ms till the time $t^n = 2.5$ s, and afterwards 62.5 ms. The dotted lines designate the time step size change. The first plots show the temperature, the vertical velocity and the vertical position pertaining to the node A at the outside of the ring, opposite the uninsulated portion. Then, the time evolutions of the relative total energy as well as of the components of the total linear and total angular momentum, respectively, are depicted. The legends in the last row indicate the components a of the momenta.

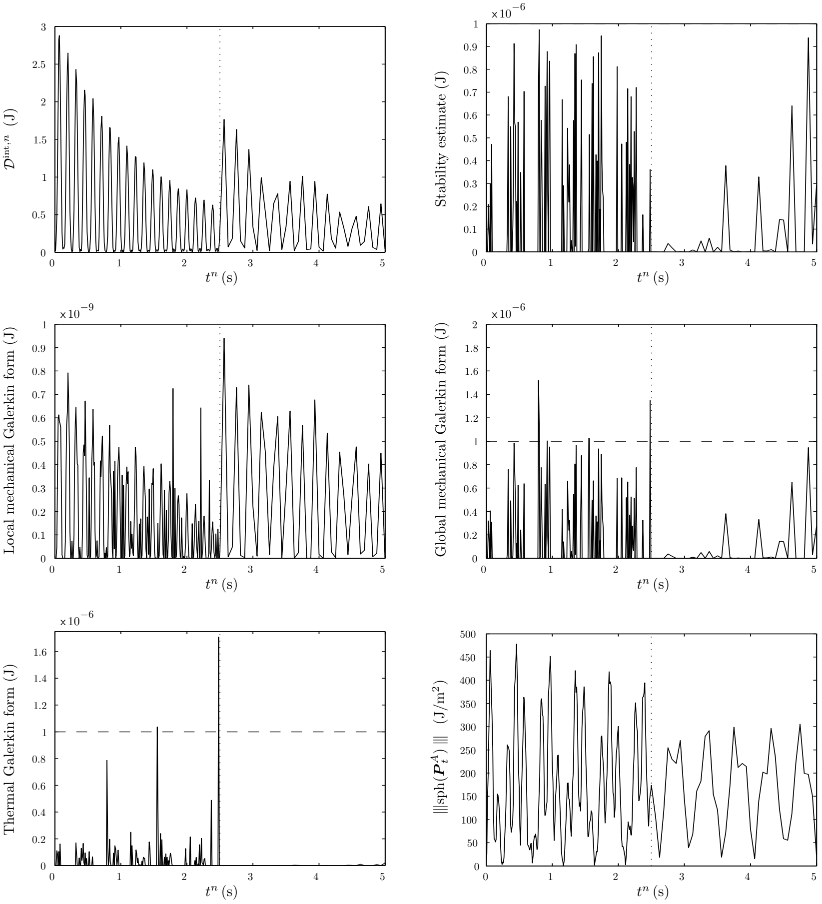

Figure 6.21. Time evolutions associated with the flying ring, calculated by the ehG(1) method with linear finite elements in time and bilinear finite elements in space. The time step size h^n is set to 10 ms till the time $t^n = 2.5$ s, and afterwards to 62.5 ms. The dotted lines indicate this change of the time step size. In the first row, the dissipated internal energy and the absolute value of the residual of Equation (2.118) is shown. The remainder plots, but the last, show the absolute values of the Galerkin forms in Appendix B. In the right plot in the last row, the time evolution of the projected first Piola-Kirchhoff stress pertaining to the node A at the outside of the ring opposite the uninsulated portion is displayed.

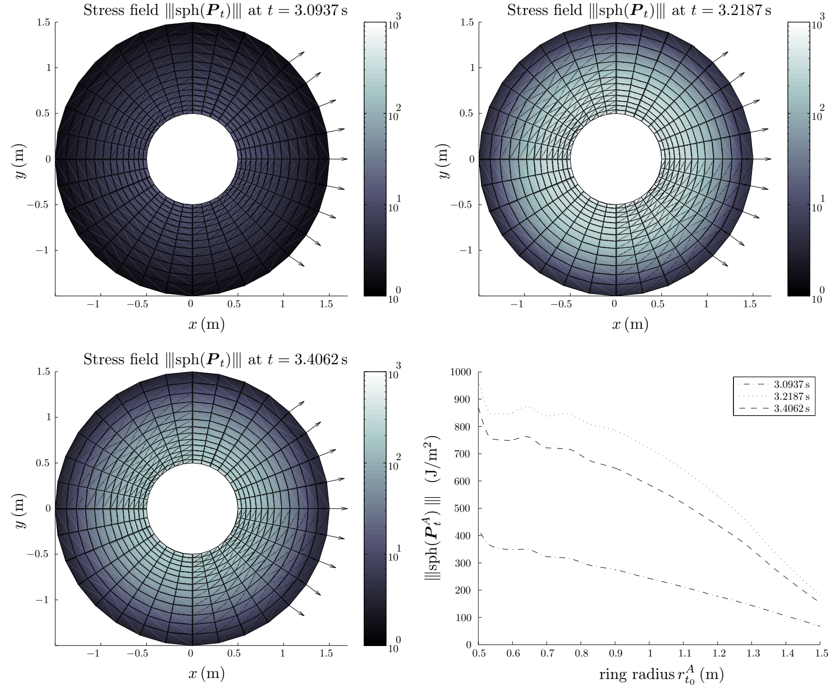

Figure 6.22. The first three plots show reference configurations pertaining to three time points after the change of the time step at time $t^n = 2.5\,\mathrm{s}$ from the size $10\,\mathrm{ms}$ to $62.5\,\mathrm{ms}$. The simulation is done by the ehG(1) method with linear finite elements in time and bilinear finite elements in space. The colour indicates the spectral norm of the spherical part pertaining to the projected first Piola-Kirchhoff stress field in Joule per square meter. The vector arrows at the spatial nodes designate the projected Piola-Kirchhoff heat flux. The plot in the bottom right corner shows the stress norm pertaining to nodes A on a radial line which ends at a node on the outside of the ring opposite the uninsulated portion. The radial positions of these nodes in the reference configuration at time $t_0 = 0$ are shown on the abscissa.

Hence, we are able to verify exactly the balance of introduced external mechanical power and saved or dissipated internal energy by applying the exactly energy consistent finite element method. Analogously, external thermal power, introduced in the continuum body by means of a Piola-Kirchhoff heat flux over the boundary $\partial_Q\mathscr{B}_0$, is incorporated by the inherently

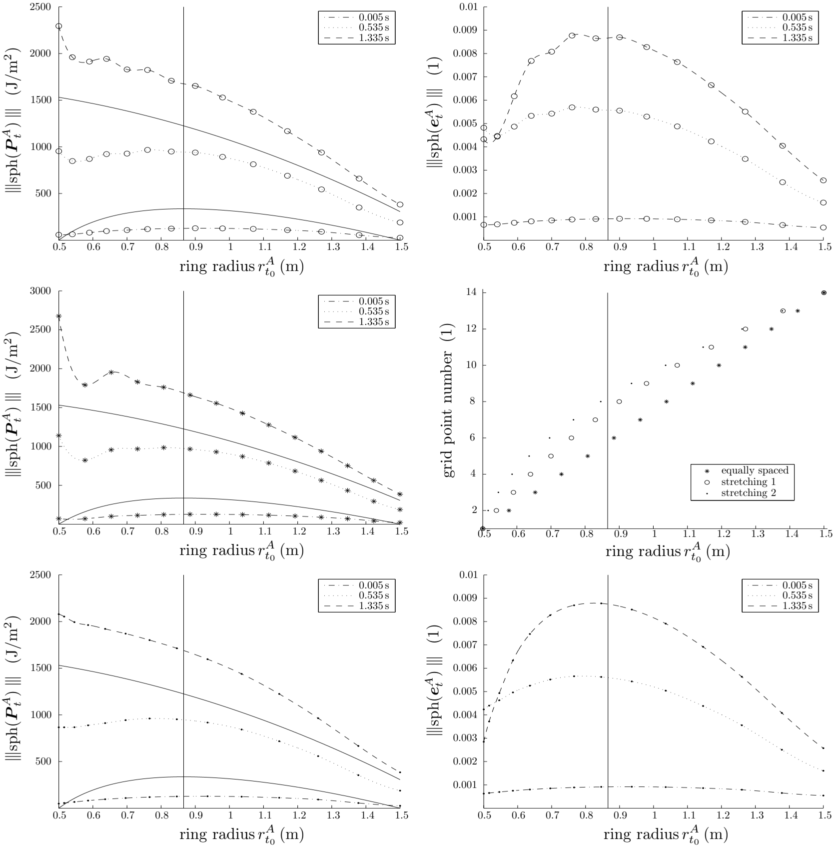

Figure 6.23. Stress and strain distributions of the ring pertaining to three time points before the time step size change at time $t^n = 2.5\,\mathrm{s}$ from 10 ms to 62.5 ms. The simulation is done by the ehG(1) method with linear finite elements in time and bilinear finite elements in space. The distributions are spectral norms pertaining to nodes A on a radial line which ends at a node on the outside of the ring opposite the uninsulated portion. The radial positions of these nodes in the reference configuration at time $t_0 = 0$ are shown on the abscissa. The ordinates of the plots in the left column indicate the spectral norm of the spherical part pertaining to the projected first Piola-Kirchhoff stress field. The ordinates of the plots in the upper right and bottom right corner designate the spectral norm of the spherical part pertaining to the projected Euler-Almansi strain field. The right plot in the middle row show the radial grid point distributions of the compared spatial meshes.

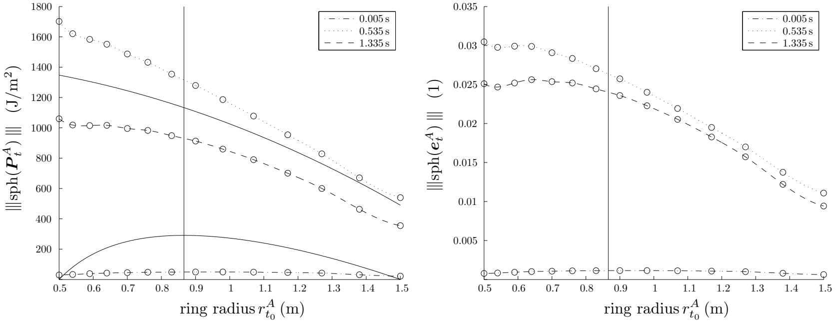

Figure 6.24. Stress and strain distribution of the ring pertaining to three time points before the time step size change at time $t^n = 2.5\,\mathrm{s}$ from 10 ms to 62.5 ms The second Lamé constant is here $\lambda = 3000\,\mathrm{J/m^2}$, and the initial mesh is used. The simulation is done by the ehG(1) method with linear finite elements in time and bilinear finite elements in space. The distributions are spectral norms pertaining to nodes A on a radial line, which ends at a node on the outside of the ring opposite the uninsulated portion. The radial positions of these nodes in the reference configuration at time $t_0 = 0$ are shown on the abscissa. The ordinate of the left plot indicates the spectral norm of the spherical part pertaining to the projected first Piola-Kirchhoff stress field. The ordinate of the right plot designates the spectral norm of the spherical part pertaining to the projected Euler-Almansi strain field.

energy consistent finite element approximation of the entropy evolution equation. Therefore, the exactly energy consistent algorithm uses exact the prescribed value of the mechanical external power and the thermal power in order to affect the primary variables of the initial boundary value problem. We show this in the following numerical simulations. Note that a Piola-Kirchhoff traction vector field and a Piola-Kirchhoff heat flux is also borne in mind in the recommended convergence criterion (see Appendix B.3). Therefore, we have not to change the global iterative solution procedure.

6.4.1. The example with boundary traction field. We consider the cross section of an axisymmetric polymer spring, consisting of the Neo-Hookean material described in Appendix C. The height of the spring is 10 m and the width is given by 12.82 m. The density ρ_0 in the cross section is $30\,\mathrm{kg/m^2}$. The first and second Lamé constant in the Neo-Hookean free energy function is chosen to be $\mu = 7500\,\mathrm{J/m^2}$ and $\lambda = 30000\,\mathrm{J/m^2}$, respectively. The thermal

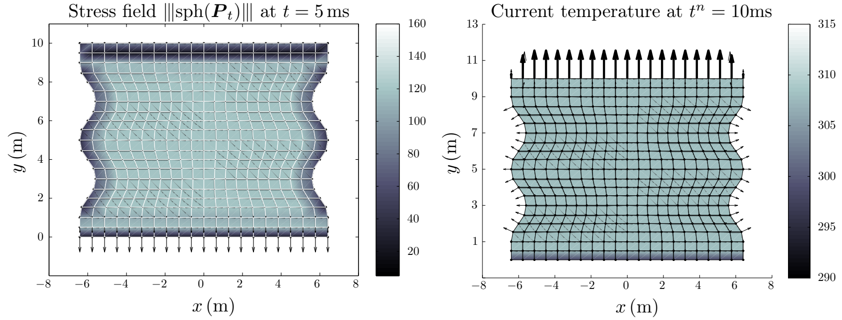

Figure 6.25. Configurations of the spring after the first time step. The simulation is done by the ehG(1) method with linear finite elements in time and bilinear finite elements in space. The boundary elements on the Neumann boundaries are linear finite elements in space. The time step size h^n is given by $10\,\mathrm{ms}$ throughout the calculation. On the left, the reference configuration of the spring at time $t = 5\,\mathrm{ms}$ is shown. The projected heat flux is depicted by vector arrows at the spatial nodes. The colour denotes the spectral norm of the spherical part of the projected first Piola-Kirchhoff stress tensor field in Joule per square meter. On the right, the current configuration of the spring is depicted at time $t^n = 10\,\mathrm{ms}$ with the uninsulated portion on its bottom. The colour indicates the Lagrangian temperature field in Kelvin. The thin vector arrows at the spatial nodes designate the Lagrangian velocity field, and the bold arrows designate the distributed boundary traction load in vertical direction.

expansion of the cross section is governed by the coefficient $\beta = 10^{-4}\,\mathrm{K}^{-1}$, and the storage of heat by the specific heat capacity $c = 1500\,\mathrm{J/m^2K}$. The heat conduction through the cross section is conditioned by the constant specific conductivity $k_0 = 0.02\,\mathrm{W/K}$. The deviatoric viscosity is set to $V_{\mathrm{dev}} = 10000\,\mathrm{Js/m^2}$ and the corresponding volumetric viscosity amounts to $V_{\mathrm{vol}} = 50000\,\mathrm{Js/m^2}$. The ambient temperature Θ_∞ of this two-dimensional continuum body amounts $298.15\,\mathrm{K}$. The temperature at the bottom of the spring coincides with the ambient temperature, and represents the only uninsulated boundary. Figure 6.25 shows the heat flux in the reference configuration over this uninsulated boundary. The remainder of the spring is heated about $10\,\mathrm{K}$. The spring bottom is clamped, and the spring sockets at the bottom and the top can only slide in vertical direction by prescribed vanishing horizontal displacements of the corresponding nodes on the sides. A vertical tension, respectively pressure, is initiated by the prescribed time-

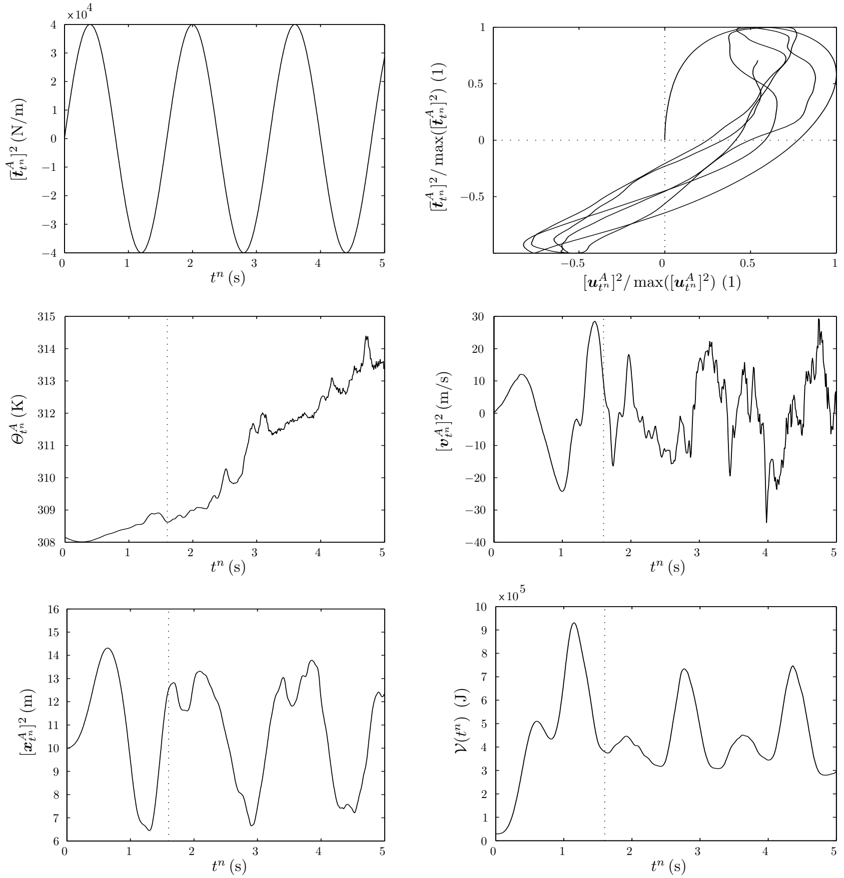

Figure 6.26. Load-displacement curve and time evolutions pertaining to the tensile test of the spring, calculated by the ehG(1) method with linear finite elements in time and bilinear finite elements in space. The boundary elements on the Neumann boundaries are linear finite elements in space. The time step size h^n is equal to 10 ms throughout the simulation. The dotted line in the time evolutions designates the end of the first loading period. The vertical traction load, the temperature, the vertical velocity and the vertical position pertaining to the middle node A on the top of the spring is depicted versus time t^n. The load-displacement curve of the same node is shown in a normalised scale. The time evolution of the relative total energy is also displayed.

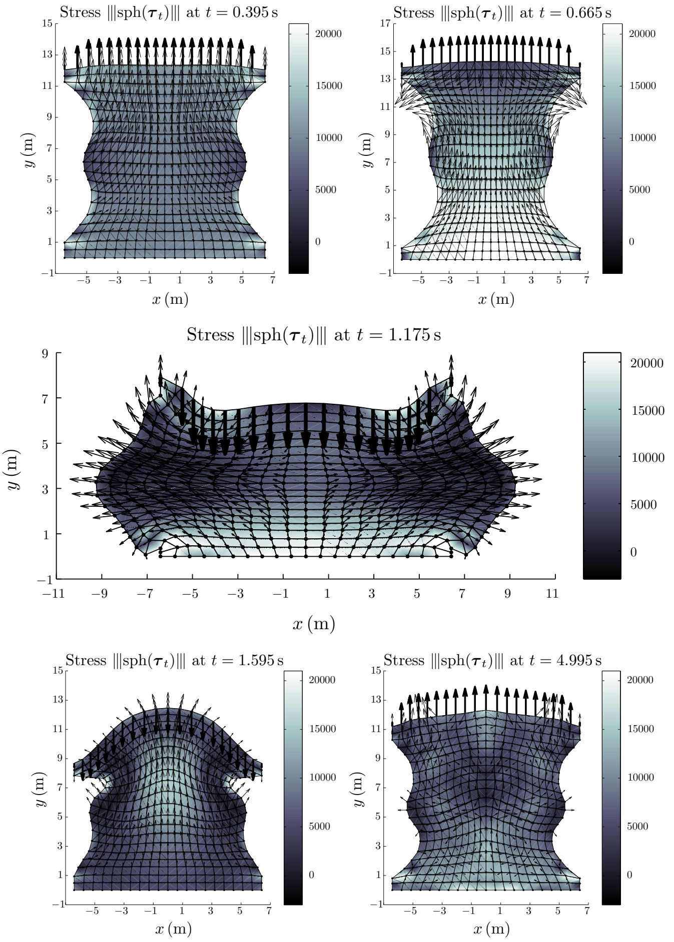

Figure 6.27. Current configurations of the tensile test of the spring. The colour indicates the spectral norm of the spherical part pertaining to the projected Kirchhoff stress field in Joule per square meter. The thin vector arrows at the spatial nodes designate the Lagrangian velocity field, and the bold arrows designate the distributed boundary traction load in vertical direction. The motion is calculated by the ehG(1) method with linear finite elements in time and bilinear finite elements in space. The boundary elements on the Neumann boundaries are linear finite elements in space. The time step size is chosen to be 10 ms throughout.

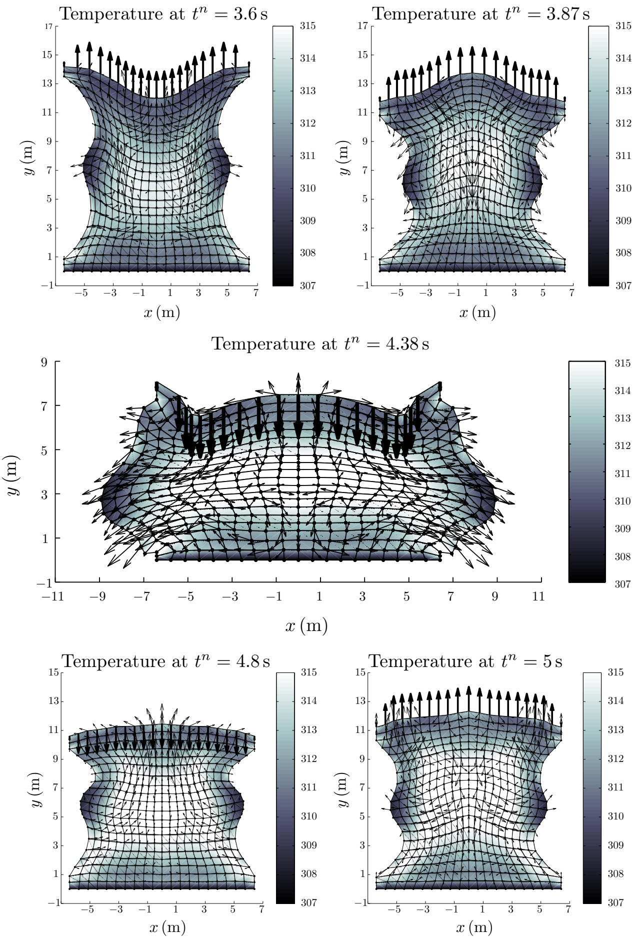
Temperature at $t^n = 3.6\,\mathrm{s}$

Temperature at $t^n = 3.87\,\mathrm{s}$

Temperature at $t^n = 4.38\,\mathrm{s}$

Temperature at $t^n = 4.8\,\mathrm{s}$

Temperature at $t^n = 5\,\mathrm{s}$

Figure 6.28. Current configurations pertaining to the tensile test of the spring. The colour indicates the Lagrangian temperature field in Kelvin. The thin vector arrows at the spatial nodes designate the Lagrangian velocity field, and the bold arrows designate the distributed boundary traction load in vertical direction. The motion is calculated by the ehG(1) method with linear finite elements in time and bilinear finite elements in space. The boundary elements on the Neumann boundaries are linear finite elements in space. The time step size h^n is chosen to be 10 ms throughout the simulation.

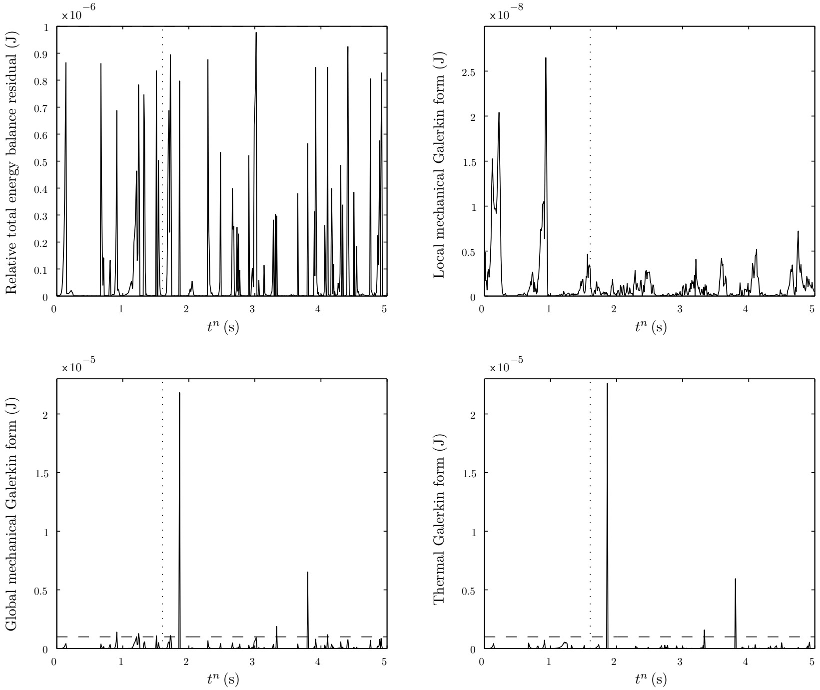

Figure 6.29. Time evolutions associated with the tensile test of the spring, calculated by the ehG(1) method with linear finite elements in time and bilinear finite elements in space. The boundary elements on the Neumann boundaries are linear finite elements in space. The time step size h^n is set to 10 ms throughout the simulation. The dotted lines indicate the end of the first loading period. In the first row to the left, the absolute value of the residual of the relative total energy balance is shown. The remainder plots show the absolute values of the Galerkin forms.

dependent Piola-Kirchhoff traction components

$$[{}^{a}\bar{\boldsymbol{t}}_t]^1 = 0 \qquad\qquad [{}^{a}\bar{\boldsymbol{t}}_t]^2 = 40000\,\frac{\mathrm{N}}{\mathrm{m}}\,\sin\left(\frac{2\,\pi}{1.6\,\mathrm{s}}\,t\right) \qquad (6.27)$$

at the free spatial element nodes a on the top. In this way, we obtain a distributed traction load. Hence, we perform a kind of stress controlled

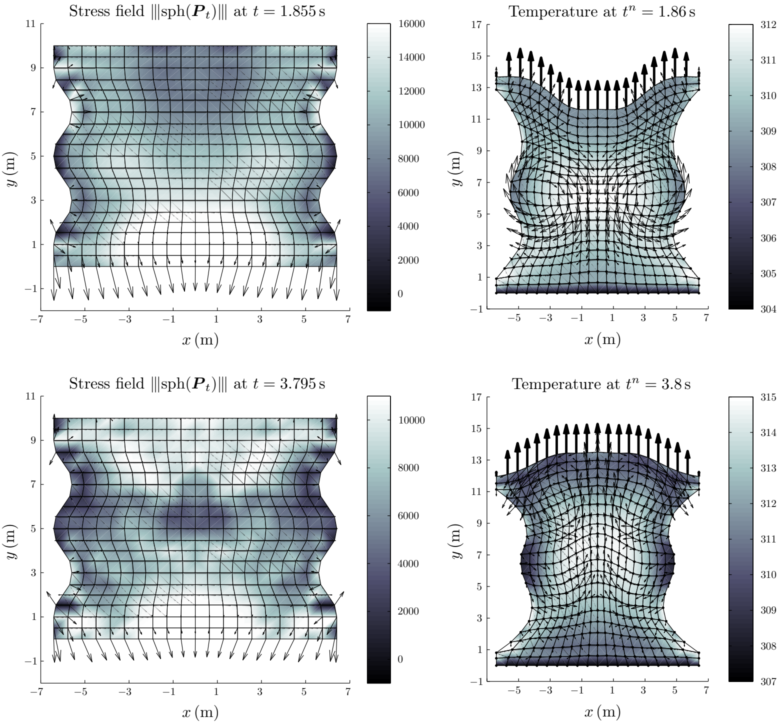

Figure 6.30. Reference configurations (left) and current configurations (right) associated with the tensile test of the spring, calculated by the ehG(1) method with linear finite elements in time and bilinear finite elements in space. The boundary elements on the Neumann boundaries are linear finite elements in space. The time step size h^n is set to 10 ms throughout the simulation. In the reference configurations, the colour indicates the spectral norm of the spherical part pertaining to the projected first Piola-Kirchhoff stress field in Joule per square meter. The vector arrows at the spatial nodes designate the projected Piola-Kirchhoff heat flux. In the current configurations, the colour denotes the Lagrangian temperature field in Kelvin. Thin vector arrows at the spatial nodes designate the Lagrangian velocity field, and bold arrows designate the distributed boundary traction load.

uniaxial extension and compression experiment (compare the real experiments in Johnson & Beatty [170, 171], and the numerical experiment in Nagtegaal & De Jong [172]). We compute with a time step size h^n of 10 ms throughout the simulation by using the ehG(1) method. We stop the calculation at time $t^n = 5\,\mathrm{s}$.

In Figure 6.26, we show the load-displacement curve and any time evolutions pertaining to this enforced vibration of the spring. For example, the amplitude of the traction load is depicted versus the simulation time. This harmonic enforcement leads to the shown load-displacement curve. We plot the curve with respect to normalised axes. The abscissa indicates the displacement of the middle node on the top of the spring. First, we recognise that the loading path is different from the unloading path according to the internal dissipation. Second, we see laterally displaced loops. This indicates a dynamical simulation by taking into account the inertia of the specimen. In this figure, we also show the primary variables pertaining to the middle node on the top of the spring. In the time evolution of the temperature, we realise an initial cooling while stretching, which changes to a heating at a certain minimum point. This effect entered into the literature as the so-called thermoelastic inversion point, at which thermal expansion and entropy contraction balance. This effect therefore depends on the linear expansion coefficient of the material (for more details see Holzapfel [135], for instance). In the time evolution of the vertical velocity, we see that the velocity course becomes more and more chaotic. Further, it is affected by high-frequent modes, which expand into the temperature evolution via the internal dissipation and also in the time evolution of the position. The time evolution of the relative total energy reveals that the pressure phases lead to greater local increases of the relative total energy as the tension phases. The reason is the extension of the free energy to the compressible range by using a high second Lamé constant as penalty parameter (see Appendix C).

In Figure 6.27, we depict current configurations pertaining to time points in the different phases of the first loading period. The two plots in the first row show the stretching phase. In the plot to the left, the loading rate is positive and the velocity field is upward oriented in direction to the prescribed loading. However, in the right plot, we recognise on the midline a stagnation point at about $y = 12\,\mathrm{m}$ with vanishing velocity, which means a singular point of the velocity field. Above this point, the velocity field is downward oriented. The reason is, the loading rate is now negative and the inertia of the spring emerge. The greatest stress occurs at the suspension. The current configuration depicts a time point pertaining to the phase with increasing pressure load. Here, we also realise a stagnation point on the midline and high stresses on edges and at the clamping. In the bottom left corner, we show a time point with decreasing pressure loading rate. We obtain a thermal expansion of the material around the midline owing to the increased Lagrangian relative temperature field. The high stress in the middle of the spring arise from this thermal expansion. In the last calculated time point, we see that the traction load causes also a second kind of a singular point in the Lagrangian velocity field. We realise vortex points, which lead to increased stresses in surrounding regions.

In Figure 6.28, current configurations pertaining to the third loading period are illustrated. We identify an increased temperature level throughout the cross section of the spring. Particularly, the region from the interior through to the edges of the bottom are heated.

In order to show the energy consistent incorporation of the Neumann boundaries, we depict in Figure 6.29 the time evolutions of the absolute values pertaining to the Galerkin forms and to the residual of the relative total energy balance. The absolute values of the latter residual are below the prescribed tolerance $\mathsf{tol} = 10^{-6}$ J of the global iterative solution procedure, owing to the used convergence criterion. Likewise, the absolute values pertaining to the spatially integrated and assembled local mechanical Galerkin form. In the time evolution corresponding to the global mechanical and thermal Galerkin form, however, we observe violations of the limit, especially at the times $t^n = 1.86\,\mathrm{s}$ and $t^n = 3.8\,\mathrm{s}$ in the simulation interval.

In Figure 6.30, we show the reference configurations and the current configurations pertaining to these time points. These two time points share vortices in the Lagrangian velocity field, however, the position of the maximal velocities (longest vector arrows) occur in different regions of the cross section. At the time point $t^n = 1.86\,\mathrm{s}$ with the highest peak in the Galerkin forms, the maximal velocities are directly around the vortex centres, while at time $t^n = 3.8\,\mathrm{s}$ the maximal velocities occur at the top of the spring. On the other hand, the Lagrangian temperature fields at these two time points show no particularities. In the reference configurations, we see the high first Piola-Kirchhoff stress in the vortex centres and the clamping on the bottom.

6.4.2. The example with boundary traction field and boundary heat flux. We simulate a further dynamic tensile test of the spring. The material data and the traction load is given as in Section 6.4.1, however, we introduce a prescribed Piola-Kirchhoff heat flux on the thermal Neumann boundary $\partial_Q \mathscr{B}_0$ on the

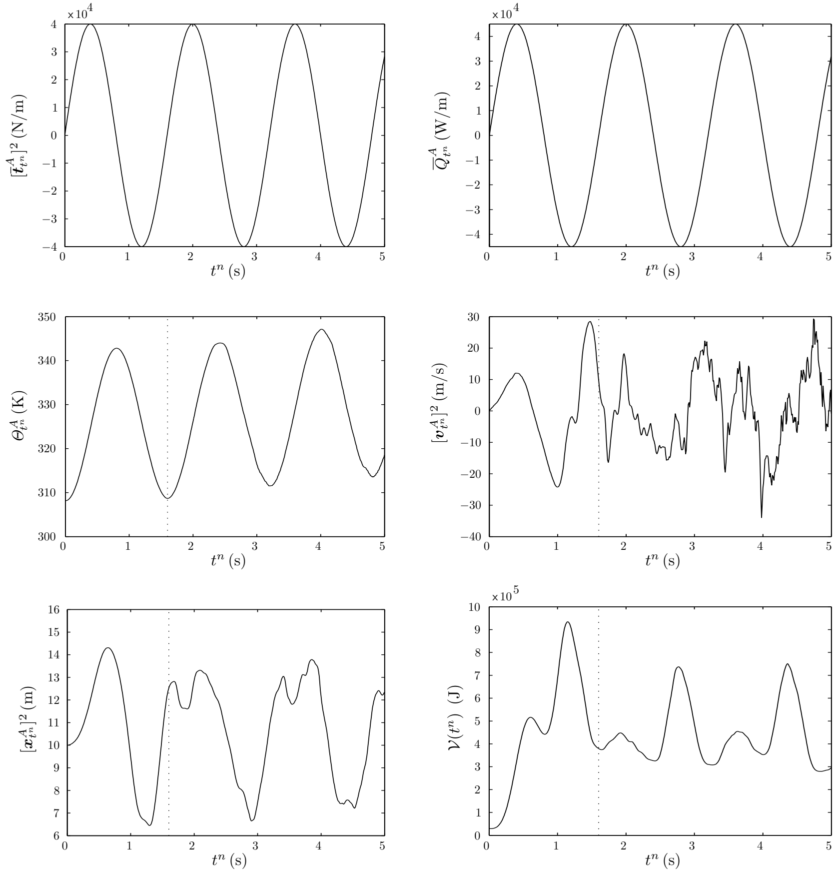

Figure 6.31. Time evolutions associated with the tensile test of the spring with prescribed boundary heat flux on the top, calculated by the ehG(1) method with linear finite elements in time and bilinear finite elements in space. The boundary elements on the Neumann boundaries are linear finite elements in space. The time step size is 10 ms throughout the simulation. The dotted line in the time evolutions designates the end of the first loading period. The first row shows the prescribed vertical traction load and the inward normal heat flux pertaining to the middle node A on the top of the spring. In the middle row, the corresponding current temperature and vertical velocity is depicted. The vertical position of the middle node A as well as the relative total energy is shown in the last row.

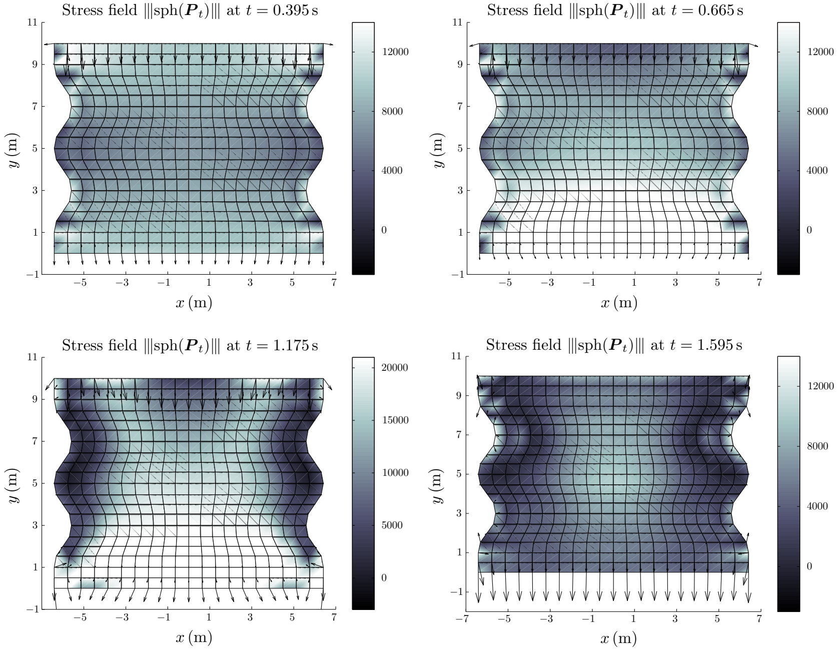

Stress field $|||\mathrm{sph}(\boldsymbol{P}_t)|||$ at $t = 0.395\,\mathrm{s}$

Stress field $|||\mathrm{sph}(\boldsymbol{P}_t)|||$ at $t = 0.665\,\mathrm{s}$

Stress field $|||\mathrm{sph}(\boldsymbol{P}_t)|||$ at $t = 1.175\,\mathrm{s}$

Stress field $|||\mathrm{sph}(\boldsymbol{P}_t)|||$ at $t = 1.595\,\mathrm{s}$

Figure 6.32. Reference configurations pertaining to the tensile test of the spring with prescribed boundary heat flux on the top. The simulation is done by the ehG(1) method with linear finite elements in time and bilinear finite elements in space. The boundary elements on the Neumann boundaries are linear finite elements in space. The time step size is given by 10 ms throughout the simulation. The colour indicates the spectral norm of the spherical part pertaining to the projected first Piola-Kirchhoff stress field in Joule per square meter. The vector arrows at the spatial nodes designate the projected Piola-Kirchhoff heat flux.

top of the spring, given by

$$ {}^{a}\overline{Q}_t = 45000\,\frac{\mathrm{W}}{\mathrm{m}}\,\sin\left(\frac{2\,\pi}{1.6\,\mathrm{s}}\,t\right) \tag{6.28} $$

at the free spatial element nodes a on the top. The sides of the spring are also insulated.

In Figure 6.31, we show the corresponding time evolutions. Again, we show

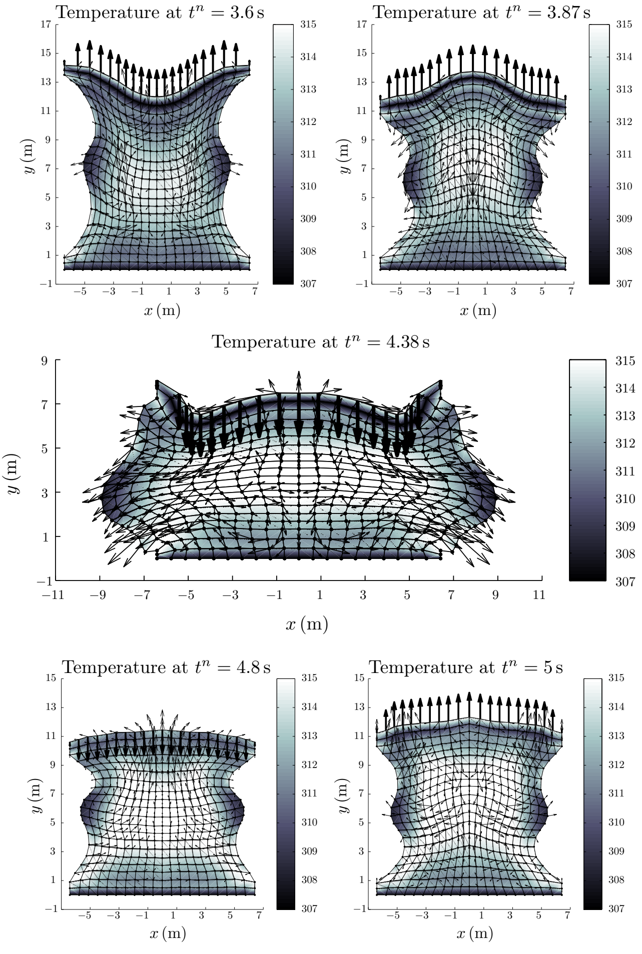

Temperature at $t^n = 3.6\,\mathrm{s}$

Temperature at $t^n = 3.87\,\mathrm{s}$

Temperature at $t^n = 4.38\,\mathrm{s}$

Temperature at $t^n = 4.8\,\mathrm{s}$

Temperature at $t^n = 5\,\mathrm{s}$

Figure 6.33. Current configurations pertaining to the tensile test of the spring with prescribed boundary heat flux on the top. The colour indicates the Lagrangian temperature field in Kelvin. The thin vector arrows at the spatial nodes designate the Lagrangian velocity field, and the bold arrows designate the distributed boundary traction load in vertical direction. The motion is calculated by the ehG(1) method with linear finite elements in time and bilinear finite elements in space. The boundary elements on the Neumann boundaries are linear finite elements in space. The time step size is throughout 10 ms.

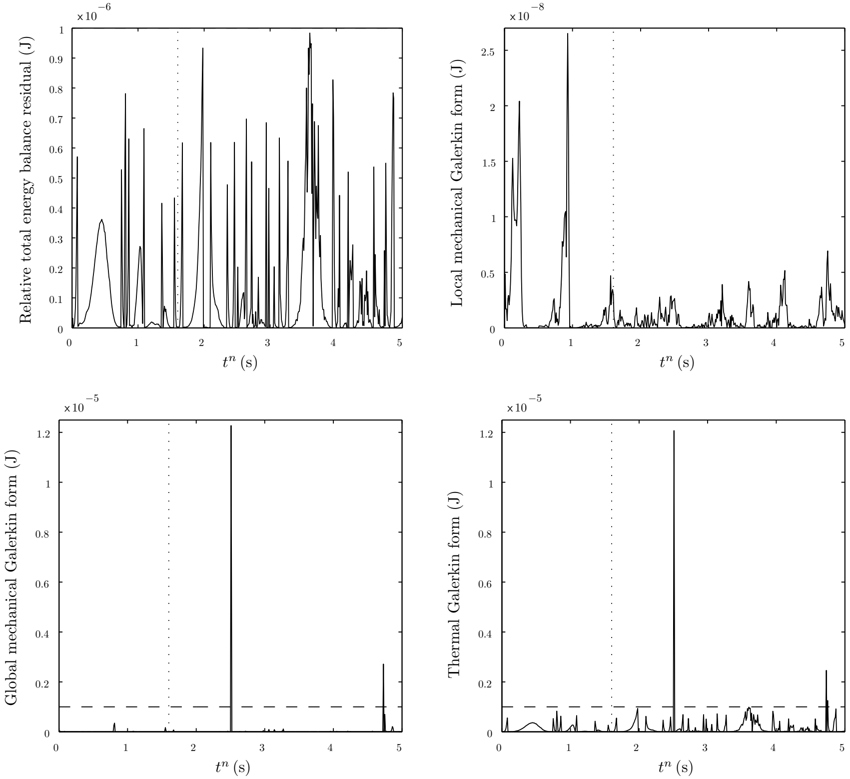

Figure 6.34. Time evolutions associated with the tensile test of the spring with prescribed boundary heat flux on the top, calculated by the ehG(1) method with linear finite elements in time and bilinear finite elements in space. The boundary elements on the Neumann boundaries are linear finite elements in space. The time step size is 10 ms throughout the simulation. The dotted lines indicate the end of the first loading period. In the first row to the left, the absolute value of the residual of the relative total energy balance is shown. The remainder plots show the absolute values of the Galerkin forms in Appendix B.

the time evolutions of the primary variables pertaining to the middle node on the top of the spring. Owing to the high specific heat capacity in comparison to the specific thermal conductivity, the heat flux has only a minor influence

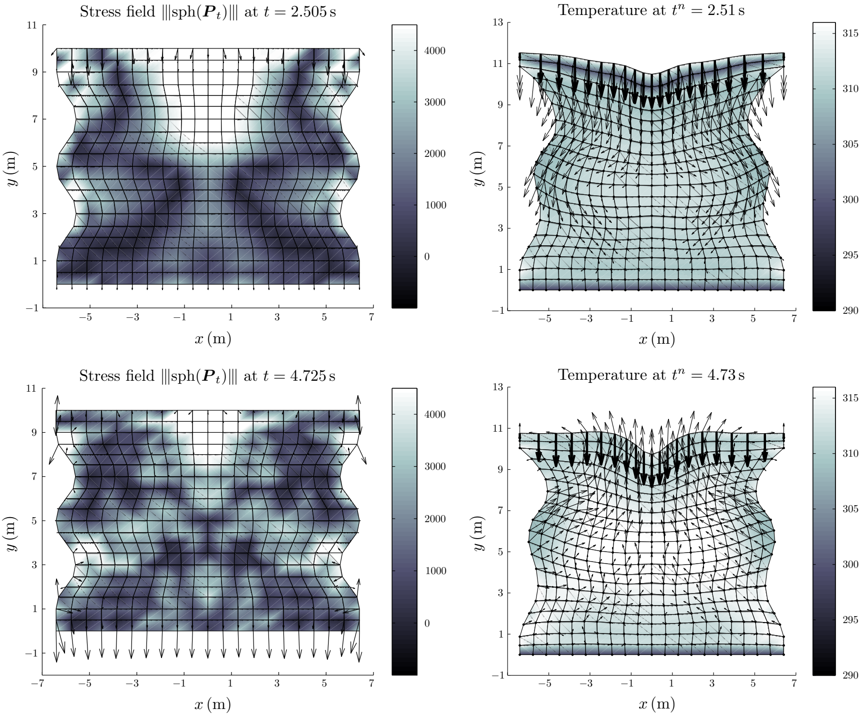

Figure 6.35. Reference configurations (left) and current configurations (right) associated with the tensile test of the spring with prescribed boundary heat flux on the top, calculated by the ehG(1) method with linear time finite elements and bilinear finite elements in space. The boundary elements are linear finite elements in space. The time step size h^n is set to 10 ms throughout the simulation. In the reference configurations, the colour indicates the spectral norm of the spherical part pertaining to the projected first Piola-Kirchhoff stress field in Joule per square meter. The vector arrows at the spatial notes denote the projected Piola-Kirchhoff heat flux. In the current configurations, the colour designates the Lagrangian temperature field in Kelvin. Thin vector arrows at the spatial nodes designate the Lagrangian velocity field, and bold arrows the distributed boundary traction load.

on the trajectory of the middle node on the top, which can be seen by the unmodified velocity and position course in comparison to Section 6.4.1. However, the time evolution of the temperature is directly affected by the heat flux course. Therefore, a well-known application of boundary heat fluxes is to solve the inverse problem of determining a time-dependent boundary heat flux in order to achieve a prescribed temperature distribution at final time (see Jiang [173]). According to the major contribution of the mechanical energies to the relative total energy, the time evolution of the relative total energy is also not conspicuously modified by the boundary heat flux.

In Figure 6.32, the effect of the boundary heat flux on the projected Piola-Kirchhoff heat flux in the reference configuration is depicted. The depicted reference configurations pertain to the first loading period. In addition to the boundary heat flux over the Dirichlet boundary at the bottom, we recognise the boundary heat flux over the Neumann boundary at the top.

In Figure 6.33, we see in the current configurations the heating and cooling of the top of the spring by the boundary heat flux.

Figure 6.34 illustrates the energy consistent incorporation of the boundary heat flux. We see, the absolute value of the residual of the relative total energy balance, and the spatially assembled and integrated local mechanical Galerkin form, are in turn below the limit of $10^{-6}\,\mathrm{J}$ prescribed in the convergence criterion. However, the global mechanical Galerkin form and the thermal Galerkin form show again two high peaks in their time evolutions. Although the fulfillment of the mechanical Galerkin form is better as in Section 6.4.1 without the boundary heat flux.

In Figure 6.35, the reference configurations and the current configurations pertaining to these two time points are shown. These time points share the distinctive first Piola-Kirchhoff stress waves in the reference configuration. Here, the velocity fields show no particularities as distinctive stagnation points or vortex points, respectively.

7. CONCLUSIONS

In this paper, we address the development and implementation of energy-momentum consistent algorithms for simulating dynamic finite deformation thermo-viscoelastic problems. Such algorithms provide an extension of energy-momentum conserving simulation algorithms for nonlinear elastodynamics. In both problem classes, the key concept is to satisfy a valid stability estimate as well as momentum balances of the initial-boundary value problem also in a discrete sense. In this way, unconditionally stable simulation algorithms are assured.

Since we aim at higher-order accurate space-time discretisations, we apply the finite element method in the space as well as in the time domain. We perform the spatial discretisation by means of a common Bubnov-Galerkin approximation. However, the discretisation in time is designed to be exactly energy-momentum consistent as follows: First of all, we design an inherently energy-momentum consistent finite element method in time. That means, we address to fulfil also in a discrete sense (a) the stability estimate exactly for exact quadrature in time, and (b) total linear and total angular momentum conservation also with numerical quadrature. In the final design step, we transform the accuracy order dependent fulfillment of the stability estimate in an exact fulfillment by keeping the momenta conserved. The inherently energy consistency is a matter of the appropriate Galerkin method for the corresponding time evolution equation. For the first order form of the equations of motion, it is well-known that the continuous Galerkin (cG) method is inherently energy consistent. In this paper, we also deduce the energy consistent Galerkin method for the used internal variable evolution equation as well as the entropy evolution equation. The former equation is solved consistently to the stability estimate by using the cG method as well. The reason is the claimed weak equality of two non-equilibrium stress tensors. Weak in the sense of an equal viscous dissipation with both stress tensors. However, the stability estimate claim to solve the entropy evolution equation by a specific discontinuous Galerkin (dG) method. The specific feature of this dG method is a jump term formulated in the internal energy. The final design step is realised by a higher-order extension of the discrete gradient method.

This extension is based on a closed-form minimisation being not restricted to gradients. In this way, we obtain two additional terms in the weak formulation, which provide the fulfillment of the stability estimate in the discrete sense, in spite of using numerical quadrature.

This space-time discretisation leads to a system of algebraic nonlinear equations, which we solve by using a monolithic solution strategy. The corresponding Newton-Raphson methods on the global and the element level are based on a consistent tangent matrix. The used convergence criteria take the inherently energy consistency into account and compare energy rates, in contrast to usual solution-based criteria. Thus, different scales in the independent variables are borne in mind in a natural manner.

Numerical simulations show that the inherently energy conserving method is higher-order accurate, and that the modifications of the inherently energy consistent Galerkin method do not affect this accuracy. Further, we compare the stability properties. In this connection, we show that the stability estimate is an indicator of the instability, however, that the instability is caused by insufficient approximations of physical quantities. Therefore, the used modifications of the Galerkin method arise from the approach of improving these insufficient approximations subject to the claim of energy consistency. One numerical simulation also reveals that an improvement can be a proper spatial mesh, which is adjusted to the material parameters. The reason for this effect is that the best approximation property of the Galerkin method depends on the element size in relation to the material parameters. Numerical simulations with mechanical and thermal excitation show the energy consistent incorporation of boundary conditions, which means the identification of the corresponding external power in the energy balances and the enhancement of the proposed convergence criterion. Thus, only the introduced external mechanical or thermal power affects the time evolution of the primary variables, and not spurious algorithmic introduced powers adulterate the numerical results.

8. OUTLOOK

Having in mind the stability estimate, we realise that the dissipated energy depends on the time step size, because the total dissipation has to be integrated numerically in time. Thus, an energy consistent finite element method can provide, independently of the time step size, only a non-negative dissipated energy, but with a time step size dependent value. In numerical simulations, the negative tangent of the decreasing relative total energy therefore depends on the time step size. A remedy would be a total dissipation, which coincides with a time derivative from a non-negative smooth convex potential function. Then, according to the fundamental theorem of calculus, the time integral in the stability estimate could be replaced, and an energy consistent finite element method leads to a non-negative dissipated energy depending not on the time step size. However, it might be that, for the heat conduction, this can be realised only by means of a non-classical formulation of thermoelasticity (see Dascalu & Maugin [174] and Maugin & Kalpakides [175]). Such a non-classical formulation also influences the appropriate Galerkin method in time (see Bargmann & Steinmann [95] and Bargmann [93]), so that it is possible that a continuous Galerkin method in time is energy consistent for the thermal evolution, contrary to the special discontinuous Galerkin method for the classical thermoelasticity in this work.

Moreover, on both sides of the stability estimate, the spatial integration has to be approximated by an element-wise numerical integration. The reachable error of the relative total energy balance (the tolerance `tol`) therefore depends on the approximation error of the spatial quadrature rule. However, the knowledge about the expectable error with a given spatial mesh and a given spatial quadrature rule would be desirable for energy consistent numerical simulations of motions.

Simulating motions of quasi-incompressible polymeric materials as rubber, it is an improvement to incorporate assumed strain formulations in space in an energy consistent way (see Armero [75] and Müller & Betsch [176]). Also useful for dynamics of rubber is a material formulation based on principal stretches, because important constitutive laws as Ogden's material are formulated in eigenvalues (compare Müller et al. [177]).

In order to simulate other engineering problems, the energy consistent incorporation of more complicated boundary conditions is advantageous. For example, a boundary pressure as configuration dependent traction load (see Simo et al. [163]), or an energy consistent coupling with a rigid body (see Betsch & Steinmann [67] and Betsch [178]) in order to simulate with time-dependent Dirichlet boundaries. The coupling of two distinct solid materials (bi-material body or body with inclusion) in an energy consistent way also opens many possible practical applications (see Johnson & Chen [179]). The problem is here that discontinuities arise in the first Piola-Kirchhoff stress field (see Mergheim & Steinmann [180]), and a transition condition for the Piola-Kirchhoff traction vector has to be enforced. Otherwise, the resulting stress jump is an unnessary burden for the time integration algorithm. This coupling also includes simulations of one material law, but with two distinct material parameter sets (see Mergheim [181]).

Also important, for tyre simulations for instance, are energy consistent contact algorithms for polymeric materials (see Laursen [157], Hesch & Betsch [182] and Hesch [183]).

In each case, a coupling in such a way, that the involved energy balances and conservation laws are exactly fulfilled, is advantageous for unconditional stability and physically meaningful numerical results. Therefore, the presented energy consistent formulation is derived by the general energy balances, which can be also formulated for these extensions.

A. DISCRETE WEAK INITIAL BOUNDARY VALUE PROBLEM

The numerical solution procedure of the derived weak initial boundary value problem involves the transformation of the continuous weak forms into a nonlinear algebraic problem. We therefore derive the fully discrete weak forms by employing the space-time finite element approximations. Then, we introduce a matrix form of this fully discrete weak forms, in order to obtain a system of nonlinear algebraic equations in Appendix B. According to the inherently energy consistent discretisation, the fully discrete weak forms arrive at energy balance equations after substituting the corresponding energy consistent nodal values for their nodal variations.

In this way, we are able to determine the energy balances by the residual equations. This is utilised for defining a converged solution in the numerical solution procedure, and in the post-processing of the numerical examples for verifying the energy consistency of the solution.

A.1. First equation of motion

We start with the left hand side of the weak form pertaining to the first equation of motion, given by Equation (4.21). First, we employ the stated finite element approximations

$$\delta\mathring{\boldsymbol{\pi}}_{\alpha}^{n,e}(\boldsymbol{\eta}) = \sum_{j=1}^{m_{eq}} \sum_{a\in\mathscr{N}_{en}^{e}\setminus\mathscr{N}_{\varphi}^{e}} \tilde{M}^{j}(\alpha)\,\rho_{0}^{e}(\boldsymbol{\eta})\,N_{a}(\boldsymbol{\eta})\,{}^{a}\delta\boldsymbol{v}_{\tilde{\alpha}_{j}}^{*,n,e} \tag{A.1}$$

and

$$\mathring{\boldsymbol{\varphi}}_{\alpha}^{n,e}(\boldsymbol{\eta}) = \sum_{i=1}^{m_{en}} \sum_{c\in\mathscr{N}_{en}^{e}\setminus\mathscr{N}_{\varphi}^{e}} \mathring{M}^{i}(\alpha)\,N_{c}(\boldsymbol{\eta})\,{}^{c}\boldsymbol{x}_{\alpha_{i}}^{n,e} \tag{A.2}$$

According to the completeness condition pertaining to the temporal shape functions M^i, $i = 1, \dots, m_{en}$, the time derivative of the Dirichlet boundary approximation due to Equation (4.17) is vanished in Equation (A.2). Since the spatial integration concerns only the spatial shape functions and the element density, we define the element mass matrices

$$\mathbf{M}^e = \int_{\mathscr{B}_\square} \rho_0^e(\boldsymbol{\eta})\,\mathbf{n}^e(\boldsymbol{\eta})\,\mathbf{n}^{*,e}(\boldsymbol{\eta})\,J_0^e(\boldsymbol{\eta}) \otimes \boldsymbol{I} \qquad (e \in \mathscr{N}_{el}) \tag{A.3}$$

where

$$\mathbf{n}^e(\boldsymbol{\eta}) = [N_a(\boldsymbol{\eta})]_{a\in\mathscr{N}^e_{en}\setminus\mathscr{N}^e_\varphi} \tag{A.4}$$

denotes the shape functions column vector and $\mathbf{n}^{*,e}(\boldsymbol{\eta})$ the corresponding row vector. The symbol $\otimes$ designates the Kronecker product of matrices. Since the nodal positions ${}^c\boldsymbol{x}^{n,e}_{\alpha_1}$ at the first time node are known, owing to the temporal continuity in the approximated body motion, we split up the sum over the time nodes α_i into two parts. As the time integration concerns only the temporal shape functions, we define the matrix components

$$[\tilde{\mathbf{a}}]^j = \int_{\mathscr{I}_\alpha} \tilde{M}^j(\alpha)\,\mathring{M}^1(\alpha) \qquad \text{and} \qquad [\tilde{\mathbf{A}}]^{j,k+1} = \int_{\mathscr{I}_\alpha} \tilde{M}^j(\alpha)\,\mathring{M}^{k+1}(\alpha) \tag{A.5}$$

$j,k = 1,\dots,m_{eq}$, for the first and second part, respectively. We obtain a matrix form by substituting matrix products for all the summations. First, we generate element matrices by combining the position nodes ${}^c\boldsymbol{x}^{n,e}_{\alpha_i}$ and the variations ${}^a\delta\boldsymbol{v}^{*,n,e}_{\tilde\alpha_j}$ in a column vector $\mathbf{x}^{n,e}_{\alpha_i}$ and in a row vector $\delta\mathbf{v}^{*,n,e}_{\tilde\alpha_j}$, respectively. In this way, we obtain the bilinear form $(e \in \mathscr{N}_{el})$

$$\sum_{a,c\in\mathscr{N}^e_{en}\setminus\mathscr{N}^e_\varphi} [{}^a\delta\boldsymbol{v}^{*,n,e}_{\tilde\alpha_j}]_d\,[\mathbf{M}^e_{ac}]^d{}_b\,[{}^c\boldsymbol{x}^{n,e}_{\alpha_i}]^b\,\frac{1}{h^n} = \delta\mathbf{v}^{*,n,e}_{\tilde\alpha_j}\,\mathbf{M}^e\,\mathbf{x}^{n,e}_{\alpha_i}\,\frac{1}{h^n} \tag{A.6}$$

Now, we assemble all spatial elements $\mathscr{B}^e_0$. A vector associated with a spatial node is then identified by a global node number $A \in \mathscr{N}_{no} = \{1,\dots,n_{no}\}$. As usual, the global node numbers and the element node numbers are related by connectivity matrices. The global numbers of the spatial nodes on the mechanical Dirichlet boundary are defined as elements of the index set $\mathscr{N}_\varphi = \{A \in \mathscr{N}_{no} | {}^A\boldsymbol{X} \in \partial_\varphi\mathscr{B}_0\}$. After the assembling of all spatial elements, the bilinear forms in Equation (A.6) leads to a bilinear form

$$\mathop{\mathsf{A}}_{e\in\mathscr{N}_{el}} \delta\mathbf{v}^{*,n,e}_{\tilde{\alpha}_j}\,\mathbf{M}^e\,\mathbf{x}^{n,e}_{\alpha_i}\,\frac{1}{h^n} = \delta\mathbf{v}^{*,n}_{\tilde{\alpha}_j}\,\mathbf{M}\,\mathbf{x}^n_{\alpha_i}\,\frac{1}{h^n} \tag{A.7}$$

where $\mathbf{M}$ denotes the global mass matrix, and the spatial node vectors $\delta\mathbf{v}^{*,n}_{\tilde{\alpha}_j}$ and $\mathbf{x}^n_{\alpha_i}$ includes the variations and nodal positions, respectively, indexed by the set $\mathscr{N}_{no}\setminus\mathscr{N}_{\varphi}$. The last step is to substitute matrix products for the remaining summations over the time nodes or temporal test nodes, respectively. We put the unknown position vectors $\mathbf{x}^n_{\alpha_{k+1}}$, $k=1,\ldots,m_{eq}$, in a column vector $\mathbf{x}^n=[\mathbf{x}^n_{\alpha_2},\ldots,\mathbf{x}^n_{\alpha_{m_{en}}}]$. Likewise, we obtain the row vector $\delta\mathbf{v}^{*,n}$ including all variations of the first space-time weak equation of motion. We arrive at the matrix form

$$\frac{1}{h^n}\,\delta\mathbf{v}^{*,n}\left[\tilde{\mathbf{a}}\otimes\mathbf{M}\,\mathbf{x}^n_{\alpha_1}\right] + \frac{1}{h^n}\,\delta\mathbf{v}^{*,n}\left[\tilde{\mathbf{A}}\otimes\mathbf{M}\right]\mathbf{x}^n \tag{A.8}$$

for the left hand side of Equation (4.21).

On the righthand side, we employ the approximation of the test function associated with the Lagrangian momentum field in Equation (A.1), and the approximation

$$\boldsymbol{v}^{n,e}_{\alpha}(\boldsymbol{\eta}) = \sum_{i=1}^{m_{en}}\ \sum_{a\in\mathscr{N}^e_{en}\setminus\mathscr{N}^e_{\varphi}} M^i(\alpha)\,N_a(\boldsymbol{\eta})\,{}^a\boldsymbol{v}^{n,e}_{\alpha_i} \tag{A.9}$$

of the Lagrangian deformation velocity field. Again, the spatial integration is only concerned with the spatial shape functions and the element density, and leads to the element mass matrices (A.3). Analogously, the time integration, in turn, is only related with the temporal shape functions. Hence, we obtain the matrix entries

$$[\tilde{\mathbf{b}}]^j = \int_{\mathscr{I}_\alpha} \tilde{M}^j(\alpha)\,M^1(\alpha) \qquad \text{and} \qquad [\tilde{\mathbf{B}}]^{j,k+1} = \int_{\mathscr{I}_\alpha} \tilde{M}^j(\alpha)\,M^{k+1}(\alpha) \tag{A.10}$$

$j,k=1,\ldots,m_{eq}$. As for the integral on the left hand side, we obtain a bilinear form by defining element velocity vectors $\mathbf{v}^{n,e}_{\alpha_i}$, which subsequently has to be assembled to global velocity vectors $\mathbf{v}^n_{\alpha_i}$. We arrive at a full matrix form by combining the unknown velocity vectors $\mathbf{v}^n_{\alpha_{k+1}}$, $k=1,\ldots,m_{eq}$, in a column vector $\mathbf{v}^n = [\mathbf{v}^n_{\alpha_2}, \dots, \mathbf{v}^n_{\alpha_{m_{en}}}]$.

In this way, we obtain the discrete weak form of the first equation of motion, given by

$$\boxed{\frac{1}{h^n}\,\delta\mathbf{v}^{*,n}\left\{\left[\tilde{\mathbf{a}}\otimes\mathbf{M}\,\mathbf{x}^n_{\alpha_1}\right]+\left[\tilde{\mathbf{A}}\otimes\mathbf{M}\right]\mathbf{x}^n\right\} = \delta\mathbf{v}^{*,n}\left\{\left[\tilde{\mathbf{b}}\otimes\mathbf{M}\,\mathbf{v}^n_{\alpha_1}\right]+\left[\tilde{\mathbf{B}}\otimes\mathbf{M}\right]\mathbf{v}^n\right\}} \tag{A.11}$$

Note that this equation can eliminate the velocity node vector $\mathbf{v}^n$ in the discrete weak form of the second equation of motion, after applying the fundamental lemma of calculus of variations.

A.2. Second equation of motion

We derive the matrix form pertaining to the second equation of motion in the same line. In the left hand side of Equation (4.24), we employ the approximations

$$\mathring{\boldsymbol{\pi}}^{n,e}_{\alpha}(\boldsymbol{\eta}) = \sum_{i=1}^{m_{en}} \sum_{a\in\mathscr{N}^e_{en}\setminus\mathscr{N}^e_{\varphi}} \mathring{M}^i(\alpha)\,\rho^e_0(\boldsymbol{\eta})\,N_a(\boldsymbol{\eta})\,{}^a\boldsymbol{v}^{*,n,e}_{\alpha_i} \tag{A.12}$$

and

$$\delta\mathring{\boldsymbol{\varphi}}^{n,e}_{\alpha}(\boldsymbol{\eta}) = \sum_{j=1}^{m_{eq}} \sum_{c\in\mathscr{N}^e_{en}\setminus\mathscr{N}^e_{\varphi}} \tilde{M}^j(\alpha)\,N_c(\boldsymbol{\eta})\,{}^c\delta\boldsymbol{x}^{n,e}_{\tilde{\alpha}_j} \tag{A.13}$$

By transforming the variations ${}^c\delta\boldsymbol{x}^{n,e}_{\tilde{\alpha}_j}$ into the associated covectors ${}^c\delta\boldsymbol{x}^{*,n,e}_{\tilde{\alpha}_j}$, and the covectors ${}^a\boldsymbol{v}^{*,n,e}_{\alpha_i}$ of the velocities at the element nodes into the corresponding vectors ${}^a\boldsymbol{v}^{n,e}_{\alpha_i}$, we obtain the components of the element mass matrices, defined in Equation (A.3). Assembling the element matrices, we arrive at the matrix form

$$\frac{1}{h^n}\,\delta\mathbf{x}^{*,n}\left[\tilde{\mathbf{a}}\otimes\mathbf{M}\,\mathbf{v}^n_{\alpha_1}\right] + \frac{1}{h^n}\,\delta\mathbf{x}^{*,n}\left[\tilde{\mathbf{A}}\otimes\mathbf{M}\right]\mathbf{v}^n \tag{A.14}$$

In the boundary integral on the righthand side of Equation (4.24), we employ the approximation of the Piola-Kirchhoff traction vector field in Equation (4.25) and the approximation of the test function, given by

Equation (A.13). According to the boundary integration, the spatial shape functions $N_c(\boldsymbol{\eta})$ of the test function leads to the reduced spatial shape functions $\bar{N}_c(\bar{\eta})$, $c \in \mathscr{N}_T^e$, on the mechanical Neumann boundary, and zero elsewhere. Since the boundary integration concerns only the reduced spatial shape functions, we obtain the boundary element matrix with the entries

$$[\overline{\mathbf{H}}^e_{ca}]^d{}_b = \left\{ \begin{array}{ll} \displaystyle\int_{\partial\mathscr{B}_\square} \bar{N}_c(\bar{\eta})\,\bar{N}_a(\bar{\eta})\bar{J}_0^e(\bar{\eta})\,[\boldsymbol{I}]^d{}_b & \text{for} \quad c, a \in \mathscr{N}_T^e, \\ 0 & \text{for} \quad c, a \in \mathscr{N}_{en}^e \setminus \mathscr{N}_\varphi^e \setminus \mathscr{N}_T^e \end{array} \right. \tag{A.15}$$

The assignment of the Piola-Kirchhoff traction load $\bar{\boldsymbol{t}}_\alpha^{n,e}$ to any temporal test node $\tilde{\alpha}_j$ in the time element $\mathscr{I}_\alpha$ takes over a time integration of the nodal load vector multiplied with the shape function $\tilde{M}^j(\alpha)$. Thus, we obtain a temporally averaged element traction load vector, which we combine in a column vector

$$[{}^a\bar{\mathbf{t}}^{n,e,j}]^b = \left\{ \begin{array}{ll} \displaystyle\int_{\mathscr{I}_\alpha} \tilde{M}^j(\alpha)[{}^a\bar{\boldsymbol{t}}_\alpha^{n,e}]^b & \text{for} \quad a \in \mathscr{N}_T^e, \\ 0 & \text{for} \quad a \in \mathscr{N}_{en}^e \setminus \mathscr{N}_\varphi^e \setminus \mathscr{N}_T^e \end{array} \right. \tag{A.16}$$

Now, we combine the variations in a row vector. Then, we assemble these element matrices. We obtain the boundary matrix $\overline{\mathbf{H}}$, which takes over the exact assignment of the traction loads to all boundary nodes independent of the size of the boundary elements. In the end, we obtain the matrix formulation

$$\sum_{j=1}^{m_{eq}} \delta\mathbf{x}^{*,n}_{\tilde{\alpha}_j} \overline{\mathbf{H}}\,\bar{\mathbf{t}}^{n,j} = \delta\mathbf{x}^{*,n}\mathbf{F}^n_{\text{ext}} \tag{A.17}$$

where the external force vector $\mathbf{F}^n_{\text{ext}}$ includes the loads for all nodes on the mechanical Neumann boundary in each direction, and zeros elsewhere.

In the volume integral, we apply the approximation of the test function in Equation (A.13), together with Equation (4.26) for calculating its Lagrangian gradient. We arrive at the internal force vector

$$[{}_c\boldsymbol{F}^{n,e,j}_{\text{int}}]^d = -\int_{\mathscr{I}_\alpha} \tilde{M}^j(\alpha) \int_{\mathscr{B}_\square} [{}_c\boldsymbol{B}^{n,e}_\alpha(\boldsymbol{\eta})]^d{}_{lk} [\boldsymbol{S}^{n,e,\square}_\alpha(\boldsymbol{\eta})]^{lk} J_0^e(\boldsymbol{\eta}) \tag{A.18}$$

where

$$[{}_c\boldsymbol{B}^{n,e}_\alpha(\boldsymbol{\eta})]^d{}_{lk} = [\mathrm{D}\boldsymbol{\varphi}^{n,e}_\alpha(\boldsymbol{\eta})]^d{}_l\,[\mathrm{D}N_c(\boldsymbol{\eta})]_k \tag{A.19}$$

denotes the entries of the so-called B-Tensor with respect to the spatial parent domain $\mathscr{B}_\square$. The tensor $\boldsymbol{S}^{n,e,\square}_\alpha(\boldsymbol{\eta})$ designates the pull-back of the second Piola-Kirchhoff stress tensor into $\mathscr{B}_\square$. This operation is analogous to pulling the Kirchhoff stress tensor $\boldsymbol{\tau}^{n,e}_\alpha(\boldsymbol{\eta})$ with respect to the current configuration back to the second Piola-Kirchhoff stress tensor with respect to the reference configuration by using the deformation gradient. Hence, we define

$$[\boldsymbol{S}^{n,e,\square}_\alpha(\boldsymbol{\eta})]^{ij} = [(\mathrm{D}\boldsymbol{\psi}^e_0)^{-1}(\boldsymbol{\eta})]^i{}_A\,[\boldsymbol{S}^{n,e}_\alpha(\boldsymbol{\eta})]^{AB}\,[(\mathrm{D}\boldsymbol{\psi}^e_0)^{-T}(\boldsymbol{\eta})]_B{}^j \tag{A.20}$$

We formulate the double contraction of the second Piola-Kirchhoff stress tensor with the B-Tensor as a matrix product. Thereby, we use the Voigt notation for the symmetric second Piola-Kirchhoff stress tensor. For a two-dimensional ambient space, any symmetric second order tensor $\boldsymbol{S}$ and any second order tensor $\boldsymbol{T}$ can be written as column vectors

$$\mathrm{vecs}(\boldsymbol{S}) = [S_{11},\, S_{22},\, S_{12}] \qquad \text{and} \qquad \mathrm{vec}(\boldsymbol{T}) = [T_{11}, T_{22}, \{T_{12} + T_{21}\}] \tag{A.21}$$

The matrix operator vecs maps the upper triangular matrix elements of a symmetric tensor $\boldsymbol{S}$ into a column vector s with the dimension $n_{\text{voi}} \times 1$, where the Voigt dimension n_{voi} coincides with $n_{\text{dim}}(n_{\text{dim}} + 1)/2$. On the other hand, to set up the matrix form of the B-tensor, we need the matrix operator vec, which maps the matrix elements of a tensor $\boldsymbol{T}$ into a $n_{\text{voi}} \times 1$ column vector t. Hence, the element matrices corresponding to the internal force vector reads

$$\mathsf{F}^{n,e,j}_{\text{int}} = -\int_{\mathscr{I}_\alpha} \tilde{M}^j(\alpha) \int_{\mathscr{B}_\square} \mathsf{B}^{n,e}_\alpha(\boldsymbol{\eta})\, \mathsf{s}^{n,e,\square}_\alpha(\boldsymbol{\eta})\, J^e_0(\boldsymbol{\eta}) \tag{A.22}$$

where

$$\mathsf{B}^{n,e}_\alpha(\boldsymbol{\eta}) = \Big[\big(\mathrm{vec}\big([{}_c\boldsymbol{B}^{n,e}_\alpha(\boldsymbol{\eta})]^{d=1}\big)\big)^T, \;\ldots\;, \big(\mathrm{vec}\big([{}_c\boldsymbol{B}^{n,e}_\alpha(\boldsymbol{\eta})]^{d=n_{\text{dim}}}\big)\big)^T\Big]_{c\in\mathscr{N}^e_{en}\setminus\mathscr{N}^e_\varphi} \tag{A.23}$$

denotes the matrix form of the B-tensor and $\mathsf{s}^{n,e,\square}_\alpha(\boldsymbol{\eta})$ designates the Voigt notation $\mathrm{vecs}(\boldsymbol{S}^{n,e,\square}_\alpha(\boldsymbol{\eta}))$ of the second Piola-Kirchhoff stress tensor, respectively. Assembling the element matrices, and combining the global force vectors at the test nodes, we obtain a matrix form analogous to Equation (A.17).

The matrix form of the additional weak term in Equation (5.18) takes the same form. Only the second Piola-Kirchhoff stress tensor field in Equation (A.18) has to be replaced by the corresponding trace tensor.

In this way, we arrive at the discrete weak form

$$\boxed{\frac{1}{h^n}\,\delta\mathbf{x}^{*,n}\left\{\left[\tilde{\mathbf{a}}\otimes\mathbf{M}\,\mathbf{v}^n_{\alpha_1}\right]+\left[\tilde{\mathbf{A}}\otimes\mathbf{M}\right]\mathbf{v}^n\right\}=\delta\mathbf{x}^{*,n}\left[\mathbf{F}^n_{\mathrm{ext}}+\mathbf{F}^n_{\mathrm{int}}+\mathbf{F}^n_{\mathrm{enh}}\right]} \tag{A.24}$$

including the virtual work of the global force vectors. Recall that the velocity note vector $\mathbf{v}^n$ can be eliminated by the first equation of motion. Then, the left side coincides with the kinetic energy increment $\mathcal{T}(t^{n+1})-\mathcal{T}(t^n)$ owing to the exact time integration (compare Equation (5.11)).

A.3. Entropy evolution equation

We use the space-time weak form of the entropy evolution in Equation (4.27) for determining the time evolution of the temperature. Hence, the temperature in the spatial notes at the time notes are the primary unknowns. On the left hand side, we employ only the approximations

$$\delta\Theta^{n,e}_{\alpha_1}(\boldsymbol{\eta})=\sum_{c\in\mathcal{N}^e_{en}\setminus\mathcal{N}^e_{\Theta}}N_c(\boldsymbol{\eta})\,{}^c\delta\Theta^{n,e}_{\alpha_1} \tag{A.25}$$

and

$$\delta\Theta^{n,e}_{\alpha}(\boldsymbol{\eta})=\sum_{j=1}^{m_{en}}\sum_{c\in\mathcal{N}^e_{en}\setminus\mathcal{N}^e_{\Theta}}M^j(\alpha)\,N_c(\boldsymbol{\eta})\,{}^c\delta\Theta^{n,e}_{\alpha_j} \tag{A.26}$$

Since the first weak term is only related to the test nodes at the first time note, we use the notation ${}^c\delta\Theta^{n,e}_{\alpha_j}\,\delta^j{}_1$ associated with a Kronecker symbol for relating these terms to all time nodes. The spatial integration in the first weak term is related to the jump of the internal energy density, to the relative temperature field at the first time node as well as to the spatial shape functions. Hence, we obtain an averaged entropy production vector

$$\mathbf{S}^{n,e,1}_{\mathrm{tra}}=\int_{\mathscr{B}_\square}\mathbf{n}^e_{\Theta}(\boldsymbol{\eta})\,\frac{\hat{e}^{n,e}_{\alpha_1}(\boldsymbol{\eta})-\hat{e}^{n,e}_{0}(\boldsymbol{\eta})}{\vartheta^{n,e}_{\alpha_1}(\boldsymbol{\eta})}\,J^e_0(\boldsymbol{\eta}) \tag{A.27}$$

where

$$\mathbf{n}^e_\Theta(\boldsymbol{\eta}) = [N_a(\boldsymbol{\eta})]_{a\in\mathscr{N}^e_{en}\setminus\mathscr{N}^e_\Theta} \tag{A.28}$$

denotes the shape functions column vector pertaining to the temperature, and the index 0 designates the initial value at t_{n-1}. We arrange the variations and the entropy trace at the element nodes in a row vector $\delta\mathbf{o}^{*,n}_{\alpha_i}$ and in a column vector $\mathbf{S}^{n,e,1}_{\text{tra}}$, respectively. The assembly of these element matrices leads to matrices in the global numbering $A \in \mathscr{N}_{no}\setminus\mathscr{N}_\Theta$. By combining the variations at all time nodes in a row vector, we obtain the matrix form

$$\sum_{j=1}^{m_{en}} \delta\mathbf{o}^{*,n}_{\alpha_j}\,\delta^j{}_1\,\mathbf{S}^{n,1}_{\text{tra}} = \delta\mathbf{o}^{*,n}\,\mathbf{S}^n_{\text{tra}} \tag{A.29}$$

where the column vector $\mathbf{S}^n_{\text{tra}}$ includes the vector $\mathbf{S}^{n,1}_{\text{tra}}$ as first entries, and zeros elsewhere.

In the second weak term, we employ the temporal approximation of the entropy in Equation (4.10). The time integration is only concerned with the temporal shape functions, and leads to the matrix components

$$[\mathbf{A}]^{ji} = \int_{\mathscr{I}^n_\alpha} M^j(\alpha)\,\mathring{M}^i(\alpha) \qquad\qquad i,j = 1,\dots,m_{en} \tag{A.30}$$

The spatial integration of the entropy at the time nodes, multiplied with the spatial shape function $N_a(\boldsymbol{\eta})$, $a \in \mathscr{N}^e_{en}\setminus\mathscr{N}^e_\Theta$, leads to the spatially averaged entropies at the element nodes. The assignment of the averaged entropy rate to the test nodes takes over the entries of the matrix $\mathbf{A}$. We obtain the column vector

$$\mathbf{S}^{n,e,j}_{\text{rat}} = \sum_{i=1}^{m_{en}} [\mathbf{A}]^{ji} \int_{\mathscr{B}_\Box} \mathbf{n}^e_\Theta(\boldsymbol{\eta})\,\eta^{n,e}_{\alpha_i}(\boldsymbol{\eta})\,J^e_0(\boldsymbol{\eta}) \tag{A.31}$$

After the assembly of the corresponding element matrices, the second weak term is given by a multiplication of a column vector $\mathbf{S}^n_{\text{rat}}$ with the row vector $\delta\mathbf{o}^{*,n}$, as in Equation (A.29).

In the first term on the righthand side of Equation (4.27), we employ the approximation of the assumed entropy flux in Equation (2.59), which is based on the temperature approximation

$$\Theta_{\alpha}^{n,e}(\boldsymbol{\eta}) = \sum_{i=1}^{m_{en}} \sum_{a \in \mathscr{N}_{en}^{e}} M^{i}(\alpha)\, N_{a}(\boldsymbol{\eta})\, {}^{a}\Theta_{\alpha_i}^{n,e} \tag{A.32}$$

where the temperatures ${}^{a}\Theta_{\alpha}^{n,e}$, $a \in \mathscr{N}_{en}^{e}$, denotes the temperatures of all element nodes, including the element nodes on the thermal Dirichlet boundary $\partial_{\Theta}\mathscr{B}_{0}^{e}$. The volume integration is confined only to the Lagrangian conductivity tensor and the Lagrangian gradient of the spatial shape functions. This Lagrangian gradient is split into to the Jacobian matrix

$$\mathrm{D}\mathbf{n}_{\Theta}^{e}(\boldsymbol{\eta}) = [\mathrm{D}N_{a}(\boldsymbol{\eta})]_{a \in \mathscr{N}_{en}^{e} \setminus \mathscr{N}_{\Theta}^{e}} \tag{A.33}$$

of the shape functions column vector and the inverse Frèchet derivative of the isoparametric transformation $\boldsymbol{\psi}_{0}^{e}(\boldsymbol{\eta})$ into the reference configuration. However, in view of the symmetry of the Lagrangian conductivity tensor, the entries of the Jacobian matrix in Equation (A.33) and the entries of the Jacobian matrix pertaining to the temperature approximation in Equation (A.32) are combined in the matrix form

$${}^{\Theta}\mathbf{B}_{\alpha}^{n,e}(\boldsymbol{\eta}) = \Big[\big(\mathrm{vec}\big(\,(\mathrm{D}\,\Theta_{\alpha}^{n,e}(\boldsymbol{\eta}))^{T}\,\mathrm{D}N_{c}(\boldsymbol{\eta})\,\big)\big)^{T}\Big]_{c \in \mathscr{N}_{en}^{e} \setminus \mathscr{N}_{\Theta}^{e}} \tag{A.34}$$

of the temperature-B-Tensor, defined analogously to Equation (A.23). Similar to the pull-back of the stress in Equation (A.20), the inverse Frèchet derivatives of the isoparametric transformation leads to a pull-back $\boldsymbol{K}_{\alpha}^{n,e,\square}(\boldsymbol{\eta})$ of the Lagrangian conductivity tensor. Time integration then leads to a temporally averaged entropy input arising from conduction of heat, given by

$$\mathbf{S}_{\mathrm{cdu}}^{n,e,j} = -\int_{\mathscr{I}_{\alpha}} M^{j}(\alpha) \int_{\mathscr{B}_{\square}} \frac{\Theta_{\infty}}{\{\Theta_{\alpha}^{n,e}(\boldsymbol{\eta})\}^{2}}\, {}^{\Theta}\mathbf{B}_{\alpha}^{n,e}(\boldsymbol{\eta})\, \mathbf{k}_{\alpha}^{n,e,\square}(\boldsymbol{\eta})\, J_{0}^{e}(\boldsymbol{\eta}) \tag{A.35}$$

where $\mathbf{k}_{\alpha}^{n,e,\square}(\boldsymbol{\eta})$ denotes the Voigt notation $\mathrm{vecs}(\boldsymbol{K}_{\alpha}^{n,e,\square}(\boldsymbol{\eta}))$. We assemble these column vectors, and subsequently combine all the entropy inputs at the time nodes in a column vector $\mathbf{S}_{\mathrm{cdu}}^{n}$.

The next weak term is concerned with the internal production of entropy.

Employing Equation (A.26) of the test function, we obtain the element matrix entries

$$\mathbf{S}_{\mathrm{dis}}^{n,e,j} = \int_{\mathscr{I}_\alpha} M^j(\alpha) \int_{\mathscr{B}_\square} \mathbf{n}_\Theta^e(\boldsymbol{\eta}) \, \frac{D_\alpha^{\mathrm{int},n,e}(\boldsymbol{\eta})}{\Theta_\alpha^{n,e}(\boldsymbol{\eta})} \, J_0^e(\boldsymbol{\eta}) \tag{A.36}$$

and finally the corresponding column vector $\mathbf{S}_{\mathrm{dis}}^n$. Likewise, we deal with the additional dissipation term in Equation (5.23). Substituting the corresponding algorithmic production of entropy for the internal dissipation in Equation (A.36), we obtain the column vector $\mathbf{S}_{\mathrm{alg}}^n$ of the algorithmic production of entropy.

In the boundary integral, we employ the test function and Equation (4.32) pertaining to the normal heat flux. The boundary integration is then concerned with the time-dependent boundary element matrix, given by the entries

$${}_{ca}\overline{\mathbf{G}}_\alpha^{n,e} = \begin{cases} \displaystyle\int_{\partial\mathscr{B}_\square} \frac{1}{\Theta_\alpha^{n,e}(\bar{\eta})} \, \bar{N}_c(\bar{\eta}) \, \bar{N}_a(\bar{\eta}) \, \bar{J}_0^e(\bar{\boldsymbol{\eta}}) & \text{for} \quad c, a \in \mathscr{N}_Q^e, \\ 0 & \text{for} \quad c, a \in \mathscr{N}_{en}^e \setminus \mathscr{N}_\Theta^e \setminus \mathscr{N}_Q^e \end{cases} \tag{A.37}$$

analogous to Equation (A.15). In a column vector $\mathbf{q}_\alpha^{n,e}$, we collect the normal heat fluxes at the element nodes in the set $\mathscr{N}_Q^e$, and account for the element nodes in the difference set $\mathscr{N}_{en}^e \setminus \mathscr{N}_\Theta^e \setminus \mathscr{N}_Q^e$ by a zero. We multiply this vector with the quadratic boundary element matrix corresponding to the entries in Equation (A.37), and obtain the temporally averaged entropy input vectors

$$\mathbf{S}_{\mathrm{ext}}^{n,e,j} = \int_{\mathscr{I}_\alpha} M^j(\alpha) \, \overline{\mathbf{G}}_\alpha^{n,e} \, \mathbf{q}_\alpha^{n,e} \tag{A.38}$$

for each element, which has to be assembled. After combining all time nodes in one column vector, we obtain the column vector $\mathbf{S}_{\mathrm{ext}}^n$ for the entropy input over the boundary.

Finally, we obtain the discrete weak form

$$\boxed{\delta\mathbf{o}^{*,n} \left[\mathbf{S}_{\mathrm{tra}}^n + \mathbf{S}_{\mathrm{rat}}^n\right] = h^n \, \delta\mathbf{o}^{*,n} \left[\mathbf{S}_{\mathrm{ext}}^n + \mathbf{S}_{\mathrm{cdu}}^n + \mathbf{S}_{\mathrm{dis}}^n + \mathbf{S}_{\mathrm{alg}}^n\right]} \tag{A.39}$$

of the space-time weak form of the entropy evolution equation.

A.4. Internal variable evolution equation

We determine the internal variable evolution locally in the spatial parent domain, by using the temporally weak form in Equation (4.33) in conjunction with the approximations

$$\delta\mathring{\boldsymbol{\Gamma}}^{n,e}_{\alpha}(\boldsymbol{\eta}) = \sum_{j=1}^{m_{eq}} \tilde{M}^{j}(\alpha)\,\delta\boldsymbol{\Gamma}^{n,e}_{\tilde{\alpha}_j}(\boldsymbol{\eta}) \qquad \text{and} \qquad \boldsymbol{\Gamma}^{n,e}_{\alpha}(\boldsymbol{\eta}) = \sum_{i=1}^{m_{en}} M^{i}(\alpha)\,\boldsymbol{\Gamma}^{n,e}_{\alpha_i}(\boldsymbol{\eta}) \tag{A.40}$$

Due to the symmetry of the internal variable in consequence of the isotropy of the material, the non-equilibrium stress tensor $\boldsymbol{\Upsilon}_{\alpha}(\boldsymbol{\eta})$ is also symmetric. In order to substitute an equivalent matrix product for the summation over the indices A and D, we apply the Voigt notation

$$\boldsymbol{\mathsf{y}}^{n,e}_{\alpha}(\boldsymbol{\eta}) = \operatorname{vec}\left(\boldsymbol{\Upsilon}^{n,e}_{\alpha}(\boldsymbol{\eta})\right) \qquad \text{and} \qquad \delta\boldsymbol{\mathsf{i}}^{*,n,e}_{\tilde{\alpha}_j}(\boldsymbol{\eta}) = \left(\operatorname{vecs}\left(\delta\mathring{\boldsymbol{\Gamma}}^{n,e}_{\tilde{\alpha}_j}(\boldsymbol{\eta})\right)\right)^{T} \tag{A.41}$$

where the first matrix is a column vector and the second matrix is a row vector.

First, we consider the left hand side of Equation (4.33). Since the time integration in this term concerns the temporal shape functions associated with the test function as well as the non-equilibrium stress tensor, we define the temporally averaged column vector

$$\boldsymbol{\mathsf{y}}^{n,e,j}(\boldsymbol{\eta}) = \int_{\mathscr{I}_{\alpha}} \tilde{M}^{j}(\alpha)\,\boldsymbol{\mathsf{y}}^{n,e}_{\alpha}(\boldsymbol{\eta}) \tag{A.42}$$

We combine the vectors of the non-equilibrium stress and the test function pertaining to all temporal test nodes in a column vector $\boldsymbol{\mathsf{y}}^{n,e}(\boldsymbol{\eta})$ and a row vector $\delta\boldsymbol{\mathsf{i}}^{*,n,e}(\boldsymbol{\eta})$, respectively. Thus, the left hand side of the weak form in Equation (4.33) reads

$$\sum_{j=1}^{m_{eq}} \delta\boldsymbol{\mathsf{i}}^{*,n,e}_{\tilde{\alpha}_j}(\boldsymbol{\eta})\,\boldsymbol{\mathsf{y}}^{n,e,j}(\boldsymbol{\eta}) = \delta\boldsymbol{\mathsf{i}}^{*,n,e}(\boldsymbol{\eta})\,\boldsymbol{\mathsf{y}}^{n,e}(\boldsymbol{\eta}) \tag{A.43}$$

On the righthand side, we cannot derive a more explicit form of the discrete problem, if employ the approximation of the internal variable. Therefore, we also use here the test function only. The approximated viscous stress tensor reads

$$\begin{aligned}[\boldsymbol{\Sigma}^{n,e}_{\alpha}(\boldsymbol{\eta})]^{AD} = {} & V_{\mathrm{dev}}\,[\boldsymbol{L}^{n,e}_{\alpha}(\boldsymbol{\eta})]^{A}{}_{C}\,[(\boldsymbol{\Gamma}^{n,e}_{\alpha})^{-1}(\boldsymbol{\eta})]^{CD} + \\ & + \frac{1}{2}\left(V_{\mathrm{vol}} - \frac{2\,V_{\mathrm{dev}}}{n_{\mathrm{dim}}}\right)\mathrm{tr}\,(\boldsymbol{L}^{n,e}_{\alpha}(\boldsymbol{\eta}))\,[(\boldsymbol{\Gamma}^{n,e}_{\alpha})^{-1}(\boldsymbol{\eta})]^{AD}\end{aligned} \tag{A.44}$$

Now, we proceed as for the non-equilibrium stress tensor. We define the temporally averaged stress tensor as in Equation (A.42). After introducing the Voigt notation and the final matrix form, we arrive at the column vector $\mathbf{z}^{n,e}$. In the end, we obtain the matrix form

$$\boxed{\delta\mathbf{i}^{*,n,e}(\boldsymbol{\eta})\,\mathbf{y}^{n,e}(\boldsymbol{\eta}) = \delta\mathbf{i}^{*,n,e}(\boldsymbol{\eta})\,\mathbf{z}^{n,e}(\boldsymbol{\eta})} \tag{A.45}$$

pertaining to the temporally weak form (4.33) of the viscous evolution equation. We refer to the left side as virtual non-equilibrium dissipation and to the right side as virtual viscous dissipation.

B. LINEARISATION OF THE ALGEBRAIC EQUATIONS

We obtain a numerical solution of the nonlinear algebraic problem derived in Appendix A by linearising the corresponding equations with respect to the primary variables, and iterating till a prescribed convergence criterion is fulfilled. The linearisation is performed by the procedure in Laursen & Meng [184]. We apply the directional derivative directly on the weak form, and introduce in the obtained scalar equations a matrix notation for the implementation.

In this way, we obtain not only the tangent matrices, but also the total Newton-Raphson method. Hence, typical implementation errors with the Voigt notation are avoided, and more appropriate convergence criteria as the norm of the solution vector can be derived.

B.1. Discrete mechanical Galerkin forms

We resolve the first equation of motion for the velocity node vector $\mathbf{v}^n$, and eliminate this vector in the weak form of the second equation of motion. First, we transform Equation (A.11) in a residual form and factor out the test vector $\delta\mathbf{v}^{*,n}$. According to the fundamental lemma of calculus of variations, the bracket has to vanish, and the velocity node vector reads

$$\mathbf{v}^n = \frac{1}{h^n}\left[\tilde{\mathbf{B}}^{-1}\tilde{\mathbf{a}}\otimes\mathbf{x}^n_{\alpha_1}\right] + \frac{1}{h^n}\left[\tilde{\mathbf{B}}^{-1}\tilde{\mathbf{A}}\otimes\mathbf{I}\right]\mathbf{x}^n - \left[\tilde{\mathbf{B}}^{-1}\tilde{\mathbf{b}}\otimes\mathbf{v}^n_{\alpha_1}\right] \tag{B.1}$$

We employ the velocity node vector in Equation (B.1) in the weak form of the second equation of motion, given by Equation (A.24), and arrive at the global mechanical Galerkin form G_{mech} depending on the nodal position vector $\mathbf{x}^n$, the nodal temperature vector $\mathbf{o}^n$, the internal variable vectors $\mathbf{i}^{n,e}(\boldsymbol{\eta})$ and the test node vector $\delta\mathbf{x}^{*,n}$. This Galerkin form takes the form

$$G_{\mathrm{mech}}(\{\mathbf{x}^n, \mathbf{o}^n, \mathbf{i}^{n,e}(\boldsymbol{\eta})\};\, \delta\mathbf{x}^{*,n}) \equiv G_{\mathrm{mech}}(\mathscr{X};\, \delta\mathbf{x}^{*,n}) \equiv \delta\mathbf{x}^{*,n}\,\mathbf{R}_{\mathrm{mech}}(\mathscr{X}) = 0 \tag{B.2}$$

where we refer to the column vector

$$
\begin{aligned}
\mathbf{R}_{\mathrm{mech}}(\mathscr{X}) := \frac{1}{(h^n)^2}\left[\tilde{\mathbf{A}}\tilde{\mathbf{B}}^{-1}\tilde{\mathbf{A}}\otimes\mathbf{M}\right]\mathbf{x}^n + \frac{1}{(h^n)^2}\left[\tilde{\mathbf{A}}\tilde{\mathbf{B}}^{-1}\tilde{\mathbf{a}}\otimes\mathbf{M}\mathbf{x}^n_{\alpha_1}\right] + \\
+ \frac{1}{h^n}\left[\tilde{\mathbf{a}} - \tilde{\mathbf{A}}\tilde{\mathbf{B}}^{-1}\tilde{\mathbf{b}}\right]\otimes\mathbf{M}\mathbf{v}^n_{\alpha_1} - \left[\mathbf{F}^n_{\mathrm{ext}} + \mathbf{F}^n_{\mathrm{int}} + \mathbf{F}^n_{\mathrm{enh}}\right]
\end{aligned}
\tag{B.3}
$$

as the residual vector. The above equation is one of two equations, which constitutes the global iteration of the coupled nonlinear equation system. In order to apply a Newton-Raphson scheme to these two equations, we begin by deriving the linearised equation

$$
\begin{aligned}
G_{\mathrm{mech}}(\mathscr{X};\,\delta\mathbf{x}^{*,n}) + \Delta_{\mathsf{x}}G_{\mathrm{mech}}(\mathscr{X};\,\delta\mathbf{x}^{*,n}) + \Delta_{\mathsf{o}}G_{\mathrm{mech}}(\mathscr{X};\,\delta\mathbf{x}^{*,n}) + \\
+ \Delta_{\mathsf{i}}G_{\mathrm{mech}}(\mathscr{X};\,\delta\mathbf{x}^{*,n}) = 0
\end{aligned}
\tag{B.4}
$$

The term $\Delta_{\mathsf{x}}G_{\mathrm{mech}}$ denotes the $\mathbf{x}$-increment of the global mechanical Galerkin form, and the terms $\Delta_{\mathsf{o}}G_{\mathrm{mech}}$ and $\Delta_{\mathsf{i}}G_{\mathrm{mech}}$ represent the $\mathbf{o}$- and $\mathbf{i}$-increment of Equation (B.2), respectively.

B.1.1. The $\mathbf{x}$*-increment of the global mechanical Galerkin form.* We start with the increment of the Galerkin form G_{mech} pertaining to the nodal position vector, given by

$$
\Delta_{\mathsf{x}}G_{\mathrm{mech}}(\mathscr{X};\,\delta\mathbf{x}^{*,n}) = \left.\frac{\mathrm{d}}{\mathrm{d}s}\right|_{s=0} G_{\mathrm{mech}}(\{\mathbf{x}^n + s\Delta\mathbf{x}^n, \mathbf{o}^n, \mathbf{i}^{n,e}(\boldsymbol{\eta})\};\,\delta\mathbf{x}^{*,n})
\tag{B.5}
$$

Assuming no displacement-depending external loads in the global mechanical Galerkin form, the first virtual energy term in the second line of Equation (B.2) as well as the internal and enhanced virtual work associated with the internal and algorithmic global force vector, respectively, contribute to $\Delta_{\mathsf{x}}G_{\mathrm{mech}}$. We obtain

$$
\Delta_{\mathsf{x}}G_{\mathrm{mech}} = \frac{1}{(h^n)^2}\,\delta\mathbf{x}^{*,n}\left[\tilde{\mathbf{A}}\tilde{\mathbf{B}}^{-1}\tilde{\mathbf{A}}\otimes\mathbf{M}\right]\Delta\mathbf{x}^n - \delta\mathbf{x}^{*,n}\left.\frac{\mathrm{d}}{\mathrm{d}s}\right|_{s=0}\left\{\mathbf{F}^n_{\mathrm{int},s} + \mathbf{F}^n_{\mathrm{enh},s}\right\}
\tag{B.6}
$$

According to Equation (A.22), the $\mathbf{x}$-increment of the internal force vector is split up into two parts. The so-called geometrical part results from linearising the B-tensor, and the linearisation of the second Piola-Kirchhoff stress tensor implies a material part. Going down to the element level, the increment takes the form

$$\begin{aligned}
-\delta\mathbf{x}^{*,n}\ \frac{\mathrm{d}}{\mathrm{d}s}\bigg|_{s=0}\mathbf{F}^{n}_{\mathrm{int},s} &= -\delta\mathbf{x}^{*,n}\left\{{}_{\mathrm{Geo}}\mathbf{K}^{n}_{\mathrm{Int}} + {}_{\mathrm{Mat}}\mathbf{K}^{n}_{\mathrm{Int}}\right\}\varDelta\mathbf{x}^{n}\\
&= -\sum_{j=1}^{m_{eq}}\delta\mathbf{x}^{*,n}_{\tilde{\alpha}_j}\sum_{k=1}^{m_{eq}}\left\{{}^{k+1}_{\mathrm{Geo}}\mathbf{K}^{n,j}_{\mathrm{Int}} + {}^{k+1}_{\mathrm{Mat}}\mathbf{K}^{n,j}_{\mathrm{Int}}\right\}\varDelta\mathbf{x}^{n}_{\alpha_{k+1}}\\
&= -\sum_{j=1}^{m_{eq}}\mathop{\mathsf{A}}_{e\in\mathscr{N}_{el}}\delta\mathbf{x}^{*,n,e}_{\tilde{\alpha}_j}\sum_{k=1}^{m_{eq}}\left\{{}^{k+1}_{\mathrm{Geo}}\mathbf{K}^{n,e,j}_{\mathrm{Int}} + {}^{k+1}_{\mathrm{Mat}}\mathbf{K}^{n,e,j}_{\mathrm{Int}}\right\}\varDelta\mathbf{x}^{n,e}_{\alpha_{k+1}}
\end{aligned}\tag{B.7}$$

where $\mathbf{K}$ symbolise a quadratic stiffness matrix. The geometrical part of the element stiffness matrix is based on the pull-back $\boldsymbol{S}^{n,e,\square}_{\alpha}(\boldsymbol{\eta})$ of the second Piola-Kirchhoff stress tensor in the parent domain, given by Equation (A.20). With this definition, we obtain the element stiffness matrix

$$\boxed{{}^{k+1}_{\mathrm{Geo}}\mathbf{K}^{n,e,j}_{\mathrm{Int}} = -\int_{\mathscr{I}_\alpha}\tilde{M}^{j}(\alpha)\,M^{k+1}(\alpha)\int_{\mathscr{B}_\square}\mathrm{D}\mathbf{n}^{e}(\boldsymbol{\eta})\,\boldsymbol{S}^{n,e,\square}_{\alpha}(\boldsymbol{\eta})\,(\mathrm{D}\mathbf{n}^{e}(\boldsymbol{\eta}))^{T}J^{e}_{0}(\boldsymbol{\eta})\otimes\boldsymbol{I}}\tag{B.8}$$

The material part of the element stiffness matrix results from linearising the stress tensor $\boldsymbol{S}^{n,e,\square}_{\alpha}(\boldsymbol{\eta})$ with respect to the nodal position vector. First, we determine the derivative of the stress tensor with respect to the right Cauchy-Green tensor $\boldsymbol{C}^{n,e,\square}(\boldsymbol{\eta})$, defined in Equation (4.31). A pull-back operation leads to the components

$$[{}^{CC}\mathbb{L}^{n,e,\square}_{\alpha}(\boldsymbol{\eta})]^{lkmn} = 2\,\frac{\partial[\boldsymbol{S}^{n,e,\square}_{\alpha}(\boldsymbol{\eta})]^{lk}}{\partial C_{CD}}\,[(\mathrm{D}\boldsymbol{\psi}^{e}_{0})^{-T}(\boldsymbol{\eta})]_{C}{}^{m}\,[(\mathrm{D}\boldsymbol{\psi}^{e}_{0})^{-T}(\boldsymbol{\eta})]_{D}{}^{n}\tag{B.9}$$

of the fourth-order material tensor ${}^{CC}\mathbb{L}^{n,e,\square}_{\alpha}(\boldsymbol{\eta})$ with respect to the spatial parent domain. Since this material tensor is symmetric in its first and second slot as well as in its third and fourth slot, we apply the Voigt matrix notation in Equation (A.21) to the first and the second double contraction. In this way, we obtain the square matrix

$$
{}^{CC}\mathbf{L}^{n,e,\square}_{\alpha}(\boldsymbol{\eta}) = \begin{bmatrix} [{}^{CC}\mathbb{L}^{n,e,\square}_{\alpha}(\boldsymbol{\eta})]^{1111} & [{}^{CC}\mathbb{L}^{n,e,\square}_{\alpha}(\boldsymbol{\eta})]^{1122} & [{}^{CC}\mathbb{L}^{n,e,\square}_{\alpha}(\boldsymbol{\eta})]^{1112} \\ [{}^{CC}\mathbb{L}^{n,e,\square}_{\alpha}(\boldsymbol{\eta})]^{2211} & [{}^{CC}\mathbb{L}^{n,e,\square}_{\alpha}(\boldsymbol{\eta})]^{2222} & [{}^{CC}\mathbb{L}^{n,e,\square}_{\alpha}(\boldsymbol{\eta})]^{2212} \\ [{}^{CC}\mathbb{L}^{n,e,\square}_{\alpha}(\boldsymbol{\eta})]^{1211} & [{}^{CC}\mathbb{L}^{n,e,\square}_{\alpha}(\boldsymbol{\eta})]^{1222} & [{}^{CC}\mathbb{L}^{n,e,\square}_{\alpha}(\boldsymbol{\eta})]^{1212} \end{bmatrix} \tag{B.10}
$$

for a two-dimensional ambient space. Finally, we linearise the right Cauchy-Green tensor $\boldsymbol{C}^{n,e,\square}_{\alpha}(\boldsymbol{\eta})$ with respect to the nodal positions of the e-th element at the time nodes. We obtain a further B-tensor with respect to the spatial parent domain $\mathscr{B}_{\square}$, given by the components

$$
[{}_a\boldsymbol{B}^{*,n,e}_{\alpha_{k+1}}(\boldsymbol{\eta})]_{mnb} = [\mathrm{D}N_a(\boldsymbol{\eta})]_m [(\mathrm{D}\boldsymbol{\varphi}^{n,e}_{\alpha_{k+1}}(\boldsymbol{\eta}))^T]_n{}^o\,\delta_{ob} \tag{B.11}
$$

Since we apply the matrix form of the material tensor in Equation (B.10), we have to introduce a matrix form $\mathbf{B}^{*,n,e}_{\alpha_{k+1}}(\boldsymbol{\eta})$ corresponding to this B-tensor. This matrix takes a form, which is analogous to the transpose of the matrix $\mathbf{B}^{n,e}_{\alpha}(\boldsymbol{\eta})$. In the end, the material part of the element stiffness matrix reads

$$
\boxed{{}^{k+1}_{\mathrm{Mat}}\mathbf{K}^{n,e,j}_{\mathrm{Int}} = -\int_{\mathscr{I}_\alpha} \tilde{M}^j(\alpha)\, M^{k+1}(\alpha) \int_{\mathscr{B}_\square} \mathbf{B}^{n,e}_{\alpha}(\boldsymbol{\eta})\ {}^{CC}\mathbf{L}^{n,e,\square}_{\alpha}(\boldsymbol{\eta})\ \mathbf{B}^{*,n,e}_{\alpha_{k+1}}(\boldsymbol{\eta})\, J^e_0(\boldsymbol{\eta})} \tag{B.12}
$$

where

$$
\mathbf{B}^{*,n,e}_{\alpha_{k+1}}(\boldsymbol{\eta}) = \left[\mathrm{vec}([{}_a\boldsymbol{B}^{*,n,e}_{\alpha_{k+1}}(\boldsymbol{\eta})]_{b=1}) \ \ldots \ \mathrm{vec}([{}_a\boldsymbol{B}^{*,n,e}_{\alpha_{k+1}}(\boldsymbol{\eta})]_{b=n_{\mathrm{dim}}})\right]_{a\in\mathscr{N}^e_{en}\setminus\mathscr{N}^e_{\varphi}} \tag{B.13}
$$

Now, we determine the linearised enhanced virtual work associated with the algorithmic global force vector $\mathbf{F}^n_{\mathrm{enh}}$. The corresponding stiffness matrix is composed of four parts. First, we have a geometrical part analogous to that in Equation (B.8), however, associated with the stress trace tensor with respect to the spatial parent domain. We obtain the geometrical tangent

$$
\boxed{{}^{k+1}_{\mathrm{Geo}}\mathbf{K}^{n,e,j}_{\mathrm{Enh}} = -\int_{\mathscr{I}_\alpha} \tilde{M}^j(\alpha)\, M^{k+1}(\alpha) \int_{\mathscr{B}_\square} \mathrm{D}\mathbf{n}^e(\boldsymbol{\eta})\, \hat{\boldsymbol{S}}^{n,e,\square}_{\alpha}(\boldsymbol{\eta})\, (\mathrm{D}\mathbf{n}^e(\boldsymbol{\eta}))^T J^e_0(\boldsymbol{\eta}) \otimes \boldsymbol{I}} \tag{B.14}
$$

where

$$[\hat{\boldsymbol{S}}_\alpha^{n,e,\square}(\boldsymbol{\eta})]^{ij} = [(\mathrm{D}\boldsymbol{\psi}_0^e)^{-1}(\boldsymbol{\eta})]^i{}_A \, [\hat{\boldsymbol{S}}_\alpha^{n,e}(\boldsymbol{\eta})]^{AB} \, [(\mathrm{D}\boldsymbol{\psi}_0^e)^{-T}(\boldsymbol{\eta})]_B{}^j \tag{B.15}$$

Then, we obtain a material stiffness matrix by linearising the derivative with respect to α of the approximated right Cauchy-Green tensor in the reference configuration. In the following, we use a shorthand notation for the lengthy fraction in Equation (5.18). The numerator is indicated by $N_S^{e,\square}(\boldsymbol{\eta})$ and the scaling term in the denominator is denoted by $D_S^{e,\square}(\boldsymbol{\eta})$. We arrive at the material tangent

$$\boxed{{}^{k+1}_{\mathrm{Mat}}\mathbf{K}^{n,e,j}_{\mathrm{Enh}} = -\int_{\mathscr{I}_\alpha} \tilde{M}^j \, \mathring{M}^{k+1} \int_{\mathscr{B}_\square} \mathbf{B}_\alpha^{n,e} \, \frac{N_S^{e,\square}}{D_S^{e,\square}} \, {}_{\mathrm{sym}}\mathbf{L}^{e,\square} \, \mathbf{B}^{*,n,e}_{\alpha_{k+1}} \, J_0^e} \tag{B.16}$$

The matrix ${}_{\mathrm{sym}}\mathbf{L}^{e,\square}$ denotes a matrix form of a fourth order tensor analogous to Equation (B.10). The corresponding fourth-order tensor coincides with the pull-back of the double partial derivative of the right Cauchy-Green tensor in the reference configuration with respect to itself into the spatial parent domain, given by

$$[{}_{\mathrm{sym}}\mathbb{L}^{e,\square}(\boldsymbol{\eta})]^{lkmn} = [(\boldsymbol{c}_0^e(\boldsymbol{\eta}))^{-1}]^{lm}[(\boldsymbol{c}_0^e(\boldsymbol{\eta}))^{-1}]^{kn} + [(\boldsymbol{c}_0^e(\boldsymbol{\eta}))^{-1}]^{ln}[(\boldsymbol{c}_0^e(\boldsymbol{\eta}))^{-1}]^{km} \tag{B.17}$$

where

$$[\boldsymbol{c}_0^e(\boldsymbol{\eta})]_{lm} = [(\mathrm{D}\boldsymbol{\psi}_0^e(\boldsymbol{\eta}))^T]_l{}^A \delta_{AB} [\mathrm{D}\boldsymbol{\psi}_0^e(\boldsymbol{\eta})]^B{}_m \tag{B.18}$$

designates the right Cauchy-Green tensor of the isoparametric transformation from the spatial parent domain in the reference configuration.

The next step comprises the linearisation of the numerator $N_S^{e,\square}(\boldsymbol{\eta})$ of the stress trace tensor, which leads to the tangent matrix

$$\boxed{{}^{k+1}_{\mathrm{Num}}\mathbf{K}^{n,e,j}_{\mathrm{Enh}} = -\int_{\mathscr{I}_\alpha} \tilde{M}^j \int_{\mathscr{B}_\square} \mathbf{B}_\alpha^{n,e} \, \frac{1}{2\,D_S^{e,\square}} \, {}_{\mathrm{sym}}\mathbf{L}^{e,\square} \, \mathring{\mathbf{c}}_\alpha^{n,e,\square} \, {}_{\mathrm{Num}}\mathbf{b}^{*,n,e}_{\alpha_{k+1}} \, J_0^e} \tag{B.19}$$

where the vector $\mathbf{c}_\alpha^{n,e,\square}$ denotes the column $\mathrm{vec}(\boldsymbol{C}_\alpha^{n,e,\square})$ of the right Cauchy-Green tensor with respect to the spatial parent domain, according to the definition in Equation (4.31) and the time approximation in Equation (5.14).

The row vector ${}_{\mathrm{Num}}\mathbf{b}^{*,n,e}_{\alpha_{k+1}}$ is composed of two terms. The first term corresponds to the time node t^{n+1} only, wherefore we introduce the Kronecker symbol $\delta^{k+1,m_{en}}$. Then, we obtain

$$\delta^{k+1,m_{en}}\left\{\mathbf{s}^{*,n,e,\square}_{\alpha_{k+1}}(\boldsymbol{\eta})-\vartheta^{n,e}_{\alpha_{k+1}}(\boldsymbol{\eta})\,\mathbf{t}^{*,n,e,\square}_{\alpha_{k+1}}(\boldsymbol{\eta})\right\}\mathbf{B}^{*,n,e}_{\alpha_{k+1}}(\boldsymbol{\eta}) \tag{B.20}$$

The star at the matrix form $\mathbf{s}^{n,e,\square}_{\alpha_{k+1}}$ of the stress tensor at the unknown time nodes with respect to the spatial parent domain indicates a row vector. The row vector $\mathbf{t}^{*,n,e,\square}_{\alpha_{k+1}}$ arise from the matrix form of the stress-temperature tensor with respect to the spatial parent domain, given by

$$\mathbf{t}^{n,e,\square}_{\alpha_i}(\boldsymbol{\eta})=\operatorname{vecs}(\boldsymbol{T}^{n,e,\square}_{\alpha_i}(\boldsymbol{\eta}))=\operatorname{vecs}(\partial_{\Theta}\boldsymbol{S}^{n,e,\square}_{\alpha_i}(\boldsymbol{\eta})) \tag{B.21}$$

The second term is a sum of time integrals, which are associated with the nodal position vectors at each unknown time node. In this term, we introduce the matrix form of the tensor $\mathbf{B}^{*,n,e}_{\alpha}$, which is analogously defined as in Equation (B.11), however, depends on the Fréchet derivative of the time approximation, given by Equation (4.17). The second term reads

$$\begin{aligned}
&+\int_{\mathscr{I}^{\eta}_{\alpha}}\mathring{M}^{k+1}(\alpha)\,\vartheta^{n,e}_{\alpha}(\boldsymbol{\eta})\,\mathbf{t}^{*,n,e,\square}_{\alpha_{k+1}}(\boldsymbol{\eta})\,\mathbf{B}^{*,n,e}_{\alpha_{k+1}}(\boldsymbol{\eta})-\\
&-\int_{\mathscr{I}_{\alpha}}\mathbf{s}^{*,n,e,\square}_{\alpha}(\boldsymbol{\eta})\left\{M^{k+1}(\alpha)\,\mathring{\mathbf{B}}^{*,n,e}_{\alpha}(\boldsymbol{\eta})+\mathring{M}^{k+1}(\alpha)\,\mathbf{B}^{*,n,e}_{\alpha}(\boldsymbol{\eta})\right\}-\\
&-\int_{\mathscr{I}_{\alpha}}M^{k+1}(\alpha)\,\mathbf{r}^{*,n,e,\square}_{\alpha}(\boldsymbol{\eta})\ {}^{CC}\mathbf{L}^{n,e,\square}_{\alpha}(\boldsymbol{\eta})\ \mathbf{B}^{*,n,e}_{\alpha_{k+1}}(\boldsymbol{\eta})+\\
&+\int_{\mathscr{I}_{\alpha}}M^{k+1}(\alpha)\,\mathring{\mathbf{i}}^{*,n,e}_{\alpha}(\boldsymbol{\eta})\ {}^{\varGamma C}\mathbf{L}^{n,e,\square}_{\alpha}(\boldsymbol{\eta})\ \mathbf{B}^{*,n,e}_{\alpha_{k+1}}(\boldsymbol{\eta})
\end{aligned} \tag{B.22}$$

The row vector $\mathbf{r}^{*,n,e,\square}_{\alpha}(\boldsymbol{\eta})$ coincides with the transposition of the column vector $\operatorname{vec}(\boldsymbol{R}^{n,e}_{\alpha}(\boldsymbol{\eta}))$, arising from the elastic deformation rate tensor with respect to the spatial parent domain. Analogous to Equation (2.47), we define

$$[\boldsymbol{R}^{n,e,\square}_{\alpha}(\boldsymbol{\eta})]_{kl}=[(\mathrm{D}\boldsymbol{\varphi}^{n,e}_{\alpha}(\boldsymbol{\eta}))^{T}]_{k}{}^{a}\,\delta_{ab}[\overset{\circ}{\overline{\mathrm{D}\boldsymbol{\varphi}^{n,e}_{\alpha}}}(\boldsymbol{\eta})]^{b}{}_{l} \tag{B.23}$$

We transform the first and the second double contraction of the material operator ${}^{\Gamma C}\mathbb{L}_{\alpha}^{n,e,\square}(\boldsymbol{\eta})$ in the corresponding matrix form. Since the row vector $\mathbf{i}_{\alpha}^{*,n,e}$ coincides with the transposition of the column vector $\operatorname{vecs}(\boldsymbol{\Gamma}_{\alpha}^{n,e})$ according to the symmetry of the internal variable, we obtain the matrix

$$
{}^{\Gamma C}\mathbf{L}_{\alpha}^{n,e,\square} = \begin{bmatrix} [{}^{\Gamma C}\mathbb{L}_{\alpha}^{n,e,\square}]^{1111} & [{}^{\Gamma C}\mathbb{L}_{\alpha}^{n,e,\square}]^{1122} & [{}^{\Gamma C}\mathbb{L}_{\alpha}^{n,e,\square}]^{1112} \\ [{}^{\Gamma C}\mathbb{L}_{\alpha}^{n,e,\square}]^{2211} & [{}^{\Gamma C}\mathbb{L}_{\alpha}^{n,e,\square}]^{2222} & [{}^{\Gamma C}\mathbb{L}_{\alpha}^{n,e,\square}]^{2212} \\ 2\,[{}^{\Gamma C}\mathbb{L}_{\alpha}^{n,e,\square}]^{1211} & 2\,[{}^{\Gamma C}\mathbb{L}_{\alpha}^{n,e,\square}]^{1222} & 2\,[{}^{\Gamma C}\mathbb{L}_{\alpha}^{n,e,\square}]^{1212} \end{bmatrix} \tag{B.24}
$$

where

$$
[{}^{\Gamma C}\mathbb{L}_{\alpha}^{n,e,\square}]^{ABlk} = \left\{ \frac{\partial[\boldsymbol{\Upsilon}_{\alpha}^{n,e}]^{AB}}{\partial C_{CD}} + \frac{\partial[\boldsymbol{\Upsilon}_{\alpha}^{n,e}]^{AB}}{\partial C_{DC}} \right\} [(\mathrm{D}\boldsymbol{\psi}_0^e)^{-T}]_C{}^{l}\, [(\mathrm{D}\boldsymbol{\psi}_0^e)^{-T}]_D{}^{k} \tag{B.25}
$$

The last part of the linearised enhanced virtual work follows from linearising the denominator $D_S^{e,\square}(\boldsymbol{\eta})$ of the Lagrange multiplier pertaining to the stress trace tensor. We obtain two terms. The first is associated with the time derivative of the right Cauchy-Green tensor, and the second corresponds to the elastic deformation rate tensor. Thus, we obtain the tangent

$$
\boxed{{}^{k+1}_{\mathrm{Den}}\mathbf{K}_{\mathrm{Enh}}^{n,e,j} = \int_{\mathscr{I}_\alpha} \tilde{M}^j \int_{\mathscr{B}_\square} \mathbf{B}_{\alpha}^{n,e}\, \frac{N_S^{e,\square}}{2\,(D_S^{e,\square})^2}\; {}_{\mathrm{sym}}\mathbf{L}^{e,\square}\; \mathring{\mathbf{c}}_{\alpha}^{n,e,\square}\; {}_{\mathrm{Den}}\mathbf{b}_{\alpha_{k+1}}^{*,n,e}\, J_0^e} \tag{B.26}
$$

where

$$
\begin{aligned} {}_{\mathrm{Den}}\mathbf{b}_{\alpha_{k+1}}^{*,n,e} = {} & \frac{1}{2}\int_{\mathscr{I}_\alpha} \mathring{\mathbf{c}}_{\alpha}^{*,n,e,\square}\; {}_{\mathrm{sym}}\mathbf{L}^{e,\square} \left\{ M^{k+1}\, \mathring{\mathbf{B}}_{\alpha}^{*,n,e} + \mathring{M}^{k+1}\, \mathbf{B}_{\alpha}^{*,n,e} \right\} + \\ & + \int_{\mathscr{I}_\alpha} \mathring{M}^{k+1}\, \mathbf{r}_{\alpha}^{*,n,e,\square}\; {}_{\mathrm{sym}}\mathbf{L}^{e,\square}\, \mathbf{B}_{\alpha_{k+1}}^{*,n,e} \end{aligned} \tag{B.27}
$$

denotes a row vector, which has to be separately integrated over the temporal parent domain.

B.1.2. The **o***-increment of the global mechanical Galerkin form.* The next step in the linearisation of the global mechanical Galerkin form in Equation (B.2) is to determine the **o**-increment pertaining to the m_{en}

unknown temperature nodes. Since we assume temperature-independent external forces, the directional derivative applied to the internal and algorithmic global force vector leads to

$$\Delta_{\mathsf{o}} G_{\mathrm{mech}}(\mathscr{Z};\, \delta\mathbf{x}^{*,n}) \;=\; -\sum_{j=1}^{m_{eq}} \mathop{\mathsf{A}}_{e\in\mathscr{N}_{el}} \delta\mathbf{x}_{\tilde{\alpha}_j}^{*,n,e} \sum_{k=1}^{m_{en}} \left\{ {}^{k}\mathbf{k}_{\mathrm{Int}}^{n,e,j} + {}^{k}\mathbf{k}_{\mathrm{Enh}}^{n,e,j} \right\} \Delta\mathbf{o}_{\alpha_k}^{n,e} \tag{B.28}$$

The tangent pertaining to the internal global force vector is based on the dependency of the second Piola-Kirchhoff stress tensor on the temperature. Therefore, this tangent depends on the stress-temperature tensor with respect to the spatial parent domain, and we arrive at

$$\boxed{{}^{k}\mathbf{k}_{\mathrm{Int}}^{n,e,j} = -\int_{\mathscr{I}_\alpha} \tilde{M}^{j}(\alpha) M^{k}(\alpha) \int_{\mathscr{B}_\square} \mathbf{B}_{\alpha}^{n,e}(\boldsymbol{\eta})\, \mathbf{t}_{\alpha}^{n,e,\square}(\boldsymbol{\eta})\, \mathbf{n}^{*,e}\, J_0^{e}(\boldsymbol{\eta})} \tag{B.29}$$

Since the denominator and the right Cauchy-Green tensor does not depend on the temperature nodes, we only have to linearise the numerator of the stress trace tensor. Therefore, we obtain only one part from linearising the algorithmic global force vector, given by

$$\boxed{{}^{k}\mathbf{k}_{\mathrm{Enh}}^{n,e,j} = -\int_{\mathscr{I}_\alpha} \tilde{M}^{j} \int_{\mathscr{B}_\square} \mathbf{B}_{\alpha}^{n,e}\, \frac{1}{2\, D_S^{e,\square}}\, {}_{\mathrm{sym}}\mathbf{L}^{e,\square}\, \mathring{\mathbf{c}}_{\alpha}^{n,e,\square}\, {}_{\mathrm{Enh}}\mathbf{n}_{\alpha_k}^{*,n,e}\, J_0^{e}} \tag{B.30}$$

where

$$\begin{aligned}
{}_{\mathrm{Enh}}\mathbf{n}_{\alpha_k}^{*,n,e}(\boldsymbol{\eta}) = {} & \left(\delta^{m_{en},k} - \delta^{1,k}\right) \vartheta_{\alpha_k}^{n,e}(\boldsymbol{\eta})\, \partial_{\Theta}\eta_{\alpha_k}^{n,e}(\boldsymbol{\eta})\, \mathbf{n}^{*,e}(\boldsymbol{\eta}) - \\
& -\int_{\mathscr{I}_\alpha^{\eta}} \left\{ \mathring{M}^{k}(\alpha)\, \vartheta_{\alpha}^{n,e}(\boldsymbol{\eta})\, \partial_{\Theta}\eta_{\alpha_k}^{n,e}(\boldsymbol{\eta}) + M^{k}(\alpha)\, \mathring{\eta}_{\alpha}^{n,e}(\boldsymbol{\eta}) \right\} \mathbf{n}^{*,e}(\boldsymbol{\eta}) - \\
& -\int_{\mathscr{I}_\alpha} M^{k}(\alpha)\, \mathbf{r}_{\alpha}^{*,n,e,\square}(\boldsymbol{\eta})\, \mathbf{t}_{\alpha}^{n,e,\square}(\boldsymbol{\eta})\, \mathbf{n}^{*,e}(\boldsymbol{\eta}) - \\
& -\int_{\mathscr{I}_\alpha} M^{k}(\alpha)\, \mathring{\mathbf{i}}_{\alpha}^{*,n,e}(\boldsymbol{\eta})\, \partial_{\Theta}\mathbf{y}_{\alpha}^{n,e}(\boldsymbol{\eta})\, \mathbf{n}^{*,e}(\boldsymbol{\eta})
\end{aligned} \tag{B.31}$$

Note that this row vector includes a part which is associated only with the element temperatures at the first and the last temporal time node, and furthermore, the time integration of the rest term is based on two different quadrature rules.

B.1.3. The i*-increment of the global mechanical Galerkin form.* Finally, we determine the i-increment of the global mechanical Galerkin form. Here, we also obtain $\mathrm{vecs}(\Delta\boldsymbol{\Gamma}^{n,e}_{\alpha_{k+1}}(\boldsymbol{\eta}))$ as the matrix form of the increment. Applying the directional derivative to the internal and algorithmic global force vector, we obtain the increment

$$\Delta_{\mathsf{i}} G_{\mathrm{mech}}(\mathscr{X};\,\delta\mathbf{x}^{*,n}) = -\sum_{j=1}^{m_{eq}} \mathop{\mathsf{A}}_{e\in\mathscr{N}_{el}} \delta\mathbf{x}^{*,n,e}_{\tilde{\alpha}_j} \sum_{k=1}^{m_{eq}} \int_{\mathscr{B}_\square} {}^{k+1}_{\mathrm{Con}}\mathbf{K}^{n,e,j}_{\mathrm{Mec}}(\boldsymbol{\eta})\,\Delta\mathsf{i}^{n,e}_{\alpha_{k+1}}(\boldsymbol{\eta})\, J_0^e(\boldsymbol{\eta}) \tag{B.32}$$

where

$$ {}^{k+1}_{\mathrm{Con}}\mathbf{K}^{n,e,j}_{\mathrm{Mec}}(\boldsymbol{\eta}) = {}^{k+1}_{\mathrm{Con}}\mathbf{K}^{n,e,j}_{\mathrm{Int}}(\boldsymbol{\eta}) + {}^{k+1}_{\mathrm{Con}}\mathbf{K}^{n,e,j}_{\mathrm{Enh}}(\boldsymbol{\eta}) \tag{B.33}$$

denotes the consistent tangent matrix for the internal variable evolution. Recall that the increments and the tangents depend on the position in the spatial parent domain. Since the matrix form pertaining to the partial derivative of the stress tensor with respect to the internal variable follows from Equation (B.24), we arrive at the tangent

$$\boxed{ {}^{k+1}_{\mathrm{Con}}\mathbf{K}^{n,e,j}_{\mathrm{Int}}(\boldsymbol{\eta}) = \int_{\mathscr{I}_\alpha} \tilde{M}^j(\alpha)\, M^{k+1}(\alpha)\, \mathbf{B}^{n,e}_{\alpha}(\boldsymbol{\eta})\, ({}^{\Gamma C}\mathbf{L}^{n,e,\square}_{\alpha}(\boldsymbol{\eta}))^T } \tag{B.34}$$

where the transpose of the negative material operator matrix ${}^{\Gamma C}\mathbf{L}$ substitute the matrix form ${}^{C\Gamma}\mathbf{L}$ pertaining to the partial derivative of the second Piola-Kirchhoff stress tensor with respect to the internal variable tensor.

The numerator of the stress trace tensor depends on the internal variable, because the free energy depends on the internal variable. In analogy to the tangent in the increment of the temperature nodes, we also obtain one tangent part, written as

$$\boxed{{}^{k+1}_{\mathrm{Con}}\mathsf{\mathbf{K}}^{n,e,j}_{\mathrm{Enh}}(\boldsymbol{\eta}) = -\int_{\mathscr{I}_\alpha} \frac{\tilde{M}^j(\alpha)}{2\, D_S^{e,\square}(\boldsymbol{\eta})}\, \mathsf{\mathbf{B}}^{n,e}_\alpha(\boldsymbol{\eta})\, {}_{\mathrm{sym}}\mathsf{\mathbf{L}}^{e,\square}(\boldsymbol{\eta})\, \mathring{\mathsf{\mathbf{c}}}^{n,e,\square}_\alpha(\boldsymbol{\eta})\, {}_{\mathrm{Enh}}\mathsf{\mathbf{l}}^{*,n,e}_{\alpha_{k+1}}(\boldsymbol{\eta})} \tag{B.35}$$

where

$$\begin{aligned} {}_{\mathrm{Enh}}\mathsf{\mathbf{l}}^{*,n,e}_{\alpha_{k+1}}(\boldsymbol{\eta}) = {}& \delta^{m_{en},k+1} \left\{ \vartheta^{n,e}_{\alpha_{k+1}}(\boldsymbol{\eta})\, \partial_\Theta \mathsf{\mathbf{y}}^{*,n,e}_{\alpha_{k+1}}(\boldsymbol{\eta}) - \mathsf{\mathbf{y}}^{*,n,e}_{\alpha_{k+1}}(\boldsymbol{\eta}) \right\} - \\ & -\int_{\mathscr{I}^\eta_\alpha} \mathring{M}^{k+1}(\alpha)\, \vartheta^{n,e}_\alpha(\boldsymbol{\eta})\, \partial_\Theta \mathsf{\mathbf{y}}^{*,n,e}_{\alpha_{k+1}}(\boldsymbol{\eta}) + \\ & + \int_{\mathscr{I}_\alpha} M^{k+1}(\alpha)\, \mathsf{\mathbf{r}}^{*,n,e,\square}_\alpha(\boldsymbol{\eta})\, ({}^{\Gamma C}\mathsf{\mathbf{L}}^{n,e,\square}_\alpha(\boldsymbol{\eta}))^T + \\ & + \int_{\mathscr{I}_\alpha} \left\{ \mathring{M}^{k+1}(\alpha)\, \mathsf{\mathbf{y}}^{*,n,e}_\alpha(\boldsymbol{\eta}) + M^{k+1}(\alpha)\, \mathring{\mathsf{\mathbf{i}}}^{*,n,e}_\alpha(\boldsymbol{\eta})\ {}^{\Gamma\Gamma}_{\mathrm{Non}}\mathsf{\mathbf{L}}^{n,e}_\alpha(\boldsymbol{\eta}) \right\} \end{aligned} \tag{B.36}$$

In the row vector ${}_{\mathrm{Enh}}\mathsf{\mathbf{l}}^{*,n,e}_{\alpha_{k+1}}(\boldsymbol{\eta})$, we have to employ the matrix form of the second partial derivative of the free energy with respect to the internal variable. Since we have on both sides of this fourth-order tensor a matrix form, which is associated with the symmetric internal variable, we obtain the matrix

$${}^{\Gamma\Gamma}_{\mathrm{Non}}\mathsf{\mathbf{L}}^{n,e}_\alpha = \begin{bmatrix} [{}^{\Gamma\Gamma}_{\mathrm{Non}}\mathbb{L}^{n,e,\square}_\alpha]^{1111} & [{}^{\Gamma\Gamma}_{\mathrm{Non}}\mathbb{L}^{n,e,\square}_\alpha]^{1122} & 2\,[{}^{\Gamma\Gamma}_{\mathrm{Non}}\mathbb{L}^{n,e,\square}_\alpha]^{1112} \\ [{}^{\Gamma\Gamma}_{\mathrm{Non}}\mathbb{L}^{n,e,\square}_\alpha]^{2211} & [{}^{\Gamma\Gamma}_{\mathrm{Non}}\mathbb{L}^{n,e,\square}_\alpha]^{2222} & 2\,[{}^{\Gamma\Gamma}_{\mathrm{Non}}\mathbb{L}^{n,e,\square}_\alpha]^{2212} \\ 2\,[{}^{\Gamma\Gamma}_{\mathrm{Non}}\mathbb{L}^{n,e,\square}_\alpha]^{1211} & 2\,[{}^{\Gamma\Gamma}_{\mathrm{Non}}\mathbb{L}^{n,e,\square}_\alpha]^{1222} & 4\,[{}^{\Gamma\Gamma}_{\mathrm{Non}}\mathbb{L}^{n,e,\square}_\alpha]^{1212} \end{bmatrix} \tag{B.37}$$

where

$$\begin{aligned} [{}^{\Gamma\Gamma}_{\mathrm{Non}}\mathbb{L}^{n,e}_\alpha(\boldsymbol{\eta})]^{ABCD} = {}& \frac{1}{4} \left\{ \frac{\partial[\boldsymbol{\Upsilon}^{n,e}_\alpha(\boldsymbol{\eta})]^{AB}}{\partial \Gamma_{CD}} + \frac{\partial[\boldsymbol{\Upsilon}^{n,e}_\alpha(\boldsymbol{\eta})]^{BA}}{\partial \Gamma_{CD}} \right\} + \\ & + \frac{1}{4} \left\{ \frac{\partial[\boldsymbol{\Upsilon}^{n,e}_\alpha(\boldsymbol{\eta})]^{AB}}{\partial \Gamma_{DC}} + \frac{\partial[\boldsymbol{\Upsilon}^{n,e}_\alpha(\boldsymbol{\eta})]^{BA}}{\partial \Gamma_{DC}} \right\} \end{aligned} \tag{B.38}$$

denotes the negative components of the second partial derivative of the free energy.

B.1.4. The increments of the local mechanical Galerkin form. The i-increment in the global mechanical Galerkin form is determined by the local mechanical Galerkin form

$$G^{e}_{\text{visc}}(\mathscr{Z};\,\delta\mathsf{i}^{*,n,e}(\boldsymbol{\eta})) \equiv \delta\mathsf{i}^{*,n,e}(\boldsymbol{\eta})\,\mathsf{R}^{e}_{\text{visc}}(\mathscr{Z}) := \delta\mathsf{i}^{*,n,e}(\boldsymbol{\eta})\,\{\mathsf{y}^{n,e}(\boldsymbol{\eta}) - \mathsf{z}^{n,e}(\boldsymbol{\eta})\} \tag{B.39}$$

pertaining to the viscous evolution equation. Since the non-equilibrium stress tensor generally depends on the nodal positions, the nodal temperatures as well as the internal variable, the total increment of the linearised equation is a sum of three increments. Hence, the corresponding linearised equation takes the form as in Equation (B.4), with the total increment

$$\begin{aligned} \mathit{\Delta} G^{e}_{\text{visc}}(\mathscr{Z};\,\delta\mathsf{i}^{*,n,e}(\boldsymbol{\eta})) = & \sum_{j,k=1}^{m_{eq}} \delta\mathsf{i}^{*,n,e}_{\tilde{\alpha}_j}(\boldsymbol{\eta})\ {}^{k+1}_{\text{Con}}\mathsf{K}^{n,e,j}_{\text{Evo}}(\boldsymbol{\eta})\,\mathit{\Delta}\mathsf{x}^{n,e}_{\alpha_{k+1}} + \\ & + \sum_{j,k=1}^{m_{eq}} \delta\mathsf{i}^{*,n,e}_{\tilde{\alpha}_j}(\boldsymbol{\eta})\ {}^{k}\mathsf{k}^{n,e,j}_{\text{Evo}}(\boldsymbol{\eta})\,\mathit{\Delta}\mathsf{o}^{n,e}_{\alpha_k} + \\ & + \sum_{j,k=1}^{m_{eq}} \delta\mathsf{i}^{*,n,e}_{\tilde{\alpha}_j}(\boldsymbol{\eta})\ {}^{k+1}\mathsf{K}^{n,e,j}_{\text{Evo}}(\boldsymbol{\eta})\,\mathit{\Delta}\mathsf{i}^{n,e}_{\alpha_{k+1}}(\boldsymbol{\eta}) \end{aligned} \tag{B.40}$$

where

$$\mathsf{K}^{n,e}_{\text{Evo}}(\boldsymbol{\eta}) = {}_{\text{Non}}\mathsf{K}^{n,e}_{\text{Evo}}(\boldsymbol{\eta}) - {}_{\text{Vis}}\mathsf{K}^{n,e}_{\text{Evo}}(\boldsymbol{\eta}) \tag{B.41}$$

denotes the tangential operators corresponding to the non-equilibrium stress tensor and the viscous stress tensor. We also assume in this equation constant viscosity parameters, so that there are no **x**- and **o**-increment from the viscous stress tensor. We only obtain the matrices

$$\boxed{\begin{aligned} {}^{k+1}_{\text{Con}}\mathsf{K}^{n,e,j}_{\text{Evo}}(\boldsymbol{\eta}) \quad &= \quad \int_{\mathscr{I}_\alpha} \tilde{M}^{j}(\alpha)\,M^{k+1}(\alpha)\,{}^{\mathit{\Gamma} C}\mathsf{L}^{n,e,\square}_{\alpha}(\boldsymbol{\eta})\,\mathsf{B}^{*,n,e}_{\alpha_{k+1}}(\boldsymbol{\eta}) \\ {}^{k}\mathsf{k}^{n,e,j}_{\text{Evo}}(\boldsymbol{\eta}) \quad &= \quad \int_{\mathscr{I}_\alpha} \tilde{M}^{j}(\alpha)\,M^{k}(\alpha)\,\partial_{\mathit{\Theta}}\mathsf{y}^{n,e}_{\alpha}(\boldsymbol{\eta})\,\mathsf{n}^{*,e}(\boldsymbol{\eta}) \end{aligned}} \tag{B.42}$$

from linearising the non-equilibrium stress tensor with respect to the nodal positions and temperatures, respectively.

The linearisation of the non-equilibrium stress tensor with respect to the internal variable leads to the matrix form in Equation (B.37), and the tangent matrices

$$\boxed{{}^{k+1}_{\text{Non}}\mathbf{K}^{n,e,j}_{\text{Evo}}(\boldsymbol{\eta}) = \int_{\mathscr{I}_\alpha} \tilde{M}^j(\alpha)\, M^{k+1}(\alpha)\ {}^{\Gamma\Gamma}_{\text{Non}}\mathbf{L}^{n,e}_\alpha(\boldsymbol{\eta})} \tag{B.43}$$

pertaining to the $k+1$ unknown nodal values of the internal variable.

The linearised form of the viscous stress tensor in Equation (A.44) is associated with fourth-order tensors for each unknown time node, which are written in matrix form analogously to Equation (B.37). The corresponding components read

$$\begin{aligned}
\big[{}^{k+1}_{\text{Vis}}\mathbb{L}^{n,e}_\alpha(\boldsymbol{\eta})\big]^{ADEF} = \frac{1}{4}\Big\{&\big[{}^{k+1}_{\boldsymbol{\mathsf{z}}}\mathbb{L}^{n,e}_\alpha(\boldsymbol{\eta})\big]^{ADEF} + \big[{}^{k+1}_{\boldsymbol{\mathsf{z}}}\mathbb{L}^{n,e}_\alpha(\boldsymbol{\eta})\big]^{DAEF}\Big\} + \\
&+ \frac{1}{4}\Big\{\big[{}^{k+1}_{\boldsymbol{\mathsf{z}}}\mathbb{L}^{n,e}_\alpha(\boldsymbol{\eta})\big]^{ADFE} + \big[{}^{k+1}_{\boldsymbol{\mathsf{z}}}\mathbb{L}^{n,e}_\alpha(\boldsymbol{\eta})\big]^{DAFE}\Big\}
\end{aligned} \tag{B.44}$$

where

$$\begin{aligned}
\big[{}^{k+1}_{\boldsymbol{\mathsf{z}}}\mathbb{L}^{n,e}_\alpha\big]^{ADEF} &= \frac{\mathring{M}^{k+1}}{h^n}\, 2\,V_{\text{dev}}\,[(\boldsymbol{\Gamma}^{n,e}_\alpha)^{-1}]^{AE}[(\boldsymbol{\Gamma}^{n,e}_\alpha)^{-1}]^{DF} + \\
&+ \frac{\mathring{M}^{k+1}}{h^n}\left(V_{\text{vol}} - \frac{2\,V_{\text{dev}}}{n_{\text{dim}}}\right)[(\boldsymbol{\Gamma}^{n,e}_\alpha)^{-1}]^{AD}[(\boldsymbol{\Gamma}^{n,e}_\alpha)^{-1}]^{EF} - \\
&- \quad 2\,M^{k+1}\left(V_{\text{vol}} - \frac{2\,V_{\text{dev}}}{n_{\text{dim}}}\right)[(\boldsymbol{\Gamma}^{n,e}_\alpha)^{-1}]^{AD}\,[\boldsymbol{L}^{n,e}_\alpha]^{E}{}_{C}\,[(\boldsymbol{\Gamma}^{n,e}_\alpha)^{-1}]^{CF} - \\
&- \quad 2\,M^{k+1}\left(V_{\text{vol}} - \frac{2\,V_{\text{dev}}}{n_{\text{dim}}}\right)\operatorname{tr}(\boldsymbol{L}^{n,e}_\alpha)\,[(\boldsymbol{\Gamma}^{n,e}_\alpha)^{-1}]^{AE}[(\boldsymbol{\Gamma}^{n,e}_\alpha)^{-1}]^{DF} - \\
&- \quad 2\,M^{k+1}\,2\,V_{\text{dev}}[(\boldsymbol{\Gamma}^{n,e}_\alpha)^{-1}]^{AE}\,[\boldsymbol{L}^{n,e}_\alpha]^{D}{}_{C}\,[(\boldsymbol{\Gamma}^{n,e}_\alpha)^{-1}]^{CF} - \\
&- \quad 2\,M^{k+1}\,2\,V_{\text{dev}}[\boldsymbol{L}^{n,e}_\alpha]^{A}{}_{C}\,[(\boldsymbol{\Gamma}^{n,e}_\alpha)^{-1}]^{CE}\,[(\boldsymbol{\Gamma}^{n,e}_\alpha)^{-1}]^{DF}
\end{aligned} \tag{B.45}$$

Here, we have employed the time approximation in Equation (4.15) pertaining to the viscous deformation rate tensor. For each test node $\tilde{\alpha}_j$, we obtain the tangent matrix blocks

$$\boxed{\;{}^{k+1}_{\text{Vis}}\mathbf{K}^{n,e,j}_{\text{Evo}}(\boldsymbol{\eta}) = \int_{\mathscr{I}_\alpha} \frac{\tilde{M}^j(\alpha)}{4}\;{}^{k+1}_{\text{Vis}}\mathbf{L}^{n,e}_{\alpha}(\boldsymbol{\eta})\;} \tag{B.46}$$

associated with the $k+1$ unknown nodal values of the internal variable.

B.1.5. The local iterative solution procedure. In order to determine the internal variable evolution, we solve the Galerkin form in Equation (B.39) on each spatial element. Therefore, the increments pertaining to the nodal positions and the nodal temperatures vanish in this case. Combining the nodal values pertaining to the temporal nodes, we arrive at a matrix form of a system of algebraic equations. Then, we apply the fundamental lemma of calculus of variations, and obtain the increment

$$\varDelta\mathbf{i}^{n,e}(\boldsymbol{\eta}) = -\left[\mathbf{K}^{n,e}_{\text{Evo}}(\boldsymbol{\eta})\right]^{-1}\mathbf{R}^{e}_{\text{visc}}(\mathscr{Z}) \tag{B.47}$$

Using locally an iterative solution procedure, we stop the iteration as soon as the Galerkin form in Equation (B.39) is numerically zero in the sense that its absolute value is less than a small tolerance tolevo. Therefore, we have to determine the variations at the test nodes corresponding to each iteration. Since the internal variable velocity lies in the test space corresponding to the local mechanical Galerkin form given by Equation (B.39), we solve a linear algebraic system at fixed and pairwise distinct points $\tilde{\xi}_k$, $k = 1, \ldots, m_{eq}$, in the temporal parent domain $\mathscr{I}_\alpha$ as in Equation (5.5). We obtain

$$\delta\mathbf{i}^{n,e}(\boldsymbol{\eta}) = \tilde{\mathbf{i}}^{n,e}(\boldsymbol{\eta}) := \left[(\tilde{\mathbf{W}})^{-1}\mathbf{W}' \otimes \boldsymbol{I}_{\text{voi}}\right]\begin{bmatrix} \mathbf{i}^{n,e}_{\alpha_1}(\boldsymbol{\eta}) \\ \mathbf{i}^{n,e}(\boldsymbol{\eta}) \end{bmatrix} \tag{B.48}$$

where $\tilde{\mathbf{W}}$ denotes the Haar matrix pertaining to the shape functions $\tilde{M}^j(\alpha)$, $j = 1, \ldots, m_{eq}$, at the points $\tilde{\xi}_k$, and the $m_{eq} \times m_{en}$ rectangular matrix $\mathbf{W}'$ has the entries $\mathring{M}^i(\tilde{\xi}_k)$ with the column index i. The identity matrix $\boldsymbol{I}_{\text{voi}}$ has the dimension $n_{\text{voi}} \times n_{\text{voi}}$. As points $\tilde{\xi}_k$, we choose the Gaussian quadrature points with respect to the interval $\mathscr{I}_\alpha$, at which we interpolate the time integrals in the Galerkin form. Employing the determined values at the test nodes, the

Galerkin form (B.39) leads to the stopping criterion

$$\boxed{\left|G^e_{\mathrm{visc}}(\mathscr{X};\tilde{\mathsf{i}}^{*,n,e}(\boldsymbol{\eta}))\right| \equiv \left|\tilde{\mathsf{i}}^{*,n,e}(\boldsymbol{\eta})\mathsf{R}^e_{\mathrm{visc}}(\mathscr{X})\right| \leqslant \mathsf{tolevo}} \tag{B.49}$$

where tolevo is a small tolerance that indicates the notion ‘numerically zero’.

The virtual viscous dissipation $\delta\mathsf{i}^{*,n,e}(\boldsymbol{\eta})\,\mathsf{z}^{n,e}(\boldsymbol{\eta})$ in the residual can be rewritten by recalling Equation (4.15) for the approximated viscous deformation rate tensor. Thus, the last term of the residual takes the form

$$h^n \int_{\mathscr{I}_\alpha} \left\{2\,V_{\mathrm{dev}}\,\mathrm{tr}\left(\{\boldsymbol{L}^{n,e}_\alpha(\boldsymbol{\eta})\}^2\right) + \left(V_{\mathrm{vol}} - \frac{2\,V_{\mathrm{dev}}}{n_{\mathrm{dim}}}\right)\{\mathrm{tr}\,(\boldsymbol{L}^{n,e}_\alpha(\boldsymbol{\eta}))\}^2\right\} \tag{B.50}$$

Since the integrand of Equation (B.50) is identical to the approximated internal dissipation $D^{\mathrm{int},n,e}_\alpha(\boldsymbol{\eta})$, this stopping criterion means that the difference between the temporally averaged non-equilibrium dissipation and the temporally averaged viscous dissipation is numerically zero, which is a discrete counterpart of Equation (2.72). Hence, we stop the iteration if the relation

$$\left|\tilde{\mathsf{i}}^{*,n,e}(\boldsymbol{\eta})\,\mathsf{y}^{n,e}(\boldsymbol{\eta}) - h^n\int_{\mathscr{I}_\alpha} D^{\mathrm{int},n,e}_\alpha(\boldsymbol{\eta})\right| \leqslant \mathsf{tolevo} \tag{B.51}$$

holds for a small tolerance tolevo. In this way, we use a physically motivated stopping criterion in contrast to the usual mathematically motivated stopping criterion of comparing any norm of the unknown nodes with tolevo. The advantage of the stopping criterion (B.49) is that the deformation of the element is taken into account, and so scaling problems are avoided.

B.1.6. The total increment of the global mechanical Galerkin form. Since the Galerkin form $G_{\mathrm{visc}}(\mathscr{X};\,\delta\mathsf{i}^{*,n,e}(\boldsymbol{\eta}))$ is numerically zero after the local iterative solution procedure, the increment in Equation (B.40) is numerically zero as well. Therefore, assuming an especially small tolerance tolevo, the fundamental lemma of calculus of variations approximately leads to the increment

$$\mathit{\Delta}\mathsf{i}^{n,e}(\boldsymbol{\eta}) = -\left[\mathsf{K}^{n,e}_{\mathrm{Evo}}(\boldsymbol{\eta})\right]^{-1} {}_{\mathrm{Con}}\mathsf{K}^{n,e}_{\mathrm{Evo}}(\boldsymbol{\eta})\,\mathit{\Delta}\mathsf{x}^{n,e} - \left[\mathsf{K}^{n,e}_{\mathrm{Evo}}(\boldsymbol{\eta})\right]^{-1} \mathsf{k}^{n,e}_{\mathrm{Evo}}(\boldsymbol{\eta})\,\mathit{\Delta}\mathsf{o}^{n,e} \tag{B.52}$$

By employing this equation in the increment $\mathit{\Delta}_{\mathsf{i}} G_{\text{mech}}$ of the global mechanical Galerkin form, we are able to express the increment $\mathit{\Delta}\mathbf{i}^{n,e}(\boldsymbol{\eta})$ pertaining to the internal variable vector by means of the increments of the nodal positions and nodal temperatures. Hence, we have to combine all the temporal nodes of the internal variable approximation in column vectors, before we are able to eliminate the increment. Then, we assemble the spatial nodes, and subsequently, we combine the temporal test nodes. In this way, the increment $\mathit{\Delta}_{\mathsf{i}} G_{\text{mech}}$ takes the form

$$\begin{aligned}
\mathit{\Delta}_{\mathsf{i}} G_{\text{mech}}(\mathscr{Z};\, \delta\mathbf{x}^{*,n}) \quad &= \quad \sum_{j=1}^{m_{eq}} \mathop{\mathsf{A}}_{e\in\mathscr{N}_{el}} \delta\mathbf{x}_{\tilde{\alpha}_j}^{*,n,e} \left[\mathbf{K}_{\text{Mec}}^{n,e,j} \mathit{\Delta}\mathbf{x}^{n,e} + \mathbf{k}_{\text{Mec}}^{n,e,j} \mathit{\Delta}\mathbf{o}^{n,e} \right] \\
&= \quad \sum_{j=1}^{m_{eq}} \delta\mathbf{x}_{\tilde{\alpha}_j}^{*,n}\, \mathbf{K}_{\text{Mec}}^{n,j} \mathit{\Delta}\mathbf{x}^{n} + \sum_{j=1}^{m_{eq}} \delta\mathbf{x}_{\tilde{\alpha}_j}^{*,n}\, \mathbf{k}_{\text{Mec}}^{n,j} \mathit{\Delta}\mathbf{o}^{n} \\
&= \quad \delta\mathbf{x}^{*,n}\, \mathbf{K}_{\text{Mec}}^{n} \mathit{\Delta}\mathbf{x}^{n} + \delta\mathbf{x}^{*,n}\, \mathbf{k}_{\text{Mec}}^{n} \mathit{\Delta}\mathbf{o}^{n}
\end{aligned} \tag{B.53}$$

where

$$\begin{aligned}
\mathbf{K}_{\text{Mec}}^{n,e,j} \quad &= \quad \int_{\mathscr{B}_\square} {}_{\text{Con}}\mathbf{K}_{\text{Mec}}^{n,e,j}(\boldsymbol{\eta}) \left(\mathbf{K}_{\text{Evo}}^{n,e}(\boldsymbol{\eta}) \right)^{-1} {}_{\text{Con}}\mathbf{K}_{\text{Evo}}^{n,e}(\boldsymbol{\eta})\, J_0^e(\boldsymbol{\eta}) \\
\mathbf{k}_{\text{Mec}}^{n,e,j} \quad &= \quad \int_{\mathscr{B}_\square} {}_{\text{Con}}\mathbf{K}_{\text{Mec}}^{n,e,j}(\boldsymbol{\eta}) \left(\mathbf{K}_{\text{Evo}}^{n,e}(\boldsymbol{\eta}) \right)^{-1} \mathbf{k}_{\text{Evo}}^{n,e}(\boldsymbol{\eta})\, J_0^e(\boldsymbol{\eta})
\end{aligned} \tag{B.54}$$

The total increment pertaining to the discrete mechanical Galerkin form then depends only on the increments of the nodal positions and nodal temperatures. After employing this increment in Equation (B.4), we arrive at the linearised equation

$$\boxed{\begin{aligned} G_{\mathrm{mech}}(\mathscr{Z};\,\delta\mathbf{x}^{*,n}) + \frac{1}{(h^n)^2}\,\delta\mathbf{x}^{*,n}\left[\tilde{\mathbf{A}}\tilde{\mathbf{B}}^{-1}\tilde{\mathbf{A}}\otimes\mathbf{M}\right]\Delta\mathbf{x}^{n} - & \\ -\,\delta\mathbf{x}^{*,n}\left[{}_{\mathrm{Geo}}\mathbf{K}^{n}_{\mathrm{Int}} + {}_{\mathrm{Mat}}\mathbf{K}^{n}_{\mathrm{Int}} - \mathbf{K}^{n}_{\mathrm{Mec}}\right]\Delta\mathbf{x}^{n} - & \\ -\,\delta\mathbf{x}^{*,n}\left[{}_{\mathrm{Geo}}\mathbf{K}^{n}_{\mathrm{Enh}} + {}_{\mathrm{Mat}}\mathbf{K}^{n}_{\mathrm{Enh}} + {}_{\mathrm{Num}}\mathbf{K}^{n}_{\mathrm{Enh}} + {}_{\mathrm{Den}}\mathbf{K}^{n}_{\mathrm{Enh}}\right]\Delta\mathbf{x}^{n} - & \\ -\,\delta\mathbf{x}^{*,n}\left[\mathbf{k}^{n}_{\mathrm{Int}} + \mathbf{k}^{n}_{\mathrm{Enh}} - \mathbf{k}^{n}_{\mathrm{Mec}}\right]\Delta\mathbf{o}^{n} = 0 & \end{aligned}} \tag{B.55}$$

Note that the coefficient matrix of each increment in Equation (B.52) can be interpreted as the solution $\mathbf{X}$ of a matrix equation of the general form $\mathbf{AX} = \mathbf{B}$, which means, in a computational implementation, we have not to calculate the inverse matrices explicitly.

B.2. Discrete thermal Galerkin form

In this section, we linearise the Galerkin form associated with the discrete weak form of the entropy evolution in Equation (A.39). We define the residual of this weak form as the discrete thermal Galerkin form

$$\begin{aligned} G_{\mathrm{ther}}(\mathscr{Z};\,\delta\mathbf{o}^{*,n}) := \delta\mathbf{o}^{*,n}\left[\mathbf{S}^{n}_{\mathrm{tra}} + \mathbf{S}^{n}_{\mathrm{rat}}\right] - & \\ -h^{n}\,\delta\mathbf{o}^{*,n}\left[\mathbf{S}^{n}_{\mathrm{ext}} + \mathbf{S}^{n}_{\mathrm{cdu}} + \mathbf{S}^{n}_{\mathrm{dis}} + \mathbf{S}^{n}_{\mathrm{alg}}\right] = 0 & \end{aligned} \tag{B.56}$$

We obtain a linearisation analogous to Equation (B.4) pertaining to the discrete mechanical Galerkin form.

B.2.1. The $\mathbf{x}$*-increment of the thermal Galerkin form.* We start with the linearisation in the column vector $\mathbf{x}^{n}$ including the nodal positions. Since the column vector $\mathbf{S}^{n}_{\mathrm{tra}}$, associated with the internal energy density jump, only depends on the initial positions, we immediately linearise the vector $\mathbf{S}^{n}_{\mathrm{rat}}$ associated with the entropy rate. The linearisation leads to the incremental virtual energy

$$\begin{aligned}
\delta\boldsymbol{\mathsf{o}}^{*,n}\,\varDelta_{\mathsf{x}}\boldsymbol{\mathsf{S}}^{n}_{\mathrm{Rat}}(\mathscr{X}) &= \delta\boldsymbol{\mathsf{o}}^{*,n}\,\frac{\mathrm{d}}{\mathrm{d}s}\bigg|_{s=0}\boldsymbol{\mathsf{S}}^{n}_{\mathrm{Rat}}(\boldsymbol{\mathsf{x}}^{n}+s\varDelta\boldsymbol{\mathsf{x}}^{n},\boldsymbol{\mathsf{o}}^{n},\boldsymbol{\mathsf{i}}^{n,e}(\boldsymbol{\eta}))\\
&= \delta\boldsymbol{\mathsf{o}}^{*,n}\,\boldsymbol{\mathsf{K}}^{n}_{\mathrm{Rat}}\;\varDelta\boldsymbol{\mathsf{x}}^{n}\\
&= \sum_{j=1}^{m_{en}}\mathop{\mathsf{A}}_{e\in N^{e}_{el}}\delta\boldsymbol{\mathsf{o}}^{*,n,e}_{\alpha_j}\sum_{k=1}^{m_{eq}}{}^{k+1}\boldsymbol{\mathsf{K}}^{n,e,j}_{\mathrm{Rat}}\,\varDelta\boldsymbol{\mathsf{x}}^{n,e}_{\alpha_{k+1}}
\end{aligned}\tag{B.57}$$

According to Equation (A.31), we have to apply the directional derivative to the entropy approximation at the time nodes. Since the entropy directly depends on the right Cauchy-Green tensor, we arrive via the linearisation of $\boldsymbol{C}^{n,e}_{\alpha_{k+1}}(\boldsymbol{\eta})$ at the third-order $\boldsymbol{B}^{*}$-tensor, defined in Equation (B.11). Taking the definition of the stress-temperature tensor into account, we obtain the matrix blocks

$$\boxed{{}^{k+1}\boldsymbol{\mathsf{K}}^{n,e,j}_{\mathrm{Rat}} = -[\boldsymbol{\mathsf{A}}]^{j,k+1}\int_{\mathscr{B}_\square}\boldsymbol{\mathsf{n}}^{e}(\boldsymbol{\eta})\,\boldsymbol{\mathsf{t}}^{*,n,e,\square}_{\alpha_{k+1}}(\boldsymbol{\eta})\,\boldsymbol{\mathsf{B}}^{*,n,e}_{\alpha_{k+1}}(\boldsymbol{\eta})\,J^{e}_{0}(\boldsymbol{\eta})}\tag{B.58}$$

of the global tangent matrix $\boldsymbol{\mathsf{K}}^{n}_{\mathrm{Rat}}$.

Since we neglect a heat surface density field $\overline{Q}_t$ which depends on the current position in the ambient space, the $\boldsymbol{\mathsf{x}}$-increment of the external load vector $\boldsymbol{\mathsf{S}}^{n}_{\mathrm{ext}}$ vanishes. The next step is therefore the linearisation of the temporally averaged entropy input arising from conduction of heat, given by

$$\delta\boldsymbol{\mathsf{o}}^{*,n}\,\varDelta_{\mathsf{x}}\boldsymbol{\mathsf{S}}^{n}_{\mathrm{cdu}}(\mathscr{X}) = \sum_{j=1}^{m_{en}}\mathop{\mathsf{A}}_{e\in N^{e}_{el}}\delta\boldsymbol{\mathsf{o}}^{*,n,e}_{\alpha_j}\sum_{k=1}^{m_{eq}}{}^{k+1}\boldsymbol{\mathsf{K}}^{n,e,j}_{\mathrm{Cdu}}\,\varDelta\boldsymbol{\mathsf{x}}^{n,e}_{\alpha_{k+1}}\tag{B.59}$$

Here, we have to linearise the determinant $J^{n,e}_{\alpha}(\boldsymbol{\eta})$ of the deformation gradient. Regarding Equation (4.20), this determinant coincides with the quotient of the Jacobian determinant pertaining to the approximated deformation mapping by the Jacobian determinant $J^{e}_{0}(\boldsymbol{\eta})$ of the spatial parametrisation. Then, we linearise the conductivity tensor on the spatial parent domain, and obtain so the matrix blocks

$$\boxed{{}^{k+1}\mathbf{K}_{\mathrm{Cdu}}^{n,e,j} = -\int_{\mathscr{I}_\alpha^\eta} M^j\, M^{k+1} \int_{\mathscr{B}_\square} \frac{\Theta_\infty}{\{\Theta_\alpha^{n,e}\}^2}\, {}^{\Theta}\mathbf{B}_\alpha^{n,e}\; {}_{\mathrm{Cdu}}\mathbf{L}_\alpha^{n,e,\square}\; \mathbf{B}_{\alpha_{k+1}}^{*,n,e}\, J_0^e} \tag{B.60}$$

where

$${}_{\mathrm{Cdu}}\mathbf{L}_\alpha^{n,e,\square}(\boldsymbol{\eta}) = k_0\, \frac{\det(\mathrm{D}\boldsymbol{\varphi}_\alpha^{n,e}(\boldsymbol{\eta}))}{J_0^e(\boldsymbol{\eta})} \left\{ \mathbf{ic}_\alpha^{n,e,\square}(\boldsymbol{\eta})\, \mathbf{ic}_\alpha^{*,n,e,\square}(\boldsymbol{\eta}) - {}_{\mathrm{sym}}^{\;C}\mathbf{L}_\alpha^{n,e,\square}(\boldsymbol{\eta}) \right\} \tag{B.61}$$

The column vector $\mathbf{ic}_\alpha^{n,e,\square}(\boldsymbol{\eta})$ coincides with the matrix notation $\mathrm{vecs}((\boldsymbol{C}_\alpha^{n,e,\square}(\boldsymbol{\eta}))^{-1})$ of the inverse right Cauchy-Green tensor on the spatial parent domain. The symmetric fourth-order tensor in Equation (B.61) is defined by substituting in Equation (B.17) the tensor $\boldsymbol{C}_\alpha^{n,e,\square}(\boldsymbol{\eta})$ for the tensor $\boldsymbol{c}_0^e(\boldsymbol{\eta})$.

Since the internal dissipation $D_\alpha^{\mathrm{int},n,e}$ and the algorithmic production of entropy in Equation (5.23) both do not depend on the nodal positions, we obtain no further $\mathbf{x}$-increments.

B.2.2. The $\mathbf{o}$*-increment of the thermal Galerkin form.* Now, we determine the increment of the temperature node vector. First, we linearise the first bracket in Equation (B.56), and obtain

$$\operatorname*{\mathsf{A}}_{e\in N_{el}^e} \delta\mathbf{o}_{\alpha_1}^{*,n,e}\, {}^{1}\mathbf{k}_{\mathrm{Tra}}^{n,e,1}\, \Delta\mathbf{o}_{\alpha_1}^{n,e} + \sum_{j=1}^{m_{en}} \operatorname*{\mathsf{A}}_{e\in N_{el}^e} \delta\mathbf{o}_{\alpha_j}^{*,n,e} \sum_{k=1}^{m_{en}} {}^{k}\mathbf{k}_{\mathrm{Rat}}^{n,e,j}\, \Delta\mathbf{o}_{\alpha_k}^{n,e} \tag{B.62}$$

In the first term, we obtain no temporal summation, because the column vector $\mathbf{S}_{\mathrm{tra}}^n$ pertaining to the entropy trace at the spatial element nodes depends only on the first temporal node, and is solely related with the variation at the first time node. Hence, the tangent includes only one non-zero block matrix, which is given by

$$\boxed{{}^{1}\mathbf{k}^{n,e,1}_{\mathrm{Tra}} = \int_{\mathscr{B}_\square} \mathbf{n}^e(\boldsymbol{\eta}) \left\{ \frac{\partial \eta^{n,e}_{\alpha_1}(\boldsymbol{\eta})}{\partial \Theta_{\alpha_1}} - \frac{[\![\hat{e}^{n,e}_{\alpha_1}(\boldsymbol{\eta})]\!]}{\{\vartheta^{n,e}_{\alpha_1}(\boldsymbol{\eta})\}^2} \right\} \mathbf{n}^{*,e}(\boldsymbol{\eta})\, J^e_0(\boldsymbol{\eta})} \tag{B.63}$$

In contrast, the column vector $\mathbf{S}^n_{\mathrm{rat}}$ depends on all unknown temperature nodes, because, according to Equation (4.10), the averaged entropy rate arise from an interpolation over the entropy rates at the time nodes. Thus, for each unknown time node, we arrive at tangent matrix blocks similar to the first term of Equation (B.63), which means

$$\boxed{{}^{k}\mathbf{k}^{n,e,j}_{\mathrm{Rat}} = [\mathbf{A}]^{jk} \int_{\mathscr{B}_\square} \mathbf{n}^e(\boldsymbol{\eta})\, \frac{\partial \eta^{n,e}_{\alpha_k}(\boldsymbol{\eta})}{\partial \Theta_{\alpha_k}}\, \mathbf{n}^{*,e}(\boldsymbol{\eta})\, J^e_0(\boldsymbol{\eta})} \tag{B.64}$$

Next, we linearise the column vector $\mathbf{S}^n_{\mathrm{ext}}$ of the entropy input over the boundary. Since we solely assume a time-dependent normal heat flux $\overline{\mathbf{Q}}^{n,e}_\alpha(\overline{\eta})$ during the motion, we have to apply the directional derivative only to the corresponding boundary element matrix in Equation (A.37). Hence, we obtain the linearised form

$$\delta\mathbf{o}^{*,n}\, \varDelta_{\mathbf{o}}\mathbf{S}^n_{\mathrm{ext}}(\mathscr{Z}) = \sum_{j=1}^{m_{en}} \mathop{\mathsf{A}}_{e\in N^e_{el}} \delta\mathbf{o}^{*,n,e}_{\alpha_j} \sum_{k=1}^{m_{en}} {}^{k}\mathbf{k}^{n,e,j}_{\mathrm{Ext}}\, \varDelta\mathbf{o}^{n,e}_{\alpha_k} \tag{B.65}$$

where

$$\boxed{{}^{k}\mathbf{k}^{n,e,j}_{\mathrm{Ext}} = -\int_{\mathscr{I}^\eta_\alpha} M^j\, M^k \begin{cases} \displaystyle\int_{\partial\mathscr{B}_\square} \frac{Q^{n,e}_\alpha}{\{\Theta^{n,e}_\alpha\}^2}\, \bar{N}_c\, \bar{N}_a\, \bar{J}^e_0 & \text{for } c,a \in \mathscr{N}^e_Q, \\ 0 & \text{for } c,a \in \mathscr{N}^e_{en}\backslash\mathscr{N}^e_\Theta\backslash\mathscr{N}^e_Q \end{cases}} \tag{B.66}$$

denotes the corresponding blocks of the tangent matrix. In order to arrived at matrix blocks which corresponds to all free nodes, we extended the matrix with zero entries, as already shown above in this work.

The linearised form of the assumed entropy flux field in the body is split into two parts, given by

$$\delta\mathbf{o}^{*,n}\,\Delta_{\mathbf{o}}\mathbf{S}^{n}_{\text{cdu}}(\mathscr{Z}) = \sum_{j=1}^{m_{en}} \mathop{\mathsf{A}}_{e\in N^{e}_{el}} \delta\mathbf{o}^{*,n,e}_{\alpha_j} \sum_{k=1}^{m_{en}} \left\{ {}^{k}_{\text{Geo}}\mathbf{k}^{n,e,j}_{\text{Cdu}} + {}^{k}_{\text{Mat}}\mathbf{k}^{n,e,j}_{\text{Cdu}} \right\} \Delta\mathbf{o}^{n,e}_{\alpha_k} \tag{B.67}$$

First, we obtain a geometrical part by linearising the Piola-Kirchhoff heat flux, and second, a material part from applying the directional derivative to the temperature in the denominator. Taking into account the Jacobian matrix of the shape functions in the first part and the definition of the temperature-B-tensor in the material part, we obtain the tangent blocks

$$\boxed{\begin{aligned} {}^{k}_{\text{Geo}}\mathbf{k}^{n,e,j}_{\text{Cdu}} &= -\int_{\mathscr{I}^{\eta}_{\alpha}} M^{j}\,M^{k} \int_{\mathscr{B}_{\square}} \frac{\Theta_{\infty}}{\{\Theta^{n,e}_{\alpha}\}^{2}} \mathrm{D}\mathbf{n}^{e}_{\Theta}\,\boldsymbol{K}^{n,e,\square}_{\alpha}\,(\mathrm{D}\mathbf{n}^{e}_{\Theta})^{T}\,J^{e}_{0} \\ {}^{k}_{\text{Mat}}\mathbf{k}^{n,e,j}_{\text{Cdu}} &= \int_{\mathscr{I}^{\eta}_{\alpha}} M^{j}\,M^{k} \int_{\mathscr{B}_{\square}} \frac{2\,\Theta_{\infty}}{\{\Theta^{n,e}_{\alpha}\}^{3}}\,{}^{\Theta}\mathbf{B}^{n,e}_{\alpha}\,\mathbf{k}^{n,e,\square}_{\alpha}\,\mathbf{n}^{*,e}\,J^{e}_{0} \end{aligned}} \tag{B.68}$$

where we used the symmetric conductivity tensor with respect to the parent domain as square matrix and as column vector, respectively.

The linearisation of the entropy production $\mathbf{S}_{\text{dis}}$ pertaining to the internal dissipation leads to one tangent part only, because D^{int}_{α} solely depends on the internal variable tensor. The corresponding block matrices read

$$\boxed{{}^{k}\mathbf{k}^{n,e,j}_{\text{Dis}} = -\int_{\mathscr{I}^{\eta}_{\alpha}} M^{j}(\alpha)\,M^{k}(\alpha) \int_{\mathscr{B}_{\square}} \mathbf{n}^{e}(\boldsymbol{\eta})\,\frac{D^{\text{int},n,e}_{\alpha}(\boldsymbol{\eta})}{\{\Theta^{n,e}_{\alpha}(\boldsymbol{\eta})\}^{2}}\,\mathbf{n}^{*,e}(\boldsymbol{\eta})\,J^{e}_{0}(\boldsymbol{\eta})} \tag{B.69}$$

We split the linearisation of the additional weak term in Equation (5.23) in two parts. First, we linearise the temperature quotient behind the test function. We arrive at a material tangent part. Then, we linearise the denominator of the large fraction. Thus, we arrive at the linearised form

$$\delta\mathbf{o}^{*,n}\,\Delta_{\mathbf{o}}\mathbf{S}^{n}_{\text{alg}}(\mathscr{Z}) = \sum_{j=1}^{m_{en}} \mathop{\mathsf{A}}_{e\in N^{e}_{el}} \delta\mathbf{o}^{*,n,e}_{\alpha_j} \sum_{k=1}^{m_{en}} \left\{ {}^{k}_{\text{Mat}}\mathbf{k}^{n,e,j}_{\text{Alg}} + {}^{k}_{\text{Den}}\mathbf{k}^{n,e,j}_{\text{Alg}} \right\} \Delta\mathbf{o}^{n,e}_{\alpha_k} \tag{B.70}$$

In order to write this matrix blocks in compact form, we introduce a shorthand notation for the large fraction in Equation (5.23). The numerator is denoted by the symbol $N_D^{e,\square}(\boldsymbol{\eta})$, and the symbol $D_D^{e,\square}(\boldsymbol{\eta})$ accounts for the corresponding denominator. Using this notation, we obtain the element matrices

$$\boxed{\begin{aligned} {}^{k}_{\mathrm{Mat}}\mathbf{k}^{n,e,j}_{\mathrm{Alg}} &= -\int_{\mathscr{I}^{\eta}_{\alpha}} M^j\, M^k \int_{\mathscr{B}_\square} \mathbf{n}^e\, \frac{N_D^{e,\square}}{D_D^{e,\square}}\, \frac{\vartheta^{n,e}_{\alpha} - \Theta_\infty}{\{\Theta^{n,e}_{\alpha}\}^3}\, \|\boldsymbol{L}^{n,e}_{\alpha}\|^4\, \mathbf{n}^{*,e}\, J^e_0 \\ {}^{k}_{\mathrm{Den}}\mathbf{k}^{n,e,j}_{\mathrm{Alg}} &= -\int_{\mathscr{I}^{\eta}_{\alpha}} M^j \int_{\mathscr{B}_\square} \mathbf{n}^e\, \frac{N_D^{e,\square}}{\{D_D^{e,\square}\}^2}\, \frac{\vartheta^{n,e}_{\alpha}}{\{\Theta^{n,e}_{\alpha}\}^2}\, {}_{\mathrm{Den}}\mathbf{n}^{n,e}_{\alpha_k}\, \|\boldsymbol{L}^{n,e}_{\alpha}\|^4\, \mathbf{n}^{*,e}\, J^e_0 \end{aligned}} \tag{B.71}$$

where

$${}_{\mathrm{Den}}\mathbf{n}^{n,e}_{\alpha_k}(\boldsymbol{\eta}) = \int_{\mathscr{I}^{\eta}_{\alpha}} 2\, M^k(\alpha)\, \frac{\vartheta^{n,e}_{\alpha}(\boldsymbol{\eta})\, \Theta_\infty}{\{\Theta^{n,e}_{\alpha}(\boldsymbol{\eta})\}^3}\, \|\boldsymbol{L}^{n,e}_{\alpha}(\boldsymbol{\eta})\|^4 \tag{B.72}$$

denotes the linearisation of the denominator with respect to the k-th time node.

B.2.3. The $\mathbf{i}$*-increment of the thermal Galerkin form.* The column vector $\mathbf{S}^n_{\mathrm{tra}}$ arising from the internal energy density jump only depends on the first time node of the internal variable. However, the column vector $\mathbf{S}^n_{\mathrm{rat}}$ associated with the entropy rate and the column vector $\mathbf{S}^n_{\mathrm{dis}}$ pertaining to the internal dissipation depends on all time nodes. Hence, a linearisation of these vectors leads to the incremental virtual energy

$$\sum_{j=1}^{m_{en}} \mathop{\mathsf{A}}_{e\in\mathscr{N}_{el}} \delta\mathbf{o}^{*,n,e}_{\alpha_j} \sum_{k=1}^{m_{eq}} \int_{\mathscr{B}_\square} \left\{ {}^{k+1}_{\mathrm{Con}}\mathbf{K}^{n,e,j}_{\mathrm{Rat}}(\boldsymbol{\eta}) + {}^{k+1}_{\mathrm{Con}}\mathbf{K}^{n,e,j}_{\mathrm{Dis}}(\boldsymbol{\eta}) \right\} \Delta\mathbf{i}^{n,e}_{\alpha_{k+1}}(\boldsymbol{\eta})\, J^e_0(\boldsymbol{\eta}) \tag{B.73}$$

The linearisation of the entropy rate with respect to the internal variable at the time nodes leads to the partial derivative of the non-equilibrium stress with respect to the temperature. Using the matrix form of this tensor, we obtain the row vectors $\mathbf{y}^{*,n,e}_{\alpha_{k+1}}$ at the unknown time nodes. We summarise the linearised internal dissipation in a time-dependent row vector $\mathbf{d}^{*,n,e}_{\alpha}$ pertaining to each unknown node. In the end, we obtain the tangent blocks

$$\boxed{\begin{aligned}
{}^{k+1}_{\mathrm{Con}}\mathbf{K}^{n,e,j}_{\mathrm{Rat}}(\boldsymbol{\eta}) &= [\mathbf{A}]^{j,k+1}\,\mathbf{n}^{e}(\boldsymbol{\eta})\,\partial_{\Theta}\mathbf{y}^{*,n,e}_{\alpha_{k+1}}(\boldsymbol{\eta}) \\
{}^{k+1}_{\mathrm{Con}}\mathbf{K}^{n,e,j}_{\mathrm{Dis}}(\boldsymbol{\eta}) &= \int_{\mathscr{I}^{n}_{\alpha}} \frac{M^{j}(\alpha)}{\Theta^{n,e}_{\alpha}(\boldsymbol{\eta})}\,\mathbf{n}^{e}(\boldsymbol{\eta})\,{}^{k+1}_{\mathrm{Dis}}\mathbf{d}^{*,n,e}_{\alpha}(\boldsymbol{\eta})
\end{aligned}} \tag{B.74}$$

The linearisation of the internal dissipation consists of the incremental value pertaining to the squared trace of the viscous deformation rate tensor on the one hand, and pertaining to the trace of the squared viscous deformation rate tensor on the other hand. Hence, we obtain a sum of two row vectors

$${}^{k+1}_{\mathrm{Dis}}\mathbf{d}^{*,n,e}_{\alpha}(\boldsymbol{\eta}) = \mathrm{tr}\left(\boldsymbol{L}^{n,e}_{\alpha}(\boldsymbol{\eta})\right)\left(V_{\mathrm{vol}} - \frac{2\,V_{\mathrm{dev}}}{n_{\mathrm{dim}}}\right){}^{k+1}_{\mathrm{Vol}}\mathbf{d}^{*,n,e}_{\alpha}(\boldsymbol{\eta}) + 2\,V_{\mathrm{dev}}\,{}^{k+1}_{\mathrm{Dev}}\mathbf{d}^{*,n,e}_{\alpha}(\boldsymbol{\eta}) \tag{B.75}$$

The first row vector is associated with the ‘viscous’ Lamé parameter, and the second is multiplied with the deviatoric viscosity parameter. Since both row vectors are based on the linearised form of the viscous deformation rate tensor, they are similar in the structure. The row vectors arise via the transposed vec-operator from the tensor components

$$\begin{aligned}
[\,{}^{k+1}_{\mathrm{Vol}}\boldsymbol{d}^{n,e}_{\alpha}(\boldsymbol{\eta})]^{ED} &= \frac{\mathring{M}^{k+1}(\alpha)}{h^{n}}[(\boldsymbol{\Gamma}^{n,e}_{\alpha}(\boldsymbol{\eta}))^{-1}]^{ED} - \\
&\quad -2\,M^{k+1}(\alpha)[\boldsymbol{L}^{n,e}_{\alpha}(\boldsymbol{\eta})]^{E}{}_{B}[(\boldsymbol{\Gamma}^{n,e}_{\alpha}(\boldsymbol{\eta}))^{-1}]^{BD} \\
[\,{}^{k+1}_{\mathrm{Dev}}\boldsymbol{d}^{n,e}_{\alpha}(\boldsymbol{\eta})]^{ED} &= \frac{\mathring{M}^{k+1}(\alpha)}{h^{n}}[\boldsymbol{L}^{n,e}_{\alpha}(\boldsymbol{\eta})]^{E}{}_{B}[(\boldsymbol{\Gamma}^{n,e}_{\alpha}(\boldsymbol{\eta}))^{-1}]^{BD} - \\
&\quad -2\,M^{k+1}(\alpha)[\boldsymbol{L}^{n,e}_{\alpha}(\boldsymbol{\eta})]^{E}{}_{A}[\boldsymbol{L}^{n,e}_{\alpha}(\boldsymbol{\eta})]^{A}{}_{B}[(\boldsymbol{\Gamma}^{n,e}_{\alpha}(\boldsymbol{\eta}))^{-1}]^{BD}
\end{aligned} \tag{B.76}$$

In a final step, we determine the $\mathbf{i}$-increment of the algorithmic production of entropy, given by the column vector $\mathbf{S}^{n}_{\mathrm{alg}}$ in the thermal Galerkin form. According to Equation (5.23), we divide the tangent matrix corresponding to this increment in three parts. The first (material) part is associated with the linearisation of the squared norm of the viscous deformation rate tensor, given by the row vector ${}^{k+1}_{\mathrm{Alg}}\mathbf{d}^{*,n,e}_{\alpha}(\boldsymbol{\eta})$ in matrix form. The blocks of the material tangent therefore reads

$$\boxed{{}^{k+1}_{\text{Mat}}\mathbf{K}^{n,e,j}_{\text{Alg}}(\boldsymbol{\eta}) = \int_{\mathscr{I}^{\eta}_{\alpha}} M^{j}(\alpha)\, \mathsf{n}^{e}(\boldsymbol{\eta})\, \frac{N_D^{e,\square}(\boldsymbol{\eta})}{D_D^{e,\square}(\boldsymbol{\eta})}\, \frac{2\,\vartheta_{\alpha}^{n,e}(\boldsymbol{\eta})}{\{\Theta_{\alpha}^{n,e}(\boldsymbol{\eta})\}^{2}}\, \|\boldsymbol{L}_{\alpha}^{n,e}(\boldsymbol{\eta})\|^{2}\ {}^{k+1}_{\text{Alg}}\mathbf{d}^{*,n,e}_{\alpha}(\boldsymbol{\eta})} \tag{B.77}$$

where

$$\begin{aligned}[{}^{k+1}_{\text{Alg}}\boldsymbol{d}^{*,n,e}_{\alpha}(\boldsymbol{\eta})]^{ED} = \frac{\mathring{M}^{k+1}(\alpha)}{h^{n}}\, [(\boldsymbol{\Gamma}^{n,e}_{\alpha}(\boldsymbol{\eta}))^{-1}]^{EA}\, [\boldsymbol{L}^{*,n,e}_{\alpha}(\boldsymbol{\eta})]_{A}{}^{D} - \\ -2\, M^{k+1}(\alpha)\, [(\boldsymbol{\Gamma}^{n,e}_{\alpha}(\boldsymbol{\eta}))^{-1}]^{EA} [\boldsymbol{L}^{*,n,e}_{\alpha}(\boldsymbol{\eta})]_{A}{}^{B} [(\boldsymbol{L}^{n,e}_{\alpha}(\boldsymbol{\eta}))^{T}]_{B}{}^{D}\end{aligned} \tag{B.78}$$

The second part arise from the linearisation of the numerator $N_D^{e,\square}(\boldsymbol{\eta})$ in Equation (5.23). The numerator consists of the time integration of the internal dissipation D_{α}^{int} on the temporal parent domain, whose linearisation is already given by Equation (B.75). The tangent matrix blocks take the form

$$\boxed{{}^{k+1}_{\text{Num}}\mathbf{K}^{n,e,j}_{\text{Alg}}(\boldsymbol{\eta}) = \int_{\mathscr{I}^{\eta}_{\alpha}} M^{j}(\alpha)\, \mathsf{n}^{e}(\boldsymbol{\eta})\, \frac{1}{D_D^{e,\square}(\boldsymbol{\eta})}\, \frac{\vartheta_{\alpha}^{n,e}(\boldsymbol{\eta})}{\{\Theta_{\alpha}^{n,e}(\boldsymbol{\eta})\}^{2}}\, \|\boldsymbol{L}_{\alpha}^{n,e}(\boldsymbol{\eta})\|^{4}\, {}_{\text{Num}}\mathbf{d}^{*,n,e}_{\alpha_{k+1}}(\boldsymbol{\eta})} \tag{B.79}$$

with

$${}_{\text{Num}}\mathbf{d}^{*,n,e}_{\alpha_{k+1}}(\boldsymbol{\eta}) = \int_{\mathscr{I}_{\alpha}} {}^{k+1}_{\text{Dis}}\mathbf{d}^{*,n,e}_{\alpha}(\boldsymbol{\eta}) - \int_{\mathscr{I}^{\eta}_{\alpha}} {}^{k+1}_{\text{Dis}}\mathbf{d}^{*,n,e}_{\alpha}(\boldsymbol{\eta}) \tag{B.80}$$

In the denominator, the derivative in direction of the i-increment also concerns the squared norm of the viscous deformation rate tensor. However, we have to integrate this linearisation with respect to time, using the integration rule pertaining to the entropy evolution equation. Hence, we arrive at the block matrices

$$\boxed{{}^{k+1}_{\text{Den}}\mathbf{K}^{n,e,j}_{\text{Alg}}(\boldsymbol{\eta}) = -\int_{\mathscr{I}^{\eta}_{\alpha}} M^{j}\, \mathsf{n}^{e}\, \frac{N_D^{e,\square}}{\{D_D^{e,\square}\}^{2}}\, \frac{\vartheta_{\alpha}^{n,e}}{\{\Theta_{\alpha}^{n,e}\}^{2}}\, \|\boldsymbol{L}_{\alpha}^{n,e}\|^{4}\ {}_{\text{Den}}\mathbf{d}^{*,n,e}_{\alpha_{k+1}}} \tag{B.81}$$

wherein

$$
{}_{\text{Den}}\mathbf{d}^{*,n,e}_{\alpha_{k+1}}(\boldsymbol{\eta}) = \int_{\mathscr{I}^n_\alpha} 2 \left\{ \frac{\vartheta^{n,e}_\alpha(\boldsymbol{\eta})}{\Theta^{n,e}_\alpha(\boldsymbol{\eta})} \, \|\boldsymbol{L}^{n,e}_\alpha(\boldsymbol{\eta})\| \right\}^2 \, {}^{k+1}_{\text{Alg}}\mathbf{d}^{*,n,e}_\alpha(\boldsymbol{\eta}) \tag{B.82}
$$

denotes the row vector pertaining to the linearisation of the denominator. By summing up all the tangents in this section, the total increment of the thermal Galerkin form with respect to the internal variable element vector $\mathbf{i}^{n,e}$ is given by

$$
\Delta_{\mathbf{i}} G_{\text{ther}}(\mathscr{X};\, \delta\mathbf{o}^{*,n}) = \sum_{j=1}^{m_{en}} \mathop{\mathsf{A}}_{e\in\mathscr{N}_{el}} \delta\mathbf{o}^{*,n,e}_{\alpha_j} \int_{\mathscr{B}_\square} {}_{\text{Con}}\mathbf{K}^{n,e,j}_{\text{The}}(\boldsymbol{\eta}) \, \Delta\mathbf{i}^{n,e}(\boldsymbol{\eta}) \, J^e_0(\boldsymbol{\eta}) \tag{B.83}
$$

where

$$
\begin{aligned}
{}_{\text{Con}}\mathbf{K}^{n,e,j}_{\text{The}}(\boldsymbol{\eta}) = {}& {}_{\text{Con}}\mathbf{K}^{n,e,j}_{\text{Rat}}(\boldsymbol{\eta}) - h^n \, {}_{\text{Con}}\mathbf{K}^{n,e,j}_{\text{Dis}}(\boldsymbol{\eta}) - \\
& - h^n \left\{ {}_{\text{Mat}}\mathbf{K}^{n,e,j}_{\text{Alg}}(\boldsymbol{\eta}) - {}_{\text{Num}}\mathbf{K}^{n,e,j}_{\text{Alg}}(\boldsymbol{\eta}) - {}_{\text{Den}}\mathbf{K}^{n,e,j}_{\text{Alg}}(\boldsymbol{\eta}) \right\}
\end{aligned} \tag{B.84}
$$

defines a shorthand notation for writing the total increment of the thermal Galerkin form in the next section in a more compact form.

B.2.4. The total increment of the thermal Galerkin form. The increment of the internal variable vector at any point in the spatial parent domain is given by Equation (B.52). Hence, we employ this equation in Equation (B.83), and obtain the tangent matrices

$$
\begin{aligned}
\mathbf{K}^{n,e,j}_{\text{The}} &= \int_{\mathscr{B}_\square} {}_{\text{Con}}\mathbf{K}^{n,e,j}_{\text{The}}(\boldsymbol{\eta}) \left(\mathbf{K}^{n,e}_{\text{Evo}}(\boldsymbol{\eta}) \right)^{-1} {}_{\text{Con}}\mathbf{K}^{n,e}_{\text{Evo}}(\boldsymbol{\eta}) \, J^e_0(\boldsymbol{\eta}) \\
\mathbf{k}^{n,e,j}_{\text{The}} &= \int_{\mathscr{B}_\square} {}_{\text{Con}}\mathbf{K}^{n,e,j}_{\text{The}}(\boldsymbol{\eta}) \left(\mathbf{K}^{n,e}_{\text{Evo}}(\boldsymbol{\eta}) \right)^{-1} \mathbf{k}^{n,e}_{\text{Evo}}(\boldsymbol{\eta}) \, J^e_0(\boldsymbol{\eta})
\end{aligned} \tag{B.85}
$$

which express the increment $\Delta_{\mathbf{i}} G_{\text{ther}}(\mathscr{X};\, \delta\mathbf{o}^{*,n})$ by means of the $\mathbf{x}$-increment and the $\mathbf{o}$-increment. We assemble the spatial element nodes, and summarise the blocks pertaining to the temporal test nodes in global tangent matrices.

We obtain the matrix form

$$\begin{aligned}\mathit{\Delta}_{\mathsf{l}} G_{\mathrm{ther}}(\mathscr{X};\, \delta\mathbf{o}^{*,n}) &= -\sum_{j=1}^{m_{en}} \mathop{\mathsf{A}}_{e\in\mathscr{N}_{el}} \delta\mathbf{o}_{\alpha_j}^{*,n,e} \left\{ \mathbf{K}_{\mathrm{The}}^{n,e,j} \mathit{\Delta}\mathbf{x}^{n,e} + \mathbf{k}_{\mathrm{The}}^{n,e,j} \mathit{\Delta}\mathbf{o}^{n,e} \right\} \\ &= -\delta\mathbf{o}^{*,n} \overset{n}{\mathbf{K}}_{\mathrm{The}}\, \mathit{\Delta}\mathbf{x}^{n} - \delta\mathbf{o}^{*,n} \overset{n}{\mathbf{k}}_{\mathrm{The}}\, \mathit{\Delta}\mathbf{o}^{n}\end{aligned} \tag{B.86}$$

The other tangent matrices are build up in the usual way. First, we assemble the increments at the spatial nodes pertaining to each time node, and then we substitute the summations over the time nodes by matrix products. Since the temperature increment of the entropy trace is solely related to one unknown time node and one temporal test node, the corresponding global matrix $\overset{n}{\mathbf{k}}_{\mathrm{Tra}}$ is zero with the exception of the block in the upper left corner. In the end, we arrive at the linearised equation

$$\boxed{\begin{aligned} G_{\mathrm{ther}}(\mathscr{X};\, \delta\mathbf{o}^{*,n}) - h^n\, \delta\mathbf{o}^{*,n}\, \overset{n}{\mathbf{K}}_{\mathrm{Cdu}}\, \mathit{\Delta}\mathbf{x}^n + \delta\mathbf{o}^{*,n} \left[\overset{n}{\mathbf{K}}_{\mathrm{Rat}} - \overset{n}{\mathbf{K}}_{\mathrm{The}} \right] \mathit{\Delta}\mathbf{x}^n - & \\ - h^n\, \delta\mathbf{o}^{*,n} \left[\overset{n}{\mathbf{k}}_{\mathrm{Ext}} + \overset{n}{\mathbf{k}}_{\mathrm{Dis}} \right] \mathit{\Delta}\mathbf{o}^n + & \\ + \quad \delta\mathbf{o}^{*,n} \left[\overset{n}{\mathbf{k}}_{\mathrm{Tra}} + \overset{n}{\mathbf{k}}_{\mathrm{Rat}} - \overset{n}{\mathbf{k}}_{\mathrm{The}} \right] \mathit{\Delta}\mathbf{o}^n - & \\ - h^n\, \delta\mathbf{o}^{*,n} \left[{}_{\mathrm{Geo}}\overset{n}{\mathbf{k}}_{\mathrm{Cdu}} + {}_{\mathrm{Mat}}\overset{n}{\mathbf{k}}_{\mathrm{Cdu}} + {}_{\mathrm{Mat}}\overset{n}{\mathbf{k}}_{\mathrm{Alg}} + {}_{\mathrm{Den}}\overset{n}{\mathbf{k}}_{\mathrm{Alg}} \right] \mathit{\Delta}\mathbf{o}^n = 0 & \end{aligned}} \tag{B.87}$$

Applying the fundamental lemma of calculus of variations, the corresponding residual vector can be solved in a global iterative solution procedure, together with the linearised mechanical Galerkin form in Equation (B.55).

B.3. Global iterative solution procedure

After linearising the global mechanical as well as the thermal Galerkin form, we determine the increments in an iterative solution procedure. First of all, we initiate the unknown position nodes by using the mechanical residual vector. We neglect in the mechanical residual the implicit terms, and solve the resulting system of algebraic linear equations for the unknown position nodes. In this way, the unknown position nodes are initiated by initial velocities and external forces. The unknown temperatures and internal variables are simply initiated by the corresponding values at the initial time points, because in the associated residuals all terms are implicit.

Then, the increments can be determined simultaneously with one large linear algebraic system, or successively with three small linear algebraic systems. We choose the last option. We first eliminate the $\mathbf{o}$-increment in the global mechanical residual, and then determine the $\mathbf{x}$-increment. Finally, we update the $\mathbf{o}$-increment (compare the solution procedure in Laursen & Meng [184]). According to Equation (B.87), the temperature increment reads

$$\Delta\mathbf{o}^n = -\left[\mathbf{k}^n_{\text{ther}}\right]^{-1}\left[\mathbf{R}_{\text{ther}}(\mathscr{X}) + \mathbf{K}^n_{\text{ther}}\Delta\mathbf{x}^n\right] \tag{B.88}$$

where $\mathbf{R}_{\text{ther}}(\mathscr{X})$ denotes the residual vector corresponding to the thermal Galerkin form. We summarise the tangent matrices of the $\mathbf{x}$-increment in the matrix $\mathbf{K}^n_{\text{ther}}$, and the tangent matrices associated with the $\mathbf{o}$-increment in the matrix $\mathbf{k}^n_{\text{ther}}$. We employ Equation (B.88) in the residual equation arising from the global mechanical Galerkin form, and obtain the linear algebraic system

$$\left\{\mathbf{X}^n\mathbf{K}^n_{\text{ther}} - \mathbf{K}^n_{\text{mech}}\right\}\Delta\mathbf{x}^n = \mathbf{R}_{\text{mech}}(\mathscr{X}) - \mathbf{X}^n\mathbf{R}_{\text{ther}}(\mathscr{X}) \tag{B.89}$$

The coefficient matrix $\mathbf{X}^n$ of the thermal residual vector $\mathbf{R}_{\text{ther}}(\mathscr{X})$ and the thermal tangent matrix $\mathbf{K}^n_{\text{ther}}$, respectively, defines the coupling to the global thermal Galerkin form. This matrix can be determined without an explicit inversion of the matrix $\mathbf{k}^n_{\text{ther}}$ by solving the matrix equation

$$\mathbf{X}^n\,\mathbf{k}^n_{\text{ther}} = \mathbf{k}^n_{\text{mech}} \tag{B.90}$$

for the thermal coupling matrix $\mathbf{X}^n$ as an intermediate step. Having solved these two linear algebraic systems, we update the $\mathbf{o}$-increment. We employ the new $\mathbf{x}$-increment in Equation (B.88), and solve the linear algebraic system

$$-\mathbf{k}^n_{\text{ther}}\Delta\mathbf{o}^n = \mathbf{R}_{\text{ther}}(\mathscr{X}) + \mathbf{K}^n_{\text{ther}}\Delta\mathbf{x}^n \tag{B.91}$$

for the $\mathbf{o}$-increment.

The iteration proceeds till a prescribed convergence criterion is fulfilled. Analogous to the local iterative solution procedure, we stop the iteration loop if the considered Galerkin forms are numerically zero. In the global iterative solution procedure, we solve three Galerkin forms in one global iteration. Hence, we derive from all Galerkin forms one physically meaningful equation, whose absolute value has to be less than a small tolerance tol. Since the weak forms are inherently energy consistent approximated, we arrive at real energy and work terms, respectively, by substituting the variations of the weak forms by real values. A physically motivated convergence criterion for all Galerkin forms then follows from the directional derivative of the approximated negative relative internal energy along the continuous time curve $\boldsymbol{\gamma}_t^n(s) = \hat{\mathscr{E}}(t+s)$ in the n-th time element, given by

$$\int_{\mathscr{T}^n}\int_{\mathscr{B}_0} -\,\dot{\eta}_t^n(\boldsymbol{X})\,\vartheta_t^n(\boldsymbol{X}) - [\boldsymbol{P}_t^{*,n}(\boldsymbol{X})]_a{}^A\,[\dot{\boldsymbol{F}}_t^n(\boldsymbol{X})]^a{}_A + [\boldsymbol{\varUpsilon}_t^n(\boldsymbol{X})]_{AB}\,[\dot{\boldsymbol{\varGamma}}_t^n(\boldsymbol{X})]^{AB} \tag{B.92}$$

By using the time transformation in Equation (4.2), we transform the integral and the time derivatives in this equation to the temporal parent domain. We are able to relate the first term of Equation (B.92) to the discrete thermal Galerkin form, because the relative temperature field is an admissible test function. The relative temperature nodes ${}^a\vartheta_{\alpha_k}^{n,e}$ therefore coincide with the variations ${}^a\delta\varTheta_{\alpha_k}^{n,e}$ of the thermal Galerkin form. Combining the relative temperatures of the mesh in the global column vector $\boldsymbol{\mathsf{u}}^n$, the first term of Equation (B.92) is equivalent to

$$-\sum_{e=1}^{n_{el}}\int_{\mathscr{I}_\alpha}\int_{\mathscr{B}_0^e}\mathring{\eta}_\alpha^{n,e}(\boldsymbol{X})\,\vartheta_\alpha^{n,e}(\boldsymbol{X}) = -\boldsymbol{\mathsf{u}}^{*,n}\boldsymbol{\mathsf{S}}_{\mathrm{rat}}^n \tag{B.93}$$

Next, we relate the second term of Equation (B.92) to the discrete mechanical Galerkin form. Therefore, we determine the corresponding variations. Since the time derivative of the deformation field is an admissible test function, the variations of the nodal positions are given by

$$\delta\boldsymbol{\mathsf{x}}^{*,n} = \tilde{\boldsymbol{\mathsf{x}}}^{*,n} := \boldsymbol{\mathsf{x}}^{*,n}\left[(\boldsymbol{\mathsf{W}}')^T(\tilde{\boldsymbol{\mathsf{W}}})^{-T}\otimes\boldsymbol{I}_\varphi\right] \tag{B.94}$$

where $\boldsymbol{I}_\varphi$ denotes an $n_\varphi \times n_\varphi$ identity matrix. The real n_φ coincides with the number $|\mathscr{N}_{no}\backslash\mathscr{N}_\varphi|$ of the free position nodes of the mesh. Taking these variations into account, the second term of Equation (B.92) reads

$$-\sum_{e=1}^{n_{el}} \int_{\mathscr{I}_\alpha} \int_{\mathscr{B}_0^e} [\boldsymbol{P}_\alpha^{*,n,e}(\boldsymbol{X})]_a{}^A \, [\mathring{\boldsymbol{F}}_\alpha^{n,e}(\boldsymbol{X})]^a{}_A = \tilde{\mathbf{x}}^{*,n,e}\mathbf{F}^n_{\text{int}} \tag{B.95}$$

In the last term of Equation (B.92), the integrals have to be interchanged by using Fubini's theorem, in order to employ the local mechanical Galerkin form. Subsequently, using the corresponding test nodes given by Equation (B.48), this integral can be written as

$$\sum_{e=1}^{n_{el}} \int_{\mathscr{I}_\alpha} \int_{\mathscr{B}_0^e} [\boldsymbol{\Upsilon}_\alpha^{n,e}(\boldsymbol{X})]_{AB} \, [\mathring{\boldsymbol{\Gamma}}_\alpha^{n,e}(\boldsymbol{X})]^{AB} = \sum_{e=1}^{n_{el}} \int_{\mathscr{B}_\square} \tilde{\mathbf{i}}^{*,n,e}(\boldsymbol{\eta}) \, \mathbf{y}^{n,e}(\boldsymbol{\eta}) \, J_0^e(\boldsymbol{\eta}) \tag{B.96}$$

by transforming the spatial integral to the corresponding parent domain. Employing Equations (B.93), (B.95) and (B.96) in Equation (B.92), the temporally averaged rate of the negative relative internal energy can be written by the nodal vectors in the corresponding residuals. We arrive at the sum

$$-\mathbf{u}^{*,n}\mathbf{S}^n_{\text{rat}} + \tilde{\mathbf{x}}^{*,n,e}\mathbf{F}^n_{\text{int}} + \sum_{e=1}^{n_{el}} \int_{\mathscr{B}_\square} \tilde{\mathbf{i}}^{*,n,e}(\boldsymbol{\eta}) \, \mathbf{y}^{n,e}(\boldsymbol{\eta}) \, J_0^e(\boldsymbol{\eta}) \tag{B.97}$$

By definition, each Galerkin form is identical zero. Hence, each Galerkin form is related to a corresponding residual equation. Each term of the sum in Equation (B.97) can be therefore expressed by the corresponding Galerkin form, and we arrive at the residual equation

$$G_{\text{ther}}(\mathscr{Z}; \mathbf{u}^{*,n}) + G_{\text{mech}}(\mathscr{Z}; \tilde{\mathbf{x}}^{*,n}) - \sum_{e=1}^{n_{el}} \int_{\mathscr{B}_\square} G_{\text{visc}}(\mathscr{Z}; \tilde{\mathbf{i}}^{*,n,e}(\boldsymbol{\eta})) \, J_0^e(\boldsymbol{\eta}) = 0 \tag{B.98}$$

This residual equation is zero only if the global and local mechanical Galerkin form as well as the global thermal Galerkin form is zero. Hence, we stop the global iteration if this residual equation is numerically zero, which means

$$\boxed{\left| G_{\text{ther}}(\mathscr{X};\mathbf{u}^{*,n}) + G_{\text{mech}}(\mathscr{X};\tilde{\mathbf{x}}^{*,n}) - \sum_{e=1}^{n_{el}} \int_{\mathscr{B}_\square} G_{\text{visc}}(\mathscr{X};\tilde{\mathbf{i}}^{*,n,e}(\boldsymbol{\eta}))\, J_0^e(\boldsymbol{\eta}) \right| \leqslant \mathsf{tol}} \tag{B.99}$$

Since the convergence criteria is derived from the temporally averaged rate of the negative relative internal energy, it has a concrete physical meaning by taking into account the definitions of the terms in the Galerkin forms. The first term of Equation (B.98) is given by

$$\begin{aligned} G_{\text{ther}}(\mathscr{X};\mathbf{u}^{*,n}) = {} & \hat{\mathcal{E}}(t_+^n) - \hat{\mathcal{E}}(t^n) + \\ & + \int_{\mathscr{T}_\eta^n} \int_{\mathscr{B}_0} \frac{\Theta_\infty}{\Theta_t^n(\boldsymbol{X})}\, D_t^{\text{tot},n}(\boldsymbol{X}) - \int_{\mathscr{T}^n} \int_{\mathscr{B}_0} D_t^{\text{int},n}(\boldsymbol{X}) \\ & + \int_{\mathscr{T}_\eta^n} \int_{\mathscr{B}_0} \dot{\eta}_t^n(\boldsymbol{X})\, \vartheta_t^n(\boldsymbol{X}) - \int_{\mathscr{T}_\eta^n} \int_{\partial_Q \mathscr{B}_0} \frac{\vartheta_t^n(\boldsymbol{X})}{\Theta_t^n(\boldsymbol{X})}\, \overline{Q}_\alpha^n(\boldsymbol{X}) \end{aligned} \tag{B.100}$$

where the index η at the n-th time element $\mathscr{T}^n$ indicates the time integration rule in the thermal weak form, and the energy $\hat{\mathcal{E}}(t_+^n)$ denotes the relative internal energy at the first time node $\tau^n(\alpha_1)$ of the time evolution. The second term of Equation (B.98) associated with the global mechanical Galerkin form reads

$$\begin{aligned} G_{\text{mech}}(\mathscr{X};\tilde{\mathbf{x}}^{*,n}) = {} & \mathcal{T}(t^{n+1}) + \hat{\mathcal{E}}(t^{n+1}) - \mathcal{T}(t^n) - \hat{\mathcal{E}}(t_+^n) - \\ & - \int_{\mathscr{T}^n} \int_{\mathscr{B}_0} [\bar{\boldsymbol{t}}_t^{*,n}(\boldsymbol{X})]_a\, [\dot{\boldsymbol{\varphi}}_t^n(\boldsymbol{X})]^a - \\ & - \int_{\mathscr{T}_\eta^n} \int_{\mathscr{B}_0} \dot{\eta}_t^n(\boldsymbol{X})\, \vartheta_t^n(\boldsymbol{X}) + \int_{\mathscr{T}^n} \int_{\mathscr{B}_0} [\boldsymbol{\Upsilon}_t^n(\boldsymbol{X})]_{AB}\, [\dot{\boldsymbol{\Gamma}}_t^n(\boldsymbol{X})]^{AB} \end{aligned} \tag{B.101}$$

In the last term of Equation (B.98), the local mechanical Galerkin forms of all elements are spatially integrated and summed up. Accordingly, this term coincides with the difference of the non-equilibrium dissipation and the viscous dissipation pertaining to the entire body, which means

$$\begin{aligned}\sum_{e=1}^{n_{el}} \int_{\mathscr{B}_\square} G_{\mathrm{visc}}(\mathscr{Z}; \tilde{\mathsf{i}}^{*,n,e}(\boldsymbol{\eta}))\, J_0^e(\boldsymbol{\eta}) = \int_{\mathscr{T}^n} \int_{\mathscr{B}_0} [\boldsymbol{\Upsilon}_t^n(\boldsymbol{X})]_{AB}\, [\dot{\boldsymbol{\Gamma}}_t^n(\boldsymbol{X})]^{AB} - \\ - \int_{\mathscr{T}^n} \int_{\mathscr{B}_0} D_t^{\mathrm{int},n}(\boldsymbol{X})\end{aligned} \tag{B.102}$$

Note that the internal dissipation in Equation (B.100) is integrated with the quadrature rule associated with the mechanical evolution equations by virtue of the algorithmic production of entropy. Employing Equations (B.100), (B.101) and (B.102) in Equation (B.98), the relative internal energies $\hat{\mathscr{E}}(t_+^n)$ as well as the non-equilibrium dissipation and viscous dissipation terms vanish. Equation (B.98) then reads

$$\begin{aligned}\mathcal{T}(t^{n+1}) + \hat{\mathcal{E}}(t^{n+1}) - \mathcal{T}(t^n) - \hat{\mathcal{E}}(t^n) + \int_{\mathscr{T}^n} \int_{\mathscr{B}_0} \frac{\Theta_\infty}{\Theta_t^n(\boldsymbol{X})}\, D_t^{\mathrm{tot},n}(\boldsymbol{X}) - \\ - \int_{\mathscr{T}^n} \int_{\mathscr{B}_0} [\bar{\boldsymbol{t}}_t^{*,n}(\boldsymbol{X})]_a\, [\dot{\boldsymbol{\varphi}}_t^n(\boldsymbol{X})]^a - \int_{\mathscr{T}_\eta^n} \int_{\partial_Q \mathscr{B}_0} \frac{\vartheta_t^n(\boldsymbol{X})}{\Theta_t^n(\boldsymbol{X})}\, \overline{Q}_t^n(\boldsymbol{X}) = 0\end{aligned} \tag{B.103}$$

Assuming conservative mechanical loads and vanishing thermal loads as in Section 2.3.2, the stopping criterion for the global iteration loop means that the absolute value of the stability estimate (5.27) is less than the small tolerance tol. Consequently, we also use a physically meaningful stopping criterion in the global iterative solution procedure.

The advantage of this stopping criterion is that the unknowns are naturally scaled while checked. Hence, great different values pertaining to the nodal displacements and nodal relative temperatures do not lead to scaling problems. Note that the convergence criterion in Equation (B.99) also works without the additional weak terms in the global Galerkin forms. However, the physical meaning is no longer that of a stability estimate.

C. NEO-HOOKEAN MODEL FOR ISOTROPIC MATERIALS

In this appendix, we derive the thermo-viscoelastic free energy, used in the numerical simulations. We consider elastomeric polymers with internal damping, which are isotropic and highly deformable. On the one hand, we have to distinguish between solid and foamed elastomeric polymers. Solid elastomeric polymers are nearly incompressible, whereas the foamed elastomers are compressible. Therefore, we apply a model for an isotropic compressible hyperelastic material, which describes an incompressible material in the limit.

On the other hand, the free energy of elastomeric polymers at fixed elongation depends on the relative temperature field of the material. We assume a constant specific heat capacity and derive a corresponding purely thermal contribution to the free energy. A constant specific heat capacity is justifiable for limited compressible materials with a sufficient accuracy (see Simo [156]). Also known is that a slight thermal expansion of elastomeric polymers governs the thermoelastic inversion phenomenon, which describes an initial cooling and a subsequent heating while stretching (see Holzapfel [135]). Hence, we extend the free energy by a thermo-mechanical contribution, modelling thermal expansion.

C.1. Model for incompressible hyperelastic materials

The considered polymers are composed of a network of long-chain molecules. This network is a randomly coiled bundle of molecule chains, which are chemically cross-linked (see Holzapfel [135]). Purely elastic behaviour occurs if the chemical crosslinks are permanent, whereas viscoelastic behaviour is governed by reforming processes of weak chemical interactions (see Reese [107]). In a stress free configuration, the network is in a state of maximum entropy. If the molecule chains are extended, the entropy is decreased.

We consider a homogenous deformation of a specimen $\mathscr{B}_0$ with the principal stretches $\lambda_t^1, \dots, \lambda_t^{n_{\dim}}$ in the current configuration $\mathscr{B}_t$. Recall that a squared principal stretch coincides with the corresponding principal value of the right

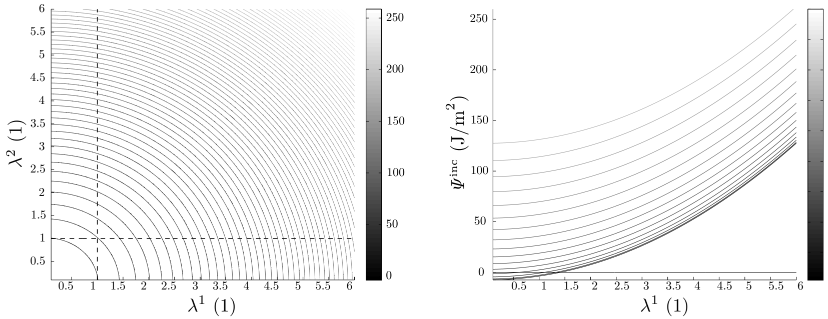

Figure C.1. On the left, the isolines of the free energy $\Psi_t^{\mathrm{inc}}(\boldsymbol{X})$ with shear modulus $\mu = 7.5\,\mathrm{J/m^2}$ is depicted in the two-dimensional case ($n_{\mathrm{dim}} = 2$) in the principal stretch space (λ^1, λ^2). The colours indicate the values of the free energy in Joule per square meter. The local minimum point of this free energy lies in the origin of the principal stretch space, and not in the intersection point of the dashed lines, denoting an undeformed current configuration. The value of the free energy in the origin is negative. On the right, the isolines of the free energy, plotted versus the first principal stretch λ^1 at constant second principal stretches λ^2, are depicted. The colours therefore denote the value of the second principal stretch.

Cauchy-Green tensor. The material is idealised as totally incompressible, such that there is no change in volume on deformation. The stretching do not lead to a storage of potential energy in the molecule chains. The change of free energy is rather determined by the degree of order of the chains, and thus by the entropy difference

$$\varDelta\eta(\boldsymbol{X}) = -\frac{N k\, m}{2} \left\{ \sum_{i=1}^{n_{\mathrm{dim}}} \left(\lambda_t^i(\boldsymbol{X})\right)^2 - n_{\mathrm{dim}} \right\} \tag{C.1}$$

of the network. Here N denotes the number of chains in a unit volume in the network, and k the Boltzmann constant. The coefficient m arise from different end-to-end distances of the molecule chains in the network and detached from their network. The free energy of the network follows from the change of entropy by integrating Equation (2.48) with respect to the temperature. We obtain the Neo-Hookean free energy at the point $\boldsymbol{X}$ in the

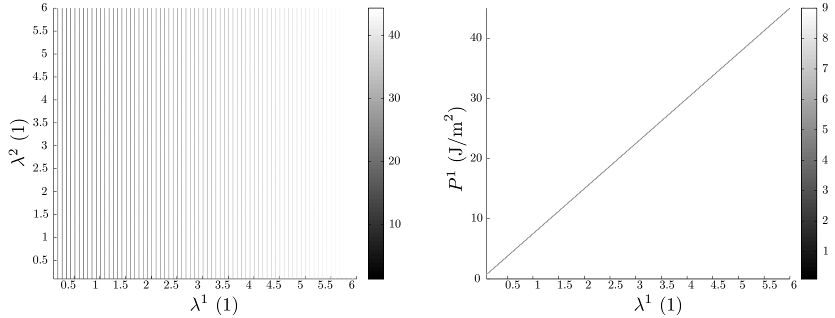

Figure C.2. On the left, the isolines of the principal value $P_t^1(\boldsymbol{X})$ associated with the free energy $\mathit{\Psi}_t^{\text{inc}}(\boldsymbol{X})$ corresponding to the shear modulus $\mu = 7.5\,\text{J/m}^2$ are depicted in the principal stretch space (λ^1, λ^2). The colours indicate the values of the principal stress in Joule per square meter. On the right, the isolines pertaining to the principal stress $P_t^1(\boldsymbol{X})$, plotted versus the first principal stretch λ^1 at constant second principal stretches λ^2, are shown. The colours denote the value of the second principal stretch. Since the first principal stress do not depend on λ^2, only one curve is visible.

reference configuration $\mathscr{B}_0$ of the specimen, given by

$$\mathit{\Psi}_t^{\text{inc}}(\boldsymbol{X}) = \frac{\mu}{2}\left\{\sum_{i=1}^{n_{\text{dim}}} \left(\lambda_t^i(\boldsymbol{X})\right)^2 - n_{\text{dim}}\right\} \tag{C.2}$$

The parameter $\mu > 0$ denotes the shear modulus or first Lamé constant of the specimen, and coincides with $N k\, m\, \mathit{\Theta}_\infty$ for a purely mechanical contribution (see Holzapfel [135]). The initial free energy in the undeformed reference configuration is set to zero. Since the sum in Equation (C.2) coincides with the trace of the right Cauchy-Green tensor $\boldsymbol{C}_t(\boldsymbol{X})$, we arrive at the free energy

$$\mathit{\Psi}_t^{\text{inc}}(\boldsymbol{X}) = \frac{\mu}{2}\left\{[\boldsymbol{C}_t(\boldsymbol{X})]_{AB}\,\delta^{BA} - n_{\text{dim}}\right\} \tag{C.3}$$

The free energy in Equation (C.2) or Equation (C.3) vanish in an undeformed state, achieved by unity principal stretches or a deformation $\boldsymbol{\varphi}_t = \text{id}$, respectively. However, this state is not a local minimum of the free energy (see Figure C.1). Therefore, the reference configuration and a

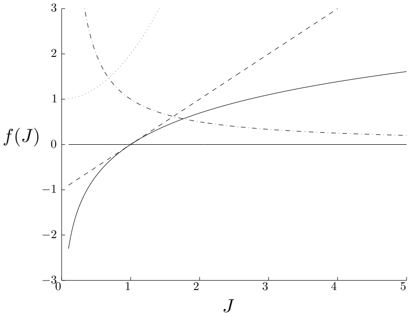

Figure C.3. The solid line denotes the $\ln(J)$ function. Its derivative $1/J$ is depicted as chain dotted line, and its tangent $J-1$ in the root is plotted as dashed line. The dotted line designates the function $1+J^2$, which is always greater than $\ln(J)$ or $J-1$, respectively.

rigid body motion is not stress free, which can be verified by means of the principal stretch space (compare Knowles & Sternberg [185]). We consider the directional derivative of the free energy $\Psi_t^{\text{inc}}(\boldsymbol{X})$ along a continuous time curve, and identify the partial derivative

$$\frac{\partial\,\Psi_t^{\text{inc}}(\boldsymbol{X})}{\partial\lambda^i} = \mu\,\lambda_t^i(\boldsymbol{X}) \tag{C.4}$$

as the principal value $P_t^i(\boldsymbol{X})$ of the first Piola-Kirchhoff stress tensor in direction of the principal stretch $\lambda_t^i(\boldsymbol{X})$. Thus, these principal stress values coincide with $\mu > 0$ in the undeformed configuration (see Figure C.2). Further, the free energy do not tend to infinity, and the stress to negative infinity, under infinite large pressure load. That means the conditions

$$\lim_{\lambda^i\to 0} \Psi_t^{\text{inc}}(\boldsymbol{X}) \longrightarrow \infty \qquad \text{and} \qquad \lim_{\lambda^i\to 0} \frac{\partial\,\Psi_t^{\text{inc}}(\boldsymbol{X})}{\partial\lambda^i} \longrightarrow -\infty \tag{C.5}$$

are violated. These properties, however, are necessary for a free energy to be meaningful in the large deformation range. Therefore, we modify the free energy function (C.3) in the next subsection.

Nevertheless, Equation (C.4) implies the strict monotonicity of the first Piola-Kirchhoff stress, which implies a strictly convex free energy in the

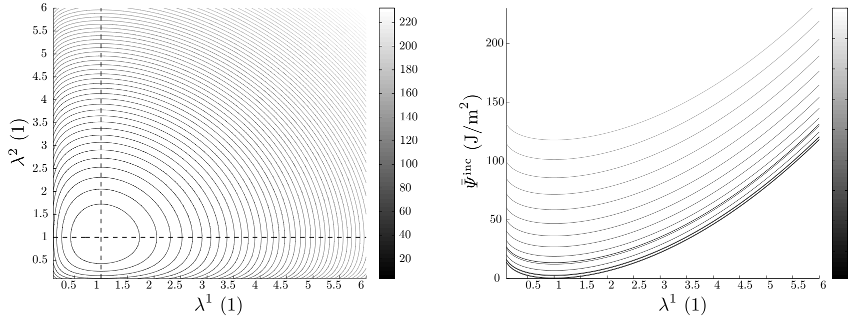

Figure C.4. On the left, the isolines of the free energy $\bar{\Psi}_t^{\mathrm{inc}}(\boldsymbol{X})$ with shear modulus $\mu = 7.5\,\mathrm{J/m^2}$ are depicted in the two-dimensional principal stretch space (λ^1, λ^2). The colours indicate the values of the free energy in Joule per square meter. The intersection point of the dashed lines indicates the minimum point of the free energy at the point $(1, 1)$, associated with an undeformed current configuration. The value of the free energy in this point is zero, where the free energy tends to infinity in the limit zone of zero principal stretches. On the right, the isolines of the free energy, plotted versus the first principal stretch λ^1 at constant second principal stretches λ^2, are shown. The colours denote the value of the second principal stretch.

principal stretch space (see also Figure C.1). A strictly convex free energy with the equilibrium state as local minimum implies the equilibrium state as strict minimiser of the Lyapunov-like function in Equation (2.113) (compare Ciarlet [133]). In turn, this is a necessary condition for formal stability of the equilibrium state during a motion (see Simo et al. [137]). Generally, a free energy $\Psi_t(\boldsymbol{X})$ is strictly convex in the principal stretch space, if for any $s_1 \in [0, 1]$ and two distinct points $\hat{\boldsymbol{\lambda}}_t(\boldsymbol{X})$ and $\boldsymbol{\lambda}_t(\boldsymbol{X})$ in the principal stretch space, the inequality

$$\Psi(s_1 \hat{\boldsymbol{\lambda}}_t(\boldsymbol{X}) + (1 - s_1)\boldsymbol{\lambda}_t(\boldsymbol{X})) < s_1\ \Psi(\hat{\boldsymbol{\lambda}}_t(\boldsymbol{X})) + (1 - s_1)\ \Psi(\boldsymbol{\lambda}_t(\boldsymbol{X})) \tag{C.6}$$

holds (see Ball [186, 187], for instance). Considering a free energy being symmetric in the principal stretches, which means the free energies of arbitrary permutations of the principal stretches coincide, the graph of the free energy is symmetric about the diagonal of the principal stretch space (compare Figure C.1). Hence, we investigate the free energy as a function of one principal stretch $\lambda_t^i(\boldsymbol{X})$, $i \in \mathscr{N}_{sd}$, and consider the remaining principal stretches $\lambda_t^j(\boldsymbol{X})$,

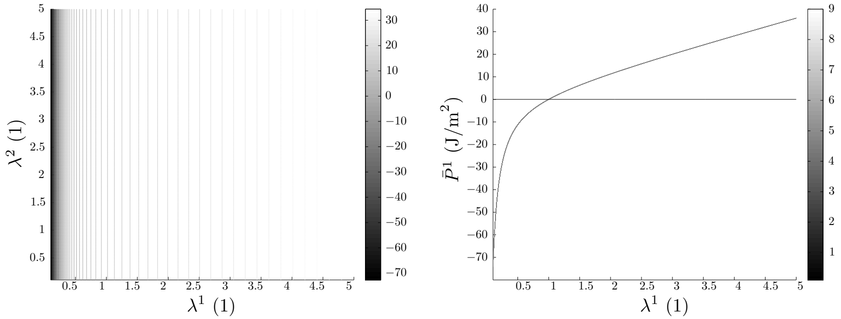

Figure C.5. On the left, the isolines of the first principal stress $\bar{P}_t^1(\boldsymbol{X})$, associated with the free energy $\bar{\Psi}_t^{\mathrm{inc}}(\boldsymbol{X})$, are depicted in the principal stretch space with a shear modulus $\mu = 7.5\,\mathrm{J/m^2}$. The colours denote the stress value in Joule per square meter. The first principal stress is zero in the equilibrium point, and tends to negative infinity as the principal stretches approaches to zero. On the right, the isolines pertaining to the principal stress $\bar{P}_t^1(\boldsymbol{X})$, plotted versus the first principal stretch λ^1 at constant second principal stretches λ^2, are shown. The colours denote the value of the second principal stretch. Since the first principal stress do not depend on λ^2, only one curve is visible.

$j \in \mathscr{N}_{sd} \setminus \{i\}$, as parameters. We apply Inequality (C.6) twice. First, on $\lambda_t^i(\boldsymbol{X})$ as first point and a perturbed state $\lambda_t^i(\boldsymbol{X}) + s_2 \varDelta\lambda_t^i(\boldsymbol{X})$, $s_2 \in (0,1]$, as second point, and then vice versa. Subsequently, for any (non-vanishing) increment $\varDelta\lambda_t^i(\boldsymbol{X})$, we obtain the relation

$$\frac{\partial \varPsi(1 + s_2 \varDelta\lambda_t^i(\boldsymbol{X}); \lambda_t^j(\boldsymbol{X}))}{\partial \lambda^i}\, \varDelta\lambda_t^i(\boldsymbol{X}) > \frac{\partial \varPsi(1; \lambda_t^j(\boldsymbol{X}))}{\partial \lambda^i}\, \varDelta\lambda_t^i(\boldsymbol{X}) \qquad \text{(C.7)}$$

by differentiating these inequalities with respect to s_1 at $s_1 = 0$, and by adding the obtained free energy differences. Here, the positivity of the real number s_2 has been taken into account. Equation (C.7) implies the strict monotonicity of the principal values of the first Piola-Kirchhoff stress tensor (compare Kuhl et al. [188]). Applying Equation (C.7) on the free energy in Equation (C.3), we obtain the relation

$$s_2\, \mu\, (\varDelta\lambda_t^i(\boldsymbol{X}))^2 > 0 \qquad \text{(C.8)}$$

Since the parameter s_2 and the first Lamé constant μ are positive, the free energy is therewith verified as being strictly convex in the entire principal

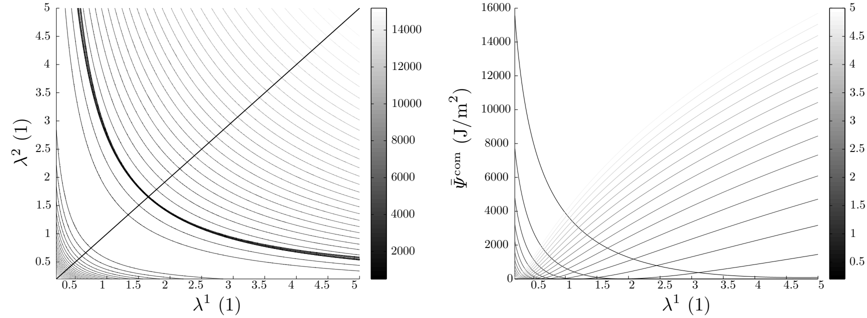

Figure C.6. The left diagram shows the isolines of the free energy $\bar{\Psi}_t^{\mathrm{com}}(\boldsymbol{X})$ associated with the penalty function $\ln(J_t(\boldsymbol{X}))$, corresponding to a shear modulus $\mu = 7.5\,\mathrm{J/m^2}$ and a second Lamé constant $\lambda = 3000\,\mathrm{J/m^2}$. The colours denote the value of the free energy in Joule per square meter. The diagonal of the principal stretch space indicates the symmetry of the free energy function. The region above the hyperbola-shaped curve represent the concave domain of the free energy function. On the right, the isolines of the free energy, plotted versus the first principal stretch λ^1 at constant second principal stretches λ^2, are shown. The colours denote the value of the second principal stretch. In this perspective, the concave region is obviously visible.

stretch space.

In cases, where the monotony condition (C.7) is not definitely fulfilled, differentiation of this condition with respect to s_2 leads to the inequality

$$\frac{\partial^2 \Psi(\lambda_t^i(\boldsymbol{X}); \lambda_t^j(\boldsymbol{X}))}{\partial\lambda^i \partial\lambda^i} \, (\Delta\lambda_t^i(\boldsymbol{X}))^2 > 0 \tag{C.9}$$

After substituting an equality sign for the inequality sign, this condition is useful in order to localise regions in the principal stretch space, in which the principle values of the first Piola-Kirchhoff stress decrease (see the next section).

C.2. Model for compressible hyperelastic materials

Since a real solid elastomeric polymer is not completely incompressible, and foamed elastomeric polymers are compressible, we extend the free energy in Equation (C.3) to the compressible range, such that a unity Jacobian

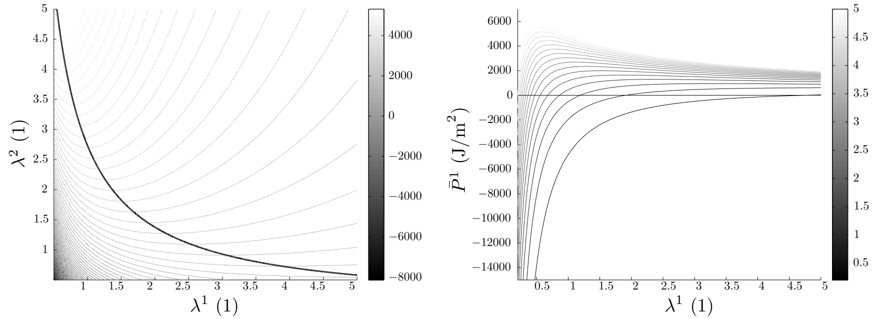

Figure C.7. In the left diagram, the first principal stress $\bar{P}^1_t(\boldsymbol{X})$, associated with the free energy $\bar{\Psi}^{\mathrm{com}}_t(\boldsymbol{X})$ corresponding to the penalty function $\ln(J_t(\boldsymbol{X}))$, is displayed in the principal stretch space (shear modulus $\mu = 7.5\,\mathrm{J/m^2}$ and second Lamé constant $\lambda = 3000\,\mathrm{J/m^2}$). The colours denote the value of the first principal stress in Joule per square meter. The region above the hyperbola-shaped curve indicates a domain of decreasing stress value. The right diagram shows the isolines pertaining to the principal stress $\bar{P}^1_t(\boldsymbol{X})$, plotted versus the first principal stretch λ^1 at constant second principal stretches λ^2. The colours denote the corresponding value of the second principal stretch. In this perspective, the decreasing of stress is obviously visible.

determinant $J_t(\boldsymbol{X})$ will be reached in the limit of incompressibility.

We start by adding a linear combination of a function H depending on the Jacobian determinant to Equation (C.3), such that we obtain a free energy

$$\bar{\Psi}^{\mathrm{inc}}_t(\boldsymbol{X}) = \Psi^{\mathrm{inc}}_t(\boldsymbol{X}) + a\,H(J_t(\boldsymbol{X})) \tag{C.10}$$

We determine the parameter a and the function H so, that the free energy (C.3) has a local minimum at a unity Jacobian determinant or unity principal stretches, respectively. Considering the directional derivative of the free energy $\bar{\Psi}^{\mathrm{inc}}_t(\boldsymbol{X})$ along the continuous time curve, the partial derivative

$$\frac{\partial\,\bar{\Psi}^{\mathrm{inc}}_t(\boldsymbol{X})}{\partial\lambda^i} = \mu\,\lambda^i_t(\boldsymbol{X}) + a\,\mathrm{D}H(J_t(\boldsymbol{X}))\,\frac{J_t(\boldsymbol{X})}{\lambda^i_t(\boldsymbol{X})} \tag{C.11}$$

denote the corresponding principal value $\bar{P}^i_t(\boldsymbol{X})$ of the first Piola-Kirchhoff stress tensor associated with the principal stretch $\lambda^i_t(\boldsymbol{X})$. The function

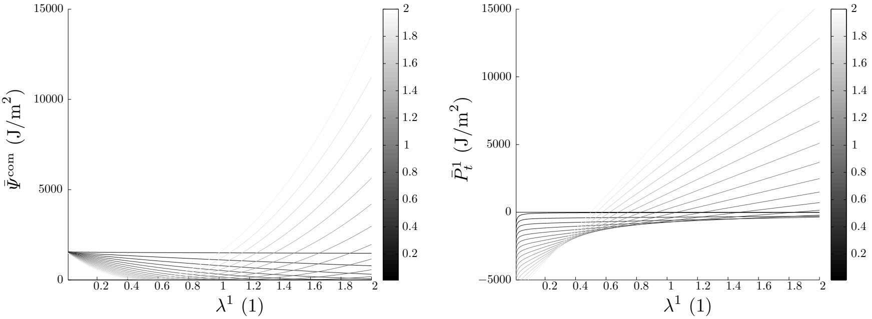

Figure C.8. On the left, the isolines of the free energy $\bar{\Psi}^{\mathrm{com}}_t(\boldsymbol{X})$ corresponding to the penalty function $J_t(\boldsymbol{X}) - 1$ are plotted versus the first principal stretch λ^1 at constant second principal stretches λ^2 (shear modulus $\mu = 7.5\,\mathrm{J/m^2}$ and second Lamé constant $\lambda = 3000\,\mathrm{J/m^2}$). The colours denote the value of the second principle stretch. In the limit of incompressibility, the free energy at the lower boundary of the principal stretch space tends to the half second Lamé constant. On the right, the isolines pertaining to the corresponding principal stress $\bar{P}^1_t(\boldsymbol{X})$ are plotted versus λ^1. The colours also indicate the value of the second principal stretch. In the limit of incompressibility, the principal stress vanish in the origin of the principal stretch space, which indicates a saddle point of the free energy.

$\mathrm{D}H(J_t(\boldsymbol{X}))$ denotes the Frèchet derivative of the function $H(J_t(\boldsymbol{X}))$. Since the minimum of the free energy is defined by vanishing partial derivatives of the free energy with respect to each of the principal stretches, the equation

$$\left(\lambda^i_t(\boldsymbol{X})\right)^2 = -\frac{a}{\mu}\,\mathrm{D}H(J_t(\boldsymbol{X}))\,J_t(\boldsymbol{X}) \tag{C.12}$$

has to lead to unity principal stretches $\lambda^i_t(\boldsymbol{X})$, $i \in \mathscr{N}_{sd}$. Further, the principal values of the first Piola-Kirchhoff stress tensor has to tend to negative infinity, if each principal stretch approaches to zero. Both is trivially fulfilled if the parameter a is equal to the negative shear modulus, and the function $\mathrm{D}H(J_t(\boldsymbol{X}))$ coincides with the inverse Jacobian determinant $J_t(\boldsymbol{X})$ for all times. The last assumption represents an ordinary differential equation with respect to the Jacobian determinant. Integrating this ordinary differential equation, we arrive at the function

$$H(J_t(\boldsymbol{X})) = \ln(J_t(\boldsymbol{X})) + c \tag{C.13}$$

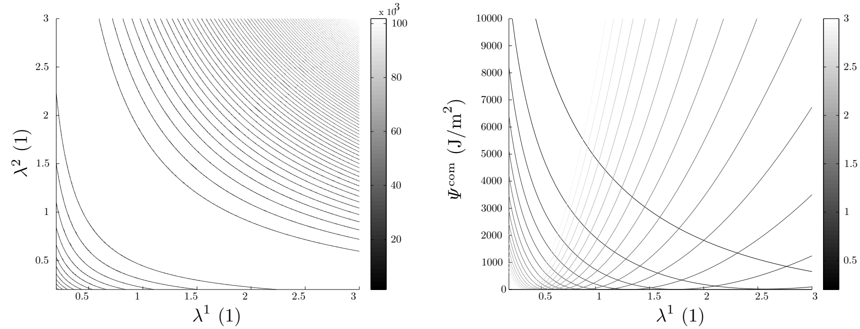

Figure C.9. On the left, the isolines of the free energy $\Psi_t^{\mathrm{com}}(\boldsymbol{X})$ corresponding to the penalty functions $J_t(\boldsymbol{X}) - 1$ and $\ln(J_t(\boldsymbol{X}))$ are plotted in the principal stretch space (shear modulus $\mu = 7.5\,\mathrm{J/m^2}$ and second Lamé constant $\lambda = 3000\,\mathrm{J/m^2}$). The colours denote the value of the free energy in Joule per square meter. On the right, the isolines of the free energy plotted versus λ^1 at constant second principal stretch are depicted. The colours indicate the value of the second principal stretch.

Obviously, the free energy function is convex in the principal stretch space.

where c denotes the integration constant (compare Figure C.3). Note that this function H can be also derived from the statistical theory of molecular chains by taking into account a change of volume in each chain (see Shu & Wenji [189]). Since we still claim that the free energy in the undeformed state vanish, the integration constant c also has to vanish. In the end, we arrive at the free energy

$$\bar{\Psi}_t^{\mathrm{inc}}(\boldsymbol{X}) = \frac{\mu}{2} \left\{ [\boldsymbol{C}_t(\boldsymbol{X})]_{AB}\, \delta^{BA} - n_{\mathrm{dim}} - 2\, \ln(J_t(\boldsymbol{X})) \right\} \tag{C.14}$$

Now, we employ the determined parameter a and the function $H(J_t(\boldsymbol{X}))$ in the corresponding principal value of the first Piola-Kirchhoff stress tensor, given by Equation (C.11). Taking Equation (C.7) into account, the monotonicity of the first Piola-Kirchhoff stress tensor imply the inequality condition

$$\left(\frac{1}{\lambda_t^i(\boldsymbol{X}) \left[\lambda_t^i(\boldsymbol{X}) + s_2 \Delta\lambda_t^i(\boldsymbol{X}) \right]} + 1 \right) \mu\, s_2 \left(\Delta\lambda_t^i(\boldsymbol{X}) \right)^2 > 0 \tag{C.15}$$

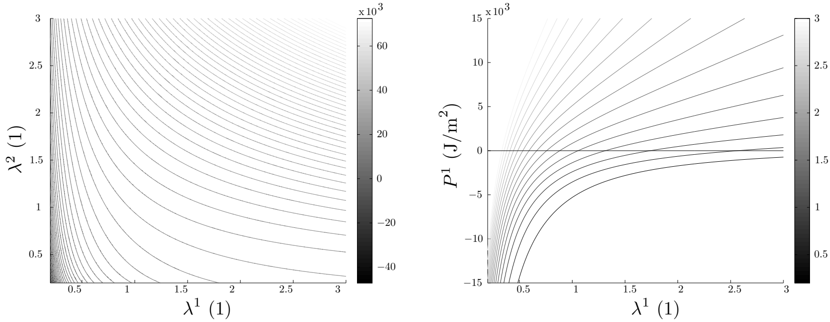

Figure C.10. In the left diagram, the first principal stress $P_t^1(\boldsymbol{X})$, associated with the free energy $\Psi_t^{\mathrm{com}}(\boldsymbol{X})$ corresponding to the penalty functions $\ln(J_t(\boldsymbol{X}))$ and $J_t(\boldsymbol{X}) - 1$, is displayed in the principal stretch space (shear modulus $\mu = 7.5\,\mathrm{J/m^2}$ and second Lamé constant $\lambda = 3000\,\mathrm{J/m^2}$). The colours denote the value of the first principal stress in Joule per square meter. The right diagram shows the isolines pertaining to the principal stress $P_t^1(\boldsymbol{X})$, plotted versus the first principal stretch λ^1 at constant second principal stretches λ^2. The colours denote the corresponding value of the second principal stretch. In this perspective, the strictly monotonically increasing principal stress is obviously visible.

Since the principal stretch value $\lambda_t^i(\boldsymbol{X})$ and its perturbed value in the brackets are both positive, this inequality is fulfilled for each increment $\Delta\lambda_t^i(\boldsymbol{X})$. Hence, the principal values of the first Piola-Kirchhoff stress tensor increases monotonically (see Figure C.5), which imply the convexity of the free energy in the principal stretch space (compare Figure C.4).

The next step is the extension to the compressible range. We apply a penalty formulation

$$\Psi_t^{\mathrm{com}}(\boldsymbol{X}) = \bar{\Psi}_t^{\mathrm{inc}}(\boldsymbol{X}) + \lambda\, G(J_t(\boldsymbol{X})) \tag{C.16}$$

by adding a penalty term, consisting of a non-negative penalty function G and the positive constant $\lambda > 0$ as penalty parameter (see Simo & Taylor [190]), which coincides in the linear theory with the second Lamé constant. Again, the function G has to vanish in an undeformed current configuration with a Jacobian determinant $J_t(\boldsymbol{X})$ which is equal to one for all points $\boldsymbol{X}$ in the reference configuration. Similarly, the corresponding principal values of the first Piola-Kirchhoff stress tensor, given by

$$(P_t^{\mathrm{com}})^i(\boldsymbol{X}) = \mu \left\{ \lambda_t^i(\boldsymbol{X}) - \frac{1}{\lambda_t^i(\boldsymbol{X})} \right\} + \lambda \, \mathrm{D}G(J_t(\boldsymbol{X})) \, \frac{J_t(\boldsymbol{X})}{\lambda_t^i(\boldsymbol{X})} \tag{C.17}$$

has to vanish at unity principal stretches. In an undeformed current configuration, the last term of Equation (C.17) vanish only if the Frèchet derivative DG vanish at a unity Jacobian determinant. Therefore, we assume a function G being quadratic in a function $\tilde{G}$ which itself vanish at unity principal stretches. We obtain the functions

$$G(J_t(\boldsymbol{X})) = \frac{1}{2} \left\{ \tilde{G}(J_t(\boldsymbol{X})) \right\}^2 \quad \text{and} \quad \mathrm{D}G(J_t(\boldsymbol{X})) = \tilde{G}(J_t(\boldsymbol{X})) \, \mathrm{D}\tilde{G}(J_t(\boldsymbol{X})) \tag{C.18}$$

Moreover, the function G has to fulfill further conditions to be physically meaningful. First, when the continuum degenerates to a single point under a pressure load, which is happened in the origin of the principal stretch space, the free energy tends to infinity and the first Piola-Kirchhoff stress tends to negative infinity, which means

$$\lim_{\lambda^i \to 0^+} \left\{ \tilde{G}(J_t(\boldsymbol{X})) \right\}^2 \longrightarrow \infty \tag{C.19}$$

and

$$\lim_{\lambda^i \to 0^+} \tilde{G}(J_t(\boldsymbol{X})) \left\{ \mathrm{D}\tilde{G}(J_t(\boldsymbol{X})) \, \frac{J_t(\boldsymbol{X})}{\lambda_t^i(\boldsymbol{X})} \right\} \longrightarrow -\infty \tag{C.20}$$

These conditions are satisfied if (1.a) $\tilde{G}$ tends to infinity and the limit of D$\tilde{G}$ is negative, or if (1.b) $\tilde{G}$ approaches to negative infinity and the limit of the brace is positive.

Second, when the continuum expands to an infinite volume under tension, which means each principal stretch $\lambda_t^i(\boldsymbol{X})$ approaches to infinity, the free energy as well as the first Piola-Kirchhoff stress tends to infinity in the sense

$$\lim_{\lambda^i \to \infty} \left\{ \tilde{G}(J_t(\boldsymbol{X})) \right\}^2 \longrightarrow \infty \tag{C.21}$$

and

$$\lim_{\lambda^i \to \infty} \tilde{G}(J_t(\boldsymbol{X})) \left\{ \mathrm{D}\tilde{G}(J_t(\boldsymbol{X}))\, \frac{J_t(\boldsymbol{X})}{\lambda_t^i(\boldsymbol{X})} \right\} \longrightarrow \infty \tag{C.22}$$

These conditions are fulfilled if (2.a) $\tilde{G}$ tends to negative infinity and $\mathrm{D}\tilde{G}$ approaches to a negative limit, or if (2.b) $\tilde{G}$ tends to infinity and the limit of the brace on the righthand side is positive.

The function $\ln(J_t(\boldsymbol{X}))$ and its tangent line $J_t(\boldsymbol{X}) - 1$ in the abscissa (see Figure C.3) are two functions, which vanish in an undeformed configuration, and are therefore two penalty functions

$$\tilde{G}_1(J_t(\boldsymbol{X})) = \ln(J_t(\boldsymbol{X})) \qquad \text{and} \qquad \tilde{G}_2(J_t(\boldsymbol{X})) = J_t(\boldsymbol{X}) - 1 \tag{C.23}$$

(compare also Shu & Wenji [189]). The function $\tilde{G}_1$ satisfies the condition (1.b) of the first case, however, violates the conditions associated with the second case, because the corresponding partial derivatives with respect to the principal stretches tends to zero according to L'Hôpital's rule. Applying the convexity condition in Equation (C.9), the implicit functions

$$1 + \left(\lambda_t^i(\boldsymbol{X})\right)^2 + \frac{\lambda}{\mu}\, \{1 - \ln\left(J_t(\boldsymbol{X})\right)\} = 0 \tag{C.24}$$

therefore defines a bound of a depression in the profile pertaining to the i-th principal value of the first Piola-Kirchhoff stress tensor (see Figure C.7). In turn, this depression in the principal stresses imply a concave domain in the profile of the free energy, which is extending while the positive quotient λ/μ is increasing.

On the other hand, the function $\tilde{G}_2$ violates the conditions associated with the first case, because of its finite value at the lower boundary of the principal stretch space. In the limit of incompressibility, the corresponding free energy $\Psi_t^{\mathrm{com}}(\boldsymbol{X})$ is therefore likewise bounded, and the principal values of the first Piola-Kirchhoff stress tensor vanish in the origin of the principal stretch space (compare Figure C.8). Nevertheless, the monotony condition

$$\mu\, s_2\, (\Delta\lambda_t^i(\boldsymbol{X}))^2 \left\{ \frac{1}{\lambda_t^i(\boldsymbol{X})\left(\lambda_t^i(\boldsymbol{X}) + s_2\, \Delta\lambda_t^i(\boldsymbol{X})\right)} + 1 + \frac{\lambda}{\mu}\, (\lambda_t^j(\boldsymbol{X}))^2 \right\} > 0 \tag{C.25}$$

corresponding to this free energy holds for any increment $\Delta\lambda_t^i(\boldsymbol{X})$, and the penalty function $\tilde{G}_2$ fulfills the condition (2.b) corresponding to the second case.

Therefore, when applying both penalty functions, all conditions are satisfied (compare Simo & Taylor [190]). Firstly, the free energy at any point $\boldsymbol{X} \in \mathscr{B}_0$ tends to positive infinity, if the volume element V_x at the corresponding deformed point $x \in \mathscr{B}_t$ tends to infinity or zero, respectively (see Figure C.9). Secondly, by applying the convexity condition in Equation (C.9), we obtain the relation

$$\mu \left(\frac{\Delta\lambda_t^i(\boldsymbol{X})}{\lambda_t^i(\boldsymbol{X})} \right)^2 \left\{ 1 + (\lambda_t^i(\boldsymbol{X}))^2 + \frac{\lambda}{\mu} \left[1 + (J_t(\boldsymbol{X}))^2 - \ln(J_t(\boldsymbol{X})) \right] \right\} > 0 \tag{C.26}$$

which holds because the bracket is greater than zero (see the illustration in Figure C.3). Hence, the principal values of the first Piola-Kirchhoff stress tensor are strictly monotonically increasing in the entire principal stretch space (see Figure C.10), and the free energy is therefore strictly convex in the principal stretch space without restrictions. Accordingly, we arrive at the recommendable free energy function

$$\boxed{\Psi_t^{\mathrm{com}}(\boldsymbol{X}) = \frac{\mu}{2} \left\{ [\boldsymbol{C}_t(\boldsymbol{X})]_{AB}\, \delta^{BA} - n_{\mathrm{dim}} - 2\, \ln(J_t(\boldsymbol{X})) \right\} + \Psi_t^{\mathrm{vol}}(\boldsymbol{X})} \tag{C.27}$$

where

$$\Psi_t^{\mathrm{vol}}(\boldsymbol{X}) = \frac{\lambda}{2} \left\{ (\ln(J_t(\boldsymbol{X})))^2 + (J_t(\boldsymbol{X}) - 1)^2 \right\} \tag{C.28}$$

for a compressible elastomeric polymer undergoing large deformations. The first term determines the distortion of the material, and the function $\Psi_t^{\mathrm{vol}}(\boldsymbol{X})$ describes a change of volume. Further volumetric free energy functions can be found in Doll & Schweizerhof [191] and in references therein.

C.3. Model for compressible thermoelastic materials

We now extend the free energy for describing absorption of heat and a thermal expansion of the body (compare Carlson [192] for a contribution within the linear theory). We show that a constant specific heat capacity $c > 0$ is a consistent assumption in conjunction with the constant material parameters in Equation (C.27) and Equation (C.28). We supplement this claim through a constant coefficient β of linear thermal expansion (compare Simo & Miehe [193]).

The specific heat capacity c at constant volume is the incremental internal energy $\mathrm{d}e_t(\boldsymbol{X})$ which is required for producing an incremental temperature change $\mathrm{d}\Theta_t(\boldsymbol{X})$ in the volume element V_x corresponding to the point $\boldsymbol{X} \in \mathscr{B}_0$. Since a change in the temperature of an isotropic material only affects a change of its volume, we view only the volumetric free energy in Equation (C.28) as a function depending on the temperature $\Theta_t(\boldsymbol{X})$ of the body. According to Equation (2.70), the corresponding incremental internal energy density reads

$$\begin{aligned}\mathrm{d}e_t^{\mathrm{vol}}(\boldsymbol{X}) = \left\{\eta_t(\boldsymbol{X}) + \frac{\partial \Psi_t^{\mathrm{vol}}(\boldsymbol{X})}{\partial \Theta}\right\} \mathrm{d}\Theta_t(\boldsymbol{X}) + \Theta_t(\boldsymbol{X})\, \mathrm{d}\eta_t(\boldsymbol{X}) + \\ + \frac{\partial \Psi_t^{\mathrm{vol}}(\boldsymbol{X})}{\partial J}\, \mathrm{d}J_t(\boldsymbol{X})\end{aligned} \tag{C.29}$$

Taking Equation (2.48) as definition of the entropy into account, the bracket drops out of the summation. Since at fixed volume the incremental change of the Jacobian determinant is zero, the incremental change of the internal energy density then takes the form

$$\mathrm{d}e_t^{\mathrm{vol}}(\boldsymbol{X}) = \Theta_t(\boldsymbol{X})\, \frac{\partial \eta_t(\boldsymbol{X})}{\partial \Theta}\, \mathrm{d}\Theta_t(\boldsymbol{X}) = \frac{\partial \eta_t(\boldsymbol{X})}{\partial \ln(\Theta)}\, \mathrm{d}\Theta_t(\boldsymbol{X}) \tag{C.30}$$

with

$$\eta_t(\boldsymbol{X}) = - \left. \frac{\partial \Psi_t^{\mathrm{vol}}(\boldsymbol{X})}{\partial \Theta} \right|_{J_t(X)} \tag{C.31}$$

Hence, the coefficient of the temperature differential $\mathrm{d}\Theta_t(\boldsymbol{X})$ in Equation (C.30) defines the specific heat capacity c of the material.

This definition can be viewed as a partial differential equation for the entropy, wherefore we integrate this equation with respect to the temperature at constant Jacobian determinant. We obtain the entropy

$$\eta_t(\boldsymbol{X}) = c\, \ln(\Theta_t(\boldsymbol{X})) + M(J_t(\boldsymbol{X})) + K_t^{\eta}(\boldsymbol{X}) \tag{C.32}$$

with the last two terms as integration constants. We choose $K_t^{\eta}(\boldsymbol{X})$ such that at ambient temperature Θ_∞ only mechanical entropy $M(J_t(\boldsymbol{X}))$ remains. We specify the mechanical entropy function M by incorporating a constant coefficient α of thermal expansion, which determines a relative change of a volume element by the relation

$$\alpha\,\{\Theta_t(\boldsymbol{X}) - \Theta_0(\boldsymbol{X})\} = \frac{V_x - V_X}{V_X} \equiv J_t(\boldsymbol{X}) - 1 \tag{C.33}$$

Determining the total differential of Equation (C.33), the coefficient α of thermal expansion relates the incremental change of the Jacobian determinant to an incremental change of the temperature of the body. For isotropic material, the coefficient of thermal expansion coincides with $n_{\text{dim}}\beta$, such that

$$n_{\text{dim}}\beta = \frac{\partial J_t(\boldsymbol{X})}{\partial \Theta} \tag{C.34}$$

Accordingly, the coefficient of thermal expansion is a differential relation between the arguments of the volumetric free energy $\Psi_t^{\text{vol}}(\boldsymbol{X})$.

According to Maxwell, there exist relations between primary variables and their cotangent vectors after applying a Legendre transform (see Holzapfel [135]). Therefore, we transform the volumetric (Helmholtz) free energy into the Gibbs free energy

$$g_t^{\text{vol}}(\boldsymbol{X}) = \Psi_t^{\text{vol}}(\boldsymbol{X}) - p_t(\boldsymbol{X})\,(J_t(\boldsymbol{X}) - 1) \tag{C.35}$$

After considering the total differential of this Gibbs free energy, the incremental change of the Jacobian determinant drops out if $p_t(\boldsymbol{X})$ coincides with the cotangent vector of the Jacobian determinant, called the hydrostatic pressure. Thus, the Gibbs free energy is a function depending on the temperature and the hydrostatic pressure

$$p_t(\boldsymbol{X}) = \left.\frac{\partial \Psi_t^{\text{vol}}(\boldsymbol{X})}{\partial J}\right|_{\Theta_t(X)} = \frac{\lambda}{J_t(\boldsymbol{X})}\left\{\ln(J_t(\boldsymbol{X})) + (J_t(\boldsymbol{X}))^2 - J_t(\boldsymbol{X})\right\} \tag{C.36}$$

in the case of employing the volumetric free energy in Equation (C.28). By a comparison of the total differentials pertaining to the left hand side and the righthand side of Equation (C.35), we arrive at the so-called Gibbs relations corresponding to this function, which here defines the Jacobian determinant and the entropy as partial derivatives of the Gibbs free energy. Applying Young's theorem of the symmetry of mixed partial derivatives of a continuous function, we arrive at the Maxwell relation

$$\left.\frac{\partial J_t(\boldsymbol{X})}{\partial \Theta}\right|_{p_t(X)} = \left.\frac{\partial \eta_t(\boldsymbol{X})}{\partial p}\right|_{\Theta_t(X)} \tag{C.37}$$

This Maxwell relation represents another partial differential equation for the entropy. According to Equation (C.34), the left hand side coincides with the coefficient of thermal expansion. Therefore, integration with respect to the hydrostatic pressure at constant temperature leads to the entropy

$$\eta_t(\boldsymbol{X}) = n_{\mathrm{dim}} \beta \, \frac{\partial \Psi_t^{\mathrm{vol}}(\boldsymbol{X})}{\partial J} + T(\Theta_t(\boldsymbol{X})) + K_t^{\eta}(\boldsymbol{X}) \tag{C.38}$$

A comparison with Equation (C.32) identifies the first term as the mechanical entropy M, the second term as the thermal entropy arising from the constant specific heat capacity, and the last term as the integration constant $K_t^{\eta}(\boldsymbol{X})$ in Equation (C.32).

Finally, employing the definition of the entropy on the righthand side and integrating over the temperature at constant Jacobian determinant, we arrive at the thermal volumetric free energy

$$\boxed{\Psi_t^{\mathrm{the}}(\boldsymbol{X}) = c \left\{ \vartheta_t(\boldsymbol{X}) - \Theta_t(\boldsymbol{X}) \, \ln\left(\frac{\Theta_t(\boldsymbol{X})}{\Theta_\infty} \right) \right\} - n_{\mathrm{dim}} \, \beta \, \vartheta_t(\boldsymbol{X}) \, \frac{\partial \Psi_t^{\mathrm{vol}}(\boldsymbol{X})}{\partial J}} \tag{C.39}$$

where we have taken into account that the total volumetric free energy has to coincide with the purely mechanical volumetric free energy $\Psi_t^{\mathrm{vol}}(\boldsymbol{X})$ at ambient temperature. Thus, starting from a constant specific heat of the material, we actually arrive at an additive split of the purely mechanical part and a thermal part.

C.4. Model for compressible thermo-viscoelastic materials

For describing a viscoelastic isotropic material, we introduce in Section 2.1.10 a symmetric Lagrangian internal variable field by transforming the right Cauchy-Green tensor in the argument of its hyperelastic free energy. Thereby, the elastic properties of the material remain unchanged. Here, we transform the elastic Neo-Hookean free energy $\Psi_t^{\mathrm{com}}(\boldsymbol{X})$ in a viscoelastic Neo-Hookean free energy

$$\begin{aligned}\Psi_t^{\mathrm{vis}}(\boldsymbol{X}) = \frac{\mu}{2}\Big\{[\boldsymbol{\Lambda}_t(\boldsymbol{X})]_A{}^A - n_{\mathrm{dim}} - 2\,\ln(\sqrt{\det(\boldsymbol{\Lambda}_t(\boldsymbol{X}))})\Big\} + \\ + \Psi^{\mathrm{vol}}(\sqrt{\det(\boldsymbol{\Lambda}_t(\boldsymbol{X}))})\end{aligned} \tag{C.40}$$

depending on the unsymmetric tensor $\boldsymbol{\Lambda}_t(\boldsymbol{X})$. Then, we arrive at a thermo-viscoelastic Neo-Hookean model for isotropic compressible materials, which introduce viscous behaviour as well as the affects of absorption of heat and thermal expansion, by defining the total free energy

$$\boxed{\Psi_t(\boldsymbol{X}) = \Psi_t^{\mathrm{com}}(\boldsymbol{X}) + \Psi_t^{\mathrm{vis}}(\boldsymbol{X}) + \Psi_t^{\mathrm{the}}(\boldsymbol{X})} \tag{C.41}$$

The iterative solution procedure of the weak forms is based on the first and second partial derivatives of the free energy. Therefore, we state the second Piola-Kirchhoff stress tensor according to Equation (2.45). By differentiating the pure mechanical free energy $\Psi_t^{\mathrm{com}}(\boldsymbol{X})$ with respect to the components of the right Cauchy-Green tensor, we obtain the mechanical part

$$[\boldsymbol{S}_t^{\mathrm{com}}(\boldsymbol{X})]^{AB} = \mu\,\delta^{AB} + F(J_t(\boldsymbol{X}))\,[(\boldsymbol{C}_t(\boldsymbol{X}))^{-1}]^{AB} \tag{C.42}$$

where

$$\begin{aligned}F(J_t(\boldsymbol{X})) &= p_t(\boldsymbol{X})\,J_t(\boldsymbol{X}) - \mu \\ &= \lambda\left\{\ln(J_t(\boldsymbol{X})) + (J_t(\boldsymbol{X}))^2 - J_t(\boldsymbol{X})\right\} - \mu\end{aligned} \tag{C.43}$$

denotes a scalar function depending on the Jacobian determinant. The viscous part of the free energy depends directly on the trace and the determinant of the tensor $\boldsymbol{\Lambda}_t(\boldsymbol{X})$, defined by Equation (2.39) via the right Cauchy-Green tensor. Hence, we apply the chain rule of differentiation, and obtain the viscous part of the second Piola-Kirchhoff stress, given by

$$[\boldsymbol{S}_t^{\mathrm{vis}}(\boldsymbol{X})]^{AB} = \mu\,[(\boldsymbol{\Gamma}_t(\boldsymbol{X}))^{-1}]^{AB} + F(\sqrt{\det(\boldsymbol{\Lambda}_t(\boldsymbol{X}))})\,[(\boldsymbol{C}_t(\boldsymbol{X}))^{-1}]^{AB} \tag{C.44}$$

The last term of the total second Piola-Kirchhoff stress tensor originate from the mechanical entropy, which leads to the thermal expansion of the material. We differentiate the free energy $\Psi_t^{\mathrm{the}}(\boldsymbol{X})$ with respect to the right Cauchy-Green tensor, where we apply the chain rule for determining the partial derivative of the Jacobian determinant. In the end, the thermal part reads

$$[\boldsymbol{S}_t^{\mathrm{the}}(\boldsymbol{X})]^{AB} = \frac{n_{\mathrm{dim}}\beta\,\lambda\,\vartheta_t(\boldsymbol{X})}{J_t(\boldsymbol{X})}\left\{\ln(J_t(\boldsymbol{X})) - (J_t(\boldsymbol{X}))^2 - 1\right\}[(\boldsymbol{C}_t(\boldsymbol{X}))^{-1}]^{AB} \tag{C.45}$$

In the viscous evolution equation, we need the non-equilibrium stress tensor. According to Equation (2.44), it coincides with the negative partial derivative of the free energy with respect to the internal variable. In the total free energy in Equation (C.41), solely the viscous part depends on the internal variable. Using a further abbreviation, we arrive at

$$[\boldsymbol{\Upsilon}_t(\boldsymbol{X})]^{AB} = \frac{\mu}{2}\,[\boldsymbol{\Omega}_t(\boldsymbol{X})]^{AB} + \frac{1}{2}\,F(\sqrt{\det(\boldsymbol{\Lambda}_t(\boldsymbol{X}))})\,[(\boldsymbol{\Gamma}_t(\boldsymbol{X}))^{-1}]^{AB} \tag{C.46}$$

where

$$[\boldsymbol{\Omega}_t(\boldsymbol{X})]^{AB} = [(\boldsymbol{\Gamma}_t(\boldsymbol{X}))^{-1}]^{AC}\,[\boldsymbol{C}_t(\boldsymbol{X})]_{CD}[(\boldsymbol{\Gamma}_t(\boldsymbol{X}))^{-1}]^{DB} \tag{C.47}$$

denotes a symmetric tensor. By multiplying the non-equilibrium stress tensor with the internal variable from the left, we obtain a stress tensor which depends only on the tensorial argument $\boldsymbol{\Lambda}_t(\boldsymbol{X})$ of the viscous free energy. According to Equation (2.74), this tensor coincides with the Mandel stress tensor. For the considered Neo-Hookean material, we obtain

$$[\boldsymbol{M}_t(\boldsymbol{X})]_A{}^B = \mu\,[\boldsymbol{\Lambda}_t(\boldsymbol{X})]_A{}^B + F(\sqrt{\det(\boldsymbol{\Lambda}_t(\boldsymbol{X}))})\,\delta_A{}^B \tag{C.48}$$

Note that this tensor function is isotropic, according to the first representation theorem, and therefore a consistent response function for the viscoelastic stress of the considered isotropic material.

Since the function $\Psi_t^{\mathrm{the}}(\boldsymbol{X})$ include the only terms of the total free energy depending on the temperature field, the entropy are given by

$$\eta_t(\boldsymbol{X}) = \frac{n_{\mathrm{dim}}\,\beta\,\lambda}{J_t(\boldsymbol{X})}\left\{\ln(J_t(\boldsymbol{X})) + (J_t(\boldsymbol{X}))^2 - J_t(\boldsymbol{X})\right\} + c\,\ln\left(\frac{\Theta_t(\boldsymbol{X})}{\Theta_\infty}\right) \tag{C.49}$$

In the material part of the **x**-increment pertaining to the global mechanical Galerkin form, for instance, the partial derivative of the second Piola-Kirchhoff stress tensor with respect to the right Cauchy-Green tensor is used (see Equation (B.9)). This material tensor corresponding to the total free energy in Equation (C.41) also consists of three parts. The mechanical part is given by

$$[{}^{CC}\mathbb{L}_t^{\mathrm{com}}]^{ABCD} = K(J_t)\,[\boldsymbol{C}_t^{-1}]^{AB}\,[\boldsymbol{C}_t^{-1}]^{CD} - F(J_t)\,[{}_{\mathrm{sym}}\overset{C}{\mathbb{L}}_t]^{ABCD} \tag{C.50}$$

with

$$K(J_t(\boldsymbol{X})) = J_t(\boldsymbol{X})\,\mathrm{D}F(J_t(\boldsymbol{X})) = \lambda\left\{1 - J_t(\boldsymbol{X}) + 2\,(J_t(\boldsymbol{X}))^2\right\} \tag{C.51}$$

The fourth-order tensor ${}_{\mathrm{sym}}\overset{C}{\mathbb{L}}_t(\boldsymbol{X})$ is defined by the fully symmetric tensor in Equation (B.17), applied to the right Cauchy-Green tensor $C_t(\boldsymbol{X})$ instead of to the right Cauchy-Green tensor $\boldsymbol{c}_0^{\mathrm{e}}$ in the spatial parent domain. The viscous part ${}^{CC}\mathbb{L}_t^{\mathrm{vis}}(\boldsymbol{X})$ of the material tensor has the same structure as the mechanical part, however, the Jacobian determinant $J_t(\boldsymbol{X})$ has to be replaced by the square root $\sqrt{\det(\boldsymbol{\Lambda}_t(\boldsymbol{X}))}$ in the arguments of the functions F and K. The thermal part of this material tensor is given by

$$\begin{aligned}[{}^{CC}\mathbb{L}_t^{\mathrm{the}}]^{ABCD} = {} & \frac{n_{\mathrm{dim}}\,\beta\,\lambda\,\vartheta_t}{J_t}\left\{2 - \ln(J_t) - (J_t)^2\right\}[\boldsymbol{C}_t^{-1}]^{AB}\,[\boldsymbol{C}_t^{-1}]^{CD} + \\ & + \frac{n_{\mathrm{dim}}\,\beta\,\lambda\,\vartheta_t}{J_t}\left\{1 - \ln(J_t) + (J_t)^2\right\}[{}_{\mathrm{sym}}\overset{C}{\mathbb{L}}_t]^{ABCD}\end{aligned} \tag{C.52}$$

In the linearised enhanced virtual work associated with the algorithmic global force vector, we employ the partial derivative of the non-equilibrium stress tensor with respect to the right Cauchy-Green tensor (see Equation (B.25)). Since the internal variable tensor $\boldsymbol{\Gamma}_t(\boldsymbol{X})$ is included only in the viscous part of the second Piola-Kirchhoff stress tensor, the total material tensor reads

$$[{}^{\Gamma C}\mathbb{L}_t]^{ABCD} = \frac{1}{2}\, K(\sqrt{\det(\boldsymbol{\Lambda}_t)})\, [\boldsymbol{\Gamma}_t^{-1}]^{AB}\, [\boldsymbol{C}_t^{-1}]^{CD} + \frac{1}{2}\, \mu\, [{}^{\Gamma}_{\mathrm{sym}}\mathbb{L}_t]^{ABCD} \tag{C.53}$$

The **i**-increment of the global mechanical Galerkin form is based on the partial derivative of the non-equilibrium stress tensor with respect to the internal variable tensor. Therefore, we differentiate the stress tensor in Equation (C.46), and obtain the corresponding material tensor in Equation (B.37) in the form

$$\begin{aligned}
[{}^{\Gamma\Gamma}_{\mathrm{Non}}\mathbb{L}_t]^{ABCD} &= -\frac{\mu}{4}\, \big\{[\boldsymbol{\Gamma}_t^{-1}]^{AC}[\boldsymbol{\Omega}_t]^{BD} + [\boldsymbol{\Gamma}_t^{-1}]^{AD}[\boldsymbol{\Omega}_t]^{BC} + \\
&\qquad + [\boldsymbol{\Omega}_t]^{AC}[\boldsymbol{\Gamma}_t^{-1}]^{BD} + [\boldsymbol{\Omega}_t]^{AD}[\boldsymbol{\Gamma}_t^{-1}]^{BC}\big\} - \\
&\quad -\frac{1}{4}\, F(\sqrt{\det(\boldsymbol{\Lambda}_t)})\, \big\{[\boldsymbol{\Gamma}_t^{-1}]^{AC}[\boldsymbol{\Gamma}_t^{-1}]^{BD} + [\boldsymbol{\Gamma}_t^{-1}]^{AD}[\boldsymbol{\Gamma}_t^{-1}]^{BC}\big\} - \\
&\quad -\frac{1}{4}\, K(\sqrt{\det(\boldsymbol{\Lambda}_t})\, [\boldsymbol{\Gamma}_t^{-1}]^{AB}\, [\boldsymbol{\Gamma}_t^{-1}]^{CD}
\end{aligned} \tag{C.54}$$

Next, we determine the stress-temperature tensor $\boldsymbol{T}_t(\boldsymbol{X})$, defined by Equation (B.21), which occur in the linearisation pertaining to the numerator of the stress trace tensor. Since only the thermal part $\boldsymbol{S}_t^{\mathrm{the}}(\boldsymbol{X})$ of the second Piola-Kirchhoff stress tensor depends on the temperature, the stress-temperature tensor reads

$$\boldsymbol{T}_t(\boldsymbol{X}) = \frac{n_{\mathrm{dim}}\beta\,\lambda}{J_t(\boldsymbol{X})}\, \big\{\ln(J_t(\boldsymbol{X})) - (J_t(\boldsymbol{X}))^2 - 1\big\}\, [(\boldsymbol{C}_t(\boldsymbol{X}))^{-1}]^{AB} \tag{C.55}$$

For the **o**-increment of the global mechanical Galerkin form, we give the partial derivative of the non-equilibrium stress and the entropy with respect to the temperature field of the body. The former partial derivative vanish for the total free energy (C.41), however, the incremental temperature change of the entropy is given by

$$\frac{\partial \eta_t(\boldsymbol{X})}{\partial \Theta} = \frac{c}{\Theta_t(\boldsymbol{X})} \tag{C.56}$$

where c denotes the specific heat capacity.

D. FREE ROTATING ELASTIC RING IN THE LINEAR THEORY

In this section, we derive the steady-state stress distribution of a free rotating linear elastic ring in the linearised theory, in order to validate the simulation result of the exactly energy consistent finite element method (for more details see Timoshenko & Goodier [194], Hahn [195] and Roark & Young [196]). Since we calculate with the Neo-Hookean model for isotropic compressible materials, given by Equation (C.41) in dependence of Lamé's first and second parameter, we also relate Poisson's ratio and Young's modulus in the case of plane stress to these two parameters.

D.1. Stress distribution in radial and transverse direction

We consider the dynamic equilibrium of a small element with a surface area of $r\,\mathrm{d}r\,\mathrm{d}\varphi$ cut out from the ring, where r and φ denote the polar coordinates (see Figure D.1). In the steady state, there is no transverse component of the inertia vector in the dynamic equilibrium. Only the radial component, also called the centrifugal force, remains in the radial direction. Further, owing to the symmetry of the ring, the stress do not dependent on the polar coordinate φ. Hence, the dynamic equilibrium is reduced to the equation

$$\sigma_r\,\mathrm{d}r\,\mathrm{d}\varphi + \,\mathrm{d}\sigma_r r\,\mathrm{d}\varphi - \sigma_\varphi\,\mathrm{d}r\,\mathrm{d}\varphi + r^2\omega^2\rho\,\mathrm{d}r\,\mathrm{d}\varphi = 0 \tag{D.1}$$

after neglecting terms not part of a differential 2-form, and employing the infinitesimal mass $\rho\,\mathrm{d}r\,\mathrm{d}\varphi$ in the centrifugal force of the element. The stress components σ_r and σ_φ pertains to the radial and transverse direction, respectively (see Figure D.2). We factor out the product $\mathrm{d}r\,\mathrm{d}\varphi$, and arrive at the differential equation

$$\frac{\mathrm{d}}{\mathrm{d}r}\left(r\,\sigma_r\right) - \sigma_\varphi + \rho\,\omega^2 r^2 = 0 \tag{D.2}$$

according to the arbitrariness of the infinitesimal change of the polar coordinates, and taking into account the chain rule of differentiation in order to simplify the terms pertaining to the stress in radial direction.

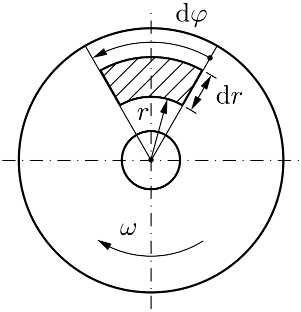

Figure D.1. A circular ring rotating around its center.

As next step, we introduce Hooke's law for plane strain in polar coordinates, given by

$$E\,\frac{\mathrm{d}u_r}{\mathrm{d}r} = \sigma_r - \nu\sigma_\varphi \qquad \text{and} \qquad E\,u_r = r\,\sigma_\varphi - \nu\,r\,\sigma_r \tag{D.3}$$

where u_r denotes the only displacement in radial direction, and the material constants ν and E designate Poisson's ratio and Young's modulus, respectively. We differentiate Equation (D.3.2) on both sides with respect to the polar coordinate r, and employ the resulting equation in Equation (D.3.1). We obtain a second differential equation for the stress distribution, which takes the form

$$\sigma_r - \nu\sigma_\varphi = \frac{\mathrm{d}}{\mathrm{d}r}\left(r\,\sigma_\varphi\right) - \nu\frac{\mathrm{d}}{\mathrm{d}r}\left(r\,\sigma_r\right) \tag{D.4}$$

By using Equation (D.2), we eliminate the stress σ_φ in transverse direction in Equation (D.4). Then, by also running the chain rule of differentiation backward, we arrive at an ordinary differential equation of second order, which can be integrated with respect to r successively. This equation reads

$$\frac{\mathrm{d}}{\mathrm{d}r}\left(r^3\,\frac{\mathrm{d}\sigma_r}{\mathrm{d}r}\right) = -\left(3+\nu\right)\rho\,\omega^2 r^3 \tag{D.5}$$

The integration leads to two integration constants, which has to be determined by boundary conditions. In the case of a free rotating circular ring, there are no forces acting on the inner and outer boundary. Therefore, the radial stress σ_r vanish at the inner radius R_i and the outer radius R_a. In the end, the radial stress distribution takes the form

$$\boxed{\sigma_r(r) = \frac{3+\nu}{8}\rho\,\omega^2\left(R_i^2 + R_a^2 - \frac{R_i^2 R_a^2}{r^2} - r^2\right)} \tag{D.6}$$

According to the boundary conditions, the minimum values lie at the boundaries. Thus, there exist a maximum value on the ring. We determine the only root pertaining to the derivative of the concave function, given by Equation (D.6). We obtain the position $\sqrt{R_i R_a}$, at which the maximum stress in radial direction amounts to

$$\sigma_r^{\max} = \frac{3+\nu}{8}\rho\,\omega^2\left(R_a - R_i\right)^2 \tag{D.7}$$

The stress distribution in transverse direction simply follows from employing Equation (D.6) in Equation (D.2). We obtain a function $\sigma_\varphi(r)$ with negative slope throughout the ring, and an inflection point at which the function changes from convex to concave with increasing polar coordinate r. Hence, the maximum value of the stress distribution

$$\boxed{\sigma_\varphi(r) = \frac{3+\nu}{8}\rho\,\omega^2\left(R_i^2 + R_a^2 + \frac{R_i^2 R_a^2}{r^2} - \frac{1+3\nu}{3+\nu}\,r^2\right)} \tag{D.8}$$

is at the inner boundary, and the minimum values lies at the outer boundary. In comparison to the maximum value of the stress in radial direction, given by Equation (D.7), the stress in transverse direction is greater throughout the ring. We obtain the bounds

$$\sigma_\varphi^{\min} = \frac{3+\nu}{4}\,\rho\,\omega^2\left(R_i^2 + \frac{1-\nu}{3+\nu}\,R_a^2\right) \tag{D.9}$$

and

$$\sigma_\varphi^{\max} = \frac{3+\nu}{4}\,\rho\,\omega^2\left(R_a^2 + \frac{1-\nu}{3+\nu}\,R_i^2\right) \tag{D.10}$$

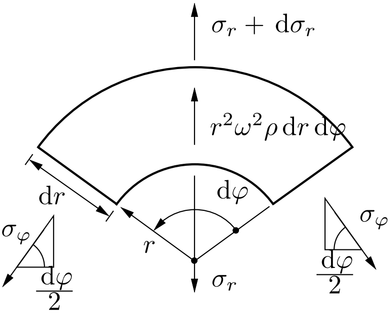

Figure D.2. An infinitesimal sector cut out from the circular ring.

of the stress in transverse direction.

D.2. Lamé's first and second parameter in the case of plane stress

In the case of linear elasticity, Lamé's first and second parameter $\mu > 0$ and $\lambda > 0$, respectively, are related to Poisson's ratio ν and Young's modulus E. However, the relations for plane stress differ from that valid for a three-dimensional body. Therefore, we derive the relations valid for a plate by starting with the second Piola-Kirchhoff stress tensor of linear finite elasticity, given by the components

$$[\boldsymbol{S}_t(\boldsymbol{X})]^{AB} = 2\mu\,[\boldsymbol{E}_t(\boldsymbol{X})]_{CD}\,\delta^{AC}\delta^{BD} + \lambda\,\operatorname{tr}(\boldsymbol{E}_t(\boldsymbol{X}))\,\delta^{AB} \tag{D.11}$$

where

$$[\boldsymbol{E}_t(\boldsymbol{X})]_{CD} = \frac{1}{2}\left([\boldsymbol{C}_t(\boldsymbol{X})]_{CD} - \delta_{CD}\right) \tag{D.12}$$

denotes the components of the Green-Lagrange strain tensor. After linearising the kinematic measures, the Green-Lagrange strain tensor in Equation (D.11) has to be substituted by its linear part, which means Cauchy's infinitesimal strain tensor $\boldsymbol{\epsilon}_t(\boldsymbol{x})$. A further consequence of the geometric linearisation is, that the deformation gradient $\boldsymbol{F}_t(\boldsymbol{X})$ coincides with the shifter with the entries ${\delta^a}_A$ in the corresponding matrix (see Guo [197]). Hence, we have not to distinguish between $\boldsymbol{X}$ and $\boldsymbol{x}$ as argument, and the Piola-Kirchhoff stress tensors $\boldsymbol{P}_t(\boldsymbol{X})$ and $\boldsymbol{S}_t(\boldsymbol{X})$ both pass into Cauchy's stress tensor $\boldsymbol{\sigma}_t(\boldsymbol{x})$ (see

Pabst [198]). In this way, we arrive at the components

$$\sigma_{11} = 2\mu\epsilon_{11} + \lambda\left(\epsilon_{11} + \epsilon_{22}\right) \qquad \sigma_{22} = 2\mu\epsilon_{22} + \lambda\left(\epsilon_{11} + \epsilon_{22}\right) \qquad \sigma_{12} = 2\mu\epsilon_{12} \tag{D.13}$$

by omitting the time index t and the argument $\boldsymbol{x}$ referring to the material point of the plate. The indices 1 and 2 indicate the axes of a Cartesian coordinate system.

On the other hand, according to Hooke's law, there are linear relations between the components σ_{ij} of stress and the components ϵ_{ij} of strain. In the case of a plate, loaded by forces parallel to the plane of the plate, the stress components are given by

$$\sigma_{11} = \frac{E}{1-\nu^2}\left(\epsilon_{11} + \nu\epsilon_{22}\right) \qquad \sigma_{22} = \frac{E}{1-\nu^2}\left(\epsilon_{22} + \nu\epsilon_{11}\right) \qquad \sigma_{12} = 2G\epsilon_{12} \tag{D.14}$$

where $E > 0$ denotes Young's modulus, and $\nu < 1$ designates Poisson's ratio. Comparing the stress σ_{12} in Equation (D.13) with that of Equation (D.14), the shear modulus G coincides with the first Lamé parameter μ. A comparison of the main diagonal elements σ_{ii} of the stress furnish the relations

$$\boxed{\nu = \frac{\lambda}{\lambda + 2\mu}} \qquad \boxed{E = 4\,\mu\,\frac{\lambda + \mu}{\lambda + 2\mu}} \tag{D.15}$$

after solving a system of algebraic linear equations, which are obviously different from the well-known relations for the three-dimensional case (see Ciarlet [133]). Particularly, in the case of plane stress, Poisson's ratio is smaller than one and not smaller than a half.

REFERENCES

[1] Belytschko T. and Schoeberle D.F. On the Unconditional Stability of an Implicit Algorithm for Nonlinear Structural Dynamics. *Journal of Applied Mechanics*, 42:865–869, 1975.

[2] Hughes T.J.R. Stability, convergence and growth and decay of energy of the average acceleration method in nonlinear structural dynamics. *Computers & Structures*, 6:313–324, 1976.

[3] Simo J.C. and Tarnow N. The Discrete Energy-Momentum Method. Conserving Algorithms for Nonlinear Elastodynamics. *Z. angew. Math. Phys.*, 43:757–792, 1992.

[4] Crisfield M.A. and Shi J. A Co-rotational Element/Time-Integration Strategy for Non-linear Dynamics. *Int. J. Numer. Methods Engrg.*, 37:1897–1913, 1994.

[5] Richtmyer R.B. and Morton K.W. *Difference Methods for Initial-Value Problems.* Interscience, New York, 2nd edition, 1967.

[6] Wood W.L. *Practical Time-stepping Schemes.* Oxford University Press, New York, 1990.

[7] LaBudde R.A. and Greenspan D. Energy and Momentum Conserving Methods of Arbitrary Order for the Numerical Integration of Equations of Motion I. Motion of a Single Particle. *Numer. Math.*, 25:323–346, 1976.

[8] LaBudde R.A. and Greenspan D. Energy and Momentum Conserving Methods of Arbitrary Order for the Numerical Integration of Equations of Motion II. Motion of a System of Particles. *Numer. Math.*, 26:1–16, 1976.

[9] Simo J.C., Tarnow N. and Wong K.K. Exact Energy-Momentum Conserving Algorithms and Symplectic Schemes for Nonlinear Dynamics. *Comput. Methods Appl. Mech. Engrg.*, 100:63–116, 1992.

[10] Gonzalez O. Exact Energy and Momentum Conserving Algorithms for General Models in Nonlinear Elasticity. *Comput. Methods Appl. Mech. Engrg.*, 190:1763–1783, 2000.

[11] Greenspan D. Conservative Numerical Methods for $\ddot{x} = f(x)$. *Journal of Computational Physics*, 56:28–41, 1984.

[12] Greenspan D. Completely Conservative, Covariant Numerical Methodology. *Computers and Mathematics with Applications*, 29:37–43, 1995.

[13] Greenspan D. *Discrete Models.* Addison-Wesley, 1973.

[14] Gonzalez O. and Simo J.C. On the Stability of Symplectic and Energy-Momentum Algorithms for Nonlinear Hamiltonian Systems with Symmetry. *Comput. Methods Appl. Mech. Engrg.*, 134:197–222, 1996.

[15] Sansour C., Wriggers P. and Sansour J. On the Design of Energy-Momentum Integration Schemes for Arbitrary Continuum Formulations. Applications to Classical and Chaotic Motion of Shells. *Int. J. Numer. Methods Engrg.*, 60:2419–2440, 2004.

[16] Groß M., Betsch P. and Steinmann P. Conservation properties of a time FE method. Part IV: Higher order energy and momentum conserving schemes. *Int. J. Numer. Methods Engng.*, 63:1849–1897, 2005.

[17] Hughes T.J.R., Caughey T.K. and Liu W.K. Finite-Element Methods for Nonlinear Elastodynamics which Conserve Energy. *Journal of Applied Mechanics*, 45:366–370, 1978.

[18] Laursen T.A. and Meng X.N. A New Solution Procedure for Application of Energy-Conserving Algorithms to General Constititive Models in Nonlinear Elastodynamics. *Comput. Methods Appl. Mech. Engrg.*, 190:6309–6322, 2001.

[19] Simo J.C. and Tarnow N. A New Energy and Momentum Conserving Algorithm for The Non-Linear Dynamics of Shells. *Int. J. Numer. Methods Engrg.*, 37:2527–2549, 1994.

[20] Simo J.C., Tarnow N. and Doblare M. Non-linear Dynamics of Three-dimensional Rods: Exact Energy and Momentum Conserving Algorithms. *Int. J. Numer. Methods Engrg.*, 38:1431–1473, 1995.

[21] Crisfield M.A. and Shi J. An Energy Conserving Co-rotational Procedure for Non-linear Dynamics with Finite Elements. *Nonlinear Dynamics*, 9:37–52, 1996.

[22] Galvanetto U. and Crisfield M.A. An Energy-conserving Co-rotational Procedure for the Dynamics of Planar Beam Structures. *Int. J. Numer. Methods Engrg.*, 39:2265–2282, 1996.

[23] Zhong H.G. and Crisfield M.A. An Energy Conserving Co-rotational Procedure for the Dynamics of Shell Structures. *Engrg. Comput.*, 15:552–576, 1998.

[24] Stander N. and Stein E. An Energy-Conserving Planar Finite Beam Element for Dynamics of Flexible Mechanisms. *Engrg. Comput.*, 6:60–85, 1996.

[25] Brank B. An Energy Conserving Non-linear Dynamic Finite Element Formulation for Flexible Composite Laminates. *Computers and Structures*, 80:677–689, 2002.

[26] Brank B., Briseghella L., Tonello N. and Damjanic F.B. On Non-linear Dynamics of Shells: Implementation of Energy-Momentum Conserving Algorithm for a Finite Rotation Shell Model. *Int. J. Numer. Methods Engrg.*, 42:409–442, 1998.

[27] Kuhl D. and Ramm E. Constraint Energy Momentum Algorithm and its Application to Non-linear Dynamics of Shells. *Comput. Methods Appl. Mech. Engrg.*, 136:293–315, 1996.

[28] Hilber H.M., Hughes T.J.R. and Taylor R.L. Improved Numerical Dissipation for Time Integration Algorithms in Structural Dynamics. *Earthquake Engineering and Structural Dynamics*, 5:283–292, 1977.

[29] Strang G. and Fix G.J. *An Analysis of the Finite Element Method.* Prentice-Hall, Englewood Cliffs, N.J., 1973.

[30] Armero F. and Romero I. On the Formulation of High-frequency Dissipative Time-Stepping Algorithmns for Nonlinear Dynamics. Part I: Low-order Methods for Two Model Problems and Nonlinear Elastodynamics. *Comput. Methods Appl. Mech. Engrg.*, 190:2603–2649, 2001.

[31] Armero F. and Romero I. On the Formulation of High-frequency Dissipative Time-Stepping Algorithmns for Nonlinear Dynamics. Part II: Second Order Methods. *Comput. Methods Appl. Mech. Engrg.*, 190:6783–6824, 2001.

[32] Ibrahimbegovic A. and Mamouri S. Energy Conserving/Decaying Implicit Time-Stepping Scheme for Nonlinear Dynamics of Three-Dimensional Beams Undergoing Finite Rotations. *Comput. Methods Appl. Mech. Engrg.*, 191:4241–4258, 2002.

[33] Gonzalez O. Time Integration and Discrete Hamiltonian Systems. *Journal of Nonlinear Science*, 6:449–467, 1996.

[34] Simo J.C. and Gonzalez O. Assessment of Energy-Momentum and Symplectic Schemes for Stiff Dynamical Systems. In *American Society of Mechanical Engineers*, New Orleans, Louisiana, 1993. ASME Winter Annual Meeting.

[35] Groß M. *Conserving Time Integrators for Nonlinear Elastodynamics.* Ph.D. Dissertation, UKL/LTM T 04-01, Department of Mechanical Engineering, University of Kaiserslautern, 2004.

[36] Eriksson K., Estep D., Hansbo P., and Johnson C. *Computational Differential Equations.* Cambridge University Press, 1996.

[37] Lasaint P. and Raviart P.A. On a finite element method for solving the neutron transport equation. In Carl de Boor (Ed.), *Mathematical Aspects of Finite Elements in Partial Differential Equations*, p. 89–123. Academic Press, 1974.

[38] Cockburn B. Discontinuous Galerkin Methods. *Z. Angew. Math. Meth.*, 11:731–754, 2003.

[39] Thomee V. *Galerkin Finite Element Methods for Parabolic Problems.* Springer, Berlin, 1997.

[40] Hughes T.J.R. and Hulbert G.M. Space-time finite element methods for elastodynamics: Formulations and error estimates. *Comput. Methods Appl. Mech. Engrg.*, 66:339–363, 1988.

[41] Hulbert G.M. Time finite element methods for structural dynamics. *Int. J. Numer. Methods Engrg.*, 33:307–331, 1992.

[42] Hulbert G.M. A unified set of single-step asymptotic annihilation algorithms for structural dynamics. *Comput. Methods Appl. Mech. Engrg.*, 113:1–9, 1994.

[43] Li X.D. and Wiberg N.E. Structural Dynamic Analysis by a Time-Discontinuous Galerkin Finite Element Method. *Int. J. Numer. Methods Engrg.*, 39:2131–2152, 1996.

[44] Li X.D. and Wiberg N.E. Implementation and Adaptivity of a Space-Time Finite Element Method for Structural Dynamics. *Comput. Methods Appl. Mech. Engrg.*, 156:211–229, 1998.

[45] Wiberg N.E. and Li X.D. Adaptive Finite Element Procedures for Linear and Non-linear Dynamics. *Int. J. Numer. Methods Engrg.*, 46:1781–1802, 1999.

[46] Bonelli A. and Bursi O.S. Iterative Solutions for Implicit Time Discontinuous Galerkin Methods Applied to Non-linear Elastodynamics. *Computational Mechanics*, 30:487–498, 2003.

[47] Bottasso C.L. A New Look at Finite Elements in Time: A Variational Interpretation of Runge-Kutta Methods. *Applied Numerical Mathematics*, 25:355–368, 1997.

[48] Bauchau O.A. and Theron N.J. Energy decaying scheme for non-linear beam models. *Comput. Methods Appl. Mech. Engrg.*, 134:37–56, 1996.

[49] Bauchau O.A. and Bottasso C.L. On the design of energy preserving and decaying schemes for flexible nonlinear multi-body systems. *Comput. Methods Appl. Mech. Engrg.*, 169:61–79, 1999.

[50] Groß M., Betsch P. and Steinmann P. Comparison of Galerkin Methods applied to Classical Mechanics. UKL/LTM J 00-07, Department of Mechanical Engineering, University of Kaiserslautern, 2000.

[51] Groß M. Time-Stepping Schemes for Nonlinear Hamiltonian Systems Based on the Discontinuous Galerkin Method. Diploma Thesis, UKL/LTM U 00-02, Department of Mechanical Engineering, University of Kaiserslautern, 2000.

[52] Wriggers P. *Nichtlineare Finite-Elemente-Methoden.* Springer, 2001.

[53] Larson M.G. and Niklasson A.J. Conservation Properties for the Continuous and Discontinuous Galerkin Methods. *Chalmers Finite Element Center*, Preprint 2000-08, Göteborg, Sweden, 2001.

[54] Douglas J. Jr. and Dupont T. Galerkin methods for parabolic equations. *SIAM J. Numer. Anal.*, 7:575–626, 1970.

[55] Swartz B. and Wendroff B. Generalized Finite-Difference Schemes. *Math. Comp.*, 23:37–49, 1969.

[56] Hulme B.L. Discrete Galerkin and Related One-Step Methods for Ordinary Differential Equations. *Mathematics of Computation*, 26:881–891, 1972.

[57] Hulme B.L. One-Step Piecewise Polynomial Galerkin Methods for Initial Value Problems. *Mathematics of Computation*, 26:415–426, 1972.

[58] Fairweather G. *Finite element Galerkin methods for differential equations.* Dekker, New York, 1978.

[59] Aziz A.K. and Monk P. Continuous Finite Element in Space and Time for the Heat Equation. *Math. Comp.*, 52:255–274, 1989.

[60] Winther R. A Stable Finite Element Method for Initial-Boundary Value Problems for First-Order Hyperbolic Systems. *Math. Comp.*, 36:65–86, 1981.

[61] French D.A. and Schaeffer J.W. Continuous Finite Element Methods which Preserve Energy Properties for Nonlinear Problems. *Applied Mathematics and Computation*, 39:271–295, 1990.

[62] French D.A. and Peterson T.E. A Continuous Space-Time Finite Element Method for the Wave Equation. *Math. Comp.*, 65:491–506, 1996.

[63] Betsch P. and Steinmann P. Inherently Energy Conserving Time Finite Elements for Classical Mechanics. *Journal of Computational Physics*, 160:88–116, 2000.

[64] Larson M.G. and Niklasson J. Conservation Properties for the Continuous and Discontinuous Galerkin Methods. Chalmers Finite Element Center, preprint 2000-08, 2001.

[65] Betsch P. and Steinmann P. Conservation Properties of a Time FE Method. Part I: Time-Stepping Schemes for N-Body Problems. *Int. J. Numer. Methods Engng.*, 49:599–638, 2000.

[66] Betsch P. and Steinmann P. Conservation Properties of a Time FE Method. Part II: Time-Stepping Schemes for Nonlinear Elastodynamics. *Int. J. Numer. Methods Engng.*, 50:1931–1955, 2001.

[67] Betsch P. and Steinmann P. Conservation Properties of a Time FE Method. Part III: Mechanical Systems with Holonomic Constraints. *Int. J. Numer. Methods Engng.*, 53:2271–2304, 2002.

[68] Simo J.C. Algorithms for Static and Dynamic Multiplicative Plasticity that Preserve the Classical Return Mapping Schemes of the Infinitesimal Theory. *Comput. Methods Appl. Mech. Engrg.*, 99:61–112, 1992.

[69] Meng X.N. and Laursen T.A. Energy Consistent Algorithms for Dynamic Finite Deformation Plasticity. *Comput. Methods Appl. Mech. Engrg.*, 191:1639–1675, 2002.

[70] Noels L., Stainier L. and Ponthot J.P. An Energy-Momentum Conserving Algorithm Using The Variational Formulation of Visco-Plastic Updates. *Int. J. Numer. Methods Engrg*, 65:904–942, 2006.

[71] Ortiz M. and Stainier L. The Variational Formulation of Viscoplastic Constitutive Updates. *Comput. Methods Appl. Mech. Engrg.*, 171:419–444, 1999.

[72] Noels L., Stainier L. and Ponthot J.P. A first-order energy-dissipative momentum-conserving scheme for elasto-plasticity using the variational updates formulation. *Comput. Methods Appl. Mech. Engrg.*, 197:706–726, 2008.

[73] Armero F. Energy-dissipative momentum-conserving time-stepping algorithms for finite strain multiplicative plasticity. *Comput. Methods Appl. Mech. Engrg.*, 195:4862–4889, 2006.

[74] Armero F. and Zambrana-Rojas C. Volume-preserving energy-momentum schemes for isochoric multiplicative plasticity. *Comput. Methods Appl. Mech. Engrg.*, 196:4130–4159, 2007.

[75] Armero F. Assumed strain finite element methods for conserving temporal integrations in non-linear solid dynamics. *Int. J. Numer. Methods Engrg.*, 74:1795–1847, 2008.

[76] Love E. and Sulsky D.L. An energy-consistent material-point method for dynamic finite deformation plasticity. *Int. J. Numer. Methods Engrg.*, 65:1608–1638, 2006.

[77] Mohr R., Menzel A. and Steinmann P. A consistent time FE-method for large strain elasto-plasto-dynamics. *Comput. Methods Appl. Mech. Engrg.*, 197:3024–3044, 2008.

[78] Mohr R. *Consistent Time-Integration of Finite Elasto-Plasto-Dynamics.* Ph.D. Dissertation, UKL/LTM T 08-04, Department of Mechanical Engineering, University of Kaiserslautern, 2008.

[79] Papadopoulos P. and Taylor R.L. On the application of multistep integration methods to infinitesimal elastoplasticity. *Int. J. Numer. Methods Engrg.*, 37:3169–3184, 1994.

[80] Büttner J. and Simeon B. Runge-Kutta methods in elastoplasticity. *Applied Numerical Mathematics*, 41:443–458, 2002.

[81] Simo J.C. and Ortiz M. A Unified Approach to Finite Deformation Elastoplastic Analysis Based on the Use of Hyperelastic Constitutive Equations. *Comput. Methods Appl. Mech. Engrg.*, 49:221–245, 1985.

[82] Pinsky P.M., Ortiz M. and Pister K.S. Numerical Integration of Rate Constitutive Equations in Finite Deformation Analysis. *Comput. Methods Appl. Mech. Engrg.*, 40:137–158, 1983.

[83] Noels L., Stainier L., and Ponthot J.P. An Energy-Momentum Conserving Algorithm for Non-linear Hypoelastic Constitutive Models. *Int. J. Numer. Methods Engrg*, 59:83–114, 2004.

[84] Noels L., Stainier L. and Ponthot J.P. On The Use of Large Time Steps with An Energy-Momentum Conserving Algorithm for Non-linear Hypoelastic Constitutive Models. *International Journal of Solids and Structures*, 41:663–693, 2004.

[85] Groß M. and Betsch P. Galerkin Methods in Time for Semi-Discrete Viscoelastodynamics. *Proc. Appl. Math. Mech.*, 5:397–398, 2005.

[86] Groß M. and Betsch P. Galerkin-based discretisation of infinite-dimensional dissipative dynamical systems. *Proceedings of the ICCES Conference in India*, p. 2646–2651, 2005.

[87] Gross M. and Betsch P. An energy consistent hyprid space-time Galerkin method for nonlinear thermomechanical problems. *Proc. Appl. Math. Mech.*, 6:443–444, 2006.

[88] Groß M. and Betsch P. An energy consistent hybrid space-time finite element method for nonlinear thermo-viscoelastodynamics. *Comp. Methods for Coupled Problems in Science and Engineering*, 2:413–416, 2007.

[89] Groß M. and Betsch P. On Deriving Higher-Order and Energy-Momentum-Consistent Time-Stepping-Schemes for Thermo-Viscoelastodynamics from a New Hybrid Space-Time Galerkin Method. *Proceedings of the Multibody Dynamics Conference in Milano*, 2007.

[90] Groß M. and Betsch P. Higher-order energy consistent time integrators for nonlinear thermo-viscoelastodynamics. *Proc. Appl. Math. Mech.*, accepted for publication.

[91] Groß M. and Betsch P. Stable long-term simulation of dynamically loaded elastomers. *Proc. Appl. Math. Mech.*, submitted for publication.

[92] Green A. and Naghdi P. A re-examination of the basic postulates of thermomechanics. *Proc. R. Soc. Lond.*, 432:171–194, 1991.

[93] Bargmann S. *Theory and numerics of non-classical thermo-hyperelasticity.* Ph.D. Dissertation, UKL/LTM T 08-02, Department of Mechanical Engineering, University of Kaiserslautern, 2008.

[94] Bargmann S. and Steinmann P. Finite element approaches to non-classical heat conduction in solids. *Comput. Model. Eng. Sci.*, 9:133–150, 2005.

[95] Bargmann S. and Steinmann P. Theoretical and computational aspects of non-classical thermoelasticity. *Comput. Methods Appl. Mech. Engrg.*, 196:516–527, 2006.

[96] Haupt P. *Continuum Mechanics and Theory of Materials.* Springer, Berlin, 2002.

[97] Green M.S. and Tobolsky A.V. A New Approach to the Theory of Relaxing Polymeric Media. *The Journal of Chemical Physics*, 14:80–92, 1985.

[98] Lubliner J. A Model of Rubber Viscoelasticity. *Mechanics Research Communications*, 12(2):93–99, 1985.

[99] Simo J.C. On a Fully Three-Dimensional Finite-Strain Viscoelastic Damage Model: Formulation and Computational Aspects. *Comput. Methods Appl. Mech. Engrg.*, 60:153–173, 1987.

[100] Holzapfel G.A. On Large Strain Viscoelasticity: Continuum Formulation and Finite Element Applications to Elastomeric Structures. *Int. J. Numer. Methods Engrg.*, 39:3903–3926, 1996.

[101] Le Tallec P., Rahier C. and Kaiss A. Three-dimensional Incompressible Viscoelasticity in Large Strains: Formulation and Numerical Approximation. *Comput. Methods Appl. Mech. Engrg.*, 109:233–258, 1993.

[102] Reese S. and Govindjee S. A Theory of Finite Viscoelasticity and Numerical Aspects. *Int. J. of Solids and Structures*, 35:3455–3482, 1998.

[103] Weber G. and Anand L. Finite Deformation Constitutive Equations and a Time Integration Procedure for Isotropic, Hyperelastic-Viscoplastic Solids. *Comput. Methods Appl. Mech. Engrg.*, 79:173–202, 1990.

[104] Miehe C. and Stein E. A canonical model of multiplicative elasto-plasticity. Formulation and aspects of the numerical implementation. *Eur. J. Mech. A/Solids*, 11:25–43, 1992.

[105] Miehe C. Exponential Map Algorithm for stress updates in anisotropic multiplicative elastoplasticity for single crystals. *Int. J. Numer. Methods Engrg.*, 39:3367–3390, 1996.

[106] Ogden R.W. *Non-Linear Elastic Deformations.* Wiley, Chichester, 1984.

[107] Reese S. *Thermomechanische Modellierung gummiartiger Polymerstrukturen.* Habilitationsschrift, F 01/4, Institut für Baumechanik und Numerische Mechanik, Universität Hannover, 2001.

[108] Diebels S., Ellsiepen P. and Ehlers W. Error-controlled Runge-Kutta Time Integration of a Viscoplastic Hybrid Two-phase Model. *Technische Mechanik*, 19:19–29, 1999.

[109] Hairer E., Norsett S. and Wanner G. *Solving Ordinary Differential Equations I.* Springer, 1987.

[110] Hairer E. and Wanner G. *Solving Ordinary Differential Equations II.* Springer, 1991.

[111] Kirchner E. and Simeon B. A Higher-Order Time Integration Method for Viscoplasticity. *Comput. Methods Appl. Mech. Engrg.*, 175:1–18, 1999.

[112] Ascher U.M. and Petzold L.R. *Computer Methods for Ordinary Differential Equations and Differential-Algebraic Equations.* SIAM, Philadelphia, 1998.

[113] Brenan K.E., Campbell S.L. and Petzold L.R. *The Numerical Solution of Initial Value Problems in Ordinary Differential-Algebraic Equations.* SIAM, New York, 2nd edition, 1995.

[114] Hartmann S. Computation in Finite-Strain Viscoelasticity: Finite Elements Based on the Interpretation as Differential-Algebraic Equations. *Comput. Methods Appl. Mech. Engrg.*, 191:1439–1470, 2002.

[115] Ellsiepen P. and Hartmann S. Remarks on the Interpretation of Current Nonlinear Finite Element Analyses as Differential-Algebraic Equations. *Int. J. Numer. Methods Engrg.*, 51:679–707, 2001.

[116] Eringen A.C. *Mechanics of Continua.* Wiley, London, 1967.

[117] Oden J.T. *Finite Elements of Nonlinear Continua.* McGraw-Hill, New York, 1972.

[118] Argyris J.H. and Doltsinis J.S. On the Natural Formulation and Analysis of Large Deformation Coupled Thermomechanical Problems. *Comput. Methods Appl. Mech. Engrg.*, 25:195–253, 1981.

[119] Argyris J.H., Doltsinis J.S., Pimenta P.M. and Wüstenberg H. Thermomechanical Response of Solids at High Strains - Natural Approach. *Comput. Methods Appl. Mech. Engrg.*, 32:3–57, 1982.

[120] Park K.C. and Felippa C.A. Partitioned Analysis of Coupled Problems. In Belytschko T. and Hughes T.J.R. (Eds.), *Computational Methods in Transient Analysis.* North-Holland, Amsterdam, 1983.

[121] Simo J.C. and Miehe C. Associative Coupled Thermoplasticity at Finite Strains: Formulation, Numerical Analysis and Implementation. *Comput. Methods Appl. Mech. Engrg.*, 98:41–104, 1992.

[122] Yanenko N.N. *The Method of Fractional Steps.* Springer, New York, 1971.

[123] Armero F. and Simo J.C. A New Unconditionally Stable Fractional Step Method For Non-linear Coupled Thermomechanical Problems. *Int. J. Numer. Methods Engrg*, 35:737–766, 1992.

[124] Miehe C. Entropic Thermoelasticity at Finite Strains: Aspects of the Formulation and Numerical Implementation. *Comput. Methods Appl. Mech. Engrg.*, 120:243–269, 1995.

[125] Holzapfel G.A. and Simo J.C. Entropy Elasticity of Isotropic Rubber-like Solids at Finite Strains. *Comput. Methods Appl. Mech. Engrg.*, 132:17–44, 1996.

[126] Farhat C., Park K.C. and Dubois Pelerin Y. An Unconditionally Stable Staggered Algorithm for Transient Finite Element Analysis of Coupled Thermoelastic Problems. *Comput. Methods Appl. Mech. Engrg.*, 85:349–365, 1991.

[127] Ibrahimbegovic A., Chorfi L., and Gharzeddine F. Thermomechanical Coupling at Finite Elastic Strain: Covariant Formulation and Numerical Implementation. *Commun. Numer. Methods Engng.*, 17:275–289, 2001.

[128] Miehe C. *Zur numerischen Behandlung thermomechanischer Prozesse.* Dissertation, F 88/6, Institut für Baumechanik und Numerische Mechanik, Universität Hannover, 1988.

[129] Holzapfel G.A. and Simo J.C. A New Viscoelastic Constitutive Model For Continuous Media at Finite Thermomechanical Changes. *Int. J. Solids Structures*, 33:3019–3034, 1996.

[130] Reese S. and Govindjee S. Theoretical and Numerical Aspects in the Thermoviscoelastic Material Behaviour of Rubber-Like Polymers. *Mechanics of Time-Dependent Materials*, 1:357–396, 1998.

[131] Marsden J.E. and Hughes T.J.R. *Mathematical Foundations of Elasticity.* Dover, New York, 1994.

[132] Abraham R., Marsden J.E. and Ratiu T.S. *Manifolds, Tensor Analysis and Applications.* Springer, New York, 1988.

[133] Ciarlet P.G. *Mathematical Elasticity.* Elsevier, Amsterdam, 1988.

[134] Bertram A. *Axiomatische Einführung in die Kontinuumsmechanik.* BI-Wissenschaftsverlag, Mannheim, 1989.

[135] Holzapfel G.A. *Nonlinear Solid Mechanics.* Wiley, Chichester, 2000.

[136] Simo J.C., Marsden J.E. and Krishnaprasad P.S. The Hamiltonian Structure of Nonlinear Elasticity: The Material and Convective Representations of Solids, Rods and Plates. *Arch. Rational Mech. Anal.*, 104:125-183, 1988.

[137] Simo J.C., Lewis D. and Marsden J.E. Stability of Relative Equilibria. Part I: The Reduced Energy-Momentum Method. *Arch. Rational Mech. Anal.*, 115:15-59, 1991.

[138] Noll W. A New Mathematical Theory of Simple Materials. *Arch. Rational Mech. Anal.*, 48:1-50, 1972.

[139] Bertram A. An alternative approach to finite plasticity based on material isomorphisms. *Int. J. of Plasticity*, 52:353–374, 1998.

[140] Bertram A. Finite thermoplasticity based on isomorphisms. *Int. J. of Plasticity*, 19:2027–2050, 2003.

[141] Bertram A. Material systems - a framework for the description of material behaviour. *Mech. Anal.*, 80:99–133, 1982.

[142] Miehe C. *Kanonische Modelle multiplikativer Elastoplastizität. Thermodynamische Formulierung und numerische Implementation.* Habilitationsschrift, F 93/1, Institut für Baumechanik und Numerische Mechanik, Universität Hannover, 1993.

[143] Betsch P. and Stein E. Numerical implementation of multiplicative elastoplasticity into assumed strain elements with application to shells at large strains. *Comput. Methods Appl. Mech. Eng.*, 179:215–245, 1999.

[144] Betsch P. and Steinmann P. Derivation of the fourth-order tangent operator based on a generalized eigenvalue problem. *Int. J. Solids Structures*, 37:1615–1628, 2000.

[145] Miehe C. *Geometrical Methods of Nonlinear Continuum Mechanics*. Lecture notes. Institute of Applied Mechanics – Chair I, Stuttgart, Germany, 2001.

[146] Truesdell C.A. and Toupin R. *The classical field theories*. In Flügge's Handbuch der Physik, Vol. 3, Part 1, p. 226-793. Springer, Berlin, 1960.

[147] Malvern L.E. *Indroduction to the Mechanics of a Continuous Medium*. Prentice-Hall, Englewood Cliffs (N.J.), 1969.

[148] Hutter K. The Foundations of Thermodynamics, Its Basic Postulates and Implications. A Review of Modern Thermodynamics. *Acta Mechanica*, 27:1–54, 1977.

[149] Simo J.C. Nonlinear stability of the time-discrete variational problem of evolution in nonlinear heat conduction, plasticity and viscoplasticity. *Comput. Methods Appl. Mech. Engrg.*, 88:111–131, 1991.

[150] Kaliske M. *Zur Theorie und Numerik von Polymerstrukturen unter statischen und dynamischen Einwirkungen*. Dissertation, Mitteilung Nr. 41-95, Institut für Statik, Universität Hannover, 1995.

[151] Gurtin M.E. *An Introduction to Continuum Mechanics*. Academic Press, New York, 1981.

[152] Kuypers F. *Klassische Mechanik*. Wiley-VCH, Berlin, 2008.

[153] Marsden J.E. and Ratiu T.S. *Introduction to Mechanics and Symmetry*. Springer, New York, 1999.

[154] Hahn W. *Stability of Motion*. Springer, Berlin, 1967.

[155] Gurtin M.E. Thermodynamics and stability. *Arch. Rational Mech. Anal.*, 59:63-96, 1975.

[156] Simo J.C. Numerical analysis and simulation of plasticity. In Ciarlet P.G and Lions J.L. (Eds.), *Handbook of Numerical Analysis*, Vol. VI. Elsevier, North Holland, 1998.

[157] Laursen T.A. On the development of thermodynamically consistent algorithms for thermomechanical frictional contact. *Comput. Methods Appl. Mech. Engrg.*, 177:273–287, 1999.

[158] Antman S.S. and Osborn J.E. The Principle of Virtual Work and Integral Laws of Motion. *Arch. Rational Mech. Anal.*, 69:231–262, 1979.

[159] Hansbo P. A note on energy conservation for Hamiltonian systems using continuous time finite elements. *Commun. Numer. Methods Engng.*, 17:863–869, 2001.

[160] Hughes T.J.R. *The Finite Element Method.* Dover, Mineola, 2000.

[161] Belytschko T., Liu W.K. and Moran B. *Nonlinear Finite Elements for Continua and Structures.* Wiley, Chichester, 2000.

[162] Oden J.T. *Finite Elements of Nonlinear Continua.* McGraw-Hill, New York, 1972.

[163] Simo J.C., Taylor R.L. and Wriggers P. A note on finite-element implementation of pressure boundary loading. *Comm. Appl. Numer. Methods*, 7:513–525, 1991.

[164] Wriggers P., Miehe C., Kleiber M. and Simo J.C. On the coupled thermomechanical treatment of necking problems via finite element methods. *Int. J. Numer. Methods Engrg.*, 33:869–883, 1992.

[165] Gonzalez O. *Design and Analysis of Conserving Integrators for Nonlinear Hamiltonian Systems with Symmetry.* Ph.D. Dissertation, SUDAM Report No. 96-x, Department of Mechanical Engineering, Stanford University, Stanford California, 1996.

[166] Denzer R., Barth F.J. and Steinmann P. Studies in elastic fracture mechanics based on the material force method. *Int. J. Numer. Methods Engrg.*, 58:1817–1835, 2003.

[167] Zienkiewicz O.C. and Zhu J.Z. The superconvergent patch recovery and a posteriori error estimates. Part I: The Recovery Technique. *Int. J. Numer. Methods Engrg.*, 33:1331–1364, 1992.

[168] Hueck U. and Wriggers P. A formulation for the 4-node quadrilateral element. *Int. J. Numer. Methods Engrg.*, 38:3007–3037, 1995.

[169] Donea J. and Huerta A. *Finite Element Methods for Flow Problems.* Wiley, Chichester, 2003.

[170] Johnson M.A. and Beatty M.F. A constitutive equation for the Mullins effect in stress controlled uniaxial extension experiments. *Continuum Mechanics and Thermodynamics*, 5:301–318, 1993.

[171] Johnson M.A. and Beatty M.F. The Mullins effect in uniaxial extension and its influence on the transverse vibration of a rubber spring. *Continuum Mechanics and Thermodynamics*, 5:83–115, 1993.

[172] Nagtegaal J.C. and De Jong J.E. Some computational aspects of elastic-plastic large strain analysis. *Int. J. Numer. Methods Engrg.*, 17:15–41, 1981.

[173] Jiang H., Nguyen T.H. and Prud'homme M. Control of the boundary heat flux during the heating process of a solid material. *International Communications in Heat and Mass Transfer*, 32:728-738, 2005.

[174] Dascalu C. and Maugin G.A. The Thermoelastic Material-Momentum Equation. *Journal of Elasticity*, 39:201–212, 1995.

[175] Maugin G.A. and Kalpakides V.K. A Hamiltonian formulation for elasticity and thermoelastcity. *J. Phys. A: Math. Gen.*, 35:10775–10788, 2002.

[176] Müller M. and Betsch P. Mechanical integrators for mixed elements in nonlinear elastodynamics. Proc. Appl. Math. Mech, accepted for publication.

[177] Müller M., Groß M. and Betsch P. Material models in principal stretches for elastodynamics. Proc. Appl. Math. Mech, submitted for publication.

[178] Betsch P. *Computational Methods for Flexible Multibody Dynamics.* Habilitation thesis, UKL/LTM T 02-02, Department of Mechanical Engineering, University of Kaiserslautern, 2002.

[179] Johnson A.R. and Chen T.K. Coupled Thermo-Mechanical Analyses of Dynamically Loaded Rubber Cylinders. *Proceedings of the 32nd International SAMPE Technical Conference*, November 5-9 2000, Boston, M.A.

[180] Mergheim J. and Steinmann P. A geometrically nonlinear FE approach for the simulation of strong and weak discontinuities. *Comput. Methods Appl. Mech. Engrg.*, 195:5037–5052, 2006.

[181] Mergheim J. *Computational Modeling of Strong and Weak Discontinuities.* Ph.D. Dissertation, UKL/LTM T 06-01, Department of Mechanical Engineering, University of Kaiserslautern, 2006.

[182] Hesch C. and Betsch P. A mortar method for energy-momentum conserving schemes in frictionless dynamic contact problems. *Int. J. Numer. Methods Engrg.*, accepted for publication.

[183] Hesch C. Mechanische Integratoren für Kontaktvorgänge deformierbarer Körper unter großen Verzerrungen. Ph.D. Dissertation, Series of the Chair for Computational Mechanics, Volume 1, Department of Mechanical Engineering, University of Siegen, 2008.

[184] Laursen T.A. and Meng X.N. A New Solution Procedure for Application of Energy-Conserving Algorithms to General Constitutive Models in Nonlinear Elastodynamics. *Comput. Methods Appl. Mech. Engrg.*, 190:6309–6322, 2001.

[185] Knowles J.K. and Sternberg E. On the ellipticity of the equations of nonlinear elastostatics for a special material. *Journal of Elasticity*, 5:341–361, 1975.

[186] Ball J.M. Strict convexity, strong ellipticity, and regularity in the calculus of variations. *Math. Proc. Camb. Phil. Soc.* 87:501–513, 1980.

[187] Ball J.M. Convexity Conditions and Existence Theorems in Nonlinear Elasticity. *Arch. Rational Mech. Anal.*, 63:337-403, 1977.

[188] Kuhl E., Menzel A. and Garikipati K. On the convexity of transversely isotropic chain network models. Philosophical Magazine, 86:3241–3258, 2006.

[189] Shu H.P. and Wenji V.C. A compressible approach in finite element analysis of rubber-elastic materials. *Computers & Structures*, 62:573–593, 1997.

[190] Simo J.C. and Taylor R.L. Penalty function formulations for incompressible nonlinear elastostatics. *Comput. Methods Appl. Mech. Engrg.*, 35:107–118, 1982.

[191] Doll S. and Schweizerhof K. On the Development of Volumetric Strain Energy Functions. *Journal of Applied Mechanics*, 67:17–21, 2000.

[192] Carlson D.E. Linear Thermoelasticity. In *Encyclopedia of Physics*, Vol. VIa/2 (Mechanics of Solids II), p. 297-345, Series Ed. Flügge S. (Volume Ed. Truesdell C.). Springer, Berlin, 1972.

[193] Simo J.C. and Miehe C. Associative coupled thermoplasticity at finite strains: Formulation, numerical analysis and implementation. *Comput. Methods Appl. Mech. Engrg.*, 98:41–104, 1992.

[194] Timoshenko S.P. and Goodier J.N. *Theory of Elasticity.* McGraw-Hill, Kogakusha, 1934.

[195] Hahn H.G. *Elastizitätstheorie.* Teubner, Stuttgart, 1985.

[196] Roark R.J. and Young W.C. *Formulas for Stress and Strain.* McGraw-Hill, New York, 1975.

[197] Guo Zhong-heng. From Finite Elasticity to Linearised Theory. *Ingenieur-Archiv*, 52:121-129, 1982.

[198] Pabst W. The linear theory of thermoelasticity from the viewpoint of rational thermomechanics. *Ceramics-Silikáty*, 49(4):242-251, 2005.

Schriftenreihe des Lehrstuhls für Numerische Mechanik

Bisher in dieser Reihe erschienen:

Band I

Mechanische Integratoren für Kontaktvorgänge deformierbarer Körper unter großen Verzerrungen,
C. Hesch, Dissertation, 2007, urn:nbn:de:hbz:467-3156

Band II

Higher-order accurate and energy-momentum consistent discretisation of dynamic finite deformation thermo-viscoelasticity,
M. Groß, Habilitationsschrift, 2009, urn:nbn:de:hbz:467-3890